Institut für Theoretische Physik

Fakultät Mathematik und Naturwissenschaften

Technische Universität Dresden

QCD equation of state of hot deconfined matter at finite baryon density

A quasiparticle perspective

Dissertation

zur Erlangung des akademischen Grades

Doctor rerum naturalium

vorgelegt von

Marcus Bluhm

geboren am 21. Dezember 1977 in Finsterwalde

Dresden 2008

Man sollte die Dinge so nehmen, wie sie kommen. Aber man sollte auch dafür sorgen, dass sie so kommen, wie man sie nehmen möchte.

Curt Goetz

1. Gutachter: Prof. Dr. Burkhard Kämpfer

2. Gutachter: Prof. Dr. Jörg Aichelin

3. Gutachter: Prof. Dr. Dirk H. Rischke

Datum des Einreichens: 21. 07. 2008

Datum der Verteidigung: 15. 12. 2008

Kurzfassung

Das Quasiteilchenmodell, mit Quarks und Gluonen als elementare Freiheitsgrade, wurde zur Beschreibung der thermodynamischen Eigenschaften eines heißen Plasmas stark wechselwirkender Materie entwickelt. Dies ist von herausragender Bedeutung sowohl für die Astrophysik und die Kosmologie als auch für die Beschreibung von relativistischen Schwerionenkollisionen. In der vorliegenden Arbeit wird dieses phänomenologische Modell erweitert, zum einen auf den Bereich imaginärer chemischer Potenziale, und zum anderen zur Betrachtung der Effekte von verschiedenen und unabhängigen chemischen Potenzialen verschiedener Quark-Spezies. Auf diese Weise kann der Einfluss endlicher Nettobaryonendichten auf die Zustandsgleichung selbstkonsistent studiert werden. Darüber hinaus wird eine Kette von Approximationen formeller mathematischer Umformungen vorgestellt, welche den Zusammenhang zwischen diesem Quasiteilchenbild und der fundamentalen Eichfeldtheorie der starken Wechselwirkung, QCD, herausstellt. Somit wird dem Modell eine theoretische Grundlage gegeben.

Die mit dem Quasiteilchenmodell erzielten Resultate für fundamentale thermodynamische Größen einschließlich verschiedene Suszeptibilitäten, darunter diagonale und nicht-diagonale Suszeptibilitäten, werden mit verfügbaren Gitter-QCD Daten verglichen. Insbesondere letztere stellen einen umfangreichen und sensiblen Test des Modells dar. Darüber hinaus werden sowohl thermodynamische Größen als auch das Phasendiagramm für imaginäres chemisches Potenzial betrachtet. Das Quasiteilchenmodell kann all diese Größen hervorragend beschreiben. Somit ist die Anwendbarkeit des Modells für die Extrapolation der Zustandsgleichung, wie sie von Gitter-QCD Rechnungen für verschwindende Baryonendichte bekannt ist, zu endlichen Baryonendichten erfolgreich getestet. Ebenso wird die Möglichkeit gezeigt, mittels des Modells zum chiralen Limes masseloser Quarks sowie zu asymptotisch großen Temperaturen zu extrapolieren. Diese Extrapolationen zeigen die Vorhersagekraft des Modells auf.

Aufgrund des Erfolgs des Modells in der Beschreibung von Gitter-QCD Resultaten, welcher das Bild stärkt, dass die heiße QCD-Phase durch Quark- und Gluonen-Freiheitsgrade mit medium-modifizierten Eigenschaften konsistent beschrieben werden kann, wird eine verlässliche Zustandsgleichung stark wechselwirkender Materie konstruiert. Effekte endlicher Baryonendichten werden ebenso untersucht, insbesondere entlang von isentropen Kurven im Phasendiagram. Skalierungseigenschaften dieser Zustandsgleichung mit fundamentalen Parametern der QCD wie der Anzahl aktiver Quark-Freiheitsgrade, deren Massen sowie dem numerischen Wert der Phasenübergangstemperatur zwischen Quark-Gluon-Plasma-Phase und hadronischer Phase werden studiert. Die Robustheit der Zustandsgleichung in den Regionen großer und kleiner Energiedichten wird diskutiert, und Unsicherheiten in der Phasenübergangsregion wird durch die Konstruktion einer ganzen Familie von Zustandsgleichungen Rechnung getragen. Die einzelnen Familienmitglieder unterscheiden sich dabei lediglich in der Form der Interpolation zwischen der Region hoher Energiedichte und einem Hadronen-Resonanz-Gas-Modell, welches eine

realistische Beschreibung für kleine Energiedichten darstellt.

Die konstruierte Familie von Zustandsgleichungen wird in hydrodynamischen Simulationen relativistischer Schwerionenkollisionen verwendet. Implikationen der Unterschiede in der Phasenübergangsregion in den einzelnen Zustandsgleichungen werden anhand von transversalen Impulsspektren und dem differenziellen elliptischen Fluss verschiedener Hadronen untersucht. In diesen Untersuchungen, welche für Bedingungen relevant am LHC und am RHIC bei maximaler Energie sind, liegt der Fokus auf direkt emittierten Hadronen, insbesondere auf seltsamen Baryonen. In Hinblick auf das FAIR-Experiment wird zusätzlich der mögliche Einfluss des QCD kritischen Punkts auf die Zustandsgleichung studiert, zunächst in einem exemplarischen Modell und dann für das Quasiteilchenmodell.

Abstract

The quasiparticle model, based on quark and gluon degrees of freedom, has been developed for the description of the thermodynamics of a hot plasma of strongly interacting matter which is of enormous relevance in astrophysics, cosmology and for relativistic heavy-ion collisions as well. In the present work, this phenomenological model is extended into the realm of imaginary chemical potential and towards including, in general, different and independent quark flavour chemical potentials. In this way, nonzero net baryon-density effects in the equation of state are self-consistently attainable. Furthermore, a chain of approximations based on formal mathematical manipulations is presented which outlines the connection of the quasiparticle model with the underlying gauge field theory of strong interactions, QCD, putting the model on firmer ground.

A comparison of quasiparticle model results with available lattice QCD data for, e. g., basic bulk thermodynamic quantities and various susceptibilities such as diagonal and off-diagonal susceptibilities, which provide a rich and sensitive testing ground, is found to be successful. Furthermore, different thermodynamic quantities and the phase diagram for imaginary chemical potential are faithfully described. Thus, the applicability of the model to extrapolate the equation of state known from lattice QCD at zero baryon density to nonzero baryon densities is shown. In addition, the ability of the model to extrapolate results to the chiral limit and to asymptotically large temperatures is illustrated by confrontation with available first-principle lattice QCD results. These extrapolations demonstrate the predictive power of the model.

Basing on these successful comparisons supporting the idea that the hot deconfined phase can be described in a consistent picture by dressed quark and gluon degrees of freedom, a reliable QCD equation of state is constructed and baryon-density effects are examined, also along isentropic evolutionary paths. Scaling properties of the equation of state with fundamental QCD parameters such as the number of active quark flavour degrees of freedom, the entering quark mass parameters or the numerical value of the deconfinement transition temperature are discussed, and the robustness of the equation of state in the regions of small and large energy densities is shown. Uncertainties arising in the transition region are taken into account by constructing a family of equations of state whose members differ from each other in the specific interpolation prescription between large energy density region and a realistic hadron resonance gas equation of state at low energy densities.

The obtained family of equations of state is applied in hydrodynamic simulations, and the implications of variations in the transition region are discussed by considering transverse momentum spectra and differential elliptic flow of directly emitted hadrons, in particular of strange baryons, for both, RHIC top energy and LHC conditions. Finally, with regard to FAIR physics, implications of the possible presence of a QCD critical point on the equation of state are outlined both, in an exemplary toy model and for an extended quasiparticle model.

Publications

1. B. Kämpfer, and M. Bluhm:
   Strangeness and charm in QCD matter,
   J. Phys. G **31**, S1141 (2005)

2. M. Bluhm, B. Kämpfer, and G. Soff:
   Quasi-particle model of strongly interacting matter,
   J. Phys. G **31**, S1151 (2005)

3. M. Bluhm, B. Kämpfer, and G. Soff:
   The QCD equation of state near T(c) within a quasi-particle model,
   Phys. Lett. B **620**, 131 (2005)

4. B. Kämpfer, M. Bluhm, R. Schulze, D. Seipt, and U. Heinz:
   QCD matter within a quasi-particle model and the critical end point,
   Nucl. Phys. A **774**, 757 (2006)

5. M. Bluhm, and B. Kämpfer:
   Quasi-particle perspective on critical end-point,
   Proc. Sci. **CPOD2006**, 004 (2006)

6. M. Bluhm, B. Kämpfer, R. Schulze, and D. Seipt:
   Isentropic equation of state of two-flavour QCD in a quasi-particle model,
   Acta Phys. Hung. A **27**, 397 (2006)

7. M. Bluhm, B. Kämpfer, R. Schulze, and D. Seipt:
   Quasi-Particle Description of Strongly Interacting Matter: Towards a Foundation,
   Eur. Phys. J. C **49**, 205 (2007)

8. M. Bluhm, B. Kämpfer, R. Schulze, D. Seipt, and U. Heinz:
   A family of equations of state based on lattice QCD: Impact on flow in ultra-relativistic heavy-ion collisions,
   Phys. Rev. C **76**, 034901 (2007)

9. M. Bluhm, R. Schulze, D. Seipt, and B. Kämpfer:
   Quasi-particle perspective on equation of state,
   AIP Conf. Proc. **892**, 387 (2007)

10. B. Kämpfer, M. Bluhm, H. Schade, R. Schulze, and D. Seipt:
    Do we know eventually p(e)?,
    Proc. Sci. **CPOD2007**, 007 (2007)

11. R. Schulze, M. Bluhm, and B. Kämpfer:
    Plasmons, plasminos and Landau damping in a quasiparticle model of the quark-gluon plasma,
    Eur. Phys. J. ST **155**, 177 (2008)

12. M. Bluhm, and B. Kämpfer:
    Quasiparticle model of quark-gluon plasma at imaginary chemical potential,
    Phys. Rev. D **77**, 034004 (2008)

13. N. Armesto, (ed.) et al.:
    Heavy Ion Collisions at the LHC - Last Call for Predictions,
    J. Phys. G **35**, 054001 (2008)

14. M. Bluhm, and B. Kämpfer:
    Flavor Diagonal and Off-Diagonal Susceptibilities in a Quasiparticle Model of the Quark-Gluon Plasma,
    Phys. Rev. D **77**, 114016 (2008)

Contents

List of Figures

1   Introduction

The visible matter in our universe consists of electrons and nucleons (protons and neutrons) where the latter, according to our understanding, emerged in an early stage of the cosmic evolution from a cooling plasma of quarks and gluons. The quark-gluon plasma was immersed in a plasma of leptons and photons. The fundamental interactions (with the exception of gravity) between these elementary constituents of matter can be described successfully within the framework of gauge field theories. For instance, quantum electrodynamics (QED) very successfully and very accurately describes electromagnetic phenomena.

Concerning strong interactions, the underlying gauge field theory is quantum chromodynamics (QCD) with quarks, carrying fractional baryonic and electric charges, and gluons (gauge bosons) as dynamical fields. In nature, six different quark flavour species are realized, namely *up*, *down*, *strange*, *charm*, *bottom* (or *beauty*) and *top*. The Lagrange density of QCD, $\mathcal{L}_{\mathrm{QCD}}$, depending on the quark fields ψ_q and the gluon fields A_{a}^{α} (cf. a basic introduction to QCD in Appendix A.1) represents the fundamental quantity describing QCD. In addition, parameters like the running coupling g, quark masses which constitute a quark mass matrix m_0, the number of different quark flavours N_f active in the system or the number of colours N_c ($N_c = 3$ is realized in nature) enter into $\mathcal{L}_{\mathrm{QCD}}$. An interesting property of QCD is asymptotic freedom [1, 2] which manifests in the fact that the strong coupling $\alpha_s = g^2/(4\pi)$ becomes small if the momentum scale Q, relevant for the considered process, becomes large. In the following chapters of the present work, the complexity of QCD, based on its non-Abelian gauge group character, will be accounted for by considering the dependencies on the various parameters mentioned above.

At finite temperature T and net baryon density n_B, strongly interacting matter in thermodynamic equilibrium is realized in a variety of different phases separated by phase transitions. The notion phase transition is used here in a loose sense as, strictly speeking, the different phases of strongly interacting matter are separated by either a true phase transition or rather an analytical crossover type of transformation. Basic quantity of interest is the QCD partition function Z (cf. Appendix A.2). From Z, all thermodynamic quantities can be evaluated via standard thermodynamic relations. The pressure $p(T, \mu)$ as a function of T and chemical potential μ follows from

$$p(T,\mu) = \frac{T}{V} \ln Z(T,\mu) \,, \tag{1.1}$$

where V is the volume of the investigated system, and from Euler's and Gibbs' relations one obtains

$$s = \frac{\partial p}{\partial T} \,, \quad n = \frac{\partial p}{\partial \mu} \,, \quad e = -p + Ts + \mu n \tag{1.2}$$

for entropy density s, net number density n associated with μ and energy density e.

Asymptotic freedom in QCD [1, 2] leads to the prediction of a transition of a QCD matter phase at low T and low n_B, which is dominated by hadrons in which quarks and gluons are confined, into a new deconfined phase of matter [3, 4] dubbed quark-gluon plasma (QGP) at high temperature and/or high baryon density. A theoretical description of the mechanism of the confinement/deconfinement process is still not established. Contrary to naive expectations, the QGP does not represent a weakly interacting gas of quarks and gluons but a strongly correlated system. Only at asymptotically high T or n_B quarks and gluons may become free.

Discussing QCD thermodynamics at moderate temperatures and baryon densities in the following, the focus represents the physically relevant case of two light (*up* and *down*) quarks and one heavier (*strange*) quark, denoted as $N_f = 2 + 1$. Individual quark flavour mass parameters read m_u, m_d and m_s for *up*, *down* and *strange* quarks, respectively. For $N_f = 2 + 1$, QCD matter changes from 8 active light hadronic degrees of freedom (3 pions, 4 kaons and eta) into 47.5 active quark and gluon degrees of freedom[1] during the deconfinement transition which is accompanied by rapid changes in e, s and p. Implicitly, temperature and chemical potential are assumed to be far below the mass scale introduced by the much heavier *charm*, *bottom* and *top* quarks which, consequently, turn out to be thermodynamically inactive in this regime. Nevertheless, heavy quarks represent interesting probes of QCD matter (see e. g. [5]).

The transition between hadronic phase and QGP phase at low n_B is found to be of crossover type for $N_f = 2 + 1$ and $N_f = 2$ (only two light quarks) in first-principle numerical calculations [6, 7]. As the transition is an analytical crossover rather than a true phase transition, the transition temperature, T_c, denotes a pseudo-critical temperature. Its numerical value reads $T_c \simeq 175$ MeV for $N_f = 2$ [6, 8, 9] and $T_c \simeq 170$ MeV for $N_f = 2 + 1$ [6, 8], respectively $T_c = 192$ MeV for $N_f = 2 + 1$ recently reported in [10] (cf. discussion in Appendix A.2). Basing on various model approaches, it is presently assumed that the transition is of first-order at large n_B for $N_f = 2 + 1$. Consequently, the line of first-order phase transitions must end in a second-order phase transition point, the QCD critical point (CP), at specific values of T^E and μ_B^E, where μ_B denotes the baryo-chemical potential associated with n_B (accounting for the energy change, when adding one more baryon into the system). This prominent landmark in the QCD phase diagram is correlated to pronounced structures in specific susceptibilities signalling phase transition behaviour.

Looking in more detail into the phase diagram of strongly interacting matter, a variety of different QCD matter phases emerges depending on temperature and net baryon density. At low T and sufficiently large n_B, a condensation of colour Cooper pairs [11, 12] near the Fermi surface takes place in analogy to the Cooper pair formation of electrons in an electric superconductor. In fact, many different colour superconducting phases may be realized in nature (cf. Appendix A.2). In addition, at $T = 0$ and not too large chemical potential μ_0, there is a liquid-gas transition of nuclear matter within the hadronic phase which is of first-order and ends in a

---

[1]This is correct for three massless quark flavours. In the case of finite quark masses the number of active degrees of freedom decreases somewhat.
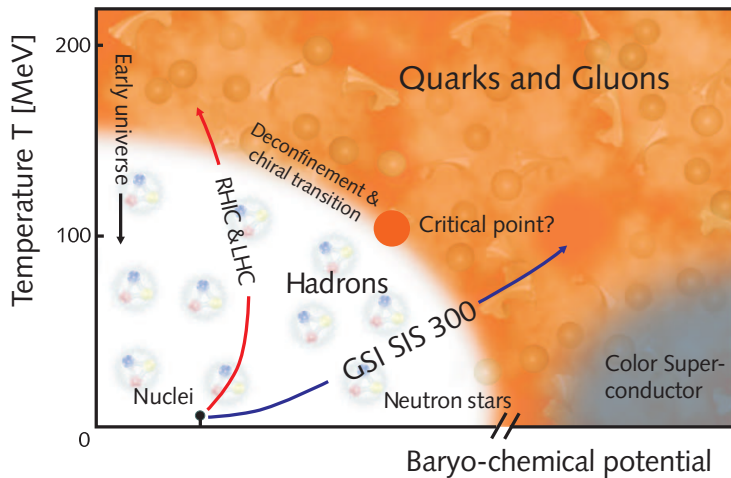
Figure 1.1: Schematic view of the phase diagram of strongly interacting matter in the physical case of $2+1$ massive (two light and one heavier) quark flavours. Shown are different phases (quark-gluon plasma, hadronic phase and colour superconducting phase) as well as some details on the phase transition topology contemporarly argued by theorists. Details are explained in Appendix A.2. For a theoretical overview cf. [13, 14]. In addition, regions in the QCD phase diagram which are relevant for the cosmic evolution of the early universe, for compact stellar objects (neutron stars, hybrid stars) as well as those regions accessible in heavy-ion collisions (denoted by RHIC, LHC and GSI SIS 300) are highlighted. Image adapted by permission from GSI (Gesellschaft für Schwerionenforschung) [15].

critical point at larger T. The ground state of nuclear matter (denoted by "Nuclei" in Figure 1.1) is located exactly at the liquid-gas phase transition line, i. e. at $T = 0$ and $\mu = \mu_0$. Neither superconducting phases nor the nuclear liquid-gas transition are an issue of this thesis, but should be mentioned for completeness. A sketchy illustration of the contemporary view on the QCD phase diagram is exhibited in Figure 1.1, which may serve as a map for rough orientation. More details, in particular a discussion of the relation between the phase diagram topology and the fundamental symmetries of QCD is relegated to Appendix A.2.

Physicists aim at exploring the fascinating structures in the QCD phase diagram under laboratory conditions in heavy-ion collisions (HIC), where transiently the quark-gluon plasma is created and its properties may be investigated experimentally. Nonetheless, for a successful theoretical description of the physics of heavy-ion collision experiments, a firm knowledge on the equation of state (EoS) of strongly interacting matter is of utmost importance. Moreover, the QCD EoS is of significance in various other fundamental aspects of physics such as the cosmic evolution of the early universe or compact stellar objects like neutron stars. It may be formulated in terms of the pressure in the form $p(T, \mu)$ related to the QCD partition function $Z(T, \mu)$ via Eq. (1.1) and describes the bulk properties of a system in thermal equilibrium such that intensive variables like T and μ can be attributed to the medium. Often, however, it is preferably given in the form $p(e, n)$

as interrelation among the thermodynamic entities. As different QCD phases are dominated by different degrees of freedom, the EoS is greatly affected by phase transitions.

Early universe

According to the Big Bang scenario, QGP matter existed for the first few microseconds in the hot early universe, where n_B was approximately zero. More precisely, from present observations and Big Bang nucleosynthesis calculations a ratio of net baryon to photon densities of $n_B/n_\gamma \sim 10^{-10}$ can be deduced. The corresponding baryo-chemical potential, according to entropy conservation, is $\mu_B/T \sim 10^{-9}$ [16]. For the isentropic expansion of the early universe a ratio of entropy per baryon of approximately $s/n_B \simeq 4.35 \times 10^{10}$ can be assumed.

The expansion rate of the hot fireball is determined from Friedmann's equations [17] reading in flat space

$$\dot{R} = CR\sqrt{e}, \quad \dot{e} = -3(e+p)C\sqrt{e}, \tag{1.3}$$

describing the evolution of the scale factor R, which parametrizes the expansion of the universe, and of the energy density with time. Here, $C = \sqrt{8\pi G/3}$, where G denotes Newton's constant being a measure for the coupling strength between geometry and matter.

As the integration of $\dot{e}$ requires the knowledge of the EoS in the form $p(e)$, at $n = 0$, the expansion of the system is to a great extent determined by the pressure. Specifically, after an initial stage, which presumably can be described by an inflationary scenario, the total pressure of the early universe, from the electroweak phase transition until confinement, was dominated by the QCD pressure [18]. This also influences the evolution of cosmological relics, e. g. abundancies of dark matter candidates, cf. [19–21].

Ultra-relativistic heavy-ion collisions

The physics of the Big Bang and of Little Bangs created in ultra-relativistic heavy-ion collisions is quite analogous. After an initial stage, which might be describable in terms of a colour glass condensate [22] (details on the initial stage are currently lively debated), the fireball's expansion is governed by the equations of relativistic hydrodynamics [5, 23, 24] from thermalization until kinetic freeze-out.

For an ideal fluid, the relativistic generalization of the Euler equation as hydrodynamic equation of motion follows from

$$\partial_\mu T^{\mu\nu} = 0, \quad \partial_\mu j_i^\mu = 0, \tag{1.4}$$

describing the local conservation of energy and momentum within the energy-momentum tensor $T^{\mu\nu} = (e+p)u^\mu u^\nu - pg^{\mu\nu}$ and of the four-current j_i^μ of conserved charge i defined in the local rest frame of the fluid. Here u^μ denotes the fluid's four-velocity with $u^\mu u_\mu = 1$ and $u^i = u^0 v^i$, and $g^{\mu\nu}$ is the Minkowski metric. As strong interactions control the physics of heavy-ion collisions due to the short time-scales involved, relevant conserved charges are baryon number, isospin and strangeness. Assuming zero isospin and strangeness net densities in the initial

state, only $j_B^\mu = n_B u^\mu$ associated with the conserved net baryon density has to be considered. The above definition of $T^{\mu\nu}$ assumes locally thermalized momentum distributions and the above relations imply a conservation of the entropy current $s^\mu = su^\mu$.

For a system with dissipative effects, the quantities entering Eq. (1.4) must be modified to $T^{\mu\nu} = (e+p)u^\mu u^\nu - pg^{\mu\nu} + \tau^{\mu\nu}$, $j_B^\mu = n_B u^\mu + \nu_B^\mu$, $s^\mu = su^\mu + \sigma^\mu$, where $\tau^{\mu\nu}$, ν_B^μ and σ^μ include transport coefficients of the medium such as bulk and shear viscosity or heat conductivity. The fluid four-velocity is, according to e. g. the Landau-Lifshitz definition, constraint by $u_\mu \tau^{\mu\nu} = 0$ and $u_\mu \nu_B^\mu = 0$. By considering dissipative effects up to linear order, the relativistic generalization of the Navier-Stokes equation is obtained. Note, however, that causality is violated in this linear approximation (cf. [25] and references therein). Viscous (causal) hydrodynamics is studied in some detail in, for instance, [26–33].

In order to solve the set of hydrodynamic equations, $p(e, n_B)$ has to be known. Then, with specified initial conditions, the dynamical evolution of the fireball is controlled by the EoS, in particular, by the velocity of sound, $c_s = \sqrt{\partial p/\partial e}$, representing the accelerating power of the fluid. It is the aim of this work to provide a reliable equation of state.

Hydrodynamics can only be applied successfully when the system, which, in principle, has to consist of a large number of particles, has reached local thermal equilibrium [34]. As created fireballs are small and, thus, pressure gradients big, and the expansion rates of created matter are large, thermalization can only be obtained by sufficiently fast momentum transfer rates demanding a life-time of the fireball which is sufficiantly larger than the inverse reaction rate among the particles. Whereas after the Big Bang the QGP existed for a rather long period of about 10^{-5} seconds, the bombarding energies reached in Little Bangs are much smaller implying much smaller life-times of the expanding medium. Commonly, a thermalization time scale of about 0.6 fm/c is assumed. This demands a rapid equilibration due to large fluctuations. The hydrodynamic description remains valid as long as the particle's mean free paths are much smaller than the geometric size of the expanding system as well as its Hubble radius.

The bombarding energy is usually specified by the centre-of-mass energy per colliding nucleon pair, $\sqrt{s_{NN}}$. With higher bombarding energies more entropy is produced. In contrast, the baryon number is restricted by the initial number of nucleons. Thus, with increasing $\sqrt{s_{NN}}$ the entropy per baryon ratio is increased. Starting with the Alternating Gradient Synchrotron (AGS) in Brookhaven with $\sqrt{s_{NN}} = 4.6$ GeV and the Super Proton Synchrotron (SPS) in Geneva with $\sqrt{s_{NN}} = 17.2$ GeV, higher bombarding energies, for studying in detail the crossover realm, were reached at the Relativistic Heavy Ion Collider (RHIC) in Brookhaven, at maximum $\sqrt{s_{NN}} = 200$ GeV. With an envisaged operation start in 2008, even larger $\sqrt{s_{NN}} = 5500$ GeV will be reached at the Large Hadron Collider (LHC) in Geneva. Turning again to smaller beam energies, scans into other fascinating regions of the QCD phase diagram including the first-order phase transition regime, the QCD critical point or even superconducting phases are envisaged. According programs include experiments at the SPS (NA61), the planned future Facility for Antiproton and Ion Research (FAIR) in Darmstadt with $\sqrt{s_{NN}} = 5 \ldots 45$ GeV starting presumably in 2015, or the systematic low energy scan at RHIC down to

energies $\sqrt{s_{NN}} = 5$ GeV in the near future. In fact, at FAIR/SIS300 phenomena at maximum baryon density reachable in heavy-ion collisions will be investigated.

In order to explore the features in the QCD phase diagram at finite T and μ_B, signalling observables need to be studied. For instance, one signature of the critical point should be the non-monotonous behaviour of fluctuations (cf. Appendix A.2) with $\sqrt{s_{NN}}$ scans [35] which increase and decrease around CP when lowering $\sqrt{s_{NN}}$. This is accompanied by divergencies in various susceptibilities which are proportional to the magnitude of the corresponding fluctuations. Close to CP, increased event-by-event fluctuations in many different experimental observables [35–40], such as electric charge, baryon number or mean transverse momentum, are expected. If only charged baryons can be detected, fluctuations in the number of protons [41] might provide a signature of CP. (For an overview cf. [42, 43] and references therein.) Besides, fluctuations, for instance in the chiral condensate [44], are debated as signatures of the confinement/deconfinement process [45].

Many indications for the transient creation of a deconfined phase of QCD matter in heavy-ion collisions have been accumulated. As the bulk of emerging particles and their yields can be described successfully by a thermal statistical model [46], the picture of a thermally equilibrated system is supported. Deduced chemical freeze-out points [47–51] $(T_{f.o.}, \mu_{B,f.o.})$ suggest a transition temperature of about 170 MeV at $\mu_B = 0$ with a plateau visible in $T_{f.o.}(\sqrt{s_{NN}})$ for increasing $\sqrt{s_{NN}}$. This is in line with Hagedorn's hypothesis of a limiting temperature [52] and should be confirmed in experiments at the LHC. In fact, by increasing $\sqrt{s_{NN}}$ it becomes easier to create more baryon–anti-baryon pairs, i. e. the number of particles in the system is increased and thus the number of scattering centres necessary for thermal equilibration. In the vicinity of CP, freeze-out points cluster in the region close to it for various different $\sqrt{s_{NN}}$ at higher $T_{f.o.}$ [53]. This is due to the divergence of the specific heat at CP and the first-order phase transition for $\mu_B > \mu_B^E$ resulting in a longer persistence of the fireball system in the critical region around CP.

Much evidence for the successful applicability of ideal relativistic hydrodynamics for describing the expansion stage of strongly interacting matter at RHIC experiments has been assembled [54–58]. For this, a rapid thermalization due to strong interactions among the constituents [22, 59–61] is required. In fact, the notion of a strongly coupled QGP was established [62]. One characteristic of the applicability of hydrodynamics is the observation of collective flow of bulk matter which is build up by strong pressure gradients. These pressure gradients provide the thermodynamic force driving the expansion.

For non-central heavy-ion collisions, i. e. with nonzero impact parameter b, the initial (almond shaped) geometry is aspherical in the plane perpendicular to the beam axis. This original high asymmetry in coordinate space translates, through the appearance of a radially non-symmetric flow governed by large pressure gradients in the plane of the collision, into an expansion velocity profile which is pronounced in that direction, as exhibited in Figure 1.2. The corresponding anisotropy in momentum space results in an azimuthal anisotropy in the particle emission for momenta, p_T, perpendicular to the beam axis. The distribution of these momenta can be quantified by a Fourier decomposition of the emitted hadrons transverse
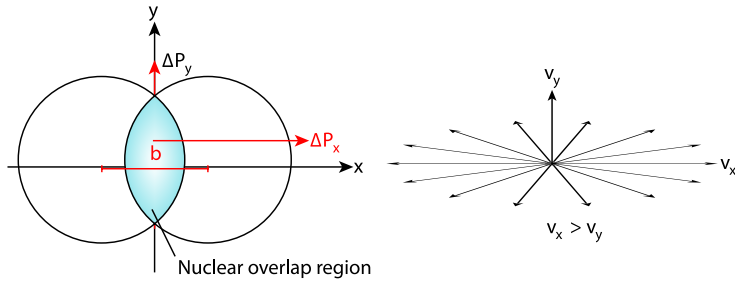
Figure 1.2: For non-central collisions, the nuclear overlap region exhibits an almond-like shape (left panel). This spatial anisotropy is accompanied by larger pressure gradients in the collision plane $(x-z)$ compared to the plane perpendicular to it $(y-z)$. As a result the velocity profile (right panel) exhibits according anisotropies which lead to a particle emission being azimuthally asymmetric in the momenta p_T perperdicular to the beam axis (z). Image adapted by permission from Macmillan Publishers Ltd: Nature [34], copyright (2007).

momentum spectra

$$\frac{dN}{p_T dp_T dy\, d\phi} = \frac{dN}{2\pi\, p_T dp_T dy} \left(1 + 2\, v_2(p_T, y) \cos 2\phi + \dots \right) \tag{1.5}$$

in the azimuthal emission angle ϕ around the beam axis relative to the reaction plane with rapidity y. The second harmonic Fourier coefficient $v_2(p_T, y) = \langle \cos 2\phi \rangle_{p_T, y}$ is called elliptic flow.

The larger the initial energy density, the longer the hydrodynamic stage and, thus, the larger the overall anisotropies. At RHIC, large v_2 was observed showing a characteristic transverse momentum, p_T, and mass dependence, i. e. $v_2(p_T)$ differs for different particle species. The observation of collective flow gives constraints on the equation of state as these experimental data cannot be explained by a purely hadronic EoS. This shows the importance of quark and gluon degrees of freedom for energy densities above a critical energy density of about $e_c = (0.7 \pm 0.2)$ GeV/fm^3.

As transverse momentum spectra or elliptic flow of various particle species observed at RHIC could successfully be described by means of ideal hydrodynamics, a small shear viscosity to entropy density ratio was deduced from experimental data [26, 63, 64]. Various approaches for a theoretical explanation of the observed smallness exist, e. g. [65, 66]. Nonetheless, it is the goal of heavy-ion collision programs to extract experimentally the equation of state as well as transport properties of the quark-gluon plasma.

Compact stellar objects

The physics of neutron stars deals with the domain of small temperatures but large baryon densities. Typical neutron stars possess a mass $M \sim 1.4\, M_\odot$ ($M_\odot$ denotes the solar mass) and radii $R \lesssim 15$ Km, while also extreme cases of neutron star candidates with $M > 2\, M_\odot$, $R > 15$ Km and rotational frequencies above 10 Hz have been observed. Their structure is dictated by the EoS which is constraint by astronomical observations. However, at these large baryon densities of about ten

times nuclear matter density, a firm knowledge on the QCD equation of state is currently rather scarce. Gross-properties like the mass, radius or the structure of spherical, non-rotating stars are determined by the Tolman-Oppenheimer-Volkov (TOV) equations reading

$$\frac{dm}{dr} = 4\pi r^2 e(r),\tag{1.6}$$

$$\frac{dp}{dr} = -\frac{G}{r^2}\left[e(r) + p(r)\right]\left(m(r) + 4\pi r^3 p(r)\right)\left[1 - \frac{2Gm(r)}{r}\right]^{-1},\tag{1.7}$$

where m is the gravitational mass inside a sphere of radius r including the gravitational binding energy.

The TOV equations can be solved by supplementing an interrelation $e(p)$ at $T \simeq 0$, where the radius R of the star is obtained from demanding $p(R) = 0$. The corresponding star mass is then given by $M = m(R)$. While neutron stars with masses $M \sim 2\,M_\odot$ are presumably nuclear or hybrid stars with quark matter cores, neutron stars with $M \lesssim 1.5\,M_\odot$ must involve some kind of exotic matter such as hyperons or quark matter. Nonetheless, strange quark matter in the colour-flavour locked phase is forbidden due to gravitational instabilities [67–69]. Although measurements of the relation between M and R can rule out some of the EoS (for instance, $M > 2.3\,M_\odot$ is not possible with any realistic EoS), only observations of the cooling behaviour can distinguish between different equations of state [70]. By adding rotational degrees of freedom, more complicated equations need to be solved.

Concept of quasiparticles

The QCD equation of state can be obtained from various systematic approaches such as first-principle numerical calculations on a discretized finite space-time grid, called lattice QCD calculations, improved perturbative QCD or chiral perturbation theory but also from various phenomenological models. All these approaches are restricted to a certain region of applicability in the QCD thermodynamic parameter space. The advantage of phenomenological models lies in the fact that their regions of applicability overlap with those of the systematic approaches, thus, giving constraints for the model parameters. For an overview, cf. Appendix A.3. In this thesis, the QCD EoS is obtained and discussed within a phenomenological quasiparticle model.

The notion of quasiparticles has proven to be a powerful and useful concept for understanding the properties of strongly correlated systems (cf. [71] for an overview). In 1941, L. D. Landau [24] introduced this concept in condensed matter physics to explain superfluidity and the thermodynamics of superfluid ^{4}He. B. M. Galitzkii and A. B. Migdal derived in 1958 [72] a consistent microscopic theory of quasiparticles using Green's functions. Accordingly, quasi-stationary excitations are expressed via the partition function Z viz

$$Z = \prod_\alpha \left(1 \mp e^{-\frac{\xi_\alpha(V)}{T}}\right)^{\mp 1} \times Z_{int},\tag{1.8}$$

where $\xi_\alpha = |\mathrm{Re}\,\omega_\alpha - \mu|$ depends on the volume and on a set of parameters α describing the system. ω_α are poles of the respective Green's functions supposing

$|\operatorname{Im}\omega_\alpha| \ll |\operatorname{Re}\omega_\alpha - \mu|$ for quasi-stationary excitations. Thus, $\omega_\alpha(\vec{p})$ quantifies the dispersion relation of the quasiparticles. Eq. (1.8) states that for describing strongly correlated systems it suffices to know the spectra of elementary quasi-stationary excitations which carry the same quantum numbers as the corresponding free particles of the system under consideration. A solid or a fluid is, thus, considered as a dilute gas of weakly interacting quasiparticles with possible mutual interactions encoded in Z_{int}.

The existence of quasi-stationary collective modes, carrying the same elementary motion, allows for an efficient description of the system in terms of single-particle states with approximately additive energies and momenta. Accumulating collective phenomena in such a way, certainly, leads to a simplification in the description of the strongly correlated many-particle system. Furthermore, the lifetime of these single-particle states is limited by the interaction among the modes.

The complexity of the correlations is encoded in the dispersion relations of the quasiparticles. In the case of QCD at finite T and μ, one can attribute effective state dependent masses $M(T,\mu)$ to the excitations such that the dispersion relation $\omega_\alpha = \omega_\alpha(k, M(T,\mu))$ becomes medium dependent. However, as first noted by Gorenstein and Yang [73], this introduces explicitly a temperature dependence into the Hamiltonian. In order to maintain thermodynamic consistency, an effective Hamiltonian $H_{eff} = H_{id} + E_0^*$ has to be considered, where $E_0^*(M(T,\mu))$ represents the system's energy in the absence of any quasiparticle excitations. For temperature independent Hamiltonians, the zero point energy is constant and, thus, usually discarded. Here, however, this zero point energy becomes T and μ dependent and cannot be subtracted from the energy spectrum, i. e. changing T and μ also affects E_0^*.

In the thermodynamic potential, medium contributions from E_0^*, which have to be taken into account, assemble in the bag function $B = \lim_{V\to\infty} E_0^*/V$ in the thermodynamic limit. This ansatz will be used in the following work. In a generalization of the argument of Gorenstein and Yang, it was recently shown [74] that innumerable other possibilities, in principle, exist for including a temperature dependent Hamiltonian. For example, one could equally well include the whole interaction energy into the quasiparticle masses as employed in a different quasiparticle model approach [75, 76].

Various different phenomenological models incorporating quasiparticles were proposed in the literature. Among these, a quark-gluon liquid model [77], a quasiparticle model with T and μ dependent confinement factor accounting for the reduction in the number of thermodynamically active degrees of freedom when approaching the phase boundary [78, 79], a HTL quasiparticle model including momentum dependent HTL self-energies, Landau damping and collective modes [80], a model including quark and gluon collisional widths [81, 82] and a dynamical quasiparticle model [83] have to be mentioned.

The focus of the present work represents the already emphasized equation of state of hot deconfined QCD matter at nonzero net baryon density. For this purpose, the formerly developed quasiparticle model [84–87] based on dressed quark and gluon degrees of freedom and aiming at an appropriate description of QCD

thermodynamics is reviewed in section 2.1 and then in the subsequent sections of chapter 2 extended into two different directions. In section 2.3, an imaginary chemical potential is considered, and in section 2.4 the model incorporating two independent real quark chemical potentials is introduced. Both extensions of the quasiparticle description of QCD matter aim at providing access into the realm of nonzero baryon densities and allow for a sensitive test of the model's ability to extrapolate to finite n_B by comparison with available first-principle lattice QCD results. In addition, in section 2.2 the employed quasiparticle picture is put on firmer ground by relating it to QCD via the Φ-functional formalism performing mathematical simplifications.

Chapter 3 is devoted to a detailed comparison of the quasiparticle model with available lattice QCD results for finite temperature and zero as well as nonzero net baryon density. Starting with QCD thermodynamics at zero n_B, basic bulk thermodynamic quantities for different numbers of active quark flavour degrees of freedom are successfully compared in section 3.1. Furthermore, the applicability of the model to extrapolate results to different quark mass parameters, in particular to the chiral limit, as well as to asymptotically large temperatures is shown which demonstrates the predictive power of the quasiparticle model. In section 3.2, effects of nonzero net baryon density are considered. In particular, investigations of baryon number, electric charge and isovector susceptibilities, of diagonal and off-diagonal susceptibilities, of QCD thermodynamics and the phase diagram for imaginary chemical potential as well as the analytic continuation of these results to real chemical potential have to be mentioned. Furthermore, studies concerning isentropic evolutionary paths in the phase diagram and the equation of state along them, physical implications of attributing different quark flavour chemical potentials and a discussion of the chemical potential dependence in the quasiparticle dispersion relations used in the model are presented. All these considerations in section 3.2 aim at proving the applicability of the quasiparticle model to extrapolate the EoS from zero net baryon density towards nonzero n_B, and indeed, the model turns out to faithfully describe the baryon-density dependence in the QCD equation of state in a consistent picture. Section 3.3 deals with the equation of state of strongly interacting matter for $N_f = 2 + 1$. Besides the important dependence $p(e, n_B)$, scaling properties of the resulting EoS with N_f, the quark mass parameters and the numerical value of T_c are worked out. In addition, it is shown that $p(e, n_B)$ is rather robust in the regions of small and large energy densities.

The constructed EoS is applied in hydrodynamic simulations for heavy-ion collision experiments in chapter 4. As the large energy density part, based on lattice QCD results parametrized by the model, does not continuously match in the transition region with a hadron resonance gas equation of state, reliable at small energy densities, an interpolation prescription is outlined in section 4.1 resulting in a whole family of equations of state. This family of equations of state takes into account uncertainties arising in the transition region which are also discussed in section 3.3. In section 4.2, exemplarily two members of the family of equations of state are employed in hydrodynamic simulations, first, with initial conditions relevant for top RHIC energies and then with assumed LHC initial conditions providing comparisons of and predictions for transverse momentum spectra and differential elliptic flow of, in particular, directly emitted strange baryons. Finally, section 4.3 is de-

voted to recent developments, discussing a new EoS which continuously combines small and large energy density regimes.

In chapter 5, effects of including static QCD critical point phenomena into the equation of state are discussed. Constructing singular contributions from a parametric representation of the thermodynamic potential in section 5.1, divergencies in appropriate susceptibilities at CP and a first-order behaviour in entropy and net baryon densities across the phase boundary in the first-order phase transition region are recovered. These considerations are, first, discussed in the context of a toy model approach in section 5.2 and, then, extended to the quasiparticle model in section 5.3. With these preparations, possible CP effects in the QCD equation of state which may be relevant for FAIR physics can be discussed in the future.

A summary and an outlook on further future investigations is given in chapter 6. More details on the theory of strong interactions, the thermodynamics of QCD and a discussion of different approaches for accessing the QCD equation of state are relegated to Appendix A. For better readability, the flow equations solving for the effective coupling, as important ingredient of the model accounting for the non-perturbative behaviour, in the entire thermodynamic parameter space are posted in Appendix B, first, for the quasiparticle model reviewed in section 2.1, but also for both extensions of the model presented in sections 2.3 and 2.4. In addition, a discussion of the chemical potential dependence in the quasiparticle dispersion relations which is related to the unique determination of different susceptibilities can be found in Appendix B. Finally, Appendix C touches the problem of extrapolating numerical lattice QCD results obtained on a finite space-time grid to thermodynamic and continuum limits.

Parts of the results presented in this work are already published in [88–99]. In addition, the extrapolation of the EoS into the region of asymptotically large temperatures in section 3.1.3, the discussion of scaling properties of the equation of state in section 3.3.3 and the properties of the new EoS combining continuously small and large energy density regions in section 4.3 represent recent and yet unpublished results.

2   Quasiparticle Model

In this chapter, the quasiparticle model (QPM), which will be used within this work, is introduced. It basically rests on the developments in [84–87] which were inspired by ideas in [100, 101]. Within the QPM, the QGP is considered as a system in thermal equilibrium consisting of prominent quasiparticle excitations with dispersion relations of the type $\omega_i^2 = k^2 + \Pi_i + m_i^2$, where Π_i is the self-energy. Assuming real self-energies, they are approximated by $\Pi_i(T, \mu)$ in a certain momentum (k) range and may be combined with m_i^2 to result in effective state dependent masses $M_i(T, \mu)$. Bulk properties, given by thermodynamic integrals, are governed by hard momenta $k \sim T$, μ such that, in the weak coupling regime [102, 103], the relevant modes are merely transversal gluons and (anti-)quark single-particle excitations. Collective modes, i. e. plasmons and (anti-)plasminos, are exponentially suppressed, instead. Soft and ultra-hard modes are expected to influence thermodynamic quantities rather less.

Details of the QPM for one independent chemical potential are explained in section 2.1 followed by a theoretical motivation in section 2.2. In sections 2.3 and 2.4, the QPM for imaginary chemical potential and for two independent chemical potentials, respectively, is considered.

2.1   Model description

Being mainly interested in providing an equation of state applicable for hydrodynamic calculations, the strangeness neutrality constraint, which is due to initial zero strangeness in heavy-ion collisions and the very short time available during the collision process, allows to set for the *strange* (*s*) quark chemical potential $\mu_s = 0$. (Matter anti-matter symmetric systems are realized for according zero chemical potential.) Furthermore, zero net electric charge in the fireball matter created near midrapidity in heavy-ion collisions as well as degenerate *up* (*u*) and *down* (*d*) quarks with chemical potentials μ_u and μ_d, respectively, can be assumed such that for the isovector chemical potential, which is fixed by the net electric charge density of the medium and associated with the (in strong interaction processes) conserved quantum number of isospin, one sets $\mu_I \equiv (\mu_u - \mu_d)/2 = 0$. In this case, a system with one independent quark flavour chemical potential $\mu_u = \mu_d = \mu$ is described such that the quark chemical potential and the baryo-chemical potential associated with net quark number and net baryon number densities, respectively, read $\mu_q \equiv (\mu_u + \mu_d)/2 = \mu$ and $\mu_B \equiv 3\mu_q = 3\mu$. Such a system will be considered in this section. In principle, however, different quark flavour chemical potentials could be taken into account altering the chemical potential dependence of the mass gaps $M_i(T, \mu)$, as discussed in section 2.4. As the number of gluons, being gauge bosons of the strong interaction, is not conserved in thermal equilibrium, the gluon chemical potential must be zero, $\mu_g \equiv 0$.

In the phenomenological quasiparticle model, the pressure p, which is considered as primary thermodynamic potential in the thermodynamic limit, is constructed by assuming a quasiparticle picture for the u, d and s quarks and for the gluons (g) viz

$$p(T,\mu) = \sum_{i=u,d,s,g} p_i(T,\mu_i, M_i(T,\mu)) - B(M_{u,d,s,g}(T,\mu)), \qquad (2.1)$$

where B depends on T and μ only via $M_i(T,\mu)$, while the partial pressures with $l = u,d,s$ read

$$p_l(T,\mu_l, M_l(T,\mu)) = \frac{d_l}{2\pi^2} T \int_0^\infty dk k^2 \left(\ln\left[1 + e^{-\{\omega_l[k, M_l(T,\mu)] - \mu_l\}/T} \right] \right.$$

$$\left. + \ln\left[1 + e^{-\{\omega_l[k, M_l(T,\mu)] + \mu_l\}/T} \right] \right), \qquad (2.2)$$

$$p_g(T,\mu_g, M_g(T,\mu)) = -\frac{d_g}{\pi^2} T \int_0^\infty dk k^2 \ln\left[1 - e^{-\omega_g[k, M_g(T,\mu)]/T} \right]. \qquad (2.3)$$

Here, $d_l = d_u = d_d = d_s = 2\,N_c$ and $d_g = N_c^2 - 1$ represent the spin-colour degeneracy factors. The two different transversal gluon polarizations are already absorbed in the integral in Eq. (2.3).

The quasiparticles are assumed to propagate on-shell, i. e. with real energies ω_i given by dispersion relations of the form $\omega_i = \sqrt{k^2 + M_i^2(T,\mu)}$ which hold for weakly interacting quarks and gluons with thermal momenta k and mass gaps $M_i(T,\mu)$. The according on-shell spectral functions result in zero residual interactions among the quasiparticles, i. e. with the notation introduced in chapter 1, $Z_{int} = 1$. Thus, the corresponding infinite mean free paths translate into a large viscosity of the plasma in contrast to experimental observations at RHIC. However, it was shown in [66] that an inclusion of finite (even large) collisional widths in the quasiparticle spectral functions yields a small viscosity in agreement with experiments and an equally good description of lattice QCD thermodynamics. As, however, the equation of state necessary for hydrodynamics is independent of the underlying microscopic picture, the much simpler on-shell quasiparticle description will be used in this work.

With Eqs. (2.1)-(2.3), the QPM pressure is expressed in terms of standard phase space integrals over thermal equilibrium distribution functions for quasiparticles with quark and gluon quantum numbers but medium dependent dispersion relations. Formally, these expressions look like the ones for the ideal gas pressures, though, with the substantial modification $M_i(T,\mu)$. The partial pressure integrals in Eqs. (2.2) and (2.3) are dominated by momenta of order $k \sim T$ for small μ. Thus, weak coupling perturbation theory suggests that the dominant propagating modes in the plasma are transversal gluon-like and (anti)quark-like excitations, whereas plasmons and (anti)plasminos are exponentially suppressed.

In principle, within Eqs. (2.1)-(2.3) different numbers of quark flavours can be investigated. For instance, a plasma containing two light and one heavier quark flavours is inherent by considering u and d quarks as degenerate while attributing a different dispersion relation to the s quark. $N_f = 2$ is then obtained by neglecting

any s quark contributions ($d_s = 0$) and other N_f systems are maintained from this by considering the appropriate number of quark degrees of freedom in the sum of Eq. (2.1).

Thermodynamic quantities like entropy density or net quark flavour number densities result from Eq. (1.2) taking into account the stationarity property of the thermodynamic potential with respect to the effective quasiparticle masses [73]

$$\left.\frac{\delta p}{\delta M_i^2}\right|_{T,\mu,M_{j\neq i}^2} = 0\,, \tag{2.4}$$

resulting in the important condition

$$\frac{\partial B}{\partial M_i^2} = \frac{\partial p_i}{\partial M_i^2}\,. \tag{2.5}$$

They read $s = \displaystyle\sum_{i=u,d,s,g} s_i = \left.\frac{\partial p}{\partial T}\right|_\mu$ with

$$
\begin{aligned}
s_l &= \frac{d_l}{2\pi^2}\int_0^\infty dk k^2 \bigg(\ln\left[1 + e^{-\{\omega_l-\mu_l\}/T}\right] + \frac{\{\omega_l - \mu_l\}/T}{\left[e^{\{\omega_l-\mu_l\}/T} + 1\right]} \\
&\quad + [\mu_l \rightarrow -\mu_l]\bigg),
\end{aligned} \tag{2.6}
$$

$$s_g = -\frac{d_g}{\pi^2}\int_0^\infty dk k^2 \left(\ln\left[1 - e^{-\omega_g/T}\right] - \frac{\omega_g/T}{\left[e^{\omega_g/T} - 1\right]} \right) \tag{2.7}$$

for the entropy density and

$$n_l = \left.\frac{\partial p}{\partial \mu_l}\right|_T = \frac{d_l}{2\pi^2}\int_0^\infty dk k^2 \left(\frac{1}{\left[e^{\{\omega_l-\mu_l\}/T} + 1\right]} - \frac{1}{\left[e^{\{\omega_l+\mu_l\}/T} + 1\right]} \right) \tag{2.8}$$

for the net quark flavour number densities. In the case applicable for heavy-ion collisions near midrapidity as considered above with $\mu_s = 0$ and $\mu_I = 0$ and assuming, furthermore, degenerate u and d quarks, one finds $n_s = 0$, $n_u = n_d$ and for the net quark number density $n_q \equiv n_u + n_d = 3\,n_B$ while the isovector density $n_I \equiv n_u - n_d = 0$. This underlines the picture that in the QPM the baryon charge is carried by quark-like quasiparticle excitations.

Entropy density as well as net quark flavour number densities are explicitly determined from quasiparticle contributions with zero residual interaction terms. The additional derivative terms associated with $M_i(T,\mu)$ are compensated by the mean field interaction term B via

$$\left.\frac{\partial B}{\partial T}\right|_\mu = \sum_{i=u,d,s,g} \left(\frac{\partial p_i(T,\mu_i,M_i(T,\mu))}{\partial M_i^2} \left.\frac{\partial M_i^2(T,\mu)}{\partial T}\right|_\mu \right)\,, \tag{2.9}$$

$$\left.\frac{\partial B}{\partial \mu}\right|_T = \sum_{i=u,d,s,g} \left(\frac{\partial p_i(T,\mu_i,M_i(T,\mu))}{\partial M_i^2} \left.\frac{\partial M_i^2(T,\mu)}{\partial \mu}\right|_T \right)\,, \tag{2.10}$$

where

$$\frac{\partial p_l}{\partial M_l^2} = -\frac{d_l}{2\pi^2} \int\limits_0^\infty dk \frac{k^2}{2\,\omega_l} \left(\frac{1}{\left[e^{\{\omega_l-\mu_l\}/T} + 1\right]} + \frac{1}{\left[e^{\{\omega_l+\mu_l\}/T} + 1\right]} \right), \quad (2.11)$$

$$\frac{\partial p_g}{\partial M_g^2} = -\frac{d_g}{\pi^2} \int\limits_0^\infty dk \frac{k^2}{2\,\omega_g} \frac{1}{\left[e^{\omega_g/T} - 1\right]}\,. \quad (2.12)$$

This assumes that, as defined in Eq. (2.1), all temperature and chemical potential dependence of the mean field interaction B is merely inherent in the functions $M_i(T,\mu)$. The explicit derivative expressions of $M_i^2(T,\mu)$ in Eqs. (2.9) and (2.10) are relegated to Appendix B.1. B is determined by an appropriate line integral in the thermodynamic parameter space viz

$$B = B_0 + \int \left(\left.\frac{\partial B}{\partial T}\right|_\mu dT + \left.\frac{\partial B}{\partial \mu}\right|_T d\mu \right) \quad (2.13)$$

with integration constant B_0 which needs to be fixed. For instance, at $\mu = 0$ the line integral is chosen along the temperature axis from the pseudo-critical temperature T_c to temperature T with integration constant $B_0 \equiv B(T_c)$.

One specific choice for the effective quasiparticle masses is

$$M_l^2(T,\mu) = m_l^2 + 2\,m_l M_{+,l}(T,\mu) + 2\,M_{+,l}^2(T,\mu)\,, \quad (2.14)$$
$$M_g^2(T,\mu) = m_\infty^2(T,\mu)\,, \quad (2.15)$$

with

$$2\,M_{+,l}^2(T,\mu) = \frac{1}{3}\left[T^2 + \frac{\mu_l^2}{\pi^2}\right]g^2\,, \quad (2.16)$$

$$m_\infty^2(T,\mu) = \frac{1}{12}\left([6 + N_f]T^2 + 3\sum_l \frac{\mu_l^2}{\pi^2}\right)g^2\,, \quad (2.17)$$

which are related to the asymptotic forms of the gauge independent hard thermal (dense) loop self-energies [102, 103]. Note again that in the case considered in this section $\mu_s = 0$ while $\mu_u = \mu_d = \mu$. Thus, the effective quasiparticle masses depend on T and one chemical potential μ, only. While the form of $M_g^2(T,\mu)$ is actually defined only for zero bare quark masses, the definition of $M_l^2(T,\mu)$ takes into account a finite bare quark mass m_l as, for instance, employed in lattice QCD calculations. In some lattice calculation set-ups, for example, the bare quark masses depend on temperature, $m_l = m_l(T)$. When comparing the QPM thermodynamics with lattice QCD results, in the following, m_l entering Eq. (2.14) will be adjusted to the values used on the lattice. (Note that $m_g = 0$.)

The approximation in Eq. (2.14) is motivated from perturbative considerations of the high temperature limit of the renormalized quark propagator for small quark masses m_l [104] and the assumption that the relation between asymptotic mass and plasma frequency known for zero quark masses holds approximately true also for small m_l. In the case of degenerate u and d quarks, $m_u = m_d \equiv m_q$ holds such that one finds $\omega_u = \omega_d \equiv \omega_q$ since $M_{+,u}^2 = M_{+,d}^2 \equiv M_{+,q}^2$.

Some of the model assumptions are inspired by perturbation theory, i. e. strictly valid only in the weak coupling regime. For instance, one assumes that also close to the pseudo-critical temperature T_c collective excitations can be neglected and that the quasiparticle dispersion relations can be approximated by the simplistic on-shell expressions stated above with energy and momentum independent self-energies. Nonetheless, perturbation theory is expected to break down in the vicinity of the phase boundary. Thus, non-perturbative effects in the vicinity of T_c need to be modeled in the QPM which is achieved by replacing the perturbative expression for the running coupling g^2 entering Eqs. (2.16) and (2.17) by an effective coupling G^2 which depends on temperature and chemical potential. The T and μ dependence in G^2 is dictated by the T and μ dependence of thermodynamic quantities from lattice QCD. Thus, comparisons with lattice QCD results serve for a test of the model and check whether the QPM can cope with the complexity of QCD. Note that the expression for p in Eqs. (2.1)-(2.3) is highly non-perturbative in G^2 as within a series expansion in powers of G^2 a thermodynamically consistent resummation of all orders in G^2 is found.

The temperature and chemical potential dependence of the effective coupling is obtained from solving a quasi-linear partial differential equation of first-order which is based on Maxwell's relation for the pressure, i. e. from

$$\frac{\partial^2 p}{\partial \mu \partial T} = \frac{\partial s}{\partial \mu} = \frac{\partial n_q}{\partial T} = \frac{\partial^2 p}{\partial T \partial \mu} \tag{2.18}$$

follows

$$a_\mu \frac{\partial G^2}{\partial \mu} + a_T \frac{\partial G^2}{\partial T} = b . \tag{2.19}$$

The coefficients a_μ, a_T and b depending on T, μ and $G^2(T,\mu)$ are listed in Appendix B.1. This flow equation Eq. (2.19) is solved for $G^2(T,\mu)$ by the method of characteristics starting from an initial condition on a Cauchy surface in the thermodynamic parameter space, for instance from knowing $G^2(T,\mu=0)$. Thus, the flow equation transports information about G^2 from the temperature axis, once the model is adjusted to lattice QCD results, to nonzero chemical potential and, thus, determines to a large extent the n_B dependence of the EoS. One possibility to parametrize $G^2(T,\mu=0)$ is via[1]

$$G^2(T,\mu{=}0) = \begin{cases} G^2_{2-\mathrm{loop}}(T), & T \geq T_c, \\[2mm] G^2_{2-\mathrm{loop}}(T_c) + b\left(1{-}\frac{T}{T_c}\right), & T < T_c . \end{cases} \tag{2.20}$$

In order to recover perturbation theory in the (massless) high temperature limit, $G^2_{2-\mathrm{loop}}$ is taken to have the same form as the perturbative running coupling at 2-loop order

$$G^2_{2-\mathrm{loop}}(T) = \frac{16\pi^2}{\beta_0 \log \zeta^2}\left(1 - \frac{2\beta_1}{\beta_0}\frac{\log(\log \zeta^2)}{\log \zeta^2}\right) \tag{2.21}$$

with $\zeta = \lambda(T - T_s)/T_c$, $\beta_0 = 11 - \frac{2}{3}N_f$ and $\beta_1 = 51 - \frac{19}{3}N_f$. This phenomenological parametrization contains two parameters, a scale parameter λ and a temperature shift T_s which regulates the infrared divergence in the logarithmic dependence of

---

[1]Different definitions for the parametrization of G^2 where studied in [105].

the coupling by shifting it somewhat below the pseudo-critical temperature, where, anyway below T_c, a continuous linear behaviour with parameter b is postulated. The parameters entering G^2 depend in general on the considered number of quark flavours and the quark mass parameters. The change in the curvature behaviour of G^2 at T_c is further discussed in chapters 3 and 5. For large T, Eq. (2.21) resembles the perturbative result of the QCD running coupling.

For nonzero chemical potential, $B(T, \mu)$ can, for instance, be determined by first integrating along the temperature axis from T_c to $\tilde{T}$ with integration constant $B_0 \equiv B(T_c)$, and then performing the line integral in Eq. (2.13) along the characteristic curve which is the solution of Eq. (2.19) emerging at $\tilde{T}$ which eventually approaches T.

Susceptibilities represent second-order derivatives of the pressure in the chemical potential direction and, thus, serve as sensible quantities probing baryon-density effects in the equation of state. For instance, the quark number susceptibility reads

$$
\begin{aligned}
\chi_q &= \left. \frac{\partial n_q}{\partial \mu} \right|_T \\
&= \frac{d_q}{2\pi^2 T} \int_0^\infty dk k^2 \left(\frac{e^{\{\omega_q - \mu\}/T}}{[e^{\{\omega_q - \mu\}/T} + 1]^2} + \frac{e^{\{\omega_q + \mu\}/T}}{[e^{\{\omega_q + \mu\}/T} + 1]^2} \right. \\
&\quad \left. - \left\{ \frac{e^{\{\omega_q - \mu\}/T}}{[e^{\{\omega_q - \mu\}/T} + 1]^2} - \frac{e^{\{\omega_q + \mu\}/T}}{[e^{\{\omega_q + \mu\}/T} + 1]^2} \right\} \frac{1}{2\omega_q} \left. \frac{\partial M_q^2}{\partial \mu} \right|_T \right), \quad (2.22)
\end{aligned}
$$

where $d_q = 2 N_c N_q$ for degenerate u and d quarks ($N_q = N_f = 2$ denotes the number of degenerate light quark flavours). The derivative of the effective quark quasiparticle mass is given by Eq. (B.3) in Appendix B.1.

2.2   Theoretical motivation

It would be desirable to relate the QPM intuitively introduced in section 2.1 with QCD as the fundamental microscopic gauge field theory of strong interactions. In order to motivate the quasiparticle model, a chain of approximations is mandatory starting from the Φ-functional approach to QCD [94, 106]. This is based on the pioneering work in [107–111] containing a more rigorous approach than the one presented below. Note that here merely formal mathematical manipulations are imposed and that the assumptions entering the model, which are based on perturbation theory, need to be justified by confronting the model with the non-perturbative lattice QCD results.

It is favourable to concentrate on entropy density s and net number density n, as both turn out to possess a simple structure supporting the picture of quasiparticle excitations. Other thermodynamic quantities such as pressure or energy density can be determined from s and n by integration.

In the Φ-functional approach to QCD, where the variational parameters are the dressed propagators [112, 113], $\ln Z$ can be expressed as a functional of dressed

propagators of gluons D, quarks S and Faddeev-Popov ghost fields G,

$$
\begin{aligned}
\ln Z[D, S, G] \;=\; & -\frac{1}{2}\mathrm{Tr}[\ln D^{-1} - \Pi D] + \mathrm{Tr}[\ln S^{-1} - \Sigma S] \\
& + \mathrm{Tr}[\ln G^{-1} - \Xi G] - \Phi[D, S, G]\,.
\end{aligned}
\tag{2.23}
$$

Here, ghost field contributions compensate for possible unphysical degrees of freedom in the gluon propagator. While the propagators in Eq. (2.23) depend on the specific gauge, $\ln Z$ must be gauge independent. For convenience, the Coulomb gauge is chosen in the following in which ghost fields do not propagate and the gluon propagator consists only of the physical transversal and longitudinal modes. The functional $\Phi[D, S]$ is given by the infinite sum of all 2-particle irreducible skeleton diagrams constructed from D and S.

The self-energies in Eq. (2.23) are related to the dressed propagators by Dyson's equations

$$
\Pi[D] = D^{-1} - D_0^{-1}\,,\ \ \Sigma[S] = S^{-1} - S_0^{-1}\,,
\tag{2.24}
$$

where D_0 and S_0 represent the bare propagators of gluon and quark fields, respectively. Demanding the stationarity of $\ln Z$ under functional variation with respect to the dressed propagators [114] viz

$$
\frac{\delta \ln Z[D, S]}{\delta D} = \frac{\delta \ln Z[D, S]}{\delta S} = 0\,,
\tag{2.25}
$$

the self-energies follow self-consistently by cutting a dressed propagator line in Φ resulting in the gap equations

$$
\Pi = 2\frac{\delta \Phi[D, S]}{\delta D}\,,\ \ \Sigma = -\frac{\delta \Phi[D, S]}{\delta S}\,.
\tag{2.26}
$$

The trace "Tr" in Eq. (2.23) has to be taken over all states of the relativistic many-particle system. In the imaginary time formalism it can be rewritten in the form $\mathrm{Tr} \to \mathrm{tr}\,\beta V T \sum_{n=-\infty}^{+\infty} \int d^3k/(2\pi)^3$. Here, $\beta = 1/T$ and "tr" denotes the remaining trace over occuring discrete indices including colour, flavour, Lorentz and spinor indices. Introducing the four-momentum $k^\nu = (\omega, \vec{k}) = (i\omega_n, \vec{k})$, the sums have to be taken over the Matsubara frequencies $\omega_n = 2n\pi T$ (or $(2n+1)\pi T - i\mu$) for gluons (or quarks). For simplicity, only one quark chemical potential μ is considered in the following. They can be evaluated by using standard contour integration techniques in the complex ω-plane [102, 103] wrapping up the poles of the propagators. Expressing the analytic propagators in terms of their spectral densities ρ, one can define

$$
\rho_{D(S)}(\omega, |\vec{k}|) = 2 \lim_{\epsilon \to 0} \mathrm{Im}\, D(S)(\omega + i\epsilon, |\vec{k}|)
\tag{2.27}
$$

for real ω. Similarly, the imaginary parts of functions of the analytic propagators obeying the same pole structures can be defined. Hence, $\ln Z$ reads with retarded propagators D and S depending on ω and $k = |\vec{k}|$

$$
\begin{aligned}
\frac{T}{V} \ln Z[D, S] \;=\; & -\mathrm{tr} \int \frac{d^4k}{(2\pi)^4} n(\omega)\, \mathrm{Im}[\ln D^{-1} - \Pi D] \\
& -2\mathrm{tr} \int \frac{d^4k}{(2\pi)^4} f(\omega)\, \mathrm{Im}[\ln S^{-1} - \Sigma S] - \frac{T}{V}\Phi[D, S]\,,
\end{aligned}
\tag{2.28}
$$

where $\int d^4k \;=\; \int d^3k \int d\omega$, and $n(\omega) = (e^{\beta\omega} - 1)^{-1}$ $(f(\omega) = (e^{\beta\{\omega-\mu\}} + 1)^{-1})$ denotes the thermal equilibrium statistical distribution function for gluons (quarks with chemical potential μ).

Due to the stationarity property in Eq. (2.25), entropy density $s = \partial(T\ln Z/V)/\partial T$ and net number density $n = \partial(T\ln Z/V)/\partial\mu$ contain only explicit temperature and chemical potential derivatives of $n(\omega)$ and $f(\omega)$, although the propagators in Eq. (2.28) depend implicitly on T and μ through their spectral densities. Using $\mathrm{Im}\,(\Pi D) = \mathrm{Im}\,\Pi\,\mathrm{Re}\,D + \mathrm{Re}\,\Pi\,\mathrm{Im}\,D$, one finds for the entropy density $s = s_g + s_q + s'$ with

$$s_g = -\mathrm{tr}\int \frac{d^4k}{(2\pi)^4} \frac{\partial n(\omega)}{\partial T}[\mathrm{Im}\ln D^{-1} - \mathrm{Im}\,\Pi\,\mathrm{Re}D]\,, \qquad (2.29)$$

$$s_q = -2\mathrm{tr}\int \frac{d^4k}{(2\pi)^4} \frac{\partial f(\omega)}{\partial T}[\mathrm{Im}\ln S^{-1} - \mathrm{Im}\,\Sigma\,\mathrm{Re}S]\,, \qquad (2.30)$$

$$\begin{aligned}
s' \;=\; & -\left.\frac{\partial(\frac{T}{V}\Phi[D,S])}{\partial T}\right|_{D,S} + 2\mathrm{tr}\int \frac{d^4k}{(2\pi)^4} \frac{\partial f(\omega)}{\partial T}\mathrm{Re}\Sigma\,\mathrm{Im}S \\
& + \mathrm{tr}\int \frac{d^4k}{(2\pi)^4} \frac{\partial n(\omega)}{\partial T}\mathrm{Re}\Pi\,\mathrm{Im}D\,.
\end{aligned} \qquad (2.31)$$

Similarly, for the net number density one finds $n = n_q + n'$ with

$$n_q \;=\; -2\mathrm{tr}\int \frac{d^4k}{(2\pi)^4} \frac{\partial f(\omega)}{\partial\mu}[\mathrm{Im}\ln S^{-1} - \mathrm{Im}\,\Sigma\,\mathrm{Re}S], \qquad (2.32)$$

$$n' \;=\; 2\mathrm{tr}\int \frac{d^4k}{(2\pi)^4} \frac{\partial f(\omega)}{\partial\mu}\mathrm{Re}\Sigma\,\mathrm{Im}S - \left.\frac{\partial(\frac{T}{V}\Phi[D,S])}{\partial\mu}\right|_{D,S}. \qquad (2.33)$$

While the sum integrals in $\ln Z$ according to Eq. (2.28) contain ultraviolet divergencies which must be regularized, the expressions for s_g, s_q and n_q in Eqs. (2.29), (2.30) and (2.32) are manifestly ultraviolet convergent because the derivatives of the statistical distribution functions vanish for $\omega \to \pm\infty$.

Self-consistent (or Φ-derivable) approximation schemes preserve the stationarity property in Eq. (2.25) of $\ln Z$ when truncating the infinite sum in Φ at a specific loop order while corresponding self-energies and propagators are self-consistently evaluated from Eq. (2.26) and Dyson's equations. Nevertheless, self-consistency does not guarantee gauge invariance which is an important issue in truncated expansion schemes. In fact, by modifying propagators but leaving vertices unaffected the Ward identities can be violated.

In the following, Φ is considered at 2-loop order which is diagrammatically represented in Figure 2.1 showing also the according self-consistent self-energies. Although vertex corrections can be implemented self-consistently [115], they turn out to be negligible at 2-loop order in Φ [109]. In addition, $s' = n' = 0$ is found for the residual contributions of entropy density and net number density in Eqs. (2.31) and (2.33) at 2-loop order [109]. Thus, in particular s exhibits an additivity of the individual quasiparticle contributions s_i which is a result of the 2-loop approach to

Figure 2.1: Diagrammatic representation of the Φ functional at 2-loop order. Wiggly (solid) lines denote gluons (quarks). The according self-energies of gluons, Π, and quarks, Σ, are obtained by cutting internal propagator lines according to Eq. (2.26).

Φ. This topological feature, being related to Eq. (2.26), has also been observed in massless ϕ^4-theory [116, 117] and in QED [118].

Concentrating on the gluonic contribution s_g, Eq. (2.29) can be rewritten by using the identity

$$
\begin{aligned}
\mathrm{Im}[\ln D^{-1}(\omega, k)] &= -\pi \mathrm{sgn}(\omega)\, \Theta(-\mathrm{Re} D^{-1}(\omega, k)) \\
&\quad + \arctan\left(\frac{\mathrm{Im}\Pi(\omega, k)}{\mathrm{Re} D^{-1}(\omega, k)}\right)
\end{aligned}
\tag{2.34}
$$

where $-\pi/2 < \arctan x < \pi/2$. Hence, s_g can be decomposed into $s_g = s_{g,QP} + s_{g,LD}$ with

$$
s_{g,QP} = \mathrm{tr} \int \frac{d^3 k}{(2\pi)^3} \int_{-\infty}^{\infty} \frac{d\omega}{2} \frac{\partial n(\omega)}{\partial T} \mathrm{sgn}(\omega)\, \Theta(-\mathrm{Re} D^{-1}),
\tag{2.35}
$$

$$
s_{g,LD} = \mathrm{tr} \int \frac{d^4 k}{(2\pi)^4} \frac{\partial n(\omega)}{\partial T} \left\{ \mathrm{Im}\Pi\, \mathrm{Re} D - \arctan\left(\frac{\mathrm{Im}\Pi}{\mathrm{Re} D^{-1}}\right) \right\}.
\tag{2.36}
$$

Here, Eq. (2.35) accounts for the contribution of dynamical quasiparticles to s_g defined by the poles of D and Eq. (2.36) represents the contribution from the continuum part of the spectral density associated with a cut below the light cone $|\omega| < k$ [81, 82, 104, 119] representing Landau damping. Applying a similar identity for $\mathrm{Im}[\ln S^{-1}(\omega, k)]$, s_q and n_q in Eqs. (2.30) and (2.32) can be decomposed similarly into quasiparticle and Landau damping contributions (cf. [94, 106]).

In Coulomb gauge, D consists of a longitudinal and a transverse part, D_L and D_T. Similarly, the (massless) quark propagator consists of two different branches with chirality either equal (positive energy states) or opposite (negative energy states) to helicity. By employing the gauge invariant hard thermal loop (HTL) expressions $\hat{\Pi}$ ($\hat{\Sigma}$) for the gluon (quark) self-energies in the following, one obtains

gauge invariant approximations of s and n. The HTL expressions read [103]

$$\hat{\Pi}_L(\omega, k) = 2m_\infty^2(T,\mu)\left(1 - \frac{\omega}{2k}\ln\frac{\omega+k}{\omega-k}\right), \qquad (2.37)$$

$$\hat{\Pi}_T(\omega, k) = \frac{1}{2}\left(2m_\infty^2(T,\mu) + \frac{\omega^2-k^2}{k^2}\hat{\Pi}_L(\omega, k)\right), \qquad (2.38)$$

$$\hat{\Sigma}_\pm(\omega, k) = \frac{M_{+,l}^2(T,\mu)}{k}\left(1 - \frac{\omega\mp k}{2k}\ln\frac{\omega+k}{\omega-k}\right), \qquad (2.39)$$

where $m_\infty^2(T,\mu)$ and $M_{+,l}^2(T,\mu)$ are defined in section 2.1. Although being derived originally for soft external momenta $\omega, k \sim gT \ll T$, they coincide on the light cone with complete 1-loop results [94, 120]. Finite quark masses, $m_l < T$, turn out to be negligible [120]. The corresponding propagators are evaluated from Dyson's equations. In this way, a first assumption inspired by perturbation theory enters into the model.

For $k \sim T, \mu$ in the weak coupling regime, the poles of both, longitudinal gluon propagator as well as abnormal fermion branch, have exponentially vanishing residues [104, 119] giving only minor contributions to the thermodynamics. Another assumption of the model is that these collective modes can be neglected also in the non-perturbative realm. Furthermore, on-shell quasiparticle dispersion relations are considered by neglecting imaginary parts in the self-energies, i. e. $\mathrm{Im}\hat{\Pi}_T = \mathrm{Im}\hat{\Sigma}_+ = 0$. In this way, also Landau damping contributions to s_g, s_q and n_q vanish.

Performing the ω-integration in Eq. (2.35) (but now for $\hat{D}_T$), the only contributions stem from $\omega^2 \geq \omega_T^2$ because of the Θ-function, where ω_T is the positive solution of $\omega^2 - k^2 - \hat{\Pi}_T(\omega, k) = 0$. Therefore, the ω-integral in Eq. (2.35) reads

$$\int_{-\infty}^{\infty}\frac{d\omega}{2}\frac{\partial n(\omega)}{\partial T}\mathrm{sgn}(\omega)\,\Theta(-\mathrm{Re}\hat{D}_T^{-1}) = \int_{\infty}^{\omega_T}\frac{d\omega}{2}\left(\frac{\partial n(-\omega)}{\partial T} - \frac{\partial n(\omega)}{\partial T}\right). \qquad (2.40)$$

The remaining integration is performed through an integration by parts using $-\partial n(\omega)/\partial T = \partial n(-\omega)/\partial T = \partial\sigma(\omega)/\partial\omega$ for the spectral function $\sigma(\omega) = -n(\omega)\ln n(\omega) + (1+n(\omega))\ln(1+n(\omega))$. Taking the trace over polarization and colour degrees of freedom for the transversal gluon modes, one finds

$$s_{g,QP} = -2(N_c^2-1)\int\frac{d^3k}{(2\pi)^3}\left(\ln(1-e^{-\beta\omega_T}) - \frac{\beta\omega_T}{e^{\beta\omega_T}-1}\right). \qquad (2.41)$$

This expression is equivalent to Eq. (2.7).

Similarly, $s_{q,QP}$ can be evaluated, where non-vanishing contributions to the ω-integration stem from $\omega \geq \omega_+$. Here, ω_+ is the solution of $\omega - k - \hat{\Sigma}_+(\omega, k) = 0$ for the positive fermion branch. Using $-\partial f(\omega)/\partial T = \partial\sigma(\omega)/\partial\omega$ for the spectral function $\sigma(\omega) = -f(\omega)\ln f(\omega) - (1-f(\omega))\ln(1-f(\omega))$, the ω-integral can be integrated by parts. Antiquarks are included by simply replacing $\mu \to -\mu$ in $f(\omega)$. Taking the trace over remaining spin, colour and flavour degrees of freedom,

assuming N_q degenerate (light) quark flavours, one finds

$$
\begin{aligned}
s_{q,QP} &= 2N_c N_q \int \frac{d^3k}{(2\pi)^3} \left(\ln(1 + e^{-\beta\{\omega_+ - \mu\}}) + \frac{\beta\{\omega_+ - \mu\}}{e^{\beta\{\omega_+ - \mu\}} + 1} \right) \\
&\quad + 2N_c N_q \int \frac{d^3k}{(2\pi)^3} \left(\ln(1 + e^{-\beta\{\omega_+ + \mu\}}) + \frac{\beta\{\omega_+ + \mu\}}{e^{\beta\{\omega_+ + \mu\}} + 1} \right). \quad (2.42)
\end{aligned}
$$

This expression is equivalent to Eq. (2.6) now for $N_f = N_q$ degenerate quark flavours with one independent chemical potential μ. $s_{g,QP}$ and $s_{q,QP}$ in Eqs. (2.41) and (2.42) represent entropy density contributions of non-interacting quasiparticles with quantum numbers of transverse gluons (quarks) and dispersion relation ω_T (ω_+).

Correspondingly, $n_{q,QP}$ is evaluated using $-\partial f(\omega)/\partial\mu = \partial f(\omega)/\partial\omega$. Adding antiquarks by $\mu \to -\mu$ in $f(\omega)$ (note, now $\partial f(\omega)/\partial\mu = \partial f(\omega)/\partial\omega$) and taking the trace, $n_{q,QP}$ reads

$$
n_{q,QP} = 2N_c N_q \int \frac{d^3k}{(2\pi)^3} \left(\frac{1}{e^{\beta\{\omega_+ - \mu\}} + 1} - \frac{1}{e^{\beta\{\omega_+ + \mu\}} + 1} \right), \quad (2.43)
$$

which is similar to Eq. (2.8) for $N_f = N_q$ degenerate quark flavours and one independent μ. The quark number susceptibility χ_q follows from straightforward differentiation with respect to μ.

Finally, the quasiparticle dispersion relations need to be specified. One possibility, guided by expressions from weak coupling expansions, was introduced in section 2.1. The entering assumption is that for thermodynamic bulk properties the form $\omega_i^2 = k^2 + \Pi_i + m_i^2$ is sufficient, where Π_i are approximated in the relevant region of ω and k by constants in $(\omega, \vec{k})$, depending only on T and μ. The expressions for Π_i are, again, guided by weak coupling results. However, the replacement of g^2 by G^2 in these dispersion relations is substantial for a proper description of non-perturbative lattice QCD results beyond the agreement for $T > 2T_c$ as presented in [109].

Natural extensions of the quasiparticle model are obvious from the above presented chain of approximations. For instance, one could also include collective modes as well as consider the full energy and momentum dependence of the HTL self-energies including imaginary parts and, thus, Landau damping contributions, as reported in [80, 105, 106].

2.3 Imaginary chemical potential

As pointed out in Appendix A.3, the notorious sign problem occuring in lattice QCD simulations with finite (real) quark chemical potential can be circumvented when formulating QCD thermodynamics, instead, in terms of a purely imaginary chemical potential. Here, information is obtained by considering $\mu^2 < 0$ which, in principle, allows for the identification $\mu = \pm i\mu_i$. Strictly speaking, μ in section 2.1 is analytically continued to complex values $\mu = \mu_r + i\mu_i$ but with the restriction to vanishing real parts $\mu_r = 0$. Results obtained in this way have to be analytically continued back to real chemical potentials into the $\mu^2 > 0$ half-plane in order to gain physical information. This task can be accomplished, for instance, within

the framework of phenomenological models which easily provide a translation between imaginary and real chemical potentials. There, the purely imaginary variable $\mu = i\mu_i$ is continued to the entire complex plane and finally the limit $\text{Im}\,\mu \to 0$ is taken. This procedure is clearly valid only within the analyticity domain of QCD thermodynamics, in which general arguments guarantee the uniqueness of this continuation.

The QCD partition function Z for imaginary chemical potential $\mu = i\mu_i$ reads according to Eq. (A.6) in Appendix A.2

$$Z(\mu_i/T) = \int \mathcal{D}\left[\psi, \bar{\psi}, A_\alpha^a\right] e^{-S_{\text{QCD}}^E} \exp\left(\int\limits_0^{1/T} d\tau \int d^3x\, i\mu_i \psi^\dagger \psi\right), \qquad (2.44)$$

which is a periodic function in μ_i/T with period $\frac{2\pi}{3}$ for the underlying gauge group of QCD, $SU(3)$, [121]. This Roberge-Weiss periodicity means that $Z(\mu_i/T) = Z(\mu_i/T + \frac{2\pi}{3}k)$ for any integer k which becomes obvious by showing that $Z(\mu_i/T)$ is invariant under $\mathcal{Z}_3$-transformations of the form $\psi \to U\psi$, $A_\alpha \to UA_\alpha U^{-1} - \frac{i}{g}(\partial_\alpha U)U^{-1}$, $\mu_i/T \to \mu_i/T + \frac{2\pi}{3}k$, where $U(\vec{x}, \tau)$ are elements of $SU(3)$ with boundary condition $U(\vec{x}, \beta) = \exp(-\frac{2}{3}\pi ik)U(\vec{x}, 0)$, $A_\alpha = t^a A_\alpha^a$ with t^a as fundamental representations of the colour $SU(3)$ Lie Algebra and τ is the Euclidean time. In addition, the QCD partition function is even in μ, i. e. $Z(\mu) = Z(-\mu)$, such that one can focus on the positive identification $\mu = i\mu_i$, in the following.

In the high temperature region, the first derivative $-d(T\ln Z(\mu_i/T))/d(\mu_i/T)$ becomes discontinuous as a function of μ_i/T at $\mu_i/T = \frac{2\pi}{3}k + \frac{\pi}{3}$ while $\ln Z(\mu_i/T)$ is analytic in the low temperature region with μ_i/T. This implies that the Roberge-Weiss periodicity is characterized by lines of first-order $\mathcal{Z}_3$-transitions at $\mu_i/T = \frac{2\pi}{3}k + \frac{\pi}{3}$ for all integers k and sufficiently high T, while for smaller temperatures thermodynamic quantities behave analytically. (The first-order phase transition nature of the Roberge-Weiss transition at high T was confirmed in finite volume first-principle lattice QCD simulations [122–126].) The endpoint of first-order transitions is determined by the crossing of the Roberge-Weiss phase transition line with the chiral critical (or deconfinement) line whose order desicively depends on the quark mass parameters and the number of quark flavours determining the behaviour of the chiral condensate (or the Polyakov loop). A sketch of the QCD phase diagram for imaginary chemical potential is illustrated in Figure 2.2. In the case of $N_f = 4$ degenerate quark flavours, for instance, the chiral phase transition is of first-order as found in lattice simulations [123].

The Roberge-Weiss periodicity implies that in the $T - \mu_i/T$ plane all sectors between $\mu_i/T = \frac{2\pi}{3}k$ and $\mu_i/T = \frac{2\pi}{3}(k + 1)$ are copies of the sector between $\mu_i/T = 0$ and $\mu_i/T = \frac{2\pi}{3}$. Furthermore, the subsector between $\mu_i/T = \pi/3$ and $\mu_i/T = 2\pi/3$ is a reflected copy of the subsector between $\mu_i/T = 0$ and $\mu_i/T = \pi/3$ mirrored at the first Roberge-Weiss transition line. As thermodynamic quantities behave non-analytically at $\mu_i/T = \pi/3$ (first Roberge-Weiss transition), an analytic continuation of results obtained for imaginary chemical potential to real μ has direct access to the region $\mu < \mu_c(T) = \pi/3\,T$ only.

Due to the severe approximations made when relating the phenomenological QPM to QCD, as discussed in section 2.2, the Roberge-Weiss periodicity inherent
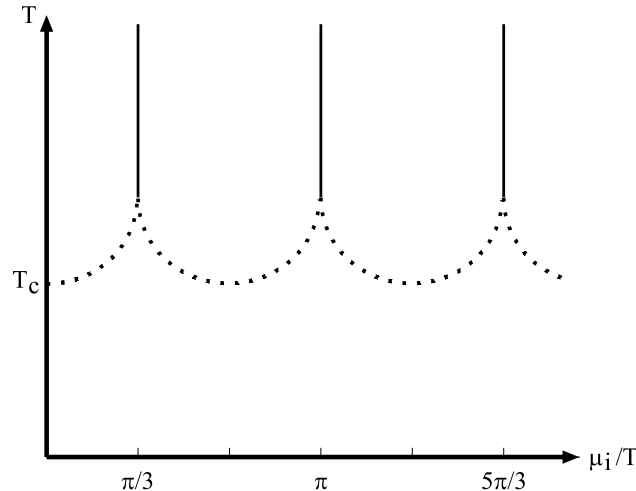
Figure 2.2: Sketch of the QCD phase diagram for imaginary chemical potential μ_i scaled by the temperature T. Solid vertical curves at $\mu_i/T = (2k+1)\frac{\pi}{3}$ depict the Roberge-Weiss phase transitions which are of first-order at high T because the Polyakov loop becomes discontinuous as function of μ_i/T. At low T the transition is of crossover type. The endpoints of the first-order Roberge-Weiss transitions are determined by the crossings with the chiral phase transition lines (dotted curves) whose order, as inferred from the behaviour of the chiral condensate, depends on the quark mass parameters as well as the number of quark flavours.

in QCD is not longer apparent in the QPM as the pressure p as thermodynamic potential is not invariant under $\mathcal{Z}_3$-transformations. Considering an extended $\mathcal{Z}_3$-transformation [127], instead, which allows additionally for the transformation $e^{\pm i\mu_i/T} \to e^{\pm i\mu_i/T} e^{\pm 2\pi ik/3}$, p would keep the same form under $\mu_i \to \mu_i + \frac{2\pi}{3}kT$ if the quasiparticle dispersion relations would be chemical potential independent. Assuming only an implicit μ_i dependence via G^2 in ω_i already requires that $G^2(T, i\mu_i) = G^2(T, i\mu_i + \frac{2\pi}{3}ikT)$. Whether this equality can be fulfilled or not is encoded in the non-trivial μ_i dependence of G^2 via the flow equation and demands future studies.

Having in mind a later comparison of the QPM with lattice QCD results obtained for $N_q = N_f = 4$ degenerate quark flavours, the thermodynamics is straightforwardly formulated by replacing μ by a purely imaginary chemical potential $\mu = i\mu_i$ in Eqs. (2.1)-(2.3) which changes the pressure expressions to [98]

$$p(T, i\mu_i) = \sum_{a=q,g} p_a(T, i\mu_i, M_a(T, i\mu_i)) - B(M_{q,g}(T, i\mu_i)) \qquad (2.45)$$

with

$$
\begin{aligned}
p_q(T, i\mu_i, M_q(T, i\mu_i)) \;=\;& \frac{d_q}{2\pi^2} T \int\limits_0^\infty dk\, k^2 \left(\ln\left[1 + e^{\{i\mu_i - \omega_q\}/T} \right] \right. \\
& \left. + \ln\left[1 + e^{\{-i\mu_i - \omega_q\}/T} \right] \right),
\end{aligned} \qquad (2.46)
$$

$$p_g(T, i\mu_i, M_g(T, i\mu_i)) = -\frac{d_g}{\pi^2} T \int\limits_0^\infty dk k^2 \ln\left[1 - e^{-\omega_g/T}\right] \qquad (2.47)$$

for quarks and gluons, respectively, leaving the notation established in section 2.1 unchanged.

From the standard thermodynamic relations in Eq. (1.2) the entropy density reads $s = s_q + s_g$ with

$$
\begin{aligned}
s_q(T, i\mu_i, M_q(T, i\mu_i)) &= \frac{d_q}{\pi^2 T} \int\limits_0^\infty dk k^2 \left(\frac{[\frac{4}{3}k^2 + M_q^2]}{\omega_q} \right. \\
&\quad \times \left\{ \frac{e^{\omega_q/T} \cos(\mu_i/T) + 1}{e^{2\omega_q/T} + 2e^{\omega_q/T} \cos(\mu_i/T) + 1} \right\} \\
&\quad \left. + \mu_i \left\{ \frac{e^{\omega_q/T} \sin(\mu_i/T)}{e^{2\omega_q/T} + 2e^{\omega_q/T} \cos(\mu_i/T) + 1} \right\} \right), \quad (2.48) \\
s_g(T, i\mu_i, M_g(T, i\mu_i)) &= \frac{d_g}{\pi^2 T} \int\limits_0^\infty dk k^2 \frac{[\frac{4}{3}k^2 + M_g^2]}{\omega_g[e^{\omega_g/T} - 1]}, \quad (2.49)
\end{aligned}
$$

which is purely real while the net quark number density, $n_q(T, i\mu_i) = -i\partial p(T, i\mu_i)/\partial\mu_i$, is given by

$$
\begin{aligned}
n_q(T, i\mu_i) &= \frac{d_q}{2\pi^2} \int\limits_0^\infty dk k^2 \left(\frac{1}{[e^{\{\omega_q - i\mu_i\}/T} + 1]} - \frac{1}{[e^{\{\omega_q + i\mu_i\}/T} + 1]} \right), \quad (2.50) \\
&= i\frac{d_q}{\pi^2} \int\limits_0^\infty dk k^2 \left(\frac{e^{\omega_q/T} \sin(\mu_i/T)}{e^{2\omega_q/T} + 2e^{\omega_q/T} \cos(\mu_i/T) + 1} \right), \quad (2.51)
\end{aligned}
$$

which is purely imaginary and positive (negative) for small positive (negative) μ_i, i. e. n_q is an odd function in μ_i.

The quasiparticle dispersion relations introduced in section 2.1 alter by changing the signs in front of the μ^2 terms in Eqs. (2.16) and (2.17) via

$$2 M_{+,q}^2(T, i\mu_i) = \frac{1}{3}\left[T^2 - \frac{\mu_i^2}{\pi^2}\right] G^2(T, i\mu_i), \qquad (2.52)$$

$$m_\infty^2(T, i\mu_i) = \frac{1}{12}\left([6 + N_f]T^2 - 3N_f \frac{\mu_i^2}{\pi^2}\right) G^2(T, i\mu_i). \qquad (2.53)$$

Consequently, also signs in the flow equation determining the effective coupling G^2 in the T-μ_i thermodynamic parameter space change as is summarized in Appendix B.2. Since, in this way, the μ dependence of the model is sensibly affected by going to purely imaginary chemical potential, a detailed comparison with first principle lattice QCD results serves for a direct examination of the proper μ dependence implementation in the model. Analytically continuing the expressions from imaginary to real chemical potential, the quasiparticle model for N_f degenerate quark flavours with one independent real quark chemical potential is recovered [98].

An effective analytic continuation requires a positive second derivative of Z with respect to μ, cf. [125, 128, 129], i.e. the quark number susceptibility $\chi_q(T, \mu) = \partial n_q(T, \mu)/\partial \mu > 0$. The QPM result for χ_q reads for imaginary chemical potential

$$
\begin{aligned}
\chi_q(T, i\mu_i) &= \frac{d_q}{2\pi^2 T} \int_0^\infty dk\, k^2 \frac{\left(2e^{3\omega_q/T}\cos(\mu_i/T) + 4e^{2\omega_q/T} + 2e^{\omega_q/T}\cos(\mu_i/T)\right)}{\left[e^{2\omega_q/T} + 2e^{\omega_q/T}\cos(\mu_i/T) + 1\right]^2} \\
&\quad + \frac{d_q}{2\pi^2 T} \int_0^\infty dk \frac{k^2}{\omega_q} \frac{\left(e^{3\omega_q/T}\sin(\mu_i/T) - e^{\omega_q/T}\sin(\mu_i/T)\right)}{\left[e^{2\omega_q/T} + 2e^{\omega_q/T}\cos(\mu_i/T) + 1\right]^2} \\
&\quad \times \frac{N_c^2 - 1}{8N_c}\left(\frac{2}{\pi^2}\mu_i G^2 - \left[T^2 - \frac{\mu_i^2}{\pi^2}\right]\frac{\partial G^2}{\partial \mu_i}\right);
\end{aligned}
\tag{2.54}
$$

it is purely real and symmetric under $\mu_i \to -\mu_i$ because of the symmetry properties of the trigonometric functions and the behaviour of $\partial G^2/\partial\mu_i$ which is also symmetric under $\mu_i \to -\mu_i$. The latter can be seen from Eq. (B.21) which reformulated reads

$$
\frac{\partial G^2}{\partial \mu_i} = \frac{b}{a_{\mu_i}} - \frac{a_T}{a_{\mu_i}}\frac{\partial G^2}{\partial T}.
\tag{2.55}
$$

For the individual expressions entering Eq. (2.55), as summarized in Appendix B.2, one finds $\mathcal{I}_1 \to -\mathcal{I}_1$, $\mathcal{I}_2 \to \mathcal{I}_2$ and $\mathcal{I}_3 \to \mathcal{I}_3$ for $\mu_i \to -\mu_i$ such that $b \to -b$, $a_T \to -a_T$ and $a_{\mu_i} \to a_{\mu_i}$. In addition, a Taylor series expansion of $G^2(T, i\mu_i)$ in powers of μ_i consists only of even powers in μ_i [90, 130] such that $\partial G^2/\partial T$ is symmetric under $\mu_i \to -\mu_i$. In the limit $\mu_i \to 0$, one obtains $\partial G^2/\partial \mu_i \to 0$ as $b \to 0$, $a_T \to 0$ while a_{μ_i} and $\partial G^2/\partial T$ remain nonzero. Thus at $\mu = i\mu_i = 0$, one finds

$$
\chi_q(T, \mu = 0) = \frac{d_q}{\pi^2 T}\int_0^\infty dk\, k^2 \frac{e^{\tilde{\omega}_q/T}}{\left[e^{2\tilde{\omega}_q/T} + 2e^{\tilde{\omega}_q/T} + 1\right]} > 0,
\tag{2.56}
$$

with $\tilde{\omega}_q = \omega_q(T, \mu = 0)$. Furthermore, for small μ_i, the first term in Eq. (2.54) is positive and dominates the second term. This implies a positive second derivative of Z, at least, for small μ_i/T.

2.4 Extension to independent chemical potentials

In this section, the QPM as introduced in section 2.1 is formulated for a set of conserved nonzero charges giving rise to a multi-valued chemical potential $\vec{\mu}$. It is straightforward to generalize the model by including two independent quark flavour chemical potentials, i.e. $\vec{\mu} \to \mu_{u,d}$. This is necessary for accessing flavour diagonal and off-diagonal susceptibilities as well as related baryon number, isovector and electric charge susceptibilities which will be compared with available lattice QCD results in chapter 3. These lattice QCD results are obtained by means of Taylor series expansions in the chemical potentials. The susceptibilities sensibly probe the model's baryon-density dependence of the EoS and allow for analyzing the impact of changes in different quark flavour sectors on this baryon-density dependence. Furthermore, a detailed knowledge about the dependence of thermodynamics on different quark flavour chemical potentials is important when discussing various

physical situations such as β-stability or electric charge neutrality e. g. in hypothetical ultra-dense hot proto-neutron stars or a fixed electric charge per baryon ratio in ultra-relativistic heavy-ion collisions.

As primary thermodynamic potential, the pressure $p(T, \mu_u, \mu_d)$ for $N_f = 2$ degenerate *up* and *down* quarks with two independent quark flavour chemical potentials μ_u and μ_d reads [99]

$$p(T, \mu_u, \mu_d) = \sum_{i=u,d,g} p_i(T, \mu_u, \mu_d, M_i(T, \mu_u, \mu_d)) - B(M_{u,d,g}(T, \mu_u, \mu_d)). \quad (2.57)$$

This special case is considered in analogy to the available lattice QCD results to be compared with in chapter 3. These data are obtained for the mass symmetric case, i. e. $m_u = m_d$. In Eq. (2.57), the partial pressures p_i are defined in analogy to Eqs. (2.2) and (2.3) via

$$
\begin{aligned}
p_l(T, \mu_l, M_l(T, \mu_u, \mu_d)) &= \frac{d_l}{2\pi^2} T \int_0^\infty dk\, k^2 \bigg(\ln\left[1 + e^{-\{\omega_l[k, M_l(T,\mu_u,\mu_d)] - \mu_l\}/T}\right] \\
&\quad + \ln\left[1 + e^{-\{\omega_l[k, M_l(T,\mu_u,\mu_d)] + \mu_l\}/T}\right] \bigg), \quad (2.58)
\end{aligned}
$$

$$
p_g(T, M_g(T, \mu_u, \mu_d)) = -\frac{d_g}{\pi^2} T \int_0^\infty dk\, k^2 \ln\left[1 - e^{-\omega_g[k, M_g(T,\mu_u,\mu_d)]/T}\right], \quad (2.59)
$$

where $l = u, d$, M_u, M_d and M_g now depend on μ_u and μ_d and the notation from section 2.1 is unchanged. The function B is again determined by demanding thermodynamic consistency and stationarity. Quark and isovector chemical potentials μ_q and μ_I, respectively, are defined from μ_u and μ_d as stated in section 2.1 but now, in general, $\mu_u \neq \mu_d$ such that $\mu_I \neq 0$. The entropy density follows as $s = s_u + s_d + s_g$ with s_l and s_q analogous to Eqs. (2.6) and (2.7) while the individual net quark flavour number densities n_u and n_d are similar to Eq. (2.8). However, these expressions substantially differ from the ones in section 2.1 as, now, the quasiparticle dispersion relations depend on both μ_u and μ_d according to Eqs. (2.16) and (2.17) which become

$$
2\,M_{+,l}^2(T, \mu_u, \mu_d) = \frac{1}{3}\left[T^2 + \frac{\mu_l^2}{\pi^2}\right] G^2(T, \mu_u, \mu_d), \quad (2.60)
$$

$$
m_\infty^2(T, \mu_u, \mu_d) = \frac{1}{12}\left([6 + N_f]T^2 + \frac{3}{\pi^2}[\mu_u^2 + \mu_d^2]\right) G^2(T, \mu_u, \mu_d). \quad (2.61)
$$

Besides the displayed explicit dependence of the effective quasiparticle masses on μ_u and μ_d (and on T), the effective coupling G^2 now depends on two different quark flavour chemical potentials (and on T) [99].

The dependence of G^2 on μ_u and μ_d is determined from consistency requirements given by Maxwell type relations and the stationarity property of p in analogy to Eq. (2.18). In the case of two independent chemical potentials, however, a system

of three coupled partial differential equations is obtained

$$\frac{\partial s}{\partial \mu_d} = \frac{\partial n_d}{\partial T}, \tag{2.62}$$

$$\frac{\partial s}{\partial \mu_u} = \frac{\partial n_u}{\partial T}, \tag{2.63}$$

$$\frac{\partial n_d}{\partial \mu_u} = \frac{\partial n_u}{\partial \mu_d}. \tag{2.64}$$

This system generalizes the flow equation in Eq. (2.19) propagating, for instance, $G^2(T, \mu_u = 0, \mu_d = 0)$ into the thermodynamic parameter space, i. e. to nonzero μ_u and μ_d.

In the basis (μ_q, μ_I), the generalized system of flow equations following Eqs. (2.62)-(2.64) reads

$$A_1 \frac{\partial G^2}{\partial \mu_I} + B_1 \frac{\partial G^2}{\partial T} = C_1, \tag{2.65}$$

$$A_2 \frac{\partial G^2}{\partial \mu_q} + B_2 \frac{\partial G^2}{\partial T} = C_2, \tag{2.66}$$

$$(A_3 - B_3) \frac{\partial G^2}{\partial \mu_q} = (A_3 + B_3) \frac{\partial G^2}{\partial \mu_I}, \tag{2.67}$$

where the coefficients $A_{1,2,3}$, $B_{1,2,3}$ and $C_{1,2}$ are relegated to Appendix B.3. The explicit structure of the flow equations' coefficients mirrors the coupling among gluon and various quark flavour sectors.

Reformulating Eqs. (2.65)-(2.67) in the basis (μ_u, μ_d) making use of the analogue of Eq. (2.67) in terms of μ_u and μ_d, the generalized system of flow equations is transformed into

$$\mathcal{A}_1 \frac{\partial G^2}{\partial \mu_u} + \mathcal{B}_1 \frac{\partial G^2}{\partial T} = \mathcal{C}_1, \tag{2.68}$$

$$\mathcal{A}_2 \frac{\partial G^2}{\partial \mu_u} + \mathcal{B}_2 \frac{\partial G^2}{\partial T} = \mathcal{C}_2, \tag{2.69}$$

which can be solved uniquely for $G^2(T, \mu_u, \mu_d)$ if the coefficients, as listed in Appendix B.3, are pairwise equal. Indeed, one finds $\mathcal{A}_1 = \mathcal{A}_2$ and $\mathcal{B}_1 = \mathcal{B}_2$ but, in general, $\mathcal{C}_1 = \mathcal{C}_2$ is only found for small values of $\mu_{u,d} \ll \pi T$, i. e. not for arbitrary μ_u and μ_d as elaborated in Appendix B.3. Actually, $\mathcal{C}_1 = \mathcal{C}_2$ is given up to order $\mathcal{O}(\mu_{u,d}^2)$ in a Taylor series expansion in terms of μ_u and μ_d whereas coefficients of third-order terms start to differ. As a consequence, G^2 can uniquely be determined only for these small μ_u and μ_d and, therefore, p and related thermodynamic quantities are restricted to the region $\mu_{u,d} \ll \pi T$. The issue of this potential limitation is further discussed in Appendix B.3. In Appendix B.4, one possible way of circumventing this shortcoming is outlined. Note that the condition $\mathcal{C}_1 = \mathcal{C}_2$ is trivially fulfilled for any value of the quark chemical potentials when $\mu_u = \mu_d$, which is a special case of $\mu_d = \mu_d(\mu_u)$, i. e. when considering one independent chemical potential.

For discussing the various susceptibilities in terms of Taylor series expansions, it is instructive to note that the Taylor coefficients are associated with generalized

quark number susceptibilities which are defined by

$$\chi_{j_u,j_d}(T) = \left. \frac{\partial^{(j_u+j_d)} p(T,\mu_u,\mu_d)}{\partial \mu_u^{j_u} \, \partial \mu_d^{j_d}} \right|_{\mu_u=\mu_d=0} . \tag{2.70}$$

Because $\ln Z(T,\mu_u,\mu_d) = V p(T,\mu_u,\mu_d)/T$ is symmetric under CP transformations, derivatives for odd $(j_u + j_d)$ vanish. Furthermore, in the flavour symmetric case, $m_u = m_d$, $\chi_{j_u,j_d}(T) = \chi_{j_d,j_u}(T)$ is found.

These generalized quark number susceptibilities represent a rich testing ground. Besides the mentioned physical meaning of susceptibilities as measures for fluctuations, they additionally constitute the Taylor coefficients of the excess pressure $\Delta p(T,\mu_u,\mu_d) \equiv p(T,\mu_u,\mu_d) - p(T,\mu_u = 0, \mu_d = 0)$, expanded simultaneously in powers of μ_u and μ_d via

$$\Delta p(T,\mu_u,\mu_d) = \sum_{j_u,j_d} \chi_{j_u,j_d}(T) \frac{\mu_u^{j_u}}{j_u!} \frac{\mu_d^{j_d}}{j_d!} , \tag{2.71}$$

thus containing information about baryon-density effects in the EoS. The excess pressure becomes increasingly important in the domain of larger values of $\mu_{u,d}$ and lower temperatures, even though, a Taylor expansion in $\mu_{u,d}$ directions may not suffice at small T for a satisfying description of the thermodynamics.

In order to calculate the Taylor coefficients, higher-order derivatives of the effective coupling with respect to the chemical potentials need to be evaluated at $\mu_u = \mu_d = 0$ or, equivalently, at $\mu_q = \mu_I = 0$ as described in chapter 3. These derivatives are obtained by mathematical manipulations of the generalized system of flow equations. However, as a result of the limitations mentioned above, susceptibility coefficients can be obtained uniquely only up to and including fourth-order. This is due to the fact that, in general, an n-th order derivative of G^2 requires derivatives up to and including the $(n-1)$-st derivative of $\mathcal{C}_1$ or $\mathcal{C}_2$. As exploited in Appendix B.3, derivatives of the effective coupling up to third-order with respect to the chemical potentials can trustfully be taken, but already $\left. \frac{\partial^4 G^2}{\partial \mu_u^4} \right|_{\mu_u=\mu_d=0}$ is not uniquely determined from the generalized system of flow equations. This derivative enters sixth- and higher-order susceptibility coefficients.

Necessary derivatives are obtained by exploiting Eqs. (2.65)-(2.67), yielding $\left. \frac{\partial G^2}{\partial \mu_q} \right|_{\mu_q=\mu_I=0} = \left. \frac{\partial G^2}{\partial \mu_I} \right|_{\mu_q=\mu_I=0} = 0$ and

$$
\begin{aligned}
\left. \frac{\partial^2 G^2}{\partial \mu_q^2} \right|_{\mu_q=\mu_I=0} = \ & \frac{1}{\mathcal{N}} \Bigg\{ \mathcal{N}_1 \bigg[2\xi_u m_u + 2\xi_u M_{+,u} + \frac{1}{3} \frac{m_u}{M_{+,u}} T G^2 \\
& + \frac{2}{3} T G^2(T) + \left(\frac{1}{3} + \frac{1}{6} \frac{m_u}{M_{+,u}} \right) T^2 \frac{\partial G^2(T)}{\partial T} \bigg] \\
& + \mathcal{N}_2 \bigg[2\xi_d m_d + 2\xi_d M_{+,d} + \frac{1}{3} \frac{m_d}{M_{+,d}} T G^2 \\
& + \frac{2}{3} T G^2(T) + \left(\frac{1}{3} + \frac{1}{6} \frac{m_d}{M_{+,d}} \right) T^2 \frac{\partial G^2(T)}{\partial T} \bigg] +
\end{aligned}
$$

$$
-\mathcal{I}_3 \frac{1}{\pi^2} G^2(T) - \mathcal{I}_4 \frac{1}{3\pi^2} G^2(T) \left(2 + \frac{m_u}{M_{+,u}} \right)
$$
$$
\left. -\mathcal{I}_5 \frac{1}{3\pi^2} G^2(T) \left(2 + \frac{m_u}{M_{+,u}} \right) \right\}, \tag{2.72}
$$

while from Eqs. (2.68) and (2.69), one finds $\left. \frac{\partial G^2}{\partial \mu_u} \right|_{\mu_u = \mu_d = 0} = \left. \frac{\partial G^2}{\partial \mu_d} \right|_{\mu_u = \mu_d = 0} = 0$ and

$$
\begin{aligned}
\left. \frac{\partial^2 G^2}{\partial \mu_u^2} \right|_{\mu_u = \mu_d = 0} &= \frac{1}{\mathcal{N}} \left\{ \mathcal{N}_1 \left[2\xi_u m_u + 2\xi_u M_{+,u} + \frac{1}{3} \frac{m_u}{M_{+,u}} T G^2 \right. \right. \\
&\quad \left. + \frac{2}{3} T G^2(T) + \left(\frac{1}{3} + \frac{1}{6} \frac{m_u}{M_{+,u}} \right) T^2 \frac{\partial G^2(T)}{\partial T} \right] \\
&\quad \left. -\mathcal{I}_3 \frac{1}{2\pi^2} G^2(T) - \mathcal{I}_4 \frac{1}{3\pi^2} G^2(T) \left(2 + \frac{m_u}{M_{+,u}} \right) \right\}, \tag{2.73}
\end{aligned}
$$

with coefficients $\mathcal{N}$, $\mathcal{N}_{1,2}$ listed in Appendix B.3, $G^2(T) = G^2(T, \mu_u = 0, \mu_d = 0)$ and $\mathcal{I}_{3,4,5}$ as well as $M_{+,u}$ and $M_{+,d}$ considered at $\mu_q = \mu_I = 0$ or, equivalently, at $\mu_u = \mu_d = 0$. Note that in the flavour symmetric case considered here Eqs. (2.72) and (2.73) are related via $\left. \frac{\partial^2 G^2}{\partial \mu_u^2} \right|_{\mu_{u,d} = 0} = \frac{1}{2} \left. \frac{\partial^2 G^2}{\partial \mu_q^2} \right|_{\mu_{q,I} = 0}$. In addition, odd derivatives with respect to the chemical potentials such as $\frac{\partial^3 G^2}{\partial \mu_u^3}$ or mixed derivatives such as $\frac{\partial^2 G^2}{\partial \mu_u \partial \mu_d}$ or $\frac{\partial^2 G^2}{\partial \mu_q \partial \mu_I}$ vanish at $\mu_u = \mu_d = 0 = \mu_q = \mu_I$. These expressions and equalities are uniquely obtained from the generalized system of flow equations.

3 Comparison with Lattice QCD Data

In this chapter, it is shown that the quasiparticle model introduced in chapter 2 provides an efficient and accurate parametrization of a variety of lattice QCD results for different numbers of dynamical quark flavours with different quark masses at zero and nonzero baryon density and temperatures $T \geq 0.75\,T_c$. In particular, the parametrization of the effective coupling as defined in Eqs. (2.20) and (2.21) turns out to be flexible enough to account appropriately for the complexity observed in some thermodynamic quantities. Sections 3.1 and 3.2 are devoted to the thermodynamics at zero and nonzero net baryon densities, respectively. In section 3.3, the equation of state for $N_f = 2+1$ is discussed and some of its properties are analyzed.

3.1 Zero baryon density

Here, the thermodynamics at zero chemical potential is studied. QPM results for pressure and entropy density as primary thermodynamic quantities are compared with corresponding lattice QCD results for $N_f = 2$ and $2+1$ in section 3.1.1. The extrapolation of results to different quark mass parameters within the quasiparticle model is tested in section 3.1.2 for pressure and interaction measure. An application is the chiral extrapolation of the EoS. In section 3.1.3, the asymptotic equation of state at zero net baryon density is examined for the pure $SU(3)$ gauge theory and for $N_f = 2 + 1$.

3.1.1 Basic thermodynamic quantities

To start with, the QPM introduced in section 2.1 is confronted with lattice QCD results for the pressure of $N_f = 2$ degenerate quark flavours at zero chemical potential, $\mu = 0$, obtained by the Bielefeld-Swansea collaboration [8,131]. The lattice simulations were performed in $N_\sigma = 16$ spatial and in $N_\tau = 4$ temporal extensions using improved fermion and gauge boson actions but rather large temperature dependent quark mass parameters $m_{u,d}(T) = \xi_{u,d}T$ with $\xi_{u,d} = 0.4$ implying a pion mass of about $m_\pi = 770$ MeV around $T = T_c$.

Usually, results obtained in lattice simulations need a proper extrapolation to the thermodynamic as well as the continuum limit due to finite size and cut-off effects. This issue is further discussed in Appendix C. It is true that employing improved actions strongly reduces lattice discretization errors at high temperatures, but, in particular, simulations with $N_\tau = 4$ temporal extensions can still exhibit large deviations from the continuum limit. One simple way of approximating the continuum limit is by multiplying the lattice QCD data for quantity X by a specific constant continuum extrapolation factor $d^{(X)}$. Note that this estimated correction factor does not necessarily have to be temperature independent, as assumed here. In fact, the lattice QCD data presented in [8] represent a continuum extrapolation
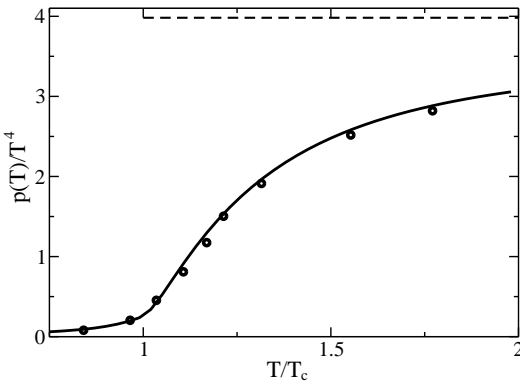
Figure 3.1: Comparison of QPM (solid curve) with lattice QCD re-
sults (circles) [8] for the scaled pressure $p(T)/T^4$ as a function of
T/T_c for $N_f = 2$ degenerate quark flavours at zero baryo-chemical
potential. The QPM parameters entering Eqs. (2.20) and (2.21)
read $\lambda = 11.5$, $T_s = 0.88\,T_c$, $b = 333.4$ and $B(T_c) = 0.17\,T_c^4$ with
$T_c = 175$ MeV as suggested in [9]. The horizontal dashed curve
indicates the value $p^{\mathrm{SB}}(T)/T^4 = (32 + 21\tilde{N}_f)\pi^2/180$ of an ideal,
non-interacting gas of quarks and gluons, where $\tilde{N}_f = g(0.4\,T)N_f$
with $N_f = 2$ and $g(0.4\,T) = 0.9672$ accounts for the considered
nonzero quark mass.

of the data in [131] by $d^{(p)} = 1.15$. This is in line with the suggestions in [131]
which advocate a continuum extrapolation of about 10-20% above the data for
$T \geq 1.2\,T_c$.

Figure 3.1 shows the lattice QCD data [8] for the scaled pressure $p(T)/T^4$ to-
gether with the QPM results according to Eqs. (2.1)-(2.3). A very good description
is found even below T_c, where a quasiparticle picture is not well justified and should
be replaced by a realistic hadron resonance gas (HRG) model. Formally, the proper
description of the lattice QCD results below T_c within the QPM requires fairly
large values of the effective coupling G^2. The corresponding excitations become
very massive, ranging to hadronic mass scales, such that these massive excitations
are sufficient to reproduce fairly well the lattice QCD data within the interval 0.75
T_c - T_c. Numerically, this is not too distinct from the HRG model, where several
resonances may be regrouped into a few representative excitations. (Vice versa, one
should mention that the HRG model [132,133] coincides with lattice QCD data also
slightly above T_c. For an even more extreme point of view on quark-hadron duality
cf. [134].) Nevertheless, due to the successful description of lattice QCD results,
the linear ansatz in Eq. (2.20) for G^2 below T_c can be considered as convenient
parametrization.

Concentrating on the physical case of $N_f = 2 + 1$ with two degenerate light
(*up* and *down*) and one heavier (*strange*) quark flavours, the goal is a proper
parametrization of the EoS in the form $p(e, n_B)$ as needed in hydrodynamic ap-
plications. For this purpose, the QPM is adjusted to lattice QCD results of the
scaled pressure from [132] which represent again a continuum extrapolation of the
lattice QCD data in [131] by $d^{(p)} = 1.15$ but now for $N_f = 2 + 1$. This is due to the
fact that discretization errors for improved actions turn out to be of equal size for
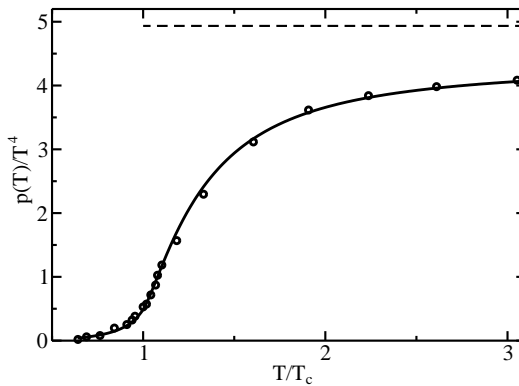
Figure 3.2: Comparison of QPM (solid curve) with lattice QCD results
(circles) [132] for the scaled pressure $p(T)/T^4$ as a function of T/T_c
for $N_f = 2 + 1$ dynamical quark flavours at zero baryo-chemical
potential. The QPM parameters entering Eqs. (2.20) and (2.21)
read $\lambda = 7.8$, $T_s = 0.8\,T_c$, $b = 347$ and $B(T_c) = 0.61\,T_c^4$ with
$T_c = 170$ MeV as suggested in [6,8]. The horizontal dashed curve
indicates the value $p^{\mathrm{SB}}(T)/T^4 = (32 + 21\tilde{N}_f)\pi^2/180$ of an ideal,
non-interacting gas of quarks and gluons, where $\tilde{N}_f = 2\,g(0.4\,T) +$
$g(T)$ with $g(0.4\,T) = 0.9672$ and $g(T) = 0.8275$ accounts for the
considered nonzero quark masses.

different N_f cases [131]. The employed quark mass parameters read $m_i(T) = \xi_i T$
with $\xi_{u,d} = 0.4$ and $\xi_s = 1$. In Figure 3.2, the lattice QCD results for $p(T)/T^4$
are exhibited together with the QPM results. As evident, the QPM accurately
parametrizes the pressure for $N_f = 2 + 1$. Accordingly, the scaled entropy density
$s(T)/T^3$ as related thermodynamic quantity is equally well described by the QPM
as shown in Figure 3.3.

3.1.2 Chiral extrapolation and conformal limit

As pointed out in section 3.1.1, the lattice QCD results are obtained for rather large
quark mass parameters. For hydrodynamic applications, however, i. e. when using
a reliable QCD equation of state of the form $p(e, n_B)$ for solving the hydrodynamic
equations of motion based on Eq. (1.4), these results need to be extrapolated to
the quark mass values realized in nature. As an approximation, one can consider
the chiral limit, for which naively $m_u = m_d = m_s = 0$ MeV can be set. This task is
easily accomplished within the QPM, as the quark mass parameters directly enter
into the model via Eq. (2.14).

Recently, lattice QCD results [135] for the QCD thermodynamics of $N_f = 2+1$
quark flavours with almost physical quark masses became available. This opens
the avenue for directly examining the incorporated quark mass dependence in the
employed quasiparticle dispersion relations. Adjusting the QPM parameters to
$p(T)/T^4$ for the heavier quark mass parameter set-up in [132] as in section 3.1.1,
one can perform a naive extrapolation to the lighter quark masses in [135] by leaving
the parameters in G^2 as well as $B(T_c)$ unchanged. In this way, a negligible impact of
the quark mass parameters on G^2 and on the pressure integration constant $B(T_c)$
is assumed. A dependence of the QPM parameters on m_l, nonetheless, could,
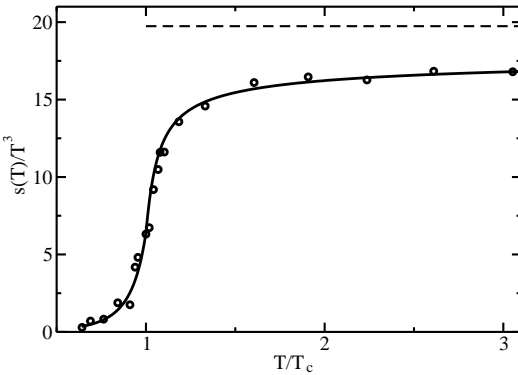
Figure 3.3: Comparison of QPM (solid curve) with lattice QCD re-
sults (circles) [132] for the scaled entropy density $s(T)/T^3$ as a
function of T/T_c for $N_f = 2 + 1$ dynamical quark flavours at zero
baryo-chemical potential. The QPM parameters are the same as
in Figure 3.2. The horizontal dashed curve indicates the value
$s^{\mathrm{SB}}/T^3 = (32 + 21\tilde{N}_f)\pi^2/45$ of an ideal, non-interacting gas of
quarks and gluons with $\tilde{N}_f$ as in Figure 3.2.

in principle, be possible. For instance, the behaviour of $p(T)/T^4$ for $T < T_c$ as
constraint by the lattice QCD results in [135] demands a readjustment of $B(T_c)$,
which mostly affects the pressure for temperatures close to and below T_c, with
changes in $m_{u,d}$ and m_s (cf. the discussion in section 4.3).

The lattice QCD results in [135] are obtained for $N_\tau = 6$ temporal extensions
and improved actions for which $T_c(N_\tau = 6) = 196$ MeV was found in [10]. Note,
that a comparison of results for $p(T)/T^4$ at $N_\tau = 4$ and $N_\tau = 6$ as well as $N_\tau = 8$ for
larger temperatures suggests that the considered lattice QCD data are already close
to the continuum limit. This justifies the use of $T_c(N_\tau \to \infty) = 192$ MeV [10] in this
section. The quark masses employed in [135] can be parametrized by $m_{u,d}(T) =
a_0 T_c^2/T + a_1 T$ with $a_0 = 0.017$ and $a_1 = 0.004$ and $m_s = 10\,m_{u,d}$, implying that
the *strange* quark mass is set to its physical value while *up* and *down* quark masses
are set such that $m_\pi = 220$ MeV close to T_c. Over a large temperature interval,
however, they can be approximated by $m_{u,d}(T) = 0.015\,T$ and $m_s = 10\,m_{u,d}$, for
simplicity, which is rather close to the chiral limit.

Applying the strategy outlined above, the parameters of G^2 employed for Fig-
ure 3.2 remain fixed while the quark mass parameters and consequently $B(T_c)$ are
changed according to [135]. The result of the mass extrapolation for $p(T)/T^4$ is
exhibited in Figure 3.4 showing an almost perfect description of the lattice QCD
results [135]. This success suggests that the quark mass dependence of the effective
coupling G^2 is indeed tiny and that the employed quasiparticle dispersion relations
are suitable for a reasonable chiral extrapolation of thermodynamic bulk proper-
ties [96]. Setting $m_u = m_d = m_s = 0$ MeV, the corresponding result is exhibited by
the dashed curve in Figure 3.4. Note that within the QPM, results obtained for the
temperature dependent quark mass parameters reported in [135] are numerically
equivalent to results obtained for constant $m_u = m_d = 0$ MeV and $m_s = 55$ MeV.

As pointed out in [136], the correct model description of the interaction mea-
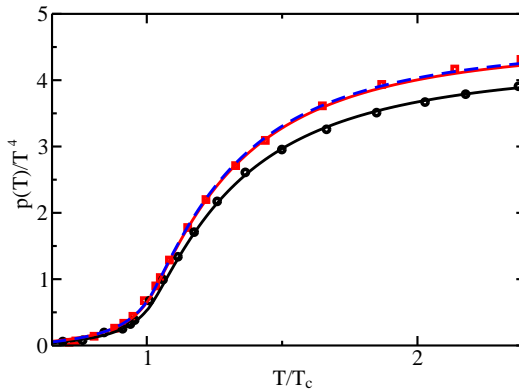
Figure 3.4: Test of the quark mass dependence in the employed quasi-
           particle dispersion relations via Eq. (2.14). Circles and squares
           exhibit lattice QCD results for the scaled pressure $p(T)/T^4$ for
           $N_f = 2 + 1$ at $\mu_B = 0$ for larger [132] and smaller [135] quark
           mass parameters, respectively, while the black (lower) solid curve
           shows the QPM parametrization from Figure 3.2 complying with
           the quark mass parameters in [132]. Red (upper) solid curve ex-
           hibits the QPM result when changing the quark masses according
           to [135] leaving the parameters in G^2 unchanged but changing
           $B(T_c) = 0.76\,T_c^4$ with $T_c = 192$ MeV [10]. The blue dashed curve
           shows the corresponding chiral limit by setting $m_u = m_d = m_s = 0$
           MeV and $B(T_c) = 0.78\,T_c^4$.

sure $(e - 3p)$ is important for constructing an appropriate hydrodynamic equation
of state. In Figure 3.5, the comparison between lattice QCD results [135] for
$(e - 3p)/T^4$ with almost physical quark masses and the QPM results employing
the parameters of G^2 from Figure 3.2 but the quark mass parameters and $B(T_c)$
according to [135] from Figure 3.4, respectively, is exhibited. A nice agreement is
found. The peak in $(e - 3p)/T^4$ located at $T = 1.08\,T_c$ is related to the softest
point in the EoS which is signalled by a minimum in p/e as a function of e. For
larger temperatures, $(e - 3p)/T^4$ approaches logarithmically zero corresponding to
the logarithmic decrease of G^2 with T in Eqs. (2.20) and (2.21), but is for $T = 10\,T_c$
already close to the conformal limit $e = 3\,p$, implying for the trace of the thermal
part of the energy-momentum tensor $\Theta^\mu_\mu(T) = 0$ (cf. Appendix A.2).

3.1.3 Asymptotic equation of state

The QCD equation of state in the form $p(e)$ at $n_B = 0$ and asymptotically large
temperatures is important for the description of the dynamics of the early universe
at $T > T_c$ via Friedmann's equations in Eq. (1.3) (cf. [18]). Until recently, first-
principle lattice QCD simulations at large T were hampered by the time-consuming
$T = 0$ simulations needed for the renormalization in the standard integral method
computation of p. In contrast, adjusting the QPM parameters to the EoS for
temperatures around T_c known from lattice QCD, the model can easily be continued
to large T.

Recently, a new method was proposed for directly evaluating the asymptotic
EoS in lattice QCD simulations [137]. Within this approach, the pressure for
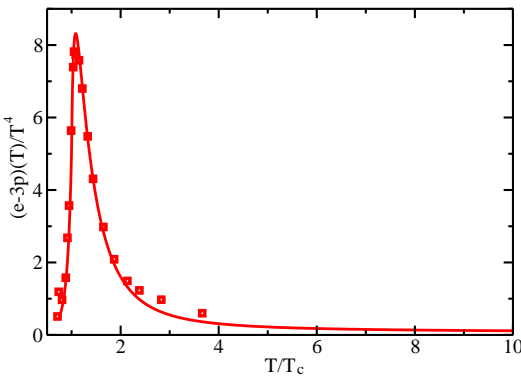
Figure 3.5: Comparison of QPM (solid curve) with lattice QCD results
(circles) [135] for the scaled interaction measure $(e - 3p)/T^4$ as a
function of T/T_c for $N_f = 2 + 1$ dynamical quark flavours at zero
baryo-chemical potential. The QPM parameters are the same as
for the red (upper) solid curve in Figure 3.4.

pure $SU(3)$ gauge theory was, first, successfully compared with former continuum
extrapolated lattice QCD results [138] calculated in the temperature interval $T_c -$
$5\,T_c$, and then, evaluated up to temperatures of the order of $10^7\,T_c$ [137, 139].
Applying a similar strategy within the QPM by adjusting the QPM parameters to
the lattice QCD data [138] in the interval T_c - $5\,T_c$ and then continuing without
any further parameter adjustment to large T, the validity of this procedure can
directly be tested. As evident from Figure 3.6, the QPM accurately parametrizes
the lattice QCD results for p/p^{SB} from [138] and also describes fairly well p/p^{SB}
for asymptotically large temperatures. This is a highly non-trivial result, as one
could argue that the QPM reproduces lattice QCD results in a restricted (small)
temperature range above T_c, only. It happens, however, that the employed QPM
parametrization catches the thermodynamically relevant QCD degrees of freedom
in a very large range of T.

Having successfully tested the applicability of the QPM for extrapolating lattice
QCD results of $N_f = 0$ known at moderate temperatures to large T, one can
proceed and predict the asymptotic EoS of $N_f = 2 + 1$. For this purpose, the QPM
parameters are adjusted to the continuum extrapolated lattice QCD results [140] for
$p(T)/T^4$ of $N_f = 2 + 1$ at zero baryo-chemical potential in the temperature interval
$0.8\,T_c$ - $2.55\,T_c$. The simulations are performed on a lattice with $N_\sigma = 18$ spatial
and $N_\tau = 6$ temporal extensions and for physical quark masses $m_{u,d} = 4.5$ MeV and
$m_s = 112.5$ MeV. In contrast to the lattice simulations examined in sections 3.1.1
and 3.1.2, non-improved actions are used in [140] resulting in increased finite size
and cut-off effects. Therefore, the lattice QCD results are extrapolated to the
continuum limit by multiplication with a constant factor $d^{(p)} = 0.663$ according
to [140] representing the ratio of the Stefan-Boltzmann pressures calculated in the
continuum limit and at $N_\tau = 6$. As exhibited in Figure 3.7, the QPM appropriately
reproduces the lattice QCD data [140] in the temperature interval $0.8\,T_c$ - $2.55\,T_c$.
Continuing to asymptotically large temperatures, the scaled pressure still shows
deviations of about 4.5% from the Stefan-Boltzmann limit for temperatures of the
order of $10^5\,T_c$ indicating that even at these large temperatures the system is not
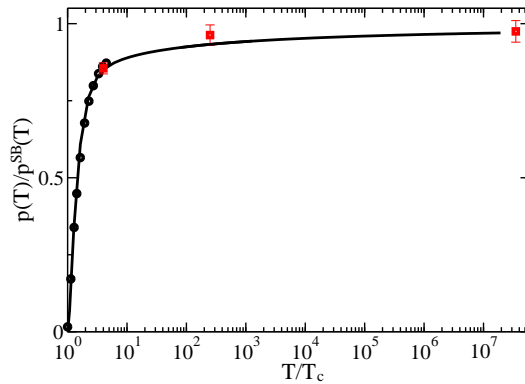
Figure 3.6: Comparison of QPM (solid curve) with lattice QCD re-
sults (circles [138] and squares [137, 139]) for the pressure of pure
$SU(3)$ gauge theory scaled by its Stefan-Boltzmann pressure p^{SB}
as a function of T/T_c for $T \geq T_c$. The QPM is adjusted to the lat-
tice QCD results from [138] between T_c and $5\,T_c$ with parameters
reading $\lambda = 5$, $T_s = 0.756\,T_c$ and $B(T_c) = 0.01\,T_c^4$ with $T_c = 271$
MeV as suggested in [6, 8] and then continued without any change
of parameters to asymptotically large temperatures.

a weakly interacting gas. Nonetheless, the EoS is rather close to the ideal gas
equation of state because the corresponding squared speed of sound is less than
0.1% below its Stefan-Boltzmann value $c_s^2 = \frac{1}{3}$.

The results exhibited in Figure 3.7 serve as predictions, while corresponding
lattice QCD results are expected in the near future. The effective quark and gluon
quasiparticle masses exhibit a behaviour $\sim T\,G$ implying that at asymptotically
large temperatures the quasiparticle excitations are fairly heavy. At $T = 10^5\,T_c$,
the dynamically generated mass parameters (self-energy parts) read $M_g \sim 12$ TeV
and $M_q \sim 8$ TeV, thus invalidating the naive picture of weakly coupled quarks and
gluons with negligible masses. On the other hand, the naive Stefan-Boltzmann
limit is approached, from below, up to 90% at $T \sim 50\,T_c$ with logarithmically
decreasing deviations when going to larger T. In addition, at these asymptotically
large temperatures, *charm* and even heavier quark degrees of freedom should be
included into the considerations in line with [88].
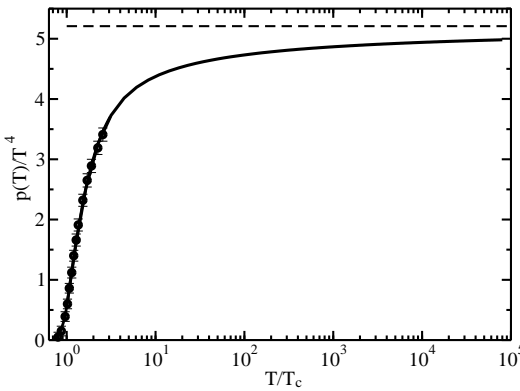
Figure 3.7: Comparison of QPM (solid curve) with lattice QCD results
(circles) [140] for the scaled pressure $p(T)/T^4$ as a function of T/T_c
for $N_f = 2 + 1$ dynamical quark flavours at zero baryo-chemical
potential. The QPM parameters are adjusted to the lattice QCD
data between $0.8\,T_c$ - $2.55\,T_c$ reading $\lambda = 1$, $T_s = 0.49\,T_c$, $b = 286$
and $B(T_c) = 0.51\,T_c^4$ with $T_c = 170$ MeV as suggested in [6,8]. For
predicting the asymptotic equation of state, the QPM is continued
to temperatures of the order of $10^5\,T_c$. The horizontal dashed curve
indicates the value $p^{\mathrm{SB}}(T)/T^4 = (32 + 21\tilde{N}_f)\pi^2/180$ of an ideal,
non-interacting gas of quarks and gluons, where $\tilde{N}_f \approx 3$ accounts
for the considered almost physical quark masses.

3.2   Nonzero baryon density

Having demonstrated the ability of the QPM to successfully reproduce lattice QCD
data for zero chemical potential, recent progress in lattice QCD simulations with
small nonzero chemical potential is exploited in this section to examine the ability
of the QPM to correctly predict the thermodynamic functions at arbitrary T and
μ. For this purpose, first, available lattice QCD data for $N_f = 2$ are investigated.
In section 3.2.1, the pressure coefficients are considered which simultaneously con-
stitute Taylor expansions of net baryon density and quark number susceptibility.
Corresponding coefficients for entropy density and energy density are studied in
section 3.2.2 providing all necessary information for discussing the isentropic evo-
lutionary paths of constant entropy per baryon in the T - μ_B plane as well as the
equation of state along them. In section 3.2.3, various susceptibilities are discussed
and related implications in different physical situations are analyzed in section 3.2.4.
Turning to the case of $N_f = 4$, nonzero baryon-density effects are studied in detail
for purely imaginary chemical potential in section 3.2.5. Pronounced structures
observed in this case allow, exemplarily, a discussion of the form of the chemi-
cal potential dependence in the quasiparticle dispersion relations as elaborated in
section 3.2.6.

3.2.1   Taylor expansion approach

Effects of finite quark chemical potential can be studied in line with lattice QCD
simulations [141] by expanding the pressure into a Taylor series in powers of (μ_q/T)

around $\mu_q = 0$ at $\mu_I = 0$ via

$$p(T, \mu_q, \mu_I = 0) = T^4 \sum_{n=0,2,4,6,\dots}^{\infty} c_n(T) \left(\frac{\mu_q}{T}\right)^n. \tag{3.1}$$

Here, $c_0(T) = p(T)/T^4$ is the scaled pressure at zero chemical potential as considered in section 3.1. Due to the invariance of $\ln Z$ under CP transformations, $c_n(T) = 0$ for odd n. The coefficients $c_2(T)$, $c_4(T)$ and $c_6(T)$ in Eq. (3.1) are defined viz

$$c_n(T) = \frac{1}{n!} \frac{\partial^n (p(T, \mu_q + \mu_I, \mu_q - \mu_I)/T^4)}{\partial(\mu_q/T)^n}\bigg|_{\mu_q=\mu_I=0}, \tag{3.2}$$

and extracted from appropriate derivatives of $\ln Z$ in [141]. The simulations in [141] are performed on a lattice with $N_\sigma = 16$ spatial and $N_\tau = 4$ temporal extensions using improved actions for $N_f = 2$ degenerate quark flavours with $m_{u,d} = \xi_{u,d} T$ and $\xi_{u,d} = 0.4$. Note that the lattice QCD data from [141] as considered in the following are not extrapolated to the continuum limit. Even though the computation of $c_n(T)$, $n \geq 2$, is not related to the expensive integral method needed when evaluating $c_0(T)$ [8], deviations from the continuum limit are expected to be of the same order of magnitude as in the case of $p(T)/T^4$ [142]; i. e. of about additional 10-20%. Nonetheless, corrections seem to increase for higher-order coefficients [142].

Starting from Eqs. (2.57)-(2.59) by noting that in the considered case of $\mu_I = 0$ one employs $\mu_u = \mu_d = \mu_q = \mu$, the Taylor coefficients $c_2(T)$, $c_4(T)$ and $c_6(T)$ can be evaluated within the QPM following Eq. (3.2). The expressions explicitly read [90]

$$c_2(T) = -\frac{d_q}{2\pi^2 T^3} \int_0^\infty dk k^2 f_q^{(1)}(\tilde{\omega}_q/T), \tag{3.3}$$

$$c_4(T) = -\frac{d_q}{48\pi^2} \int_0^\infty dk k^2 \left(\frac{2}{T^3} f_q^{(3)}(\tilde{\omega}_q/T) \right.$$
$$\left. + \frac{3}{T^2 \tilde{\omega}_q} f_q^{(2)}(\tilde{\omega}_q/T) \frac{\partial^2 M_q^2}{\partial \mu_q^2}\bigg|_0 \right), \tag{3.4}$$

$$c_6(T) = -\frac{d_q}{1440\pi^2} \int_0^\infty dk k^2 \left(\frac{2}{T^3} f_q^{(5)}(\tilde{\omega}_q/T) \right.$$
$$+ \frac{10}{T^2 \tilde{\omega}_q} f_q^{(4)}(\tilde{\omega}_q/T) \frac{\partial^2 M_q^2}{\partial \mu_q^2}\bigg|_0 + \frac{15}{2T \tilde{\omega}_q{}^2} f_q^{(3)}(\tilde{\omega}_q/T) \left(\frac{\partial^2 M_q^2}{\partial \mu_q^2}\right)^2\bigg|_0$$
$$\left. + \frac{5}{\tilde{\omega}_q} f_q^{(2)}(\tilde{\omega}_q/T) \left[\frac{\partial^4 M_q^2}{\partial \mu_q^4}\bigg|_0 - \frac{3}{2\tilde{\omega}_q{}^2} \left(\frac{\partial^2 M_q^2}{\partial \mu_q^2}\right)^2\bigg|_0 \right] \right). \tag{3.5}$$

Here, $d_q = 2 N_c N_q$ with $N_q = N_f = 2$, $f_q(a) = (e^a + 1)^{-1}$, $f_q^{(n)}(a) = \partial^n f_q(a)/\partial a^n$, $\tilde{\omega}_q = \omega_q(T, \mu_q = 0, \mu_I = 0)$ and the derivatives of M_q^2 with respect to μ_q, which need to be evaluated at $\mu_q = \mu_I = 0$, are relegated to Appendix B.1. In this way, $c_2(T)$ depends on $G^2(T)$, $c_4(T)$ depends on $G^2(T)$ and its second derivative
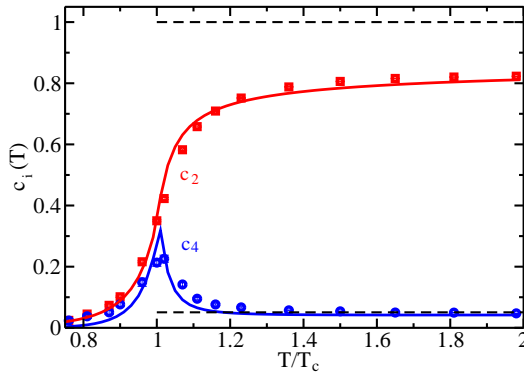
Figure 3.8: Comparison of QPM results (solid curves) and lattice
QCD results [141] (symbols) for $c_2(T)$ (red curve and squares)
and $c_4(T)$ (blue curve and circles). The refitted QPM parameters
read $\lambda = 12$, $T_s = 0.87\,T_c$ with $T_c = 175$ MeV and $b = 426.05$.
The horizontal dashed curves represent the corresponding Stefan-
Boltzmann results for $\bar{c}_2 = N_f/2$ and $\bar{c}_4 = N_f/(4\pi^2)$ with $N_f = 2$.
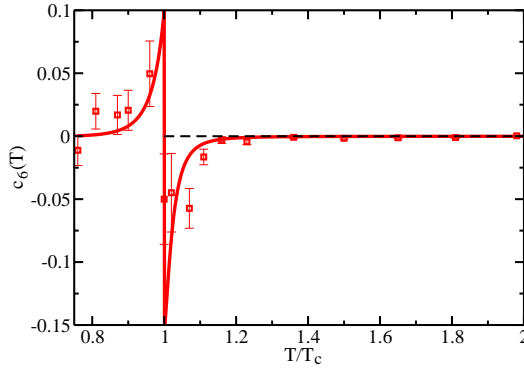
Figure 3.9: Comparison of QPM results (solid red curve) and lattice
QCD results [141] (squares) for $c_6(T)$. The QPM parameters are
the same as in Figure 3.8. The horizontal dashed curve represents
the Stefan-Boltzmann value for $\bar{c}_6 = 0$.

with respect to μ_q and $c_6(T)$ depends on $G^2(T)$ as well as its second and fourth
derivative with respect to μ_q.

Applying the QPM parametrization for the continuum extrapolated results of
$c_0(T)$, as summarized in Figure 3.1, now to $c_2(T)$ according to Eq. (3.3), the
description of the lattice QCD results [141] is not perfect, but exhibits some devi-
ations [90]. In particular, for $0.9\,T_c$-T_c the QPM underestimates the lattice QCD
data by about 50% whereas for $T \geq 1.02\,T_c$ the agreement is impressive. This
demands a slight refit of the QPM parameters to the lattice QCD results of $c_2(T)$
as exhibited in Figure 3.8. The quality of the model is tested by its ability to also
reproduce $c_4(T)$ and $c_6(T)$ with this parametrization. As evident from Figures 3.8
and 3.9, the QPM gives an excellent description of $c_2(T)$ and, simultaneously, yields
an impressive agreement with the lattice QCD data for $c_4(T)$ and $c_6(T)$. In par-
ticular, the pronounced structures seen in $c_4(T)$ and $c_6(T)$ in the vicinity of the
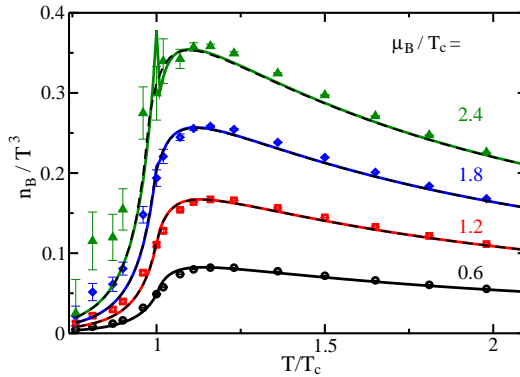
Figure 3.10: Scaled net baryon density n_B/T^3 as a function of T/T_c, for $\mu_B/T_c = 2.4$, 1.8, 1.2, 0.6 (from top to bottom). QPM results from the truncated expansion in Eq. (3.7) (solid curves) are compared with lattice QCD results (symbols) from [141] for $N_f = 2$ based on the same truncation. Dashed curves represent the full QPM result for $n_B = n_q/3$ according to $n_q = n_u + n_d$ and Eq. (2.8) for the individual net quark flavour number densities. The QPM parameters are the same as in Figure 3.8.

transition temperature are quantitatively reproduced as a result of the change in the curvature of $G^2(T)$ at $T = T_c$ according to Eq. (2.20). The peak structure in $c_4(T)$, giving the dominant μ_B-dependent contribution to the quark number susceptibility according to

$$\frac{\chi_q(T, \mu_q)}{T^2} = 2c_2(T) + 12c_4(T)\left(\frac{\mu_q}{T}\right)^2 + \mathcal{O}(\mu_q^4), \qquad (3.6)$$

can be interpreted as an indication for some critical behaviour in $\chi_q(T, \mu_q)$ across the quark-hadron phase transition.

Other thermodynamic quantities can equally be constructed from these Taylor coefficients by means of expansions of the form in Eqs. (3.1) or (3.6). For instance, the net baryon density, using $c_{2,4,6}(T)$, reads

$$\frac{n_B(T, \mu_B)}{T^3} = \frac{2}{3}c_2(T)\left(\frac{\mu_B}{3T}\right) + \frac{4}{3}c_4(T)\left(\frac{\mu_B}{3T}\right)^3 + 2c_6(T)\left(\frac{\mu_B}{3T}\right)^5 + \mathcal{O}\left(\mu_B^7\right), \quad (3.7)$$

yielding a truncated expansion for n_B. In Figure 3.10, QPM results for the full expression of n_B/T^3 defined in chapter 2 as well as for the truncated expansion up to $\mathcal{O}(\mu_B^5)$ according to Eq. (3.7) are compared with lattice QCD results [141] based on the same truncation. In this way, the truncation error can be estimated. For $\mu_B/T_c \leq 1.8$, truncated and exact results for n_B/T^3 agree within the linewidth. Only for $\mu_B/T_c = 2.4$, significant deviations between truncated and exact results become evident near $T = T_c$ which are of about 23% [89, 90]. These deviations, however, can be traced back to an artificial mechanical instability of the form $\partial p/\partial n_B \leq 0$ in the truncated expressions. The full QPM expression, in contrast, is free of this artifact providing a thermodynamically consistent description.
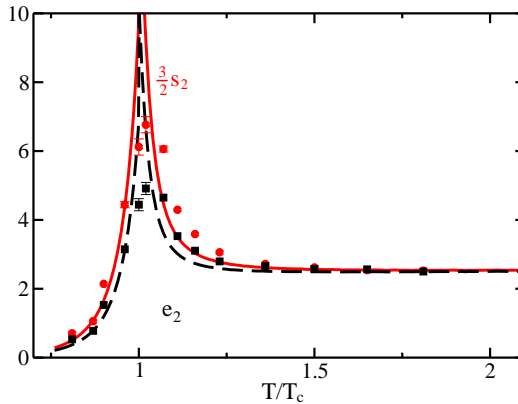
Figure 3.11: Comparison of the Taylor coefficients $e_2(T)$ (squares/black dashed curve) and $s_2(T)$ (circles/red solid curve) for $N_f = 2$ from [9] (symbols) with corresponding QPM results (curves). The QPM parameters are the same as in Figure 3.8.

3.2.2 Isentropic trajectories

As entropy and net baryon densities are locally conserved in ideal fluid dynamics, the specific entropy s/n_B of each fluid cell stays constant in its comoving frame. Although different cells usually start out with different initial specific entropies, and thus the expanding fireball as a whole maps out a broad band of widely varying s/n_B values, each fully equilibrated fluid cell follows a single line of constant s/n_B in the $T-\mu_B$ phase diagram. It is therefore of interest to study the characteristics of these isentropic expansion trajectories, in particular the behaviour of the EoS along them.

The isentropic trajectories for different values of s/n_B follow directly from the first-principles evaluation of the lattice EoS and its QPM parametrization considered in sections 3.1.1 and 3.2.1. In the following, needed thermodynamic quantities are considered within truncated expansions like in Eq. (3.7) for n_B. In a similar way, energy and entropy densities can be decomposed via

$$\frac{e(T,\mu_q)}{T^4} = \sum_n e_n(T) \left(\frac{\mu_q}{T}\right)^n , \qquad e_n(T) = 3c_n(T) + c'_n(T) , \qquad (3.8)$$

$$\frac{s(T,\mu_q)}{T^3} = \sum_n s_n(T) \left(\frac{\mu_q}{T}\right)^n , \qquad s_n(T) = (4-n)c_n(T) + c'_n(T) , \qquad (3.9)$$

where the $c_n(T)$ are defined in section 3.2.1 and $c'_n(T) \equiv T\, dc_n(T)/dT$. The Taylor coefficients $e_n(T)$ and $s_n(T)$ were calculated in [9] via fine but finite difference approximations of the Taylor coefficients $c_n(T)$. Since they contain both, $c_n(T)$ and their derivatives with respect to T, they provide a more sensitive test of the QPM than the pressure coefficients alone. Figures 3.11 and 3.12 exhibit the comparison of the lattice QCD data [9] with the QPM results for $e_{2,4}(T)$ and $s_{2,4}(T)$ obtained in the same way as in [9] finding a fairly good agreement. Applying a somewhat coarser finite difference approximation, the agreement, in particular in the vicinity of T_c, improves to some extent [93].

For $N_f = 2$ dynamical quark flavours, truncated Taylor expansions for n_B and
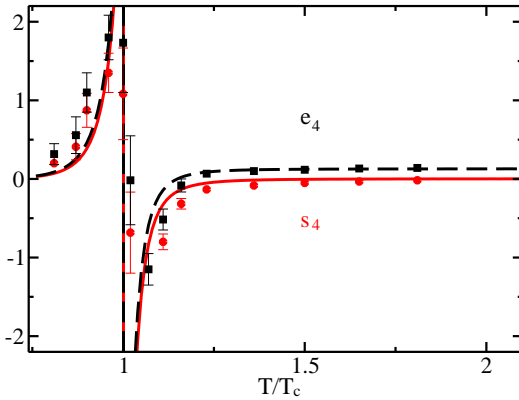
Figure 3.12: Comparison of the Taylor coefficients $e_4(T)$ (squares/black dashed curve) and $s_4(T)$ (circles/red solid curve) for $N_f = 2$ from [9] (symbols) with corresponding QPM results (curves). The QPM parameters are the same as in Figure 3.8.

s up to $\mathcal{O}((\mu_B/T)^6)$ were employed in [9] to determine the isentropic trajectories for $s/n_B = 300$, 45, 30, sampling those regions of the phase diagram which can be explored with heavy-ion collisions at RHIC, SPS, and at AGS or FAIR/SIS300, respectively. In the same way, n_B and s are evaluated within the QPM according to Eqs. (3.7) and (3.9) up to $\mathcal{O}((\mu_B/T)^6)$.

In Figure 3.13, lattice QCD and QPM results are compared for $s/n_B = 300$ and 45 employing simultaneously the two separately optimized QPM parametrizations for $c_0(T)$ and $c_2(T)$ (cf. Figures 3.1 and 3.8) [93]. Although both QPM parametrizations are almost the same, this approach would give up thermodynamic consistency of the model. Employing instead one single self-consistent parametrization for both $c_0(T)$ and $c_2(T)$, trajectories for large s/n_B remain unchanged whereas those for smaller s/n_B disagree with the results exhibited in Figure 3.13 in the vicinity of T_c [95]. This is mainly caused by differences in $s(T)/T^3$ and translates, for a given isentropic trajectory, into large variations of μ_B near T_c while causing only small differences of about 6% at large T. In particular, the pronounced structures of the isentropic trajectory near the estimated phase boundary are lost in the self-consistent fit procedure. This shows that the pattern of the isentropic expansion trajectories is quite sensitive to details in the EoS (cf. the discussion in [95]).

Also, the results exhibited in Figure 3.13 depend on the value of T_c. Changing the deconfinement transition temperature to $T_c = 170$ MeV results in a shift of the trajectories by about 10% in μ_B direction near T_c but has negligible consequences for $T \geq 1.5\,T_c$. At asymptotically large T, where $c_{0,2}(T)$ are essentially flat, the relation $\frac{\mu_B}{T} = 18\frac{c_0}{c_2}(\frac{n_B}{s})$ holds for small μ_B, i. e. lines of constant specific entropy are essentially given by lines of constant μ_B/T, as is the case in a quark-gluon plasma with perturbatively weak interactions.

Figure 3.13 also exhibits the chemical freeze-out points deduced from hadron multiplicity data for Au+Au collisions at $\sqrt{s} = 130\,A$ GeV at RHIC ($T_{f.o.} = 169 \pm 6$ MeV and $\mu_{B,f.o.} = 38 \pm 4$ MeV [49]) and for $158\,A$ GeV Pb+Pb collisions at SPS ($T_{f.o.} = 154.6 \pm 2.7$ MeV and $\mu_{B,f.o.} = 245.9 \pm 10.0$ MeV [50]). Applying the
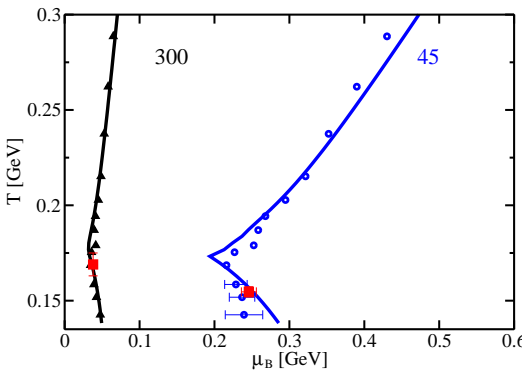
Figure 3.13: Isentropic evolutionary paths. Triangles and circles in-
dicate $N_f = 2$ lattice QCD data from [9] for $s/n_B = 300$ and 45,
respectively. Corresponding QPM results are depicted for a mixed
parametrization where $c_0(T)$ and $c_2(T)$ are fitted independently
according to Figures 3.1 and 3.8. Full red squares show chemical
freeze-out points deduced in [49,50] from hadron multiplicity data,
as summarized in [51].

statistical model in [46], the specific entropies at these freeze-out points can be
deduced to $s/n_B = 200$ for RHIC-130 and $s/n_B = 30$ for SPS-158, i.e. to only
about $2/3$ of the values corresponding to the QPM parametrization of the QCD
lattice data. One should remember, though, that the phenomenological values are
deduced from experimental data using a complete spectrum of hadronic resonances
whereas the lattice simulations were performed for only $N_f = 2$ dynamical quark
flavours with not quite realistic quark masses.

Figure 3.14 shows that along isentropic expansion lines the EoS is almost in-
dependent of the value of s/n_B [93, 95]. Accordingly, the squared speed of sound
c_s^2, controlling the build-up of hydrodynamic flow, is essentially independent of the
specific entropy. Note that the results exhibited in Figure 3.14 do not significantly
depend on the employed fit procedure outlined above. The EoS along the isen-
tropes remains almost unaffected; for large energy densities $e \gtrsim 30\,\mathrm{GeV/fm^3}$ the
differences in $p(e)$ are less than 2% [95].

3.2.3   Susceptibilities

Information on various susceptibilities has been accumulated from first-principle
lattice QCD calculations, cf. [141, 143–145] to mention some of them. (For more
information cf. references in [99].) Keeping in mind limitations due to finite-size,
numerical set-up and quark mass effects they represent a source of insight into
baryon-density effects in the hot quark-gluon medium. Phenomenologically, these
lattice QCD results can be described within models such as the hadron resonance
gas model [146,147] for $T \leq T_c$. Above T_c, different models including various bary-
onic bound states [148], Nambu–Jona-Lasinio model [149] and Polyakov loop exten-
sions thereof [150–154] or quasiparticle models [90,96] deliver a suitable agreement.
In addition, qualitative agreement with lattice QCD results [144] was obtained for
$T \geq 1.5\,T_c$ within the Φ-functional approach to QCD [155].
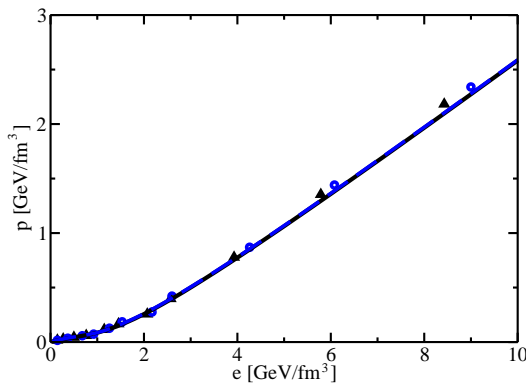
Figure 3.14:   Lattice QCD data [9] of p as a function of e for $N_f =$ 2 along isentropes with $s/n_B = 300$ (triangles) and 45 (circles), compared with the corresponding QPM results (blue solid and black dashed curves, respectively) being indistinguishable for the different s/n_B.

In this section, the QPM as extended in section 2.4 towards two independent quark flavour chemical potentials is confronted with lattice QCD data of various susceptibilities for $N_f = 2$ degenerate quark flavours. In the following, two different expansions are considered: An expansion in terms of μ_q and μ_I in line with the lattice QCD simulations in [141] and an expansion in terms of μ_u and μ_d in line with the considerations in [143, 145]. Even though μ_I is defined differently in [143, 145] via $\mu_I = \frac{1}{4}(\mu_u - \mu_d)$ compared to the definition in [141] and in chapter 2, expressions in chapter 2 as well as results exhibited in this section turn out to be unaffected by different definitions of μ_I.

Besides the quark number susceptibility defined in Eq. (3.6), also isovector as well as diagonal and off-diagonal susceptibilities have been calculated in [141] in terms of an expansion in μ_q/T at $\mu_I = 0$. The isovector susceptibility $\chi_I(T, \mu_q)$ obeys the expansion

$$\frac{\chi_I(T, \mu_q)}{T^2} = 2c_2^I(T) + 12c_4^I(T)\left(\frac{\mu_q}{T}\right)^2 + \mathcal{O}(\mu_q^4),\qquad(3.10)$$

where the susceptibility coefficients as in the case of $c_n(T)$ follow from differentiating the pressure, now via

$$c_n^I(T) = \left.\frac{1}{n!}\frac{\partial^n(p(T, \mu_q + \mu_I, \mu_q - \mu_I)/T^4)}{\partial(\mu_I/T)^2\partial(\mu_q/T)^{n-2}}\right|_{\mu_q = \mu_I = 0}.\qquad(3.11)$$

Due to the invariance of $\ln Z$ under CP transformations, $c_n^I(T) = 0$ for odd n.

As in section 3.2.1, the QPM expressions for $c_n^I(T)$ follow from Eqs. (2.57)-(2.59)
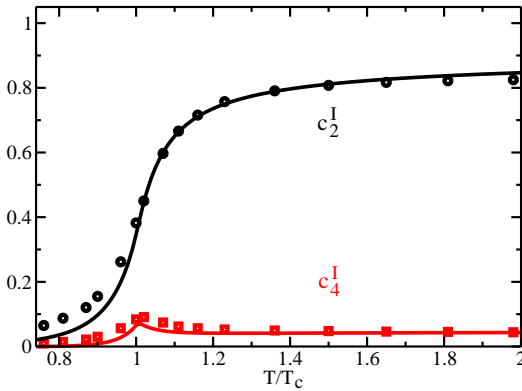
Figure 3.15: Comparison of QPM results (solid curves) with lattice QCD data [141] (symbols) for $c_n^I(T)$ (back curve and circles for $n = 2$ and red curve and squares for $n = 4$) for $N_f = 2$ quark flavours. The QPM parameters are the same as in Figure 3.8.

reading (cf. [99]) with the notation of section 3.2.1

$$c_2^I(T) = -\frac{d_q}{2\pi^2 T^3} \int\limits_0^\infty dk k^2 f_q^{(1)}(\tilde{\omega}_q/T), \qquad (3.12)$$

$$c_4^I(T) = -\frac{d_q}{48\pi^2} \int\limits_0^\infty dk k^2 \left(\frac{2}{T^3} f_q^{(3)}(\tilde{\omega}_q/T) \right.$$
$$\left. +\frac{2}{T^2\tilde{\omega}_q} f_q^{(2)}(\tilde{\omega}_q/T) \left[2\frac{\partial^2 M_q^2}{\partial\mu_u^2}\bigg|_0 - \frac{1}{2}\frac{\partial^2 M_q^2}{\partial\mu_q^2}\bigg|_0 \right] \right), \qquad (3.13)$$

which implies $c_2^I(T) = c_2(T)$ within the QPM. The derivatives of M_q^2 evaluated at zero chemical potentials entering $c_4^I(T)$ are relegated to Appendix B.1 and the incorporated second derivatives $\frac{\partial^2 G^2}{\partial\mu_q^2}\bigg|_{\mu_q=\mu_I=0}$ and $\frac{\partial^2 G^2}{\partial\mu_u^2}\bigg|_{\mu_u=\mu_d=0}$ of the effective coupling G^2 are given in Eqs. (2.72) and (2.73).

The numerically evaluated QPM results for $c_2^I(T)$ and $c_4^I(T)$ are exhibited in Figure 3.15 and compared with lattice QCD data [141] finding a fairly good agreement. Similar to $c_4(T)$, the expansion coefficient $c_4^I(T)$ slightly underestimates the lattice QCD data [141] approaching its Stefan-Boltzmann limit $N_f/(4\pi^2)$, while $c_2^I(T)$ agrees remarkably well with the data for $T \geq T_c$ approaching its Stefan-Boltzmann limit $N_f/2$ asymptotically. Whereas $\chi_q(T, \mu_q)$, due to the growing importance of the higher-order coefficients with increasing chemical potential, exhibits a significant peak structure close to T_c for large μ_q/T, $\chi_I(T, \mu_q)$ does not develop such pronounced structures. This behaviour is a consequence of the much less pronounced peak in $c_4^I(T)$ compared to $c_4(T)$. Similar findings were reported in [41], where a phenomenological sigma model was considered.

The behaviour of the electric charge susceptibility $\chi_Q(T, \mu_q)$ is strongly related to $\chi_q(T, \mu_q)$ and $\chi_I(T, \mu_q)$ via $\chi_Q = \frac{1}{4}\left(\chi_I + \frac{1}{9}\chi_q\right)$. The corresponding Taylor
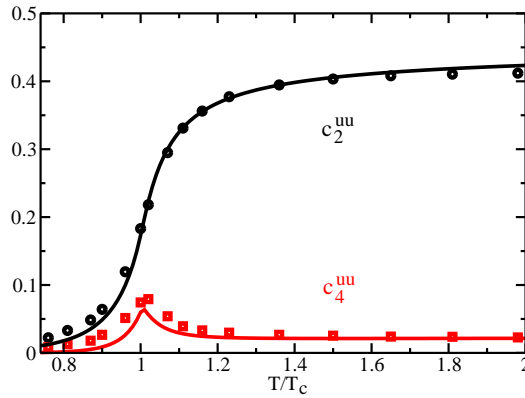
Figure 3.16: Comparison of QPM results (solid curves) for the coefficients $c_n^{uu}(T)$ of the flavour diagonal susceptibility $\chi_{uu}(T, \mu_q)$ with lattice QCD data [141] (black curve and circles for $n = 2$, red curve and squares for $n = 4$). QPM parameters as in Figure 3.8.

expansion reads

$$\frac{\chi_Q(T, \mu_q)}{T^2} = 2c_2^Q(T) + 12c_4^Q(T) \left(\frac{\mu_q}{T}\right)^2 + \mathcal{O}(\mu_q^4), \tag{3.14}$$

with coefficients $c_n^Q(T) = \frac{1}{4}\left(c_n^I(T) + \frac{1}{9}c_n(T)\right)$. From the definition of $c_n^Q(T)$ it is clear that the structures appearing in higher-order coefficients are mainly influenced by contributions from $c_n^I(T)$. Thus, similar to $\chi_I(T, \mu_q)$, $\chi_Q(T, \mu_q)$ exhibits a much less pronounced behaviour at large μ_q/T than $\chi_q(T, \mu_q)$.

Correlations between fluctuations in different flavour components can be discussed by considering flavour diagonal, $\chi_{uu} = \frac{1}{4}(\chi_q + \chi_I)$, and off-diagonal, $\chi_{ud} = \frac{1}{4}(\chi_q - \chi_I)$, susceptibilities. They read

$$\frac{\chi_{uu}(T, \mu_q)}{T^2} = 2c_2^{uu}(T) + 12c_4^{uu}(T) \left(\frac{\mu_q}{T}\right)^2 + \mathcal{O}(\mu_q^4) \tag{3.15}$$

for the flavour diagonal susceptibility and

$$\frac{\chi_{ud}(T, \mu_q)}{T^2} = 2c_2^{ud}(T) + 12c_4^{ud}(T) \left(\frac{\mu_q}{T}\right)^2 + \mathcal{O}(\mu_q^4) \tag{3.16}$$

for the flavour off-diagonal susceptibility, where the individual coefficients are defined by $c_n^{uu}(T) = (c_n(T) + c_n^I(T))/4$ and $c_n^{ud}(T) = (c_n(T) - c_n^I(T))/4$.

The susceptibilities $c_n^{uu}(T)$ and $c_n^{ud}(T)$ for $n = 2, 4$ are exhibited in Figures 3.16 and 3.17, respectively, and compared with lattice QCD data [141]. The diagonal coefficients $c_{2,4}^{uu}(T)$ show a similar pattern as $c_{2,4}(T)$ and $c_{2,4}^I(T)$, approaching their Stefan-Boltzmann limits $N_f/4$ asymptotically in the case of $c_2^{uu}(T)$ and $N_f/(8\pi^2)$ for $T > 2\,T_c$ in the case of $c_4^{uu}(T)$. The pronounced peak structure in the off-diagonal coefficient $c_4^{ud}(T)$ is well reproduced, while $c_2^{ud}(T)$ is zero for all temperatures, in contrast to the data [141], which are numerically small but differ noticeably from zero in the region $T \lesssim T_c$. $c_2^{ud}(T) = 0$ is a consequence of $c_2^I(T) = c_2(T)$ in the QPM. As the flavour off-diagonal susceptibilities $c_n^{ud}(T)$
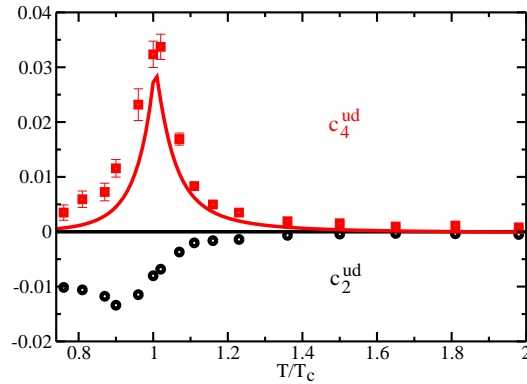
Figure 3.17: Comparison of QPM results (solid curves) for the coefficients $c_n^{ud}(T)$ of the flavour off-diagonal susceptibility $\chi_{ud}(T, \mu_q)$ with lattice QCD data [141] (black curve and circles for $n = 2$, red curve and squares for $n = 4$). QPM parameters as in Figure 3.8.

rapidly approach zero for all n, $\chi_{ud}(T, \mu_q)$ vanishes for large T indicating that fluctuations in different flavour channels are uncorrelated at high temperatures. On the other hand, $\chi_{ud}(T, \mu_q)$ increases rapidly with increasing μ_q in the vicinity of T_c, indicating increasing correlations between fluctuations in different flavour channels in the phase transition region. This explains the observed different behaviour in $\chi_q(T, \mu_q$ and $\chi_I(T, \mu_q)$: While peak structures effectively add up in χ_q, they approximately cancel each other in χ_I.

Turning to the expansion of thermodynamic quantities in terms of μ_u and μ_d, in the following, the QPM is confronted with lattice QCD data [143, 145] of some generalized quark number susceptibilities $\chi_{j_u,j_d}(T)$ as defined in Eq. (2.70). The lattice simulations [143, 145] are performed for $N_f = 2$ degenerate quark flavours on a lattice with spatial and temporal extensions $N_\sigma = 16$ and $N_\tau = 4$. In this respect, the lattice calculation set-up in [141] and in [143, 145] is identical. However, the employed quark mass parameter reads $m_u = m_d = 0.1\,T_c$ and is constant for a given value of T_c, i. e. it is temperature independent in contrast to the lattice set-up in [141]. Consequently, some of the coefficients in the generalized system of flow equations change as summarized in Appendix B.3.

Furthermore, non-improved actions are employed in [143, 145]. Thus, cut-off effects in these numerical results are sizeably increased compared to results of simulations using improved actions. While the lattice QCD data from [141] were assumed to be rather close to the continuum limit in the previous section 3.2.1 and the above discussion in this section, the lattice QCD results in [143, 145] must be appropriately extrapolated to the continuum limit. By investigating different N_τ at fixed large temperature T in [156–158], temperature independent continuum extrapolation factors were estimated reading $d^{(\chi_2)} = 0.47$ for $\chi_{2,0}(T)/T^2$ [156–158] and $d^{(\chi_4)} = 0.32$ for $\chi_{4,0}(T)$ [158]. These correction factors are applied to the lattice QCD data in [143, 145] for all T although they are strictly valid only for large temperatures. Similar to the findings in [142] as discussed in section 3.2.1, continuum limit corrections increase for higher-order coefficients.

This estimate of the continuum limit is necessary for making a meaningful

comparison between the two different expansions in terms of (μ_q, μ_I) and (μ_u, μ_d) possible. In fact, flavour diagonal and off-diagonal susceptibilities are closely related to the generalized quark number susceptibilities via [99]

$$c_2^{uu} = \frac{1}{2}\frac{\chi_{2,0}}{T^2}, \tag{3.17}$$

$$c_2^{ud} = \frac{1}{2}\frac{\chi_{1,1}}{T^2}, \tag{3.18}$$

$$c_4^{uu} = \frac{1}{24}\left(\chi_{4,0} + 2\chi_{3,1} + \chi_{2,2}\right), \tag{3.19}$$

$$c_4^{ud} = \frac{1}{24}\left(2\chi_{3,1} + 2\chi_{2,2}\right). \tag{3.20}$$

From Eqs. (2.70) and (2.57)-(2.59), some of the generalized quark number susceptibilities explicitly read [99]

$$\frac{\chi_{2,0}(T)}{T^2} = -\frac{d_q}{2\pi^2 T^3}\int_0^\infty dk k^2 f_q^{(1)}(\tilde{\omega}_q/T), \tag{3.21}$$

$$\chi_{4,0}(T) = -\frac{d_q}{2\pi^2}\int_0^\infty dk k^2 \left(\frac{1}{T^3}f_q^{(3)}(\tilde{\omega}_q/T)\right.$$
$$\left. +\frac{3}{2T^2\tilde{\omega}_q}f_q^{(2)}(\tilde{\omega}_q/T)\left.\frac{\partial^2 M_q^2}{\partial\mu_u^2}\right|_0\right), \tag{3.22}$$

$$\chi_{2,2}(T) = -\frac{d_q}{2\pi^2}\int_0^\infty dk k^2 \frac{1}{2T^2\tilde{\omega}_q}f_q^{(2)}(\tilde{\omega}_q/T)$$
$$\times\left(\left.\frac{\partial^2 M_q^2}{\partial\mu_q^2}\right|_0 - \left.\frac{\partial^2 M_q^2}{\partial\mu_u^2}\right|_0\right), \tag{3.23}$$

where $\chi_{1,1}(T) = 0$ and $\chi_{3,1}(T) = 0$ for all temperatures. Again, the derivatives of M_q^2 entering Eqs. (3.22) and (3.23) are evaluated at zero chemical potentials as summarized in Appendix B.1 and the embedded derivatives $\left.\frac{\partial^2 G^2}{\partial\mu_q^2}\right|_{\mu_q=\mu_I=0}$ and $\left.\frac{\partial^2 G^2}{\partial\mu_u^2}\right|_{\mu_u=\mu_d=0}$ are given in Eqs. (2.72) and (2.73).

The relation $\chi_{3,1}(T) = 0$ holds because the above derivatives of the effective coupling are related with each other in the flavour symmetric case as noted in section 2.4. Furthermore, $\chi_{1,1}(T) = 0$ because $c_2^{ud}(T) = 0$ for all temperatures. In particular $\chi_{1,1}(T)$ vanishes because flavour-mixing effects, which describe the dependence of one quark flavour sector on changes in another one, are inherent in the QPM only via the quasiparticle dispersion relations resulting in terms which vanish at $\mu_{u,d} = 0$. Qualitatively, the observed deviations in the flavour off-diagonal susceptibilities, can be understood from perturbative QCD arguments. In a perturbative expansion of the thermodynamic potential different partonic sectors start to couple only at order $\mathcal{O}(g^3)$ of the QCD running coupling. However, these plasmon term contributions $\propto g^3$ are not completely reproduced in a similar expansion of the QPM thermodynamic potential, cf. [80]. Similar findings, pointing to the necessity
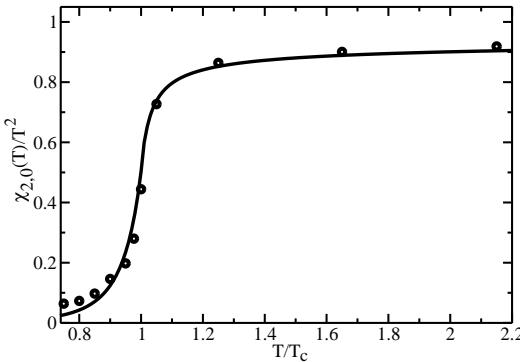
Figure 3.18: Comparison of QPM results (solid curve) with the continuum limit estimate of the lattice QCD results [143, 145] (circles) for $\chi_{2,0}(T)/T^2$. The refitted QPM parameters read $\lambda = 7$, $T_s = 0.76\,T_c$ with $T_c = 175$ MeV and $b = 431$.
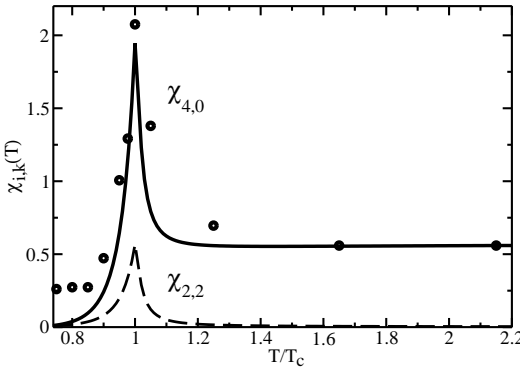
Figure 3.19: Comparison of QPM results (solid curve) with the continuum limit estimate of the lattice QCD results [143,145] (circles) for $\chi_{4,0}(T)$. The QPM parameters are the same as in Figure 3.18. The corresponding QPM result for $\chi_{2,2}(T)$ is exhibited by the dashed curve.

of properly including flavour-mixing effects for affecting the flavour off-diagonal susceptibilities, were reported in [159].

In Figures 3.18 and 3.19, the QPM results for $\chi_{2,0}(T)/T^2$ and for $\chi_{4,0}(T)$, respectively, are compared with the corresponding lattice QCD results [143, 145] extrapolated to the continuum limit by the correction factors summarized above. As the simulation set-up between [141] and [143, 145] differs noticeably, the QPM parameters have to be readjusted to $\chi_{2,0}(T)/T^2$ and then the quality of the QPM is probed by predicting, according to Eqs. (3.22) and (3.23), $\chi_{4,0}(T)$ and $\chi_{2,2}(T)$, which are exhibited in Figure 3.19. Note that the lattice QCD results for $2c_2^{uu}(T)$ from [141] and the depicted results for $\chi_{2,0}(T)/T^2$ would agree fairly well except for the transition region, if a continuum extrapolation factor of $d^{(c_2)} = 1.1$ in line with [142] would be applied to the data from [141].

3.2.4 Physical applications

As pointed out in sections 2.4 as well as 3.2.1 and 3.2.3, susceptibility coefficients constitute the Taylor expansions of various thermodynamic quantities such as pressure or net baryon density and, thus, carry information on baryon-density effects in the equation of state. Basing on these Taylor expansions, some bulk properties of deconfined quark matter of $N_f = 2$ dynamical quark flavours are discussed in this section. It turns out that the interplay between the different quark flavour sectors decisively dictates the baryon-density dependence of bulk thermodynamic quantities in various physical situations [99]. Clearly, these considerations are limited by the range of validity of such an approach, say by conservatively guessing the quark flavour chemical potentials to be individually restricted by $\mu_{u,d}/T < 1$.

In terms of the generalized quark number susceptibilities discussed at the end of section 3.2.3, the net baryon density n_B can be decomposed into

$$n_B(\mu_u, \mu_d) \approx \frac{1}{3}\left\{ (\chi_{2,0} + \chi_{1,1})(\mu_u + \mu_d) + \left(\frac{\chi_{4,0}}{3!} + \frac{\chi_{3,1}}{3!}\right)(\mu_u^3 + \mu_d^3) \right.$$
$$\left. + \frac{1}{2}(\chi_{3,1} + \chi_{2,2})(\mu_u^2\mu_d + \mu_u\mu_d^2) \right\}, \qquad (3.24)$$

including only terms up to $\mathcal{O}(\mu^3)$ and omitting the explicit notation of the T dependence in the following. Thus, the net baryon density simultaneously depends on two independent chemical potentials, μ_u and μ_d. (This is similarly the case for a non-interacting gas of gluons and massless quarks with two independent quark flavour chemical potentials.) Only in the special case of $\mu_I = 0$, i. e $\mu_u = \mu_d = \mu_q$, n_B is a function of one chemical potential alone ensuring constant net baryon density for constant $\mu_B = 3\mu_q$. This illustrates the importance of a detailed knowledge on the quark flavour chemical potential dependencies in bulk thermodynamic quantities.

In Figure 3.20, the interrelation between μ_u and μ_d for various physical situations is exhibited. Curves of constant μ_B are given by $\frac{\mu_d}{T} = \frac{2}{3}\frac{\mu_B}{T} - \frac{\mu_u}{T}$ as, for instance, shown by the linear short-dashed curve in Figure 3.20 for $\frac{\mu_B}{T} = 1$. In this case, $\frac{\mu_u}{T} + \frac{\mu_d}{T} = \frac{2}{3}$ ensuring that the considerations stay within the range of validity of the employed Taylor expansion approach. The individual net quark number densities read

$$n_u = \chi_{2,0}\mu_u + \chi_{1,1}\mu_d + \frac{\chi_{4,0}}{3!}\mu_u^3 + \frac{\chi_{3,1}}{2}\mu_u^2\mu_d + \frac{\chi_{3,1}}{3!}\mu_d^3 + \frac{\chi_{2,2}}{2}\mu_u\mu_d^2, \qquad (3.25)$$

$$n_d = \chi_{2,0}\mu_d + \chi_{1,1}\mu_u + \frac{\chi_{4,0}}{3!}\mu_d^3 + \frac{\chi_{3,1}}{2}\mu_u\mu_d^2 + \frac{\chi_{3,1}}{3!}\mu_u^3 + \frac{\chi_{2,2}}{2}\mu_u^2\mu_d. \qquad (3.26)$$

In the QPM, $\chi_{1,1} = \chi_{3,1} = 0$, such that lines of constant n_u or n_d are approximately given by lines of constant μ_u or μ_d. Only at temperatures $T \approx T_c$, where the influence of $\chi_{2,2}$ is non-negligible, the simple pattern is deformed somewhat. For $\mu_u = \frac{2}{3}T$ and $\mu_d = 0$ or $\mu_u = 0$ and $\mu_d = \frac{2}{3}T$, $n_B/T^3 \approx 0.187$ at $T = 1.1\,T_c$ according to Eq. (3.24). Considering constant scaled net baryon density $n_B/T^3 = 0.187$, the interrelation between μ_u/T and μ_d/T is depicted by the solid curve in Figure 3.20, for which $\mu_B/T > 1$ except for $\mu_u = 0$ or $\mu_d = 0$. Due to the small differences between curves of constant μ_B and curves of constant n_B as exhibited in Figure 3.20, one is tempted to conclude that variations in the individual quark
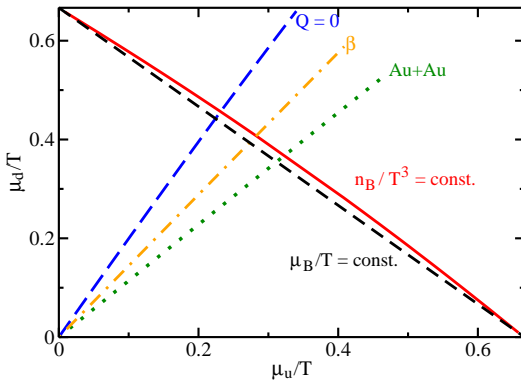
Figure 3.20:   Dependencies $\mu_d(\mu_u)$ for various side conditions or
physical situations. Bulk thermodynamic quantities are discussed
within truncated Taylor expansions using the generalized quark
number susceptibilities $\chi_{2,0}$, $\chi_{4,0}$ and $\chi_{2,2}$ exhibited in Figures 3.18
and 3.19. $\mu_B = T$ is depicted by the short-dashed curve, whereas
constant $n_B/T^3 = 0.187$ holds along the solid curve where $\mu_B \geq T$.
Electric charge neutrality is given along the long-dashed curve for
pure $N_f = 2$ quark matter, while the dash-dotted curve includes
additionally electrons, imposing β-equilibrium. The dotted curve
reflects the situation in $Au + Au$ heavy-ion collisions. (The curves
end where $\mu_u/T + \mu_d/T \geq 1$.) In all cases, $T = 1.1\,T_c$.

flavour chemical potentials affect thermodynamic quantities only little as long as
μ_B is constant.

However, there are physical situations, where the corresponding side condi-
tions require the separate knowledge about the non-trivial μ_u and μ_d dependencies
of bulk thermodynamic quantities. In heavy-ion collisions one often relates the
quantum numbers of the entrance channel with the ones of the emerging fire-
ball. Isospin-symmetric nuclear matter, for instance, is characterized by an electric
charge per baryon ratio of 1:2. This translates into $\frac{2}{3}n_u - \frac{1}{3}n_d = \frac{1}{2}n_B$ which is
fulfilled for $\mu_d = \mu_u$. Discussing, instead, $Au + Au$ collisions, the electric charge
per baryon ratio is approximately 0.4. The corresponding dependence $\mu_d(\mu_u)$ for
$T = 1.1\,T_c$ is depicted by the dotted curve in Figure 3.20.

Another important issue concerns electric charge neutrality in bulk matter. In
pure $N_f = 2$ quark matter, electric charge neutrality would require $\frac{2}{3}n_u - \frac{1}{3}n_d = 0$.
The according dependence $\mu_d(\mu_u)$ is depicted in Figure 3.20 by the long-dashed
curve, again for $T = 1.1\,T_c$. More relevant for hypothetical very hot neutron star
matter in a deconfined state is β-equilibrium. Flavour changing weak currents give
rise to the balance equation $d \leftrightarrow u + e + \bar{\nu}_e$, i. e. in weak interaction equilibrium
$\mu_e = \mu_d - \mu_u$, where μ_e is the electron chemical potential, as the produced neutrinos
are supposed to leave the star and do not participate in the balance. The electron
net density can be approximated by $n_e = \frac{1}{3}\mu_e T^2 + \frac{1}{3\pi^2}\mu_e^3$, and electrically neutral
bulk matter is determined by the condition $\frac{2}{3}n_u - \frac{1}{3}n_d - n_e = 0$. The corresponding
dependence $\mu_d(\mu_u)$ is depicted by the dash-dotted curve in Figure 3.20 for $T =
1.1\,T_c$. Along this line, the equation of state has to be determined as important
ingredient for solving the TOV equations in Eqs. (1.6) and (1.7). n_d decreases by

requiring β-equilibrium, demanding also a nonzero electron density for electrically neutral bulk matter whereas n_u is not affected when including electrons and β-equilibrium. This is in contrast to findings for the cold colour-flavour locked phase of QCD [160] for $N_f = 2 + 1$ dynamical quarks, where no electrons are required.

3.2.5 Imaginary chemical potential

In the following section, the QPM formulated for imaginary chemical potential μ_i in section 2.3 is confronted with lattice QCD results [125, 161] at finite T and μ_i. In particular, net quark number density and corresponding quark number susceptibility are investigated as functions of imaginary chemical potential exhibiting prominent structures which serve as further sensitive test of the model. For the net baryon density, results for imaginary chemical potential are analytically continued to real chemical potential and an interesting scaling behaviour is found. In addition, features of the phase diagram for real and imaginary chemical potential are discussed.

The simulations are performed on a lattice with spatial and temporal extensions $N_\sigma = 16$ and $N_\tau = 4$ for $N_f = 4$ degenerate quark flavours with $m_q = \xi_q T$ and $\xi_q = 0.2$. Basic quantity of interest is the net quark number density n_q and the corresponding net baryon density, which are purely imaginary and positive for imaginary $\mu_i > 0$ as discussed in section 2.3. As non-improved actions are used in the simulations [125, 161], a proper extrapolation of the lattice QCD data to the continuum limit is required. Taking the Stefan-Boltzmann result n_B^{SB}/T^3 calculated for $N_\tau = 4$ [125] and applying the same strategy as in section 3.1.3 now for n_B, a continuum extrapolation factor for the net quark number density can be estimated to $d^{(n_q)} = 0.456$ assuming that the continuum extrapolations for QCD and for the non-interacting gas of massless quarks and gluons are similar (cf. discussion in Appendix C). This compares well with continuum extrapolation factors reported in [162] reading 0.446 and in [156–158] reading 0.47, where similar actions have been used in the lattice simulations (cf. section 3.2.3).

In Figure 3.21, QPM results are compared with continuum estimated lattice QCD data [125, 161] for the imaginary part of the scaled net quark number density as a function of μ_i/T_c at constant $T \geq T_c$. The QPM parameters of the effective coupling $G^2(T, \mu_i = 0)$ are adjusted to perfectly describe n_q/T^3 at $T = 1.1\,T_c$. This is because the pronounced bending close to the critical chemical potential $\mu_c/T_c = 11\pi/30$ of the Roberge-Weiss transition for $T = 1.1\,T_c$ represents the most sensitive test of the QPM. In fact, the description of the linear behaviour of n_q/T^3 with μ_i for all temperatures is rather robust under slight variations of the parameters, whereas the onset of the pronounced structure at $T = 1.1\,T_c$ decisively depends on the parameter values. Therefore, a minimum χ^2-fit to all available lattice QCD data [125, 161] is rather equivalent to a perfect parametrization of the data at $T = 1.1\,T_c$ [98].

The continuum extrapolated lattice QCD results, in particular the pronounced bending of n_q/T^3 for $T = 1.1\,T_c$, are impressively well described by the QPM parametrization summarized in Figure 3.21. The drastic change in the slope of n_q/T^3 for $T = 1.1\,T_c$ signals the onset of the Roberge-Weiss transition, where n_q exhibits a discontinuity according to [125, 161]. In the QPM, this change in slope
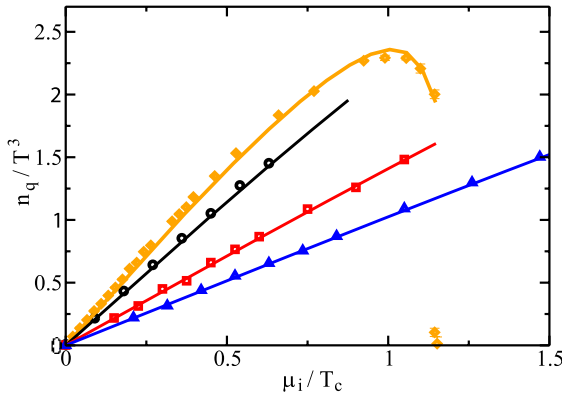
Figure 3.21: Comparison of QPM results (solid curves) for the scaled
net quark number density n_q/T^3 for $N_f = 4$ degenerate quark
flavours as a function of μ_i/T_c with continuum estimates of the lat-
tice QCD data [125, 161] for temperatures $T = 1.1, 1.5, 2.5, 3.5\,T_c$
(diamonds, circles, squares and triangles, respectively). The QPM
parameters are adjusted to n_q/T^3 at $T = 1.1\,T_c$ and read $\lambda = 40$
and $T_s = 0.95\,T_c$. For the case at hand, $T_c = 163$ MeV according
to [123] is utilized. The obvious discontinuity in the lattice data of
n_q/T^3 takes place at the Roberge-Weiss critical chemical potential
$\mu_c/T = \pi/3$ for $T = 1.1\,T_c$.

is driven by the behaviour of the effective quasiparticle mass with μ_i as exhibited
in Figure 3.22 for constant T, which also determines the dependence of G^2 on μ_i as
dictated by the flow equation in Eq. (B.21). For decreasing μ_i/T, i. e. for small μ_i
or increasing T, the effective quasiparticle mass shows decreasing sensitivity on μ_i
while nonzero chemical potential effects become important close to $\mu_c = \frac{\pi}{3}T$. The
chemical potential dependence in the quasiparticle dispersion relations is further
discussed in section 3.2.6.

For larger temperatures and small μ_i, n_q/T^3 exhibits a linear dependence on
μ_i. In fact, exhibiting n_q/T^3 as a function of μ_i/T, it shows an independence of
the explicit value of T for temperatures $T \geq 1.5\,T_c$ and not too large μ_i/T. This
independence can be understood from Eq. (2.51) as long as ω_q is approximately in-
dependent of μ_i (cf. Figure 3.22). Below T_c, however, n_q/T^3 displays a qualitatively
different behaviour being continuous and periodic as a function of μ_i/T [125].

Performing a naive chiral extrapolation by simply putting $m_q = 0$ but keeping
the parametrization of $G^2(T, \mu_i = 0)$ fixed, modifies n_q/T^3 by less than 1% for the
considered range of temperatures and chemical potentials. In principle, however, a
general quark mass dependence of the parameters λ and T_s in the effective coupling
would be conceivable as noted in section 3.1.2.

Within the QPM, results obtained for purely imaginary chemical potential can
uniquely be analytically continued to real μ for $\mu < \mu_c(T)$ keeping the QPM param-
eters λ and T_s fixed [98]. These results may be compared with other analytic contin-
uations. For instance, in [125], a polynomial fit to n_q/T^3 was considered. Despite
the fact that a polynomial fit $n_q(T, \mu_i, m_q) = a(T, m_q)\mu_i + b(T, m_q)\mu_i^3$ for imag-
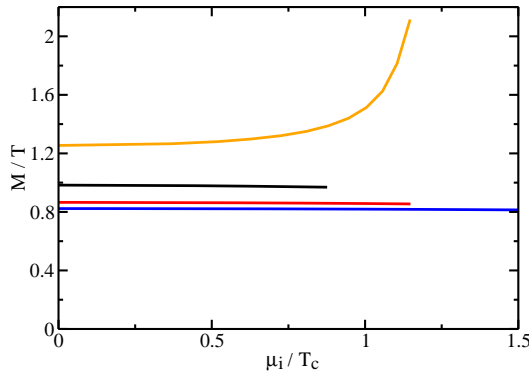
Figure 3.22: Effective quark quasiparticle mass $M \equiv M_q(T, \mu_i)$ scaled
by T (solid curves) as a function of μ_i/T_c for $T = 1.1, 1.5, 2.5, 3.5\,T_c$
(from top to bottom) employing the QPM parameters from Figure 3.21.

inary chemical potential, with analytic continuation $n_q(T, \mu, m_q) = a(T, m_q)\mu - b(T, m_q)\mu^3$, cannot account for the change in slope observed for $T = 1.1\,T_c$ at large μ_i/T_c, its coefficients a and b have to be temperature and quark mass dependent in order to follow the trend observed in lattice QCD. In addition, the behaviour of analytic continuations of polynomial fits decisively depends on the considered maximum order in μ_i^2, as discussed in [126, 163]. In contrast, λ and T_s are once adjusted to n_q/T^3 at $T = 1.1\,T_c$ (cf. Figure 3.21) and then kept fixed for all temperatures and chemical potentials, where the QPM contains all orders of μ_i^2 respecting the symmetry $\ln Z(\mu) = \ln Z(-\mu)$. For decreasing T, the analytic continuations of QPM and of the polynomial fit of order $\mathcal{O}(\mu^3)$ start to increasingly deviate for smaller μ/T_c. Due to the pronounced structure in n_q/T^3 close to $\mu_c(T)$, a sensible analytic continuation is required.

In Figure 3.23, the net baryon density n_B/T^3 is exhibited as a function of T/T_c for constant imaginary (solid curves) as well as for real baryo-chemical potential (dashed curves). As for small μ_B or large temperatures n_B depends linearly on chemical potential, the results for real μ_B significantly deviate from the original results for imaginary chemical potential only at large μ_B and temperatures close to T_c. Note that in these considerations μ_B is restricted to $|\mu_B| \leq \pi T$.

Furthermore, one finds an interesting scaling for the ratio n_B/n_B^{SB} as depicted in Figure 3.24, where n_B^{SB} denotes the Stefan-Boltzmann expression of the net baryon density. When considering n_B/n_B^{SB} either for real or for imaginary chemical potential, in both cases, μ_B effects become visible only in the vicinity of T_c. In fact, for the baryo-chemical potentials considered in Figure 3.24, the ratio n_B/n_B^{SB} is found to be independent of μ_B for $T \geq 1.2\,T_c$. Besides, $n_B/n_B^{SB} = 1$ is approached only asymptotically, signalling the expected strong deviations from the free field behaviour. Apart from the observed differences in the ratio between real and imaginary chemical potentials close to T_c, an interesting pattern develops: n_B/n_B^{SB} decreases with increasing baryo-chemical potential for real μ_B, while the ratio increases in the case of imaginary chemical potential. This is partly caused by differences in n_B/T^3 between real and imaginary chemical potential which become smaller for increasing temperature (cf. Figure 3.23). But it is also related to
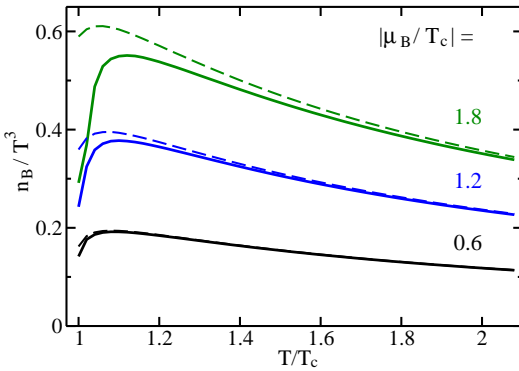
Figure 3.23:   Scaled net baryon density n_B/T^3 for $N_f = 4$ degen-
erate quark flavours as a function of T/T_c for constant imagi-
nary $\mu_B/T_c = 3i\mu_i/T_c$ (solid curves) and for corresponding real
μ_B/T_c (dashed curves). Note that for all temperatures, $\partial n/\partial T > 0$
is fulfilled, as required from thermodynamic stability conditions.
n_B/T^3 exhibits the same shape as in Figure 3.10 for $N_f = 2$ de-
generate quark flavours.

different signs in n_B^{SB} for real or imaginary chemical potential as elaborated in [98].

The quark number susceptibility χ_q represents also a sensitive probe of the
QPM. In Figure 3.25, χ_q/T^2 is exhibited for $T = 1.1\,T_c$ as a function of μ_i/T_c,
where both, lattice QCD results [161] as well as QPM results are obtained by
numerical differentiation of n_q. The behaviour of χ_q is, thus, determined from the
behaviour of n_q with μ_i; possible systematic differences between QPM and lattice
QCD results should enhance, accordingly, in this higher-order derivative. However,
as the comparison of QPM results with the lattice QCD data does not point to
such a behaviour, the agreement depicted in Figure 3.25 serves for an impressive
test of the QPM.

With the above comparisons at hand, the deconfinement phase transition line
can be discussed for $N_f = 4$ degenerate quark flavours. For this purpose, the
QPM parameters λ and T_s remain fixed to the values in Figure 3.21. Within the
QPM, the characteristic curve emerging at $T = T_c$ and $\mu = 0$ as solution of the
flow equation in Eq. (B.21) can be considered as an indicator of the pseudo-critical
curve. The phase transition line was calculated in lattice QCD simulations [123]
for imaginary chemical potential. The lattice QCD data were analyzed by applying
polynomial fits which were analytically continued to real μ [123].

In Figure 3.26, the phase diagram is exhibited in a specific coordinate system
in which both, purely imaginary baryo-chemical potential as well as real μ_B are
depicted. Diamonds represent the polynomial fit from [123] for imaginary chemical
potential and the corresponding analytically continued results. For comparison,
the QPM characteristic (solid) curve starting at $T = T_c$ for imaginary chemical
potential as well as for real μ_B is also shown. Deviations become visible only for
larger $|\mu_B/T_c|$, where small differences in the imaginary chemical potential sector
turn into larger deviations in the sector of real μ_B, in particular for $\mu_B \geq 330$ MeV.

In Figure 3.26, the first two Roberge-Weiss transition lines (characterized by
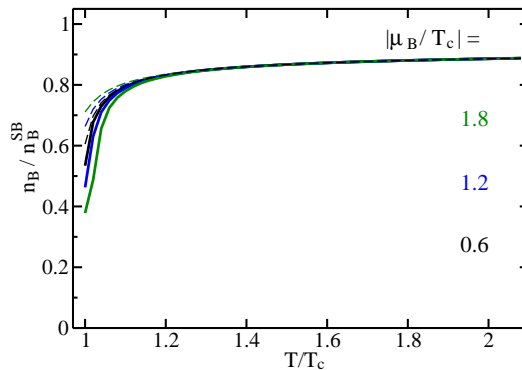
Figure 3.24: Ratio n_B/n_B^{SB} as a function of T/T_c for different imaginary and real baryo-chemical potentials. Dashed curves represent results for imaginary baryo-chemical potential, with $|\mu_B/T_c| = 0.6, 1.2, 1.8$ from bottom to top, while solid curves depict corresponding results for real μ_B, with $|\mu_B/T_c| = 0.6, 1.2, 1.8$ in inverted order, i. e. from top to bottom.

$\mu_B^2/T_c^2 = -T^2\pi^2(2k+1)^2/T_c^2$ for $k = 1, 2$) are shown with fat dashed sections indicating the analytic region and fat solid section indicating a first-order phase transition. In addition, the first $\mathcal{Z}_3$ centre symmetry line is exhibited (characterized by $\mu_B^2/T_c^2 = -4T^2\pi^2/T_c^2$) by the dotted curve. The repeated copies of these sectors for $k \geq 2$ are not displayed in Figure 3.26.

Numerically, one finds that the characteristic curve emerging at $T = T_c$ and the first Roberge-Weiss phase transition line cross each other at $T^*/T_c = 1.112$ and $(\mu_B^*)^2/T_c^2 = -12.214$, whereas the lattice QCD simulations [123, 125] report $T^*/T_c = 1.095$ and $(\mu_B^*)^2/T_c^2 = -11.834$. These tiny differences can hardly be resolved on the scale displayed in Figure 3.26. For larger imaginary μ_B, the characteristic curve is mirrored at the Roberge-Weiss phase transition line (as displayed in the section in the left edge below the first Roberge-Weiss phase transition line in Figure 3.26).

In addition, the quark mass dependence of found results can be discussed by naively setting $m_q \to 0$. For imaginary chemical potential, quark mass effects turn out to be negligible. For real μ_B/T_c, quark mass effects are also small (at most 3%) and visible only for very small temperatures. Decreasing the quark mass implies a larger curvature of the estimated phase boundary and thus a smaller critical chemical potential at $T = 0$ [98]. Similar minor quark mass dependencies with the same trend when decreasing m_q was found in lattice QCD simulations [164].

3.2.6 Discussion of the chemical potential dependence in the quasiparticle dispersion relations

In order to examine the importance of the chemical potential dependence in the effective quasiparticle masses (dubbed BKS effect in [148]) on the found results, one can, for instance, omit the explicit μ_i^2/π^2 terms in Eqs. (2.52) and (2.53) or flip their signs. For simplicity, the dependence of G^2 on μ_i, as dictated by the flow equation, is left unchanged, for the moment being. While altering in this way the
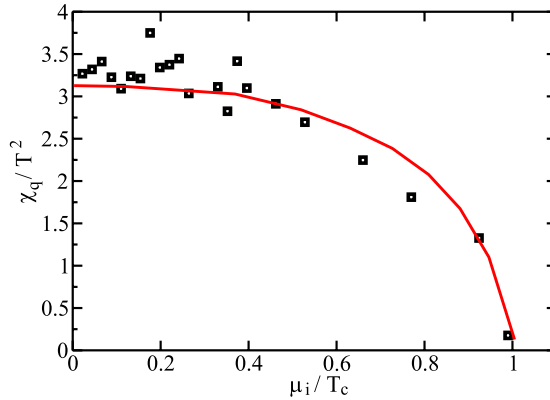
Figure 3.25: Comparison of QPM results (solid curve) for χ_q/T^2 as a
             function of $\mu_i/T_c \leq 1$ for $T = 1.1\,T_c$ with the continuum estimate
             of the lattice QCD results [161].
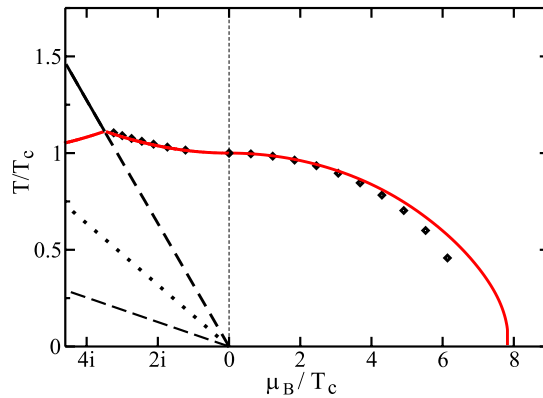

Figure 3.26:   Phase diagram for imaginary and real baryo-chemical
             potential. Details are explained in the text.

effective quasiparticle masses, the QPM parameters found in section 3.2.5 are kept
fixed. In both cases, n_q/T^3 is only affected for large μ_i, where the attenuation of μ_i^2
by $1/\pi^2$ becomes smaller and the term proportional to μ_i^2 in Eqs. (2.52) and (2.53)
cannot be neglected compared to the term proportional to T^2. This implies that
for larger T significant effects can only be seen at sufficiently large values of μ_i.

Thermodynamic self-consistency, however, requires in both cases of changing
the effective quasiparticle masses also changes in the flow equation in Eq. (B.21)
affecting the coefficients b, a_T and a_{μ_i} according to Maxwell's relation. In such
thermodynamically self-consistent approaches, found results are indistinguishable
from the QPM results exhibited in Figure 3.21. The QPM results turn out to be
rather independent of the explicit form of the μ_i dependence in the quasiparticle
dispersion relations. However, a general dependence of the dispersion relations on
chemical potential and on temperature is important for a proper description of
lattice QCD data.
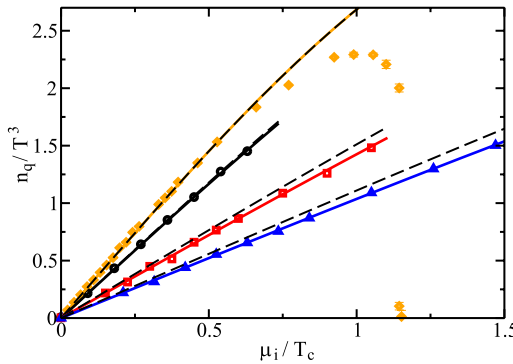
Figure 3.27: Comparison of n_q/T^3 as a function of μ_i/T_c employing either a constant mass parameter $M = 0.21$ GeV (dashed curves) or readjusting $M/T = 1.17, 0.90, 0.81, 0.77$ for $T = 1.1, 1.5, 2.5, 3.5\,T_c$ (solid curves from top to bottom) with the continuum extrapolated lattice QCD data (symbols) exhibited in Figure 3.21.
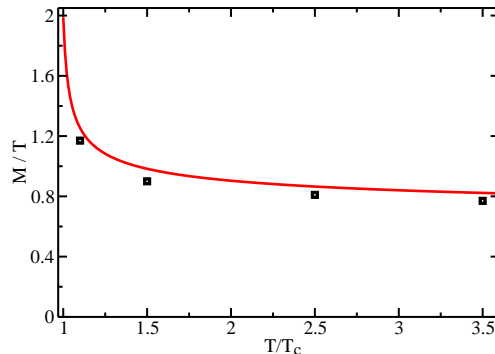
Figure 3.28: Comparison of found M/T values (squares) from Figure 3.27 as a function of T/T_c with the effective quark quasiparticle mass $M/T \equiv M_q(T, \mu_i = 0)/T$ employing the QPM parameters from Figure 3.21.

This can be illustrated by considering n_q in Eq. (2.51) with dispersion relation $\omega_q^2 = k^2 + M^2$. When neglecting μ_i completely in M, thermodynamic self-consistency dictates also an independence of T in M which significantly changes results. Even though the almost linear behaviour of n_q/T^3 at $T = 1.1\,T_c$ for small μ_i/T_c can be reproduced by adjusting $M = 0.21$ GeV as shown in Figure 3.27 (dashed top curve), increasing deviations from the lattice QCD data for $\mu_i/T_c > 0.66$, in particular in the vicinity of the Roberge-Weiss critical chemical potential, can be observed. This was already discussed in [161] by considering the ratio $n(\mu_i)/n(\mu_i)_{free}$ signalling clear deviations of the lattice QCD data from a free (ideal) gas behaviour. Furthermore, for increasing T, the description of the lattice QCD data becomes less and less accurate for smaller μ_i/T_c suggesting a general dependence of M on T (cf. Figure 3.27). Readjusting M individually for each temperature, ignoring for the moment being thermodynamic self-consistency, the results are depicted by solid curves in Figure 3.27. The found scaled mass parameters

M/T for the temperatures considered here are exhibited in Figure 3.28 (squares) and compared with the scaled effective quark quasiparticle mass $M_q(T, \mu_i = 0)/T$ (solid curve) employing the parametrization of Figure 3.21. Both results agree fairly well, indicating the importance of a T dependence in ω_q and that nonzero chemical potential effects are tiny for small μ_i/T.

Nevertheless, the pronounced behaviour for $T = 1.1 \, T_c$ close to μ_c cannot be obtained when neglecting the μ_i dependence in the quasiparticle dispersion relations. The above considerations prove that ω_i must be chemical potential dependent whereas the explicit form of this dependence is of negligible impact.

3.3 QCD equation of state

The heart of hydrodynamics is the equation of state relating thermodynamically the pressure of the medium to its energy density and net baryon density (or, equivalently, to its temperature and baryo-chemical potential). In this section, the QCD equation of state for $N_f = 2 + 1$ dynamical quark flavours is investigated. Anchored to lattice QCD results, the QPM parametrization established in section 3.1.1 (Figure 3.2) is used as well as the chirally extrapolated results from section 3.1.2 (Figure 3.4). In this way, a lattice QCD based QPM EoS of the form $p(e)$ at zero net baryon density is obtained in section 3.3.1. Finite baryon-density effects result from solving the full QPM flow equation based on Maxwell's relation as discussed in section 3.3.2. The found EoS, as elaborated in section 3.3.3, exhibits some interesting scaling properties with the pseudo-critical deconfinement temperature as well as with the quark mass. In section 3.3.4, the robustness of the QPM EoS against variations in various entering parameters is discussed and shown that, in particular in the high energy density region, $p(e, n_B)$ is rather stable against these variations. Only in the transition region, the equation of state exhibits some sensitivity. Parts of this section are reported in [95], whereas the investigations concerning the scaling properties of the QPM EoS represent recent results.

3.3.1 Pressure as a function of energy density at $n_B = 0$

In Figure 3.29, the QPM equation of state $p(e)$ at $n_B = 0$ is compared with the corresponding lattice QCD results [132] deduced from p and e data at $n_B = 0$ in the energy density domain explored by heavy-ion collisions at RHIC. The employed QPM parameters are the same as in Figure 3.2 established by adjustment to $p(T)/T^4$. The physical scale is set to $T_c = 170$ MeV according to [6,8], neglecting for the moment being remaining variations due to uncertainties in the exact value of T_c. In the transition region, the energy density $e(T)$ varies by 300% within a temperature interval of $\Delta T \approx 20$ MeV while $p(T)$ rises much more slowly. This indicates a rapid but smooth crossover for the phase transition from hadronic to quark-gluon matter. At large energy densities, $e \geq 30 \, \text{GeV}/\text{fm}^3$, the EoS follows roughly the ideal gas relation $p = \frac{1}{3}e$.

For the sake of comparison, a bag model equation of state describing a gas of massless non-interacting quarks and gluons by $p = \frac{1}{3}e - B$ with bag constant $B^{1/4} = 230$ MeV is also exhibited in Figure 3.29 (straight dotted curve) showing
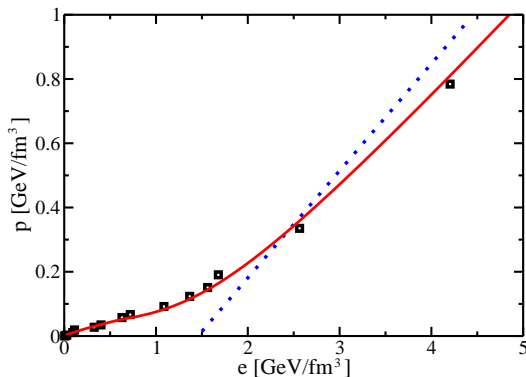
Figure 3.29: $N_f = 2{+}1$ QPM equation of state of strongly interacting
matter at zero net baryon density (solid curve) compared with
corresponding continuum extrapolated lattice QCD results [132]
(squares).   The dotted curve represents $p(e, n_B = 0)$ for a gas
of massless non-interacting quarks and gluons with bag constant
$B^{1/4} = 230 \, \text{MeV}$.

strong deviations from the lattice QCD based EoS. Considering p/e as a function
of e, as softest point $(p/e)_{\min} = 0.075$ at $e_c = 0.92 \, \text{GeV/fm}^3$ is found.

3.3.2   Baryon-density effects

Since for hydrodynamics the relation $p(e, n_B)$ matters, the n_B dependence of the
pressure at fixed energy density is considered in the following. Relying on the suc-
cess of the QPM in reproducing nonzero n_B lattice QCD results for $N_f = 2$ and
$N_f = 4$ dynamical quark flavours in section 3.2, the n_B dependence is obtained by
exploiting the full QPM rather than utilizing truncated Taylor expansions (cf. dis-
cussion in section 3.2.1). In this way, the parametrization found at $\mu_B = 0$ is used
to determine required thermodynamic observables at nonzero μ_B according to the
Maxwell relation in Eq. (2.18).

Figure 3.30 shows that a significant baryon-density dependence of the pressure
at fixed energy density arises only for $e \leq 2 \, \text{GeV/fm}^3$. At the smallest energy
densities considered here, the dependence of p on n_B cannot be determined over the
entire n_B region shown since the flow equation in Eq. (2.19) has no unique solution
for $G^2(T, \mu_B)$ at large μ_B and temperatures far below the estimated transition
temperature $T_c(\mu_B)$ (cf. discussion in [130]). However, in the family of equations
of state that is constructed and employed in chapter 4, this peculiar feature for
small e will not occur.

Whereas sizeable net baryon densities are relevant at AGS and SPS energies
or the future CBM (Compressed Baryonic Matter) project at the FAIR/SIS300
facility, they are, at least in the midrapidity region, comparably small at top RHIC
energies and even smaller at LHC energies. Thus, as evident from Figure 3.30, finite
baryon-density effects on the equation of state can be safely neglected under RHIC
and LHC conditions at all energy densities for which the QPM can be applied.
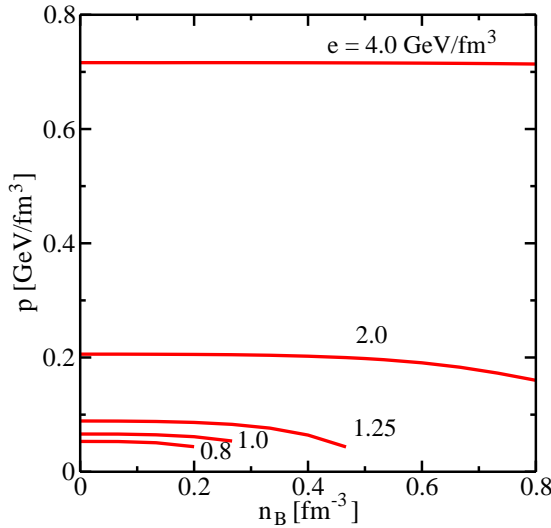
Figure 3.30: Net baryon-density dependence of the EoS $p(e, n_B)$ at constant energy density e as indicated. The curves end where the solution of the flow equation in Eq. (2.19) is not longer unique.

3.3.3 Scaling properties of the QPM EoS

Starting from the QPM expression for the pressure p as function of temperature and zero chemical potential including Eqs. (2.1)-(2.3) and Eqs. (2.9)-(2.13), some interesting scaling properties of the equation of state can be deduced. Reformulating p in terms of dimensionless entities, one schematically obtains

$$\frac{p(T, \mu = 0)}{T^4} = \sum_i \epsilon_i \frac{d_i}{\pi^2} \int_0^\infty dx x^2 \ln\left(1 + \epsilon_i e^{-\tilde{\omega}_i(T)/T}\right) - \frac{B(T_c)}{T^4}$$

$$+ \sum_i \frac{d_i}{2\pi^2 T^4} \int_1^{T/T_c} \frac{d\tilde{M}_i^2(T')}{dT'} \left(\int_0^\infty \frac{dx x^2}{\tilde{\omega}_i(T')/T'} \frac{1}{e^{\tilde{\omega}_i(T')/T'} + \epsilon_i}\right) \left(\frac{T'}{T_c}\right)^2 d\left(\frac{T'}{T_c}\right), (3.27)$$

where $\epsilon_l = 1$, $\epsilon_g = -1$, $B(T_c)/T^4 = b_0/(T/T_c)^4$ with real number b_0, for instance $b_0 = 0.61$ in Figure 3.2, $\tilde{\omega}_i(T)/T = \sqrt{x^2 + \tilde{M}_i^2(T)/T^2}$ and $\tilde{M}_i^2(T) \equiv M_i^2(T, \mu = 0)$ as well as according derivatives with respect to T given in Eqs. (2.14) and (2.15) as well as (B.1) and (B.2), respectively. Since only $G^2(T)$, which enters $\tilde{M}_i^2(T)$ and the derivatives of $\tilde{M}_i^2(T)$, depends on T_c, but in the scaled form T/T_c, where T_s/T_c is a given real number in the QPM parametrization, $p/T^4(\xi) \equiv \phi(\xi)$ displayed as a function of ξ, with $\xi \equiv T/T_c$, is independent of the explicit value of T_c. In contrast, $\tilde{M}_l^2(T)$ depends explicitly on the quark mass parameters m_l such that $p(T)/T^4$ in Eq. (3.27) is clearly a function of the employed quark mass parameters. Decreasing m_l, thus, leads to increasing pressure as observed in Figure 3.4.

Considering first the scaling of the QPM EoS at $n_B = 0$ with T_c, one notes reformulated in terms of ξ that $p = T_c^4 \xi(\phi \xi^3)$. Imposing $\phi(\xi) = \phi(\xi')$ from Eq. (3.27), this implies that with changing T_c to T_c', p, considered as a function of T/T_c, changes
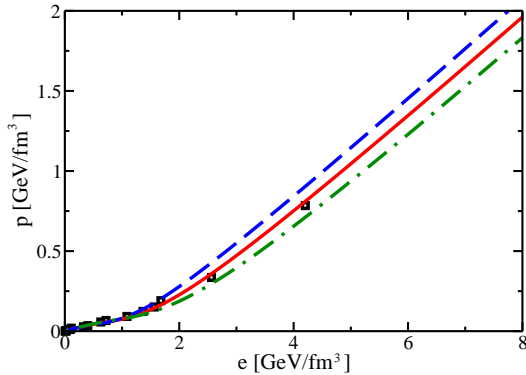
Figure 3.31: Dependence of the QPM EoS for $N_f = 2+1$ on the chosen value of the physical scale T_c. Dashed, solid and dash-dotted curves correspond to $T_c = 160$, 170 and 180 MeV, respectively. Lattice QCD data (squares) from [132].

according to

$$p' = \left(\frac{T_c'}{T_c}\right)^4 p\,. \tag{3.28}$$

Consequently, the energy density $e = -p + \xi\partial p/\partial\xi$ changes via

$$e' = \left(\frac{T_c'}{T_c}\right)^4 e\,. \tag{3.29}$$

For the EoS in the form $p(e)$, this implies that the linear section in Figure 3.29 which can be approximated by $p(e) = \alpha e + p_0$ becomes $p'(e') = \alpha e' + (T_c'/T_c)^4 p_0$ with the same slope α but different off-set $p_0' = (T_c'/T_c)^4 p_0$. For $T_c' > T_c$, the linear section of $p(e)$ is, thus, parallely shifted downward whereas for $T_c' < T_c$ it is shifted upward as evident from Figure 3.31. In other regions of $p(e)$ similar changes occur. For instance, $p(e) = \tilde{\alpha}\sqrt{e} + \tilde{p}_0$ with $\tilde{\alpha} \approx 0.07$ can be approximated for $e = 0.5...1$ GeV/fm^3 (cf. Figure 3.29). Changing T_c to T_c', the EoS changes into $p'(e') = \tilde{\alpha}'\sqrt{e'} + \tilde{p}_0'$ with $\tilde{\alpha}' = (T_c/T_c')^4\alpha$ and $\tilde{p}_0' = (T_c'/T_c)^4\tilde{p}_0$ implying a change in the off-set $\tilde{p}_0$ but also a flatter curve, $\tilde{\alpha}' < \tilde{\alpha}$, for $T_c' > T_c$ and a steeper curve, $\tilde{\alpha}' > \tilde{\alpha}$, for $T_c' < T_c$. This behaviour is also exhibited in Figure 3.31.

As empirically evident from Figure 3.4, the pressure changes by decreasing the quark mass parameters according to

$$p' = m(\xi)p\,. \tag{3.30}$$

Numerically, one finds $m(\xi) = 1.107...1.081$ in the interval $\xi = 1.5...3$ implying small changes in $m(\xi)$ with ξ whereas $m(\xi) = 1.33$ for $\xi = 0.8$ and $m(\xi) = 1.51$ for $\xi = 0.9$. This change is a result of the procedure employed in Figure 3.4. (When decreasing the quark mass parameters but not changing $B(T_c)$ in the QPM parametrization as done in Figure 3.4, even $m(\xi) = 4.47$ for $\xi = 0.8$ is found.) Thus, for small ξ changes in $m(\xi)$ with ξ turn out to be sizeable when performing the (naive) extrapolation to smaller quark mass values. According to Eq. (3.30), the energy density is affected via

$$e' = m(\xi)e + \xi p\frac{\partial m(\xi)}{\partial\xi}\,. \tag{3.31}$$
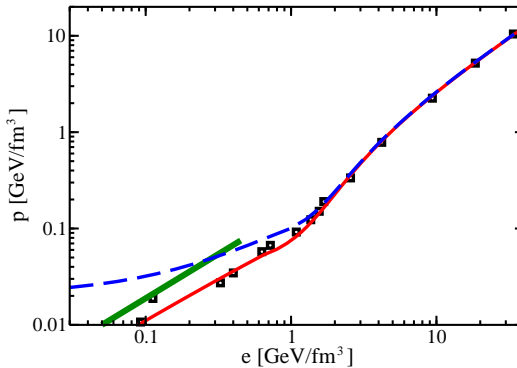
Figure 3.32:   QPM EoS for $N_f = 2+1$ (solid red curve) at $n_B = 0$
and its naive chiral extrapolation to zero quark masses $m_l = 0$
MeV (long-dashed blue curve) leaving also $B(T_c) = 0.61\,T_c^4$ with
$T_c = 170$ MeV unchanged. Squares show lattice QCD data [132]
using unphysical quark masses (cf. section 3.1.1). The solid green
curve exhibits a hadron resonance gas model EoS.

Considering, again, the linear section in the EoS $p(e) = \alpha e + p_0$, it changes according
to Eqs. (3.30) and (3.31) to

$$p' = \frac{\alpha}{1 + \frac{\alpha\xi}{m}\frac{\partial m(\xi)}{\partial\xi}}e' + p_0\frac{m}{1 + \frac{\alpha\xi}{m}\frac{\partial m(\xi)}{\partial\xi}} \equiv \alpha'e' + p_0'\,. \tag{3.32}$$

The numerical result for the chirally extrapolated EoS $p(e)$ at $n_B = 0$ leaving,
though, the value of T_c and also $B(T_c)$ unchanged (naive chiral extrapolation) is ex-
hibited in Figure 3.32. For energy densities $e \geq 2$ GeV/fm^3, quark mass effects are
seen to be negligible, whereas in the transition region ($e \sim 1\,\text{GeV/fm}^3$) the chirally
extrapolated result exceeds the original QPM equation of state (cf. Figure 3.29) by
approximately 10%. Adjusting $B(T_c)$ in line with Figure 3.4 to $B(T_c) = 0.78\,T_c^4$,
the original QPM EoS (cf. Figure 3.29) is notably affected only in the region of
very small e, whereas by changing the value of T_c according to the employed quark
mass parameters, the EoS is changed in line with the considerations above. Con-
sequences of this behaviour are further discussed in section 4.3. For the chirally
extrapolated QPM EoS, the softest point moves slightly upward compared to the
result noted in section 3.3.1 to $(p/e)_{min} = 0.087$ at $e_c = 1.1\,\text{GeV/fm}^3$. However,
both results are in good agreement with the lattice QCD data which show a softest
point $(p/e)_{min} = 0.080$ at $e_c = 1\,\text{GeV/fm}^3$.

The negligible quark mass dependence observed in the linear section of $p(e)$ can
be explained from Eq. (3.32). The found numerical results demand that the off-set
in $p(e)$ is almost not changed by Eqs. (3.30) and (3.31), implying that $m(\xi)$ follows
the differential equation $m^2 - m = \alpha\xi\partial m(\xi)/\partial\xi$ which is solved by

$$m(\xi) = \frac{-C}{\xi^{1/\alpha} - C}\,. \tag{3.33}$$

The constant C must be determined from an additional condition. As, obviously,
also $\alpha' \approx \alpha$, one finds $C \ggg 1$ by determining $\partial m(\xi)/\partial\xi$ from Eq. (3.33) which
implies that $m(\xi) \approx 1$ and $\partial m(\xi)/\partial\xi \approx 0$. Both conditions are approximately
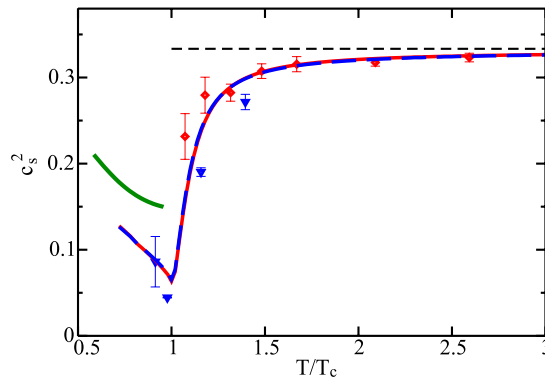
Figure 3.33: QPM results for the squared speed of sound c_s^2 as a function of T/T_c for $N_f = 2+1$ compared with lattice QCD data [165] (diamonds and triangles) for $N_f = 2$. Differences between the QPM parametrization (solid red curve) and its naive chiral extrapolation (long-dashed blue curve) are almost invisible. The solid green curve denotes the corresponding result for the HRG model EoS exhibited in Figure 3.32. Short-dashed horizontal curve indicates the Stefan-Boltzmann value $c_s^2 = \frac{1}{3}$.

fulfilled in the linear region of larger energy densities (and asymptotically also expected) explaining the observations in Figure 3.32. Nonetheless, for smaller e, and in particular in the transition region, both conditions hold less and less (apart from the fact that a different approximation for the dependence $p(e)$ has to be investigated for smaller e) resulting in $\alpha' \neq \alpha$ and $p'_0 \neq p_0$ as evident from Figure 3.32. In this region, the term $\propto \partial m(\xi)/\partial \xi$ in Eq. (3.31) cannot be neglected.

For $e \leq e_1 \equiv 0.45$ GeV/fm^3, the fat solid (green) curve in Figure 3.32 shows a hadron resonance gas model EoS with physical mass spectrum in chemical equilibrium.[1] Obviously, it exceeds both the lattice QCD data [132] and their QPM parametrization. The QPM EoS obtained by the naive chiral extrapolation procedure, instead, approaches and interesects the hadron resonance gas EoS but still does not match the HRG EoS at e_1. This mismatch will be of relevance in chapter 4 when constructing equations of state which are applied in hydrodynamic calculations.

The small differences observed in Figure 3.32 between the lattice QCD adjusted QPM EoS and its naively chirally extrapolated version can be further analyzed by studying the squared speed of sound c_s^2. In Figure 3.33, c_s^2 is shown as a function of T/T_c for both versions of the QPM EoS and compared with lattice QCD results [165] available only for $N_f = 2$. As far as c_s^2 is concerned, both versions of the QPM EoS have almost identical driving power for collective hydrodynamic flow. Thus, the extrapolation of the QPM EoS to the chiral limit has no discernible consequences.

---

[1] A tabulated version of the EoS for a HRG in chemical equilibrium (EoS Q files named aa1*.dat) is available at http://www.physics.ohio-state.edu/~froderma/.

Even though lattice QCD as well as QPM results for p and e deviate from their corresponding Stefan-Boltzmann limits for an ideal gas of non-interacting massless quarks and gluons by about 15-20% at $T \geq 3\,T_c$ (cf. Figure 3.2 for p), these deviations are of similar magnitude in both, p and e, such that c_s^2 is close to its Stefan-Boltzmann limit $\frac{1}{3}$ (dashed horizontal curve in Figure 3.33) for $T \gtrsim 2\,T_c$. Thus, concerning stiffness and accelerating power, lattice QCD as well as QPM EoS are almost indistinguishable from that of an ideal parton gas for temperatures $T \gtrsim 2\,T_c$. On the other hand, as exhibited in Figure 3.33, c_s^2 drops abruptly below $\frac{1}{3}$ for $T < 2\,T_c$ reaching a value that is about a factor of 3 smaller close to T_c. This leads to a significant softening in the EoS compared to that of an ideal massless gas.

3.3.4　Robustness of the QPM EoS

As shown in section 3.3.3, the QPM EoS at $n_B = 0$ is rather robust against changes in the employed quark mass parameters, in particular in the region of larger energy densities, although individual thermodynamic quantities sensitively depend on m_l as evident from Figure 3.4, for instance. A similar behaviour is observed for moderate changes in the value of the physical scale T_c. Even though $p(e)$ varies by about $\pm$ 20% for changes in T_c by $\pm$ 10 MeV in the intermediate energy density region (cf. Figure 3.31), the EoS is fairly robust against such variations for small e and for large $e \geq 5$ GeV/fm^3 as far as the accelerating power is concerned.

When finally applying the EoS in hydrodynamic simulations in chapter 4, these uncertainties in the intermediate e region are taken into account by an interpolation procedure between QPM EoS in the high e region and a HRG EoS in the low energy density region. This interpolation is anyhow mandatory, as both regions do not automatically match (cf. Figure 3.32). The weak dependence on T_c at large e is, thus, irrelevant in practice. However, using the recently reported value of $T_c = 192$ MeV [10], this picture changes to some extent in agreement with the observed quark mass behaviour in the transition region. This issue is discussed in section 4.3.

Furthermore, the EoS $p(e)$ for $N_f = 2+1$ at $n_B = 0$ is rather similar for different existing lattice QCD simulations [132, 140, 166] which differ in their lattice calculation set-up including lattice action, lattice spacing, spatial and temporal extensions or bare quark masses etc. These differences in the set-up are reflected in deviations in basic thermodynamic quantities such as the pressure $p(T)/T^4$ exhibited in Figure 3.34. As evident from Figure 3.34, the differences in $p(T)/T^4$ can be absorbed by adjusting individually the QPM parameters. However, when presenting these results in the form of an EoS $p(e)$, they all coincide for $e \geq 5\,\mathrm{GeV/fm}^3$ as shown in Figure 3.35. The agreement is excellent up to $e \approx 30\,\mathrm{GeV/fm}^3$ while at even higher energy densities small differences between the equations of state from [132] and [140] begin to develop. In this large energy density region, the EoS can be parameterized by $p = \alpha e + p_0$ with $\alpha = 0.310 \pm 0.005$ and $p_0 = -(0.56 \pm 0.07)$ GeV/fm^3. The robustness of the lattice QCD EoS for $e \geq 5\,\mathrm{GeV/fm}^3$ implies that it can be considered as stable input for hydrodynamic simulations of heavy-ion collisions, and that the equation of state is well constrained at high energy densities. Even reasonable variations in the necessary continuum extrapolation procedures manifest themselves only weakly in the EoS and are completely negligible for $e \geq 5\,\mathrm{GeV/fm}^3$.
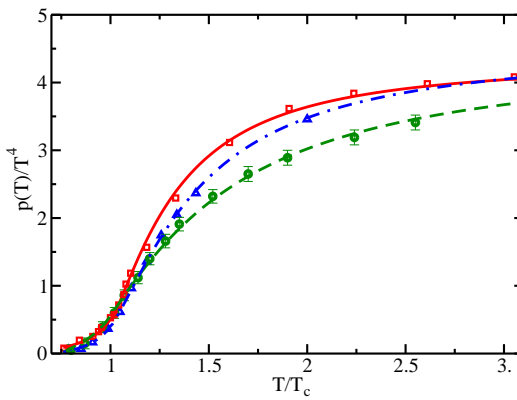
Figure 3.34: The scaled pressure $p(T)/T^4$ at $\mu_B=0$ for $N_f = 2+1$ from different lattice QCD calculations ([132] (squares, cf. Figure 3.2), [140] (circles, cf. Figure 3.7) and [166] (triangles)), together with corresponding separate QPM parametrizations (solid curve employing the QPM parameters from Figure 3.2, short-dashed curve employing the QPM parameters from Figure 3.7 and dash-dotted curve employing $\lambda = 2.35$, $T_s = 0.385\,T_c$, $b = 425$ and $B(T_c) = 0.51\,T_c^4$ with $T_c = 170$ MeV). The simulations in [166] are performed in $N_\tau = 6$ temporal extensions employing as quark mass parameters $m_{u,d} = 0.1\,m_s$ and $m_s \approx 78$ MeV. Note that in [166] improved actions are used and results for $N_\tau = 4$ and 6 show only minor deviations. Therefore, no continuum extrapolation of the lattice QCD data from [166] was applied here.

As an aside, differences in $p(e)$ at $n_B=0$ arising from considering different numbers N_f of dynamical quark flavours are investigated in Figure 3.36. Comparing the QPM result for $N_f = 2+1$ with the result for $N_f = 2$, the latter exceeds the $N_f = 2+1$ result in the transition region by about 12% at $e = 1$ GeV/fm^3. For smaller energy densities $e \leq 0.7$ GeV/fm^3 and for larger energy densities $e \geq 3$ GeV/fm^3, the EoS is found to be fairly independent of N_f even though at fixed T both $p(T)$ (cf. Figures 3.1 and 3.2) and $e(T)$ are significantly smaller for $N_f = 2$ than for $N_f = 2+1$. As in both cases, p and e, the deviations with N_f are, however, of similar magnitude, the dependence in $p(e)$ on N_f approximately compensates.
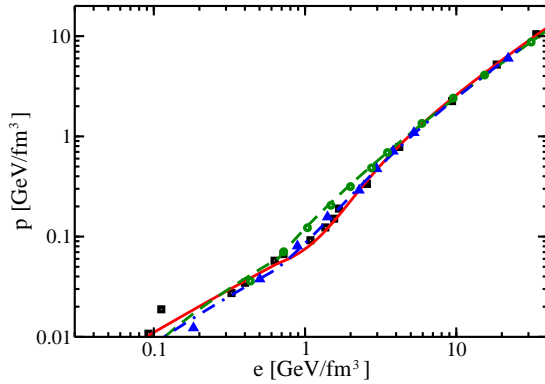
Figure 3.35: The EoS $p(e)$ at n_B=0 corresponding to the lattice QCD data and QPM parametrizations of $p(T)/T^4$ shown in Figure 3.34. In particular for $e \geq 5$ GeV/fm^3, the EoS is almost the same for the different simulations [132,140,166] despite the observed differences in $p(T)/T^4$.
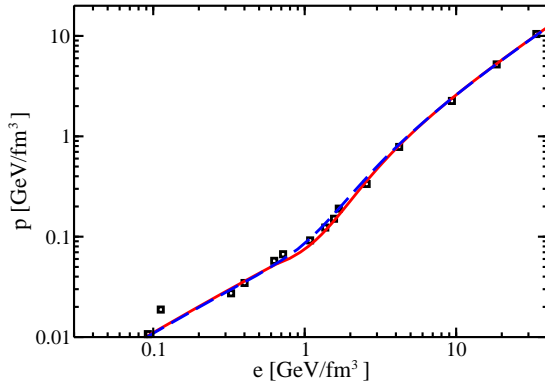
Figure 3.36: QPM EoS at $n_B = 0$ for $N_f = 2$ (dashed curve) employing the QPM parameters from Figure 3.1 compared with $N_f = 2 + 1$ QPM results (solid curve) and corresponding lattice QCD data [132] (cf. Figure 3.29). The QPM EoS in the form $p(e)$ exhibits a scaling with N_f in the low and high energy density regions.

4 Application of the QPM EoS in Hydrodynamic Simulations

In this chapter, the equation of state discussed in chapter 3 is applied in hydrodynamic simulations for ultra-relativistic heavy-ion collisions. As the chirally extrapolated QPM EoS does not continuously match with a realistic hadron resonance gas equation of state at low energy densities, an interpolation procedure between QPM and HRG sections in the transition region becomes necessary. This is elaborated in section 4.1. The linear interpolation applied in section 4.1, however, is not unique and thus, a whole family of equations of state can be constructed. Different family members deviate from each other only in the transition region allowing for an investigation of the influence of details in the transition region of the EoS. In this way, the sensitivity of the EoS in the transition region as discussed in section 3.3.4 is incorporated in the following considerations.

In particular, transverse momentum spectra as well as differential elliptic flow of directly emitted hadrons are studied in section 4.2. Focussing on regions of small net baryon density, first, strange baryons for top RHIC energy conditions are considered in section 4.2.1 and the calculated differential elliptic flow is compared with experimental data. In section 4.2.2, these considerations are performed for future LHC energies. These results are reported in [95, 97]. Finally, in section 4.3, a different QPM equation of state is discussed which, as a result of employing almost physical quark mass parameters as well as the corresponding recently reported lattice QCD value for the deconfinement transition temperature, continuously matches the hadron resonance gas equation of state in the transition region while, simultaneously, it describes available lattice QCD results.

4.1 Matching the QPM EoS to a realistic HRG EoS

While most existing hydrodynamic simulations use a realistic hadron resonance gas EoS below the deconfinement transition temperature, building upon the measured spectrum of hadronic resonances either with full [55, 56, 58, 167, 168] or partial [54, 169–172] chemical equilibrium among the hadron species, they usually rely on simple analytical models for the EoS of the quark-gluon plasma phase which are based on the assumption of weak coupling among the deconfined quarks and gluons. This assumption, however, is inconsistent with the phenomenological success of hydrodynamics requiring rapid thermalization [59] and, therefore, strong interactions among the constituents [22, 60, 61, 64].

As in the temperature region $T_c < T < 2\,T_c$, which is explored during the early stages of Au+Au collisions at RHIC [54–56, 58, 167–170], the lattice QCD equation of state significantly differs from that of an ideal massless parton gas, hydrodynamic evolution codes must be supplied with a model EoS that can faithfully reproduce

lattice QCD results above T_c. Therefore, the QPM EoS discussed in section 3.3 is considered, in the following, as reliable approach to the QCD equation of state in the deconfined phase while the transition to a realistic HRG EoS at lower energy densities allows for an explicit contact with experimentally observed final state hadrons after decoupling from the expanding medium. In this way, an equation of state is obtained which can be applied to all stages of the hydrodynamic expansion of the hot matter created in relativistic heavy-ion collisions.

As shown in Figure 3.32, the QPM EoS at high energy densities, which is naively extrapolated to the chiral limit, does not automatically match smoothly with the hadron resonance gas EoS at low e. Although the gap between the two branches of the EoS is much smaller than for models which assume non-interacting quarks and gluons above T_c [54–56, 58, 62, 167–172], a certain degree of ambiguity remains in the necessary interpolation process. For this reason, a set of different interpolation prescriptions is explored in this section yielding a family of equations of state based on lattice QCD results. This family of equations of state, exhibiting slight differences in the phase transition region, allows for a discussion of the impact of EoS details in the quark-hadron phase transition region on the flow pattern. In this way, the sensitivity of the flow pattern on the uncertainties arising in the transition region pointed out in sections 3.3.3 and 3.3.4 can be explored and the results can be confronted with experimental data from RHIC and future LHC. For instance, quark mass effects on the EoS matter most at the lower end of $p(e)$ where the transition from the QPM EoS to the HRG EoS must anyhow be implemented.

For the hadron resonance gas EoS [52, 173], the implementation developed for the (2+1)-dimensional hydrodynamic code package AZHYDRO[1] is employed which provides this EoS in tabulated form on a grid in the (e, n_B) plane. Specifically, EoS "aa1" from the OSCAR website up to $e_1 = 0.45$ GeV/fm^3 is used. This EoS describes a thermalized, but chemically non-equilibrated hadron resonance gas, with hadron abundance yield ratios fixed at all temperatures at their chemical equilibrium values at $T = T_c = 170$ MeV, as found empirically [174] in Au+Au collisions at RHIC.

As $p(e)$ of the hadron resonance gas EoS does not join smoothly to that of the QPM EoS at $e_1 = 0.45$ GeV/fm^3, irrespective of whether one uses directly the QPM adjustment to the lattice QCD data [132] which incorporate unphysical quark masses (cf. solid red curve in Figure 3.32) or naively extrapolates the QPM to the chiral limit (dashed blue curve in Figure 3.32), a thermodynamically consistent treatment requires a Maxwell like construction, equating the two pressures at a common temperature T_c and baryo-chemical potential μ_B.

Here, however, a slightly different approach is followed which has the advantage of allowing a systematic exploration of the impact of details in the EoS near T_c, such as stiffness or accelerating power, on hydrodynamic flow patterns: $p(e, n_B)$ is interpolated at fixed baryon density n_B linearly between the HRG ("aa1") value at $e = e_1$ and its value in the QPM EoS at a larger value e_m, keeping e_1 fixed but letting the matching point value e_m vary. In this procedure $T(e_m) \geq T(e_1)$, so $T(e)$ is also interpolated linearly, as is the baryo-chemical potential $\mu_B(e)$ at fixed

---

[1]A link to the hydrodynamic code AZHYDRO can be found at the OSCAR website http://nt3.phys.columbia.edu/people/molnard/OSCAR/ and descriptions in the references given there.
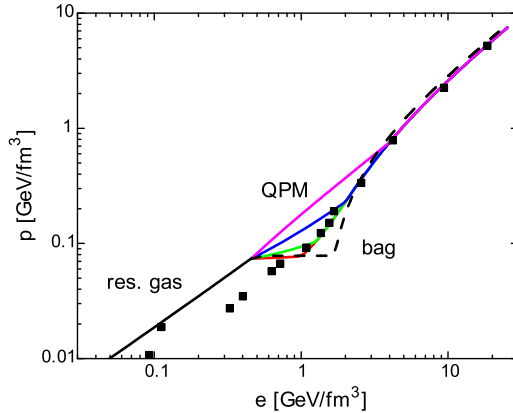
Figure 4.1: A family of equations of state for $N_f = 2 + 1$, combining the QPM EoS at high energy densities with a hadron resonance gas model ("res. gas") EoS in the low energy density regime through linear interpolation. Shown is the range of energy densities relevant for collisions at RHIC. The solid curves show $p(e)$ at $n_B = 0$ for EoS QPM(4.0), QPM(2.0), QPM(1.25), and QPM(1.0) (from top to bottom), where the numerical label indicates the matching point e_m in GeV/fm^3. On the given scale, effects of varying n_B between zero and $0.5\,\mathrm{fm}^{-3}$ are not visible. For comparison, lattice QCD data [132] (squares) incorporating unphysical quark masses are also exhibited. A bag model ("bag") EoS with a sharp first-order phase transition is shown by the dashed curve.

n_B. This is a convenient pragmatic procedure for interpolating the special tabular forms of the EoS employed in the hydrodynamic simulations between e_1 and e_m. Complete thermodynamic consistency would, though, require involved polynomials for temperature and chemical potential interpolation. As the hydrodynamic evolution equations, however, do not explicitly refer to T and μ_B in the interpolation region, i. e. only $p(e, n_B)$ matters, the linearized structures for T and μ_B can safely be utilized.

Due to this interpolation procedure, a family of equations of state is produced whose members are labelled by the matching point energy density e_m. In Figure 4.1, the range $1.0\,\mathrm{GeV/fm}^3 \leq e_m \leq 4.0\,\mathrm{GeV/fm}^3$ is explored. As stated in section 3.3, quark mass effects in the EoS become visible only for small energy densities below $1\,\mathrm{GeV/fm}^3$. Thus, for the here employed values of e_m, it does not matter whether the direct QPM parametrization or its naive chiral extrapolation is employed. Figure 4.1 shows the result for four selected e_m values, $e_m = 1.0, 1.25, 2.0$, and $4.0\,\mathrm{GeV/fm}^3$ (from bottom to top). For $e_m = 3.0\,\mathrm{GeV/fm}^3$ one obtains a curve $p(e)$ (not exhibited) that extrapolates the HRG EoS with approximately constant slope all the way to the QPM EoS. The dashed curve in Figure 4.1 depicts the Maxwell construction between the hadron resonance gas and the bag model equation of state (cf. dashed curve in Figure 3.29) with $c_s^2 = \frac{1}{3}$. Due to this construction, a strong first-order phase transition with latent heat $\Delta e_{\mathrm{lat}} = 1.1\,\mathrm{GeV/fm}^3$ is found (this EoS is named EoS Q in [56, 167, 168]).
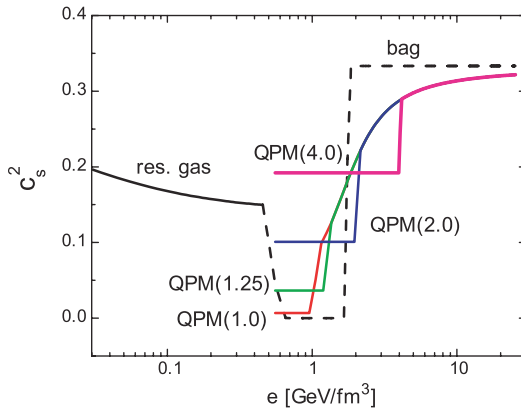
Figure 4.2: Squared speed of sound c_s^2 as a function of energy density e along an isentropic expansion trajectory with $s/n_B = 100$, for the EoS family $QPM(e_m)$ depicted in Figure 4.1. Baryon-density effects are not visible on the given scale as long as $n_B < 0.5\,\mathrm{fm}^{-3}$.

Different phenomenological equations of state of strongly interacting matter were proposed in previous studies [54–56,58,62,167–173], exhibiting either a strong first-order phase transition with different values of latent heats [54–56, 167–170, 172, 173], a smooth but rapid crossover [58], or no phase transition at all [173]. These equations of state differ significantly in their high energy density regions and softest points as well as in the squared speed of sound which controls details of the developing flow pattern. Investigating the hydrodynamic consequences of different equations of state helps to establish benchmarks for tracing specific phase transition signatures and distinguishing them from other dynamical features such as, so far, poorly explored viscous effects.

The construction utilized here differs, for instance, from the approach explored in [54] where the hadron resonance gas is matched to an ideal quark-gluon gas with varying values for the latent heat Δe_{lat}. Varying, for example, the latent heat in EoS Q from $\Delta e_{\mathrm{lat}} = 0.4\,\mathrm{GeV/fm}^3$ to $0.8\,\mathrm{GeV/fm}^3$ and to $1.6\,\mathrm{GeV/fm}^3$, the pressure $p(e_0, n_B = 0)$ at a typical initial energy density $e_0 = 30\,\mathrm{GeV/fm}^3$ for central Au+Au collisions at RHIC decreases by 1.4% and 4.3%, respectively, with correspondingly small changes in the entropy density s_0. In the linear interpolation approach discussed above, however, the entropy density s_0 at e_0 is fixed by lattice QCD constraints and significantly, i. e. by about 15%, smaller. Note that EoS QPM(1.0), which interpolates linearly between QPM EoS and HRG EoS at $e_m = 1.0\,\mathrm{GeV/fm}^3$, is quite similar to EoS Q, except for the rather large latent heat in EoS Q, whereas EoS QPM(1.0) does not exhibit a first-order phase transition.

Figure 4.2 shows the corresponding squared speed of sound as a function of energy density e. The linear interpolation between the hadron resonance gas at $e \leq e_1 = 0.45\,\mathrm{GeV/fm}^3$ and the QPM at $e \geq e_m$ leads to a region of constant squared speed of sound for $e_1 \leq e \leq e_m$. This constant increases monotonically with the matching point value e_m. As noted above, for $e_m = 3\,\mathrm{GeV/fm}^3$, the hadron resonance gas EoS is extrapolated approximately smoothly to the QPM EoS. Thus, the corresponding EoS QPM (3.0) exhibits no soft region of small c_s^2. In this case, the typical phase transition signature of a softening of the EoS near T_c is minimized

(also for EoS QPM (4.0)), leading to a minimal phase transition influence on the development of hydrodynamic flow. Still, the corresponding squared speed of sound exhibits a jump at e_{m}.

4.2 Azimuthal anisotropy and transverse momentum spectra

Assuming no transverse flow at a certain initial time τ_0, at which the hydrodynamic expansion stage starts, the azimuthal asymmetry in the particle emission for momenta perpendicular to the beam axis is completely determined by the acting pressure. Therefore, the azimuthal asymmetry represents an ideal probe for the equation of state. Equipped with the QCD based family of equations of state discussed in section 4.1, effects of fine structures in the EoS near T_c on the evolution of hydrodynamic flow can be studied.

In this section, transverse momentum spectra $dN/(dy\, p_T dp_T\, d\phi)$ (cf. Eq. (1.5)) and differential elliptic flow $v_2(p_T)$ for a variety of hadron species are analyzed. The final anisotropy in the momentum distribution depends on the rescatterings among the particles serving as measure for the degree of local thermalization. In order to emphasize flow effects, here, only directly emitted hadrons are considered and resonance decay distortions are neglected.

For the hydrodynamic simulations, P. Kolb's 2+1 dimensional relativistic hydrodynamic program package version 0.0 as available from the OSCAR website with Cooper-Frye freeze-out formalism used in [55, 56, 58, 167–170] is exploited. It assumes longitudinally boost-invariant expansion à la Bjorken. Clearly, this is appropriate only near midrapidity, $y \approx 0$, but sufficient for purposes of these qualitative investigations. In addition, a constant-temperature freeze-out prescription is applied.

Nonetheless, no systematic comparison with RHIC data is attempted here. Previous studies [54,56,58,167,168] have already qualitatively established that existing RHIC data are best described by an EoS with either a phase transition or a rapid crossover of significant strength exhibiting both, a soft section near T_c and a hard section not too far above T_c. More quantitative statements about a preference of one form of the EoS over another require a discussion that goes beyond the pure ideal fluid dynamical approach discussed here, due to well-known strong viscous effects on the evolution of elliptic flow in the late hadron resonance gas phase [175]. Studying the effects of EoS variations within a more complete framework that allows to account for non-ideal fluid behaviour in the very early and late stages of the fireball expansion is an important task for the future. Staying within the ideal fluid approach, the discussion presented here improves over that in [58] by employing below T_c a chemically non-equilibrated hadron resonance gas EoS which correctly reproduces the measured hadron yields, irrespective of the selected value for the hydrodynamic decoupling temperature. This is also in contrast to considerations in [176], where a full equilibrium HRG EoS is used and the decoupling surface is dynamically determined from comparing the hydrodynamic expansion rate with the local pion-pion scattering rate.

While the study presented in [56,167,168] shows that at top RHIC energies most

of the finally observed momentum anisotropy develops before the completion of the quark-hadron phase transition, the build-up of elliptic flow still occurs mostly in the temperature region where lattice QCD data significantly deviate from the ideal quark-gluon gas. It is therefore of interest to investigate effects of these deviations and of variations in the exact shape of the EoS in the transition region on the final elliptic flow in some detail, both at RHIC energies, where they are expected to matter, and at higher LHC energies where most (although not all [177]) of the anisotropic flow will develop before the system enters the phase transition region, thus reducing its sensitivity to details in the transition region. This is explored in the following.

4.2.1   Top RHIC energy

Considering, first, top RHIC energy, the corresponding initial conditions are fixed according to [56, 167, 168]:

$$s_0 = 110\,\mathrm{fm}^{-3}, \quad n_0 = 0.4\,\mathrm{fm}^{-3}, \quad \tau_0 = 0.6\,\mathrm{fm/c}\,. \tag{4.1}$$

These parameters, describing the initial conditions in the fireball centre for central ($b = 0\,\mathrm{fm}$) Au+Au collisions, are required input for the hydrodynamic code. Initial profiles for non-central collisions are calculated from these initial conditions using the Glauber model [56, 167, 168]. In the case of the QPM EoS, the values in Eq. (4.1) translate, independently of the QPM EoS version of the family used, into $e_0 = 29.8\,\mathrm{GeV/fm}^3$, $p_0 = 9.4\,\mathrm{GeV/fm}^3$ and $T_0 = 357\,\mathrm{MeV}$. Since the physical scale is set by the value of T_c in the QPM EoS, a variation of T_c in the range $(170 \pm 10)\,\mathrm{MeV}$ would result in a variation of e_0 between 25 and 33 GeV/fm³ when keeping s_0 fixed in order to maintain the same final charged particle multiplicity $dN_{\mathrm{ch}}/dy \propto s_0\tau_0$.

The calculations assume zero initial transverse velocity, $v_{T,0} = 0$ at $\tau = \tau_0$. In the hadron phase, the Kolb-Rapp chemical off-equilibrium EoS [172] is used to account for frozen-out chemical reactions. The employed freeze-out criterion is $e_{f.o.} = 0.075\,\mathrm{GeV/fm}^3$, corresponding to a freeze-out temperature of about 100 MeV, at which all hadrons are assumed to freeze out. This freeze-out temperature is rather small compared to different approaches, e. g. [176], where about 140 - 150 MeV are used.

Usually, when analyzing data, the set of initial and final conditions is adjusted to keep the transverse momentum spectra of a given set of hadron species fixed. Then, variations in v_2 are studied. Here, instead, the impact of details in the EoS on these observables is illustrated by using a fixed set of initial and freeze-out parameters. In the following, a fixed impact parameter $b = 5.2\,\mathrm{fm}$, is explored, being adjusted to best reproduce minimum bias data from the STAR collaboration.

In Figures 4.3 and 4.4, transverse momentum spectra and differential elliptic flow for directly emitted Λ, Ξ, and Ω hyperons are shown, respectively. These hadron species are not expected to receive large resonance decay contributions. Thus, by comparing the results for directly emitted particles with the measured spectra, one can obtain a reasonable feeling for the level of quality of the model description. Here, only results obtained with the two extreme equations of state, EoS QPM(4.0) and the bag model EoS (exhibited by the dashed curve in Figure 4.1) are
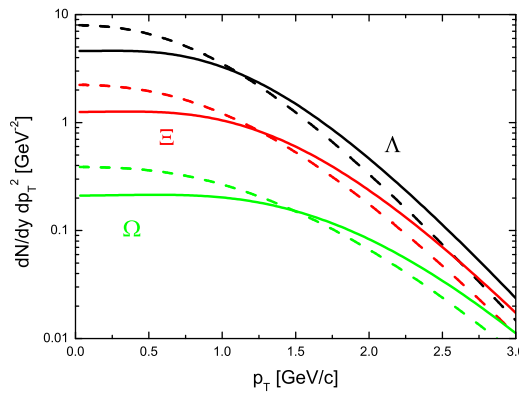
Figure 4.3: Transverse momentum spectra for directly emitted strange
baryons. Solid and dashed curves are for EoS QPM(4.0) and the
bag model EoS, respectively. Details are explained in the text.
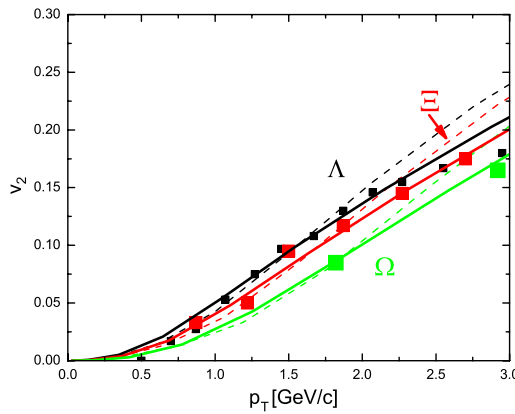
Figure 4.4: Differential elliptic flow $v_2(p_T)$ for directly emitted strange
baryons. Solid and dashed curves exhibit results for the equations
of state employed also in Figure 4.3. The symbols represent data
from the STAR collaboration [178] (small squares Λ, middle-sized
squares Ξ and large squares Ω). Details are explained in the text.

displayed. The results for EoS QPM(1.0) are very similar to those of the bag model
EoS, although the latter features a large latent heat. The two remaining equations
of state, EoS QPM(1.25) and EoS QPM(2.0), interpolate smoothly between the
two extreme cases exhibited in Figures 4.3 and 4.4.

From Figure 4.3 it is evident that EoS QPM(4.0) generates significantly larger
radial flow, resulting in flatter transverse momentum spectra especially for the
heavy hadrons considered here. This can be understood from Figures 4.1 and 4.2,
since EoS QPM(4.0) does not feature a soft region with small squared speed of
sound around T_c. Flatter transverse momentum spectra generically result in smaller
Fourier coefficients $v_2(p_T)$ [56, 167, 168]. But Figure 4.3 clearly indicates that for
$p_T < 1.5\,\mathrm{GeV}/c$ EoS QPM(4.0) actually produces larger $v_2(p_T)$ than the bag model
EoS. This implies that EoS QPM(4.0) also produces a larger overall momentum
anisotropy, i. e. p_T-integrated elliptic flow, than the bag model EoS, again, due to

the absence of a soft region near T_c. Only at large $p_T > 2\,\mathrm{GeV}/c$, where the ideal fluid dynamic picture is known to begin to break down [57], EoS QPM(4.0) gives smaller elliptic flow than the bag model EoS, as naively expected [56,167,168] from the flatter slope in the single particle transverse momentum distribution.

The larger $v_2(p_T)$ at low $p_T < 1.5\,\mathrm{GeV}/c$ from EoS QPM(4.0) is not favoured by the experimental data. In this sense, the qualitative conclusion from earlier studies [54,56,58,167,168] is confirmed that the data are best described by an EoS with a soft region near T_c followed by a rapid increase in the speed of sound above T_c.

4.2.2   LHC estimates

Turning to predictions for Pb+Pb collisions at the LHC, these involve a certain amount of guesswork about the initial conditions at the higher collision energy. Not embarking upon a systematic exploration by varying initial conditions, as proposed e. g. in [179], proper LHC initial conditions are conservatively guessed as

$$s_0 = 330\,\mathrm{fm}^{-3}, \quad \tau_0 = 0.6\,\mathrm{fm/c}, \tag{4.2}$$

keeping all other parameters unchanged. This corresponds to three times larger final multiplicities than measured at RHIC. Within the QPM these initial parameters translate into $e_0 = 127\,\mathrm{GeV/fm}^3$, $p_0 = 42\,\mathrm{GeV/fm}^3$ and $T_0 = 515\,\mathrm{MeV}$ for the peak values in central Pb+Pb collisions. Again, collisions at impact parameter $b = 5.2\,\mathrm{fm}$ are investigated using the Glauber model to calculate the corresponding initial density profiles from the above ($b = 0\,\mathrm{fm}$) parameters.

As in section 4.2.1, only the two extreme equations of state, EoS QPM(4.0) and the bag model EoS, are considered. In Figures 4.5 and 4.6, transverse momentum spectra of directly emitted Λ, Ξ, and Ω hyperons as well as of directly emitted protons (p), kaons (K) and pions (π) are exhibited, respectively. Figures 4.7 and 4.8 display the corresponding differential elliptic flow. Generally, the p_T spectra for LHC initial conditions are flatter than for RHIC initial conditions (cf. Figures 4.3 and 4.5), since the higher initial temperature, and correspondingly longer fireball life-time, results in stronger radial flow. Figures 4.5 and 4.6 show again that EoS QPM(4.0), which lacks a soft region near T_c, generates even larger radial flow, i. e. flatter transverse momentum spectra, than the bag model EoS, whose results are similar to those obtained for EoS QPM(1.0). The radial flow effects are particularly strong for the heavy hyperons.

The overall momentum anisotropy, i. e. the p_T-integrated elliptic flow, increases but not very much from RHIC to LHC [56]. This is naturally expected, since the longer QGP phase life-time expected at LHC translates into a longer persistence of pressure gradients generating elliptic flow. However, since the LHC spectra are flatter in particular for heavier particles, i. e. have more weight at larger p_T, than the RHIC spectra (cf. Figures 4.3 and 4.5), the differential elliptic flow at fixed p_T must, therefore, decrease. This is clearly seen when comparing Figure 4.4 with Figure 4.7. The decrease is particularly strong for the hyperons at low p_T where the LHC transverse momentum spectra become extremely flat (cf. Figure 4.5). This behaviour is induced by the increased importance of the flow velocity for heavier particles which overcompensates the increased flow asymmetry. Similar findings for the v_2 of protons are reported in [180].
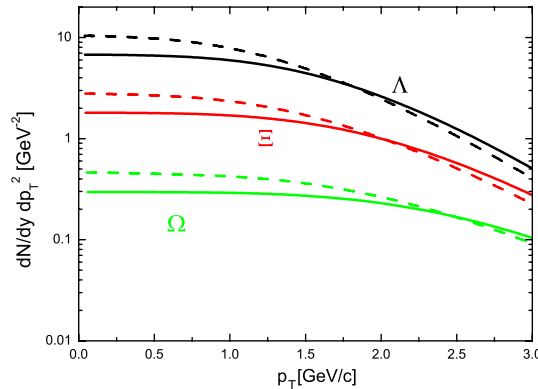
Figure 4.5: Transverse momentum spectra for strange baryons. The spectra show only directly emitted hadrons. Solid and dashed curves are for EoS QPM(4.0) and the bag model EoS being similar to EoS QPM(1.0), respectively.
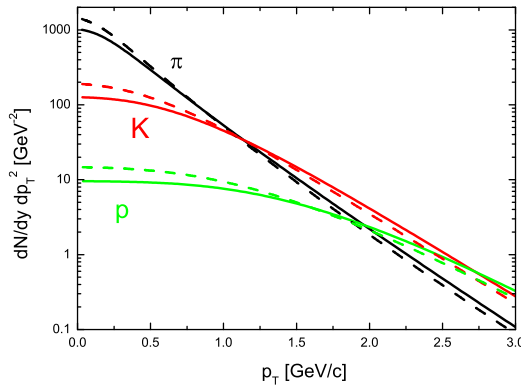

Figure 4.6: Transverse momentum spectra for pions (π), kaons (K) and protons (p). The spectra show only directly emitted hadrons. Solid and dashed curves are for EoS QPM(4.0) and the bag model EoS, respectively.

4.3 Future prospects

As the lattice QCD simulations reported in [132] employ unphysically large quark masses, the pressure at small energy densities is too small in order to match with a realistic hadron resonance gas. For this to happen, smaller quark masses are necessary to account for the partial pressure which is generated by the light pion modes and their remnants for temperatures in the vicinity but below T_c. On the other hand, it was shown in [132,133] that the HRG yields results which are consistent with the lattice QCD data in [132] below T_c when appropriately modifying the HRG mass spectrum according to the lattice calculation set-up. In this respect, the HRG model with physical quark mass spectrum [52,173] can be seen as appropriate approximation of the hadronic phase [181].

With the availability of lattice QCD results [135] which employ almost realistic quark masses, one feature of the QPM, namely the possibility of extrapolating
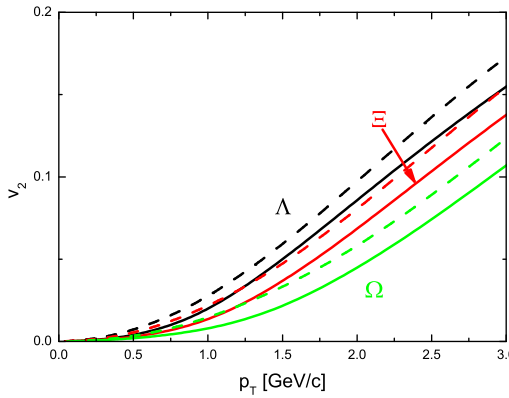
Figure 4.7: Azimuthal anisotropy $v_2(p_T)$ for directly emitted strange
baryons. Solid and dashed curves are for EoS QPM(4.0) and the
bag model EoS, respectively.
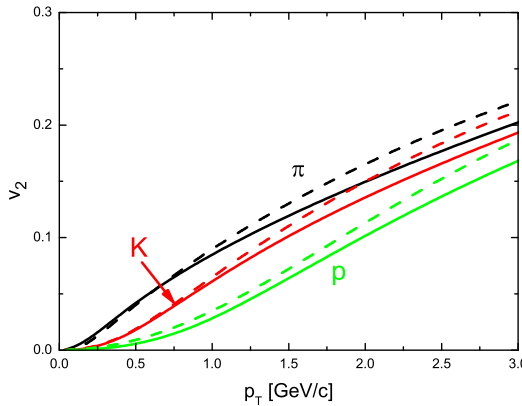
Figure 4.8:   Azimuthal anisotropy $v_2(p_T)$ for directly emitted pions
(π), kaons (K) and protons (p). Solid and dashed curves are for
EoS QPM(4.0) and the bag model EoS, respectively.

to different quark mass parameters, could successfully be applied (cf. Figure 3.4
and the discussion in section 3.1.2). Nonetheless, the chirally extrapolated QPM
EoS, which is numerically not too distinct from the result one would obtain for the
nonzero but almost physical quark masses employed in [135] (cf. Figure 3.4), does
not smoothly match the HRG EoS at e_1 as evident from Figure 3.32. Therefore,
an interpolation procedure between both sections of the equation of state became
necessary (cf. section 4.1). In these considerations, so far, the physical scale $T_c =$
170 MeV was kept fixed. Changing, however, in addition the value of T_c according
to the lighter quark mass parameters to $T_c = 192$ MeV [10], low energy density and
high energy density regions continuously combine with each other as exhibited in
Figure 4.9.

This new QPM equation of state is, thus, free from interpolation ambiguities.
The corresponding squared speed of sound, as exhibited in Figure 4.10, shows an
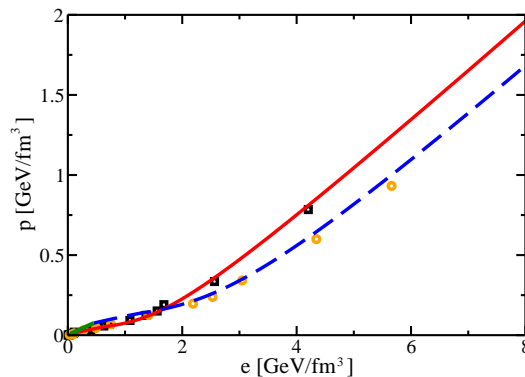
Figure 4.9:   Equation of state $p(e)$ at $n_B = 0$ for $N_f = 2 + 1$. For
comparison, lattice QCD results [132] (squares) and correspond-
ing QPM results (solid red curve) for unphysical quark masses are
exhibited. Performing an extrapolation of this QPM parametriza-
tion to almost physical quark masses in line with [135] and using
$T_c = 192$ MeV [10] to set the physical scale, the corresponding re-
sult is depicted by the dashed blue curve together with the accord-
ing lattice QCD data [135] (circles). This new QPM EoS smoothly
matches the HRG EoS (solid green curve in the lower left edge) at
e_1.

almost identical behaviour compared to the EoS discussed in the previous sections.
Consisting of a very soft sector in the transition region followed by a rapid change
into a hard section above T_c, the new QPM EoS exhibits those features which are
necessary for reproducing experimentally observed data of transverse momentum
spectra and elliptic flow in hydrodynamic simulations. In fact, concerning acceler-
ating power and stiffness, the new QPM EoS is rather similar to EoS QPM (1.0),
featuring a rapid but smooth crossover behaviour in the transition region. It will,
though, be an issue of future investigations to study the influence of this new QPM
EoS on hydrodynamics.

For the observed smooth approach between QPM EoS and HRG EoS, both,
lighter quark masses as well as a corresponding change in the value of T_c are
equally mandatory. This is in line with the scaling properties of the QPM EoS
discussed in section 3.3.3. However, the continuous matching can only be observed
when performing a naive chiral extrapolation leaving also $B(T_c)$ unchanged (in
contrast to the procedure employed in Figure 3.4). This mainly affects $p(T)/T^4$ in
the transition region and for $T < T_c$. The result for $p(T)/T^4$, which is necessary
for saturating the pressure at lower energy densities in order to match the HRG
pressure, is exhibited in Figure 4.11 (dashed curve) showing some deviations from
the lattice QCD results [135] for $T < T_c$.
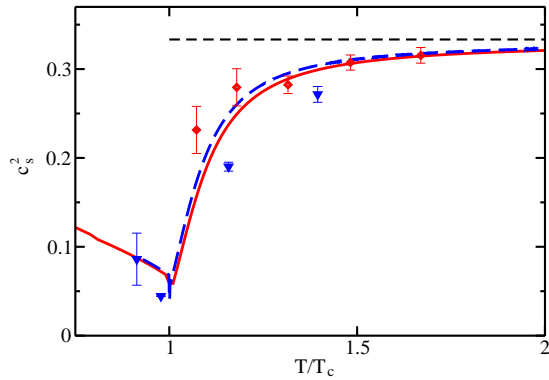
Figure 4.10:   Squared speed of sound as a function of T/T_c for the
two QPM EoS exhibited in Figure 4.9 (same line code). Symbols
denote lattice QCD results [165] for $N_f = 2$ and short-dashed
horizontal curve exhibits the Stefan-Boltzmann limit $c_s^2 = \frac{1}{3}$.
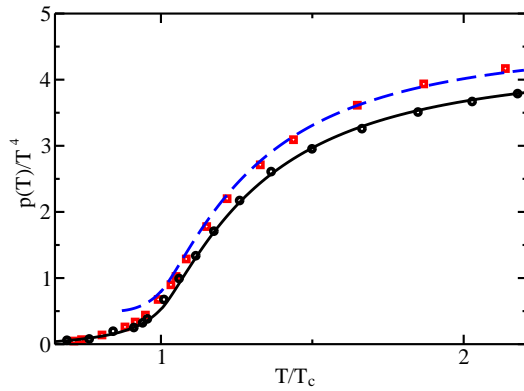
Figure 4.11:   Naive extrapolation of the scaled pressure $p(T)/T^4$ as
a function of T/T_c from the unphysical quark mass set-up (solid
curve, cf. Figure 3.2) to almost physical quark masses (dashed
curve) leaving, here, also $B(T_c)$ unchanged (cf. Figure 3.4). The
increase in $p(T)/T^4$ compared to the lattice QCD data [135]
(squares) becomes necessary in order to produce the behaviour
of the new QPM EoS observed in Figure 4.9.

5 Study of QCD Critical Point Effects

In this chapter, the impact of the QCD critical point on the equation of state is analyzed for the $N_f = 2$ case. In particular, the influence on higher-order derivatives of the thermodynamic potential, such as quark number susceptibility or specific heat, and on the behaviour of the isentropic trajectories is investigated. In this way, effects of CP on the hydrodynamic expansion of the hot and dense fireball can be studied. Here, in line with the arguments presented in Appendix A.2, the existence of the QCD CP is assumed at $T^E \approx 162$ MeV and $\mu_B^E = 360$ MeV [182]. Apart from that, the extension of the critical region around CP, which might be crucial for searches of CP signals in future heavy-ion collision experiments, is fairly unknown [183, 184].

In section 5.1, a singular contribution to the entropy density assembling the critical properties of the 3-dimensional Ising model is parametrically constructed following [185]. Section 5.2 deals with the phenomenological implementation of this singular entropy density contribution into a toy model. The ideas presented here base on the work in [186]. Henceforth, the impact of the size of the critical region on the pattern of isentropic trajectories is analyzed. Furthermore, the relative strength of singular and regular contributions to the thermodynamics can be studied. Finally, QCD CP features are phenomenologically included into the QPM for one independent chemical potential in a similar way in section 5.3. These considerations, however, are constraint by lattice QCD results at finite net baryon density which, supposed the numerical accuracy is sufficient, take into account all the complexity of QCD. The results presented in this chapter are reported in [91,92].

5.1 Construction of QCD critical point phenomena

Starting point is the decomposition of the entropy density into $s = s_{reg} + s_{sing}$ with a regular part s_{reg} and a singular part s_{sing}. While s_{reg} is defined according to the considered analytic model, which will be specified in the following sections, s_{sing} is related to phase transitions and critical phenomena [187], instead. It is constructed from the parametric representation [185] of the Gibbs' free energy density $G(r, h)$ with critical behaviour belonging to the universality class of the 3-dimensional Ising model. The order parameter of the 3-dimensional Ising model is the magnetization $M(r, h)$. $G(r, h)$ and $M(r, h)$ are functions of reduced temperature $r \equiv (T - T_c)/T_c$ and external magnetic field h.

From [185], the parametric form of G in terms of new, implicitly defined, parameters R and θ reads

$$G = F(M, r) - Mh, \tag{5.1}$$

where the free energy density $F(M, r) = h_0 M_0 R^{2-\alpha} g(\theta)$, $M = M_0 R^\beta \theta$ and M_0, h_0 are normalization constants. The variables in this representation of the 3-

dimensional Ising model are defined by

$$r \;=\; R\left(1 - \theta^2\right)\,, \tag{5.2}$$

$$h \;=\; h_0 R^{\beta\delta} \sum_{i=0}^{2} a_{2i+1}\theta^{2i+1}\,, \tag{5.3}$$

where $R \geq 0$, $|\theta| \geq 1.154$. The corresponding critical exponents read $\beta = 0.326$ and $\delta = 4.80$ for the order parameter $M(r,h)$, $\alpha = 2 - \beta\left(1 + \delta\right)$ and $\gamma = \beta(\delta - 1)$ according to Rushbrouke's and Griffith's equalities for the specific heat and the magnetic susceptibility, respectively, while $a_1 = 1$, $a_3 = -0.76201$, and $a_5 = 0.00804$. The function $g(\theta)$ in $F(M,r)$ follows from solving the differential equation

$$\sum_{i=0}^{2} a_{2i+1}\theta^{2i+1}\left(1 - \theta^2 + 2\beta\theta^2\right) = 2(2 - \alpha)\theta g(\theta) + (1 - \theta^2)g'(\theta) \tag{5.4}$$

with integration constant $g(\theta = 1) = 0.04242$ which stems from $h = (\partial F/\partial M)|_r$. Following these definitions, $M(r,h)$ shows the correct critical behaviour $M(r = 0,h) \sim \mathrm{sgn}(h)|h|^{1/\delta}$, $M(r < 0, h = 0^+) \sim |r|^{\beta}$ close to $r = 0$, $h = 0$ when choosing M_0, h_0 appropriately. The critical point is, by construction, located at $r = 0$ and $h = 0$.

In Figures 5.1 and 5.2, the mappings between the variables of the 3-dimensional Ising model (r,h) and the parametric representation (R,θ) of the Gibbs' free energy density in Eq. (5.1) is illustrated. Regions of opposite sign in the external magnetic field h are separated in the (R,θ) parameter space. Striking, however, is that by construction, the parametrization is continuous for $r > 0$, whereas it exhibits a discontinuity for $r < 0$ at $h = 0$. Thus, identifying $(r = 0,\ h = 0)$ with (T^E, μ_B^E) and choosing appropriately the orientation of the coordinate system (r,h) in the QCD thermodynamic parameter space (T, μ_B), the anticipated phase transition
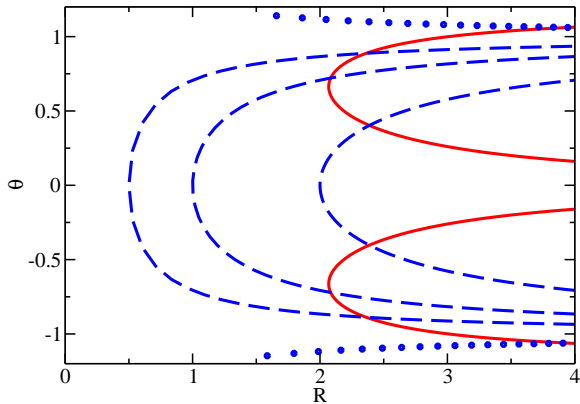
**Figure 5.1:** Mapping of Ising model variables (r,h) to the parameters (R,θ) in the parametric representation of G in [185] according to Eqs. (5.2) and (5.3). Solid curves depict lines of constant $h = 0.5$ (-0.5) for the upper (lower) curve. Dashed curves exhibit lines of constant $r > 0$ ($r = 0.5, 1, 2$ from left to right), whereas dotted lines represent constant negative $r = -0.5$.
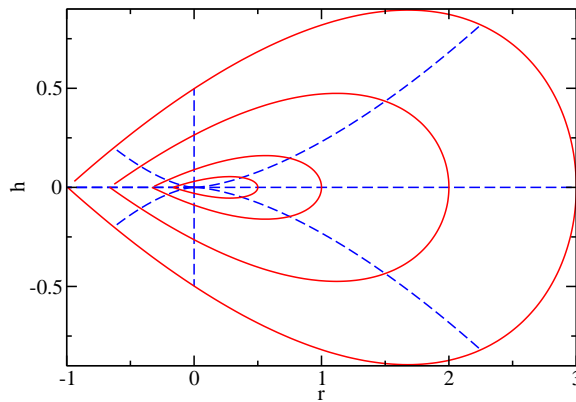
Figure 5.2:   Inverse mapping $(R, \theta) \rightarrow (r, h)$. Solid curves denote lines of constant $R = 0.5, 1, 2, 3$ from inner to outer ring, dashed curves lines of constant θ: For $h < 0$, θ is negative ($\theta = -1.1, -1$ (here $r = 0$) and -0.5 from left to right); for $h > 0$, θ is positive ($\theta = 1.1, 1$ (here $r = 0$) and 0.5 from left to right). For $h = 0$, $\theta = \pm 1.154$ for $r < 0$ and $\theta = 0$ for $r > 0$.

pattern in the QCD phase diagram can be generated featuring a first-order phase transition for $\mu_B > \mu_B^E$ and an analytic crossover for $\mu_B < \mu_B^E$.

The singular part of the entropy density near the QCD critical point can be constructed from the dimensionless quantity

$$S_c(T, \mu_B) = - \sqrt{(\Delta T_c)^2 + (\Delta \mu_{B,c})^2} \left(\frac{\partial G}{\partial T} \right) \Bigg|_{\mu_B}. \tag{5.5}$$

Assuming a rectangular critical region around CP, its extension in T and μ_B directions is approximated by ΔT_c and $\Delta \mu_{B,c}$. (This is clearly an idealization. Investigations of the critical slowing down phenomenon near CP suggest rather a bending of the critical region along the phase boundary [184].) Attributing the correct dimensions to Eq. (5.5), $S_c(T, \mu_B)$ quantifies the rapidity with which the entropy density s changes across the r-axis. As for $r < 0$ $S_c(T, \mu_B)$ exhibits a discontinuity at $h = 0$, implying a discontinuity in s and thus a first-order phase transition, it is feasible to mimic the QCD phase transition line by the r-axis.

5.2   Study of QCD critical point effects in a toy model

As pointed out in section 5.1, the variables of the 3-dimensional Ising model need to be mapped into the T-μ_B plane in the vicinity of CP. The coordinate transformation incorporating the correct QCD phase transition features is illustrated in Figure 5.3. The depicted phase boundary is estimated by $T_c(\mu_B) = T_c \left(1 + \frac{1}{2} d (\frac{\mu_B}{3 T_c})^2 \right)$ with $d = -0.122$ which agrees with the solution of the QPM flow equation emanating at $T_c(\mu_B = 0) = 175$ MeV [130] for small μ_B. Note that the same curvature for the estimated phase boundary was found in section 3.2.5 for $N_f = 4$ degenerate quark flavours and in lattice QCD simulations [164] a similar $d = -0.146$ was reported. This estimate for the phase transition line, however, implies a slightly different $T^E = 170$ MeV compared to [182] at fixed $\mu_B^E = 360$ MeV, which is used in the
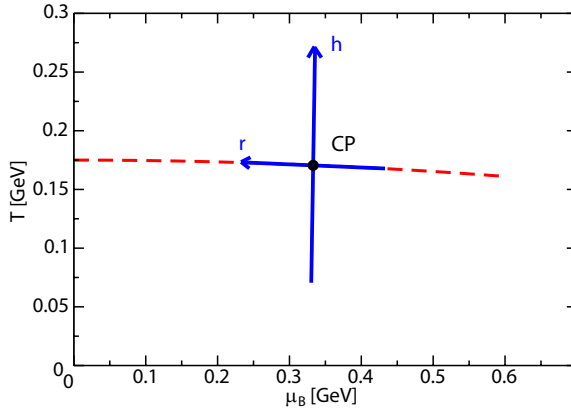
Figure 5.3:   Visualization of the coordinate transformation between
(T, μ_B) and (r, h). CP is located according to [182] on the esti-
mated phase boundary $T_c(\mu_B)$ and identified with $r = 0$, $h = 0$.
The r-axis is defined to be tangential to $T_c(\mu_B)$ at CP and oriented
such that $r > 0$ denotes the crossover region, $r < 0$ the region of
first-order phase transitions. The h-axis is put perpendicular to
the r-axis.

following. From Figure 5.3 it is clear that this phenomenological construction is
limited in accuracy by the increasing discrepancy between the r-axis and the actual
phase transition line in regions out of the vicinity of CP. Thus, this procedure works
best if CP is located at small μ_B in the flat region of $T_c(\mu_B)$.

In order to study CP effects, first, a simple toy model is considered. The regular
contribution to s is defined via a Taylor expansion for small μ_B

$$s_{reg}(T, \mu_B) = 4\bar{c}_0 T^3 + \frac{2}{9}\bar{c}_2 \mu_B^2 T \tag{5.6}$$

with constant $\bar{c}_0 = (32 + 21 N_f)\pi^2/180$ and $\bar{c}_2 = N_f/2$ resembling the entropy
density of an ideal gas of gluons and N_f quarks. The construction of the singular
entropy density contribution together with the complex task of relating (T, μ_B)
with Eqs. (5.1) and (5.5) is performed in line with the ideas presented in [186]. It
reads

$$s_{sing}(T, \mu_B) = \frac{2}{9}\bar{c}_2 \mu_B^2 T A \tanh\left[S_c(T, \mu_B) \right] , \tag{5.7}$$

obeying the correct dimension of an entropy density. In this way, s_{sing} includes the
proper critical exponents of the 3-dimensional Ising model and is continuous for
$\mu_B < \mu_B^E$, while it is discontinuous for $\mu_B > \mu_B^E$ signalling the region of first-order
phase transitions. The parameter A describes the relative strength of the singular
contribution s_{sing} in s compared to s_{reg} and $\tanh\left[S_c(T, \mu_B) \right]$ binds the function
$S_c(T, \mu_B)$ between $+1$ and -1, for convenience. The ansatz in Eq. (5.7) is chosen
such that $s_{sing} \to 0$ for $T \to 0$ or for $\mu_B \to 0$.

The net baryon density n_B follows from

$$n_B(T, \mu_B) - n_B(0, \mu_B) = \int\limits_0^T \frac{\partial s(T', \mu_B)}{\partial \mu_B} dT' \tag{5.8}$$

with integration constant $n_B(0, \mu_B) = \frac{4}{3}\bar{c}_4 \left(\frac{\mu_B}{3}\right)^3$ and $\bar{c}_4 = \frac{N_f}{4\pi^2}$ which is completely determined from the regular part of the underlying thermodynamic potential. Thus, $n_B \to 0$ for $\mu_B \to 0$.

The parameters in s_{sing} have to be chosen such that the standard thermodynamic consistency conditions

$$\left(\frac{\partial s}{\partial T}\right)_{n_B} > 0\,, \tag{5.9}$$

$$\left(\frac{\partial n_B}{\partial \mu_B}\right)_T > 0 \tag{5.10}$$

are satisfied [186,188]. First, a critical region with moderate extension is considered by applying $\Delta T_c = 15$ MeV and $\Delta \mu_{B,c} = 30$ MeV. In Figure 5.4, the impact of CP on the pattern of isentropic trajectories, characterized by constant s/n_B, is exhibited. For comparison, trajectories with $s_{sing} = 0$ by setting $A = 0$ are depicted by dashed curves. Increasing $A > 0$ results in an increasing bending of isentropic trajectories towards larger μ_B where trajectories approaching the phase boundary at $\mu_B > \mu_B^E$ show the clear first-order phase transition signature of a finite latent heat. In general, trajectories lying originally in the crossover region are attracted by CP whereas those lying originally in the first-order phase transition realm seem to be repelled. Shrinking the extension of the critical region towards $\Delta T_c = 0.6$ MeV and $\Delta \mu_{B,c} = 0.6$ MeV, this general pattern remains unchanged, even though the bending strength of CP towards larger μ_B decreases as exhibited in Figure 5.5. In particular, the sections of isentropic trajectories in the hadronic phase are less influenced.

The pattern observed in Figures 5.4 and 5.5 seems to be generic. Even though isentropic trajectories are bent into the opposite direction for $A < 0$, this situation implies that s and n_B increase along the trajectory in the vicinity of the first-order phase transition line during the adiabatic expansion of the hot and dense fireball and its related cooling. As a result, thermodynamic consistency conditions are violated which excludes negative values for the strength parameter A. Nonetheless, this statement crucially bases on the employed ansatz for s, in particular in the hadronic phase, as it also influences n_B in the quark-gluon plasma phase according to Eq. (5.8) (cf. [186] for a different ansatz for s). Clearly, Eqs. (5.6) and (5.7) cannot account for the complexity of QCD.
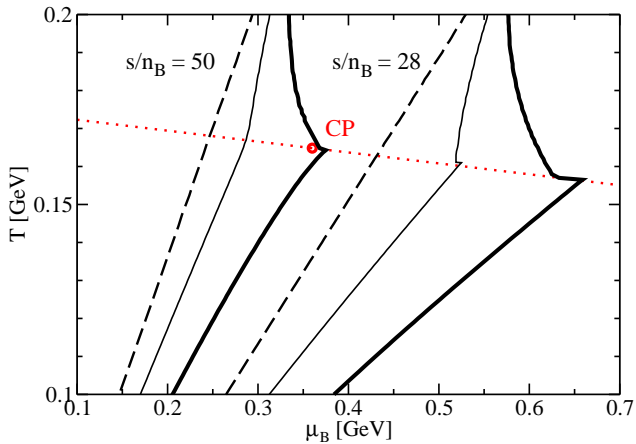
Figure 5.4: Isentropic trajectories in the toy model depending on the strength parameter A for $s/n_B = 50, 28$. Dashed, thin and solid curves exhibit results for $A = 0., 0.5, 1.0$, respectively. Dotted curve represents the r-axis defined tangentially to the estimated phase boundary at CP. The extension of the critical region is parametrized by $\Delta T_c = 15$ MeV, $\Delta\mu_{B,c} = 30$ MeV.
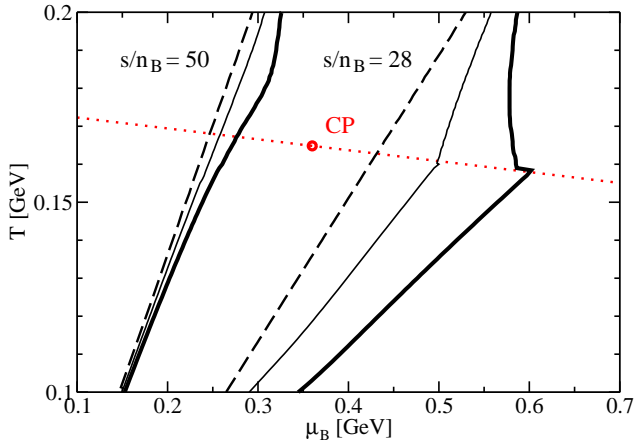
Figure 5.5: Isentropic trajectories as in Figure 5.4. Here, $\Delta T_c = 0.6$ MeV, $\Delta\mu_{B,c} = 0.6$ MeV.

5.3 QPM with QCD critical point

The quasiparticle model introduced in section 2.1 *per se* does not include an explicit critical behaviour. The rapid changes in the vicinity of T_c observed in energy density e and entropy density s for vanishing chemical potential (cf. Figure 3.3) or in second-order Taylor coefficients of thermodynamic quantities for finite μ (cf. Figures 3.8 and 3.11) are described by the rapid increase in the effective coupling $G^2(T)$ for $T \to T_c^+$ making the active degrees of freedom rather heavy. Nonetheless, the

change in the curvature of these thermodynamic quantities at $T = T_c$ dictates a change in the parametrization of $G^2(T)$ for $T < T_c$ as advocated in Eq. (2.20).

In principle, a parametrization for $G^2(T)$ could be constructed such that $G^2(T)$ would be continuously differentiable to arbitrary orders with respect to T at $T = T_c$. However, such an ansatz cannot meet lattice QCD constraints while the parametrization defined in Eqs. (2.20) and (2.21) can as successfully demonstrated in chapter 3. In fact, the correct description of pronounced structures in higher-order Taylor coefficients of thermodynamic quantities within the QPM is related to higher-order derivatives of $G^2(T)$ exhibiting a discontinuity at T_c. In this way, the change in the curvature of $G^2(T)$ mimics phase transition effects. Note, however, that e, s and n_B are continuous as any contributions stemming from derivatives of $G^2(T)$ are compensated by the bag function B due to thermodynamic consistency as elaborated in section 2.1.

Arming the QPM with explicit CP features following the procedure presented in section 5.2, the regular contribution s_{reg} has to be adjusted to the known EoS outside of the critical region. Thus, s_{reg} can be defined by Eq. (3.9) together with the QPM parametrization employed in Figure 3.8. Then, the singular contribution, fulfilling thermodynamic consistency requirements, reads

$$s_{sing}(T, \mu_B) = \frac{2}{9} c_2(T) \mu_B^2 T A \tanh \left[S_c(T, \mu_B) \right] , \qquad (5.11)$$

where $c_2(T)$ is defined in Eq. (3.3). Another conceivable possibility of defining s_{sing} would be to employ a μ_B^3 dependence rather than the advocated $\mu_B^2 T$ dependence. The remaining parameters A and ΔT_c, $\Delta \mu_{B,c}$ must be adjusted such that lattice QCD results for the entropy density can be described by $s_{reg} + s_{sing}$. The net baryon density follows similarly to Eq. (5.8) by integration of $s_{reg} + s_{sing}$ with $n_B(0, \mu_B) = \frac{4}{3} c_4(T) \left(\frac{\mu_B}{3} \right)^3$ and $c_4(T)$ defined in Eq. (3.4).

As for small μ_B, lattice QCD data for s are already successfully reproduced by s_{reg} alone, one has to choose, for example, $\Delta T_c = \Delta \mu_{B,c} = 2$ MeV and $A = 0.1$ mimicking a small critical region and a weak singular contribution compared to s_{reg} for small μ_B. (In contrast, applying the strategy of describing lattice QCD results for small μ_B, in particular the pronounced structures in the Taylor coefficients, by increasing the strength of the singular contribution and decreasing the influence of the regular contribution turns out not to be successful.) In this way, bulk thermodynamic quantities are represented to a large extend by their regular contributions as evident from Figure 5.6. For small μ_B, the influence of CP on the EoS, here exhibited for the pattern of isentropic trajectories, is negligible. Only in the vicinity of CP, the trajectories are slightly modified leaving, however, the general pattern unchanged. A significant change of this pattern by increasing A or ΔT_c and $\Delta \mu_{B,c}$ seems to be excluded by lattice QCD constraints.

Note that in this approach s_{reg} and therefore s_{sing} are based on a Taylor expansion which is limited by its radius of convergence, $\mu_B/T \leq 1.8$ [164]. It is therefore impractical to examine isentropic trajectories approaching the phase boundary at $\mu_B > \mu_B^E$. In contrast, the full QPM is not hampered by these shortcomings. It would, therefore, be feasible to apply the QPM entropy density s from Eqs. (2.6) and (2.7) as regular part, defining $s_{sing} = A s_{reg} \tanh[S_c]$ in future investigations.

The small effect observed in Figure 5.6 for small μ_B can be understood by the numerical smallness of s_{sing} as exhibited in Figure 5.7. Thus, based on the assumption of a small critical region [14, 43], CP effects turn out to be small for small net baryon densities, in particular on averaged hydrodynamics. (Quark-meson model based studies combined with the proper-time renormalization group method [184] also point to CP effects concentrated on a fairly narrow region.) It will be an issue of future investigations to study, in line with [189–191], the impact of a CP supplemented EoS in hydrodynamic simulations for heavy-ion collision experiments.

Nevertheless, for μ_B close to μ_B^E,   baryon number susceptibility χ_B =
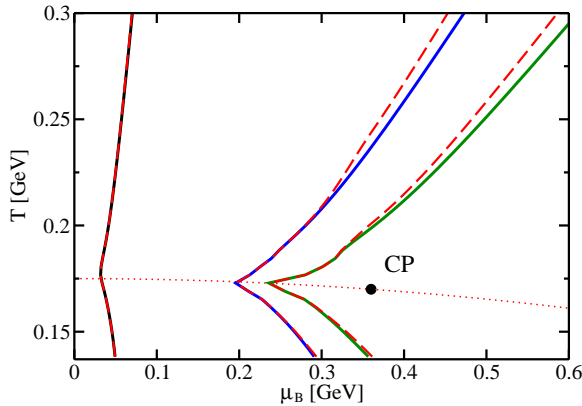
Figure 5.6:   Influence of the QCD CP on the pattern of isentropic trajectories $s/n_B = 300, 45, 35$ (from left to right). Solid curves represent only the regular contributions as shown in Figure 3.13 for $s/n_B = 300, 45$ while dashed curves exhibit results for the QPM with implemented CP.
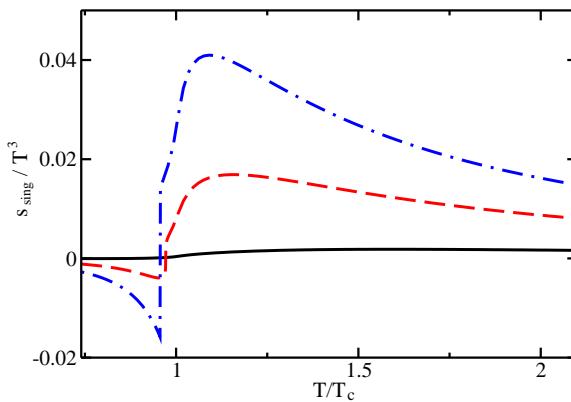
Figure 5.7:   Scaled singular part of the entropy density s_{sing}/T^3 as a function of T/T_c for different $\mu_B = 210, 360, 450$ MeV (solid, dashed and dash-dotted curves, respectively). At CP, the slope of s_{sing} becomes infinite resulting in a divergence of the specific heat c_H. For $\mu_B > 360$ MeV, s_{sing} shows the significant discontinuity across the phase transition line of first-order.
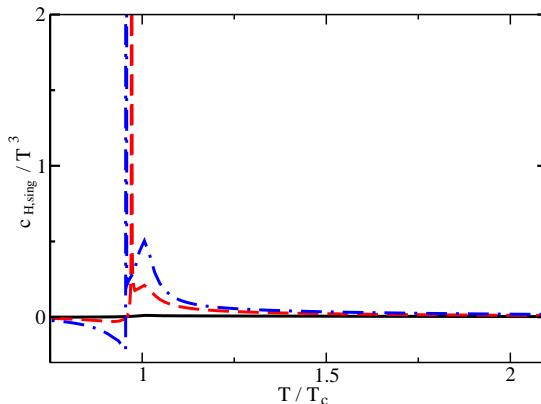
Figure 5.8:   Scaled singular contribution to the specific heat corre-
sponding to s_{sing} exhibited in Figure 5.7. $\mu_B = 210, 360, 450$
MeV for solid, dashed and dash-dotted curves, respectively. At CP,
$c_{H,sing}$ diverges while for $\mu_B > \mu_B^E$ it develops a discontinuity at
$T = T_c(\mu_B)$ plus, strictly speaking, a contribution $\delta(T - T_c(\mu_B))z$,
where z is the height of the discontinuity in s_{sing}.

$(\partial n_B/\partial \mu_B)|_T$ or specific heat $c_H = T \left(\partial s/\partial T\right)|_{\mu_B}$ are strongly influenced by the
QCD critical point. At CP, c_H diverges due to its singular part, as depicted in
Figure 5.8 while in the region of first-order phase transitions c_H is characterized
by a discontinuity across the phase boundary. Strictly speaking, as a result of the
discontinuity in s_{sing}, c_H receives a contribution from a delta-distribution weighted
by the height of the discontinuity in s_{sing} at $T_c(\mu_B)$.

In order to visualize the effects on χ_B, A is increased to $A = 1$ which does
not alter the qualitative behaviour of the observables. In the QPM with imple-
mented CP, the baryon number density n_B as a function of μ_B shows the expected
continuous behaviour in the crossover regime and also for $T > T_c$ as exhibited in
Figure 5.9. At CP, however, the slope becomes infinite turning into a disconti-
nuity of finite height across the first-order phase transition line. Correspondingly,
its derivative χ_B as measure for fluctuations in n_B diverges at CP and develops
a discontinuity, like c_H, across the phase transition line whereas χ_B remains fi-
nite for temperatures $T > T^E$. This is illustrated in Figure 5.10. A suppression
of baryon number fluctuations when approaching $T_c(\mu_B)$ for constant T from the
confined phase (solid, dashed and dash-dotted curves in Figure 5.10) is evident
in the vicinity of CP, whereas this is not the case when considering temperatures
$T > T_c(\mu_B = 0)$ (dotted curve in Figure 5.10). Nonetheless, some influence of the
presence of CP is still observed for $T = 176$ MeV. This behaviour is caused by
the form of the singular contribution to n_B (cf. Figure 5.9). Moreover, χ_B in the
confined phase is found to be approximately $\frac{1}{3}$ of χ_B in the deconfined phase. This
is in line with investigations reported in [147], which identify quasiparticles with
the quantum numbers of quarks as predominant carriers of the baryonic charge in
the hot deconfined phase.

The isovector susceptibility χ_I, in contrast, is expected to remain finite when
approaching CP [141]. In this section, the behaviour of χ_B for constant tempera-
tures is examined. In [192] it was argued that a verified signal of CP would require

a non-monotonic behaviour of χ_B along the phase boundary $T_c(\mu_B)$.
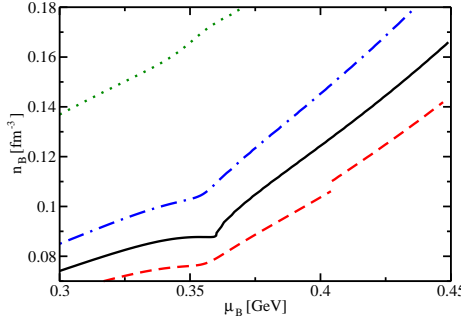
Figure 5.9: Baryon number density n_B as a function of μ_B for different
constant temperatures $T = T^E - 1.25$ MeV, T^E, $T^E + 1.25$ MeV
and $T = 176$ MeV (dashed, solid, dash-dotted and dotted curves,
respectively). For $T > T^E$, $n_B(\mu_B)$ is continuously increasing,
however showing an increasing influence of CP's presence by a
tiny slope depression when approaching T^E. At $T = T^E$, the
slope becomes infinite at μ_B^E, and for $T < T^E$, $n_B(\mu_B)$ exhibits
the discontinuous behaviour of a first-order phase transition when
crossing the phase boundary.
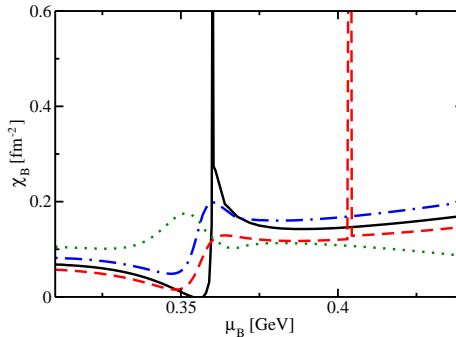
Figure 5.10:   Baryon number susceptibility χ_B as function of μ_B
(same line code as in Figure 5.9). The divergence of χ_B at μ_B^E
is clearly seen. For $T = T^E - 1.25$ MeV at $\mu_B = 0.41$ GeV, χ_B ex-
hibits a discontinuity plus a contribution from a delta-distribution
weighted by the height of the discontinuity in n_B. Note that in
order to maintain thermodynamic consistency, one is restricted in
the choice of parameters such that negative χ_B is avoided which, in
principle, would be possible due to the form of the singular baryon
density contribution.

6   Summary and Outlook

In this thesis, the equation of state of strongly interacting matter in the hot deconfined phase at finite net baryon densities is examined within a phenomenological quasiparticle model. A detailed knowledge on the QCD equation of state is of significant importance in various aspects of fundamental physics such as the hydrodynamic description of heavy-ion collision experiments, the evolution of the early universe or the properties of compact stellar objects like neutron stars. Due to the complexity of QCD showing non-perturbative behaviour over a wide range of temperatures and baryon densities, a direct evaluation of QCD thermodynamics is impractical. The most rigorous approach based on first principles is the evaluation of the QCD partition function and of related quantities on a discretized space-time lattice. However, phenomenological approaches, simplifying the theory to a description of relevant contributions in thermodynamic equilibrium, allow for a more pictorial view onto the nature of QCD matter at finite temperature and chemical potential. For this purpose, the quasiparticle model developed for the description of the thermodynamics of the hot deconfined phase is applied and its results are confronted with available lattice QCD data which, first, have to be extrapolated to thermodynamic and continuum limits for making a comparison meaningful.

In particular, QCD thermodynamics at nonzero net baryon density is considered, here. For this reason, the successful quasiparticle model is extended in a thermodynamically consistent way into two directions: Imaginary chemical potential, where found results have to be analytically continued towards real chemical potential, and two independent real chemical potentials, which have to be considered for accessing various susceptibilities. Both realms represent a huge and sensitive testing ground for the applicability of the model to extrapolate the QCD equation of state known from lattice QCD for zero or small baryon densities to large n_B. Specifically, Taylor series expansions of various bulk thermodynamic quantities, baryon number, isovector and electric charge susceptibilities as well as diagonal and off-diagonal susceptibilities are studied. In addition, isentropic evolutionary paths and the equation of state along them, and pronounced structures in the net quark number density as well as the phase diagram for imaginary chemical potential are investigated. All these successful applications presented here show that a reliable QCD equation of state is attainable in a consistent way via this phenomenological approach.

The performed studies also aim at a systematic exploration of the dependence of the underlying gauge field theory, QCD, on various entering parameters such as the number of active quark flavours, the quark mass parameters or the value of the deconfinement transition temperature. Specifically, the dependence of bulk thermodynamics and of the equation of state on variations in these parameters is investigated. In this respect, the applicability of the quasiparticle model to extrapolate available lattice QCD results for thermodynamic quantities to the chiral limit

is successfully tested. In addition, the scaling behaviour of the QCD equation of state with quark mass and the numerical value of T_c is examined. Whereas quark mass effects in the equation of state turn out to play a role only for small energy densities, changes in T_c can have some influence on the whole pattern. Moreover, the equations of state for $N_f = 2$ and $N_f = 2 + 1$ show some small deviations only in the phase transition region. Also, the extrapolation of bulk thermodynamics to asymptotically large temperatures is investigated. All these considerations demonstrate the predictive power of the model. As the quasiparticle model accurately reproduces first-principle lattice QCD results, its consequently expected connection with the theory of strong interactions, based on formal mathematical simplifications of a more rigorous approach to QCD via the Φ-functional formalism, is outlined.

The ultimate goal of these considerations is the construction of reliable QCD equations of state applicable in hydrodynamic simulations of the expansion stage of heavy-ion collisions, in particular at top RHIC energies. As a lattice QCD based and via the QPM parametrized QCD equation of state, relevant at large energy densities, is found not to naturally match with a realistic hadron resonance gas equation of state, relevant at low energy densities, in the transition region, an interpolation procedure between both regimes becomes mandatory. This results in a whole family of equations of state, whose members deviate from each other only in the deconfinement transition region. In this way, possible uncertainties in the equation of state, arising in the transition region from uncertainties in, e. g., the numerical value of T_c or the quark mass dependence, are taken into account. In contrast, the equation of state in the region of large e is found to be rather robust. Exemplarily, transverse momentum spectra and differential elliptic flow are studied and the deduced v_2 is successfully compared with experimental data for strange baryons. Also, implications of variations in the transition region of the equation of state are discussed. In addition, larger initial energy densities assumingly relevant for LHC physics are considered, predicting substantially smaller differential elliptic flow but stronger radial flow for (directly emitted) strange baryons at LHC compared to RHIC. Finally, an equation of state based on most recent lattice QCD findings is discussed which does not require any interpolation prescription in the transition region.

Even though nonzero baryon-density effects are tiny in the midrapidity region for RHIC conditions, and assumed to be even smaller for LHC, the successful comparison of the quasiparticle model with lattice QCD results at finite n_B opens the avenue for providing a realistic QCD equation of state relevant for FAIR physics. This will be a task for future investigations. An important milestone concerning this issue, however, is already discussed within this work: One possibility of including QCD critical point phenomena into the model is presented. Indeed, the impact of the QCD critical point on the equation of state relevant for FAIR and on related detectable phase transition signatures are lively debated. Within the approach discussed in this thesis, critical point effects on the equation of state are found to be small except for chemical potentials equal or larger than the critical value. On the other hand, some susceptibilities start to develop pronounced structures in the vicinity of the critical point and in the region of first-order phase transitions. Thus, phenomena related to the critical point might lead to easily detectable signals

at FAIR depending, however, on the position of CP in the QCD phase diagram (supposed there is any critical point at all). In this respect, the impact of a critical point supplemented equation of state on hydrodynamic simulation results has to be examined in the future.

Immediate considerations to be performed in the near future concern predictions for or a direct systematic explanation of experimental data from the ALICE experiment at LHC. In particular, the hadrons' azimuthal distribution of momenta or transverse momentum spectra should be investigated. Interesting, also, is the implementation of heavier charm or bottom quark degrees of freedom which provide deeper insight into the process of hadronization or hierarchy phenomena. These plans highlight the importance of the tide interrelation between theory and experiment. In addition, a systematic extension of the employed ideal relativistic hydrodynamic approach to a causal viscous relativistic hydrodynamic description of heavy-ion collisions should be envisaged.

Appendix A   QCD and QCD Thermodynamics

A.1   Quantum chromodynamics

QCD is the accepted basic gauge field theory of strong interactions with quarks and gluons as fundamental degrees of freedom. Whereas quarks carry fractional electric and baryonic charges, the rather massive hadrons carry corresponding integer charges and are thought to be particle excitations in which quarks and gluons are confined. The classical Lagrange density underlying QCD reads [193]

$$\mathcal{L}_{\mathrm{QCD}} = \bar{\psi}\left(i\gamma^\alpha D_\alpha - m_0\right)\psi - \frac{1}{4}F_a^{\alpha\beta}F_{\alpha\beta}^a. \tag{A.1}$$

Here, ψ denotes the quark fields with flavour and colour indices being suppressed, $\bar{\psi} = \psi^\dagger \gamma^0$ the Dirac adjoint quark fields, $F^{\alpha\beta}$ is the field strength tensor defined as

$$F_{\mathrm{a}}^{\alpha\beta} = \partial^\alpha A_{\mathrm{a}}^\beta - \partial^\beta A_{\mathrm{a}}^\alpha + g f_{\mathrm{abc}} A^{\mathrm{b}\alpha} A^{\mathrm{c}\beta} \tag{A.2}$$

with gauge fields (gluons) A_{a}^α and m_0 is, in principle, a diagonal quark mass matrix.[1] The part in the classical Lagrangian including only $F_a^{\alpha\beta}F_{\alpha\beta}^a$ is called Yang-Mills Lagrangian [194]. The corresponding quantized theory is called pure gauge theory. The gauge covariant derivative D_α which reads

$$D_\alpha = \partial_\alpha - ig A_\alpha^{\mathrm{a}} T_{\mathrm{a}} \tag{A.3}$$

acting on the colour-triplet ($N_c = 3$) quark fields ensures minimal coupling between quarks and gluons with coupling strength g, where T_{a} denote the generators of the local $SU(3)$ gauge group in the fundamental representation forming a Lie algebra via

$$[T_{\mathrm{a}}, T_{\mathrm{b}}] = i f_{\mathrm{abc}} T^{\mathrm{c}} \tag{A.4}$$

with totally antisymmetric structure constants f_{abc}. Within this notation, the field strength tensor can be reformulated via

$$-ig F_{\mathrm{a}}^{\alpha\beta} T^{\mathrm{a}} = \left[D^\alpha, D^\beta\right]. \tag{A.5}$$

The non-Abelian $SU(3)$ gauge group character of Yang-Mills type underlying QCD becomes evident in the terms cubic and quartic in the gauge fields A_α entering $F_a^{\alpha\beta}F_{\alpha\beta}^a$ which represent self-interactions among the gluons carrying colour charge themselves. This is unlike to QED, which is an Abelian gauge theory, because the corresponding gauge bosons (photons) do not carry electromagnetic charge.

---

[1]While Greek indices α, $\beta = 0, ..., 3$ refer to the Minkowski space-time (spatial contributions are denoted by roman indices i, j, k), indices a, b, $c = 1...8$ are adjoint colour indices taking the eight coloured gauge bosons (gluons) realized in nature into account.

The canonical quantization of the classical theory requires additional gauge fixing contributions and furthermore a compensation of occuring unphysical degrees of freedom by introducing Fadeev-Popov [195] ghost fields in Eq. (A.1). QCD is a renormalizable gauge field theory and, thus, the strong coupling $\alpha_s = g^2/(4\pi)$ depends on the relevant momentum scale Q. In fact, as $Q \to \infty$ (or the separation distance between partons (quarks and gluons) vanishes) the strong coupling α_s becomes very small signalling asymptotic freedom [1,2] of quarks and gluons which has been experimentally observed in deep inelastic scattering experiments. On the other hand, as Q becomes small (or the separation distance between partons large), α_s becomes large resulting in the fact that only hadrons representing colour-singlet composite objects can be observed in a detector.

A.2   QCD thermodynamics and the QCD phase diagram

The equilibrium thermodynamics of QCD can most straightforwardly be analyzed when quantizing the classical Lagrangian in Eq. (A.1) via the path integral formalism as the path integral is closely related to the thermodynamic grand canonical partition function Z via [102, 103]

$$Z = \int \mathcal{D}\left[\psi, \bar{\psi}, A_\alpha^a\right] e^{-S_{\mathrm{QCD}}^E} \exp\left(\int\limits_0^{1/T} d\tau \int d^3x\, \mu\psi^\dagger\psi\right), \qquad (A.6)$$

describing ensembles in which the exchange of energy as well as of conserved charges with the environment is allowed. Here, S_{QCD}^E denotes the Euclidean action for QCD and the $d\tau d^3x$ integration is performed in Euclidean space. In Euclidean space, the time coordinate of Minkowski space is Wick rotated, $t \to -i\tau = -i(x_4)_E$, such that the Euclidean 4-vector is given by $(x_\mu)_E = (\tau, \vec{x})$. The Euclidean action is then defined as $S_{\mathrm{QCD}}^E = \int_0^{1/T} d\tau \int d^3x \mathcal{L}_{\mathrm{QCD}}^E$, where $\mathcal{L}_{\mathrm{QCD}}^E$ is obtained from $\mathcal{L}_{\mathrm{QCD}}$ in Eq. (A.1) (supplemented by gauge fixing and ghost field contributions) by formally replacing $\mathcal{L}_{\mathrm{QCD}} \to -\mathcal{L}_{\mathrm{QCD}}^E$ using the Euclidean space expressions instead (cf. [103]). Furthermore, the term $\mu\psi^\dagger\psi$ in Eq. (A.6) takes a finite chemical potential μ associated with a nonzero quark flavour net number density into account. Here, one unique quark chemical potential attributed to the quark fields ψ is assumed. In section 2.4, different and independent quark flavour chemical potentials μ_f are considered. From Z as basic quantity, other thermodynamic quantities follow from the thermodynamic consistency conditions defined in Eqs. (1.1) and (1.2). In addition, thermodynamic stability conditions (cf. Eqs. (5.9) and (5.10)) have to be fulfilled [188].

In chapter 1, a variety of different QCD matter phases in the phase diagram depending on temperature and baryo-chemical potential has already been mentioned (cf. also Figure 1.1). In addition, the nature of the transition between hadronic and QGP phases and topological features in the phase diagram have been addressed.

The phase structures of QCD are related to the symmetry properties of QCD such as chiral symmetry, colour symmetry or the $\mathcal{Z}_3$ centre symmetry and changes in these symmetry patterns. Symmetry changes are reflected in the behaviour of an order parameter. Depending on the region considered in thermodynamic parameter

space, an order parameter is nonzero in the region where the symmetry is broken (in this case, the system is not invariant under the symmetry transformation), and vanishes when the symmetry becomes restored [187]. In QCD, changes in the local $SU(3)$ colour symmetry are related to the occurance of colour superconducting phases, the $\mathcal{Z}_3$ centre symmetry is associated with the confinement/deconfinement phase transition and the spontaneous breaking of chiral symmetry is related to the generation of Goldstone bosons.

The $\mathcal{Z}_3$ centre symmetry is connected with the periodicity properties of quark (gluon) fields which must be antiperiodic (periodic) in Euclidean time with period $1/T$ in the path integral formulation of Z in Eq. (A.6). The $\mathcal{Z}_3$ centre symmetry is characterized by the fact that the path integral for Z is symmetric under discrete rotations of multiples of $\frac{2\pi}{3}$ [196]. In a pure $SU(3)$ gauge theory, the $\mathcal{Z}_3$ centre symmetry is an exact symmetry. The corresponding order parameter is the Polyakov loop defined by the trace Tr in colour space over the time-like Wilson line

$$\hat{\Phi} = \mathrm{Tr}\,\mathcal{P}\,exp\left(ig\int_0^{1/T} A_4(\tau, \vec{x})\,d\tau\right).\tag{A.7}$$

Here, $\mathcal{P}$ denotes the path ordering of the exponential, and $\hat{\Phi}$ is sometimes normalized by N_c.

Its thermal expectation value

$$\langle\hat{\Phi}\rangle \;=\; exp\left(-\frac{\mathcal{F}}{T}\right)\tag{A.8}$$

is connected to the free energy $\mathcal{F}$ of a static (infinitely heavy) test quark and illustrates the confinement property of QCD serving as an order parameter for the deconfinement transition. At low temperature T, colour is confined into hadrons and, thus, the free energy of the test quark is infinite implying $\langle\hat{\Phi}\rangle = 0$. Therefore, the $\mathcal{Z}_3$ centre symmetry is not broken in the hadronic phase. At high T, in contrast, colour is deconfined and accordingly $\mathcal{F}$ of the test quark is finite and thus $\langle\hat{\Phi}\rangle \neq 0$. This implies, that the $\mathcal{Z}_3$ centre symmetry is spontaneously broken. In the presence of dynamical quarks, the $\mathcal{Z}_3$ centre symmetry is explicitly broken but remains an approximate symmetry of QCD implying that $\langle\hat{\Phi}\rangle$ is also nonzero (but small) in the confined phase though, still, exhibits a drastic change from confined to deconfined QCD matter. This holds true when considering the behaviour with T at finite but not too large baryon density.

For vanishing individual quark masses m_q entering m_0, the classical Lagrangian in Eq. (A.1) is chirally symmetric. This implies that in the chiral limit, i. e. for $m_q = 0$, left- and right-handed quark fields of flavour q do not mix in the Lagrange density. However, in the quantized theory, the vacuum is not chirally symmetric. Thus, also at low temperature T, chiral symmetry is spontaneously broken which is connected to the existence of massless hadronic Goldstone bosons, whereas at high T chiral symmetry becomes restored. The corresponding order parameter for chiral symmetry restoration is the chiral condensate $\langle\bar{\psi}\psi\rangle$ being related to the pressure by [5]

$$\langle\bar{\psi}_q\psi_q\rangle \;=\; -\left.\frac{\partial p}{\partial m_q}\right|_{T,\mu}.\tag{A.9}$$

$\langle \bar{\psi}\psi \rangle$ is nonzero in the hadronic phase in which chiral symmetry is spontaneously broken (due to the strong interaction between quarks in the massive hadrons, confined quarks obtain an effective mass which is much larger than the mass of the corresponding current quarks) and $\langle \bar{\psi}\psi \rangle = 0$ in the chirally symmetric QGP phase.

In nature, however, quarks possess a finite mass such that chiral symmetry is explicitly broken. For instance, *up* and *down* quarks possess current quark masses of about $m_{u,d} \sim 5-10$ MeV. Thus, chiral symmetry is only approximately realized in nature implying that the Goldstone bosons (pions) obtain a finite mass. As a result, $\langle \bar{\psi}\psi \rangle$ is also nonzero in the QGP phase but, as in the case of the thermal expectation value of the Polyakov loop, depicts a significant change from the hadronic phase to the QGP.

The condensation of quark fields into colour Cooper pairs at low T and sufficiently large n_B is dominated by diquark correlations. Local $SU(3)$ colour symmetry is spontaneously broken which is signalled by the behaviour of the diquark condensate $\langle \psi\psi \rangle \neq 0$ serving as an order parameter. Depending on the colour-flavour-spin structure of the order parameter, many different ordered quark matter phases are possibly realized such as crystallized phases, colour superconducting phases [197–199] as well as strange quark matter [200–203]. In the latter case, chiral symmetry in the presence of *strange* quarks is broken by the colour-flavour locking mechanism at large baryon densities [204]. The value of the associated chemical potential is proportional to the scale of QCD, Λ_{QCD}.

The occurrence of a scale in QCD, $\Lambda_{\text{QCD}} \sim 200$ MeV, is related to another symmetry breaking. In the chiral limit, the classical Lagrangian in Eq. (A.1) possesses no dimensionful parameter and the theory is thus invariant under scale transformations of the fields (dilatational symmetry transformations). Finite, but small, quark masses break this symmetry explicitly, but still, it is approximately realized. By quantization of the theory, however, the symmetry is explicitly broken as the dilatational current is not conserved for $g \neq 0$. The latter is related to the expectation value of the trace of the energy-momentum tensor which serves as order parameter. The thermal contribution to this trace is related to standard thermodynamic quantities at $\mu = 0$, $\Theta^\mu_\mu(T) = e - 3p$, while vacuum contributions are related to quark and gluon condensates. A symmetry breaking by quantum effects is called an anomaly. In the conformal limit, one finds $e = 3p$. QCD, however, shows large deviations from $\Theta^\mu_\mu(T) = 0$ in the vicinity of T_c (cf. section 3.1.2) approaching zero only asymptotically as $e - 3p$ is controlled by the logarithmic running of the QCD coupling [205] at large T.

The nature of the transitions between the different QCD phases - whether they are of first-order, second-order or rather crossover type of transformations - depends decisively on the number of active quark flavours N_f as well as the quark mass values. Applying universality arguments when examining the mentioned QCD symmetries, predictions on the order of the transitions can be made.

First, zero net baryon density is considered. In pure gauge theory, i. e. $N_f = 0$ ($m_{u,d,s}$ are infinite), the transition between hadronic phase and QGP phase is of first-order [206]. This was confirmed in first-principle lattice QCD calculations in [138, 207]. Similarly, for $N_f = 3$ in the chiral limit, i. e. $m_u = m_d = m_s = 0$, the transition is also of first-order [208]. Increasing the quark mass of the degenerate

quarks, the transition will eventually become a crossover. Both regions, first-order and crossover transformation, must therefore be separated by a second-order transition at a critical quark mass m^c. Distinguishing between $m_u = m_d$ and m_s, a whole line of second-order transitions emerges separating crossover and first-order transition regions which must end in a tricritical point (TCP), where three different phases coexist, at $m_u = m_d = 0$ and a critical value of the *strange* quark mass parameter m_s^c [209].

In the case $N_f = 2$ ($m_s \rightarrow \infty$) in the chiral limit, i. e. $m_u = m_d = 0$, the transition might be second-order [209] but could be of first-order as well. In lattice QCD calculations [210, 211] for $N_f = 2$ with $m_u = m_d \neq 0$, the transformation was found to be of crossover type. In [212, 213], it was shown that for $m_s \sim \mathcal{O}(150 \text{ MeV})$ the critical mass is $m_s^c \approx \frac{1}{2}m_s$. Thus, in the physical case of $N_f = 2 + 1$ with the quark masses realized in nature, the transformation between hadronic phase and QGP phase should be a crossover [7, 212].

The actual value of the transition temperature, T_c, depends decisively on N_f and the considered quark masses [6]. T_c is determined in first-principle lattice QCD calculations by locating the onset of rapid changes in the order parameters $\langle \hat{\Phi} \rangle$ and $\langle \bar{\psi}\psi \rangle$ with temperature. These rapid changes are signalled by pronounced peak structures in the corresponding susceptibilities which represent second-order derivatives of the thermodynamic potential. Astonishingly, the rapid changes in the order parameters for both, deconfinement transition and chiral symmetry restoration, seem to be located at the same pseudo-critical temperature [8].

The reported numerical values (cf. chapter 1) read $T_c \simeq 170$ MeV for $N_f = 2 + 1$, $T_c \simeq 175$ MeV for $N_f = 2$ and $T_c = 271$ MeV for pure gauge theory in earlier calculations [6, 8, 9], while recently a larger $T_c = 192$ MeV for $N_f = 2 + 1$ was found in [10]. Nonetheless, the value of T_c for $N_f = 2 + 1$ is currently lively debated [214, 215] as in [214] a different $T_c = 151$ MeV is stated. In fact, in [214] even different values for the transition temperature of deconfinement phase transition and chiral symmetry restoration are reported, as the found peak positions for Polyakov loop associated susceptibility and chiral susceptibility read $T_c = 176$ MeV and $T_c = 151$ MeV, respectively. However, since the transformation is an analytic crossover, different T_c for different observables are not unexpected.

Considering nonzero baryon density, the transition temperature decreases with increasing μ_B [164, 182]. Even though at moderate n_B the transformation is an analytic crossover, rapid changes in thermodynamic quantities, such as s or e, or peaks in suitable susceptibilities allow for a determination of the pseudo-critical line. At large n_B, the order of the transition between the hadronic world and other ordered quark matter phases is less firm known. In fact, depending on the examined model, the transition is of first-order in the MIT bag model, linear σ models [216] and Random Matrix models [217, 218], while it is of first- [216, 219] or of second-order [220] in the Nambu–Jona-Lasinio model depending on the choice of parameters. (For an overview of results from various models cf. [14, 43] and references therein.) However, it is presently accepted that in the case of $N_f = 2 + 1$ with physical quark masses the transition at large baryo-chemical potential is of first-order, even though this conjecture is questioned [221, 222] quite recently.

It is obvious that, when accepting a first-order phase transition for large n_B

while the transition is a crossover type of transformation at small baryon density, by continuity, the line of first-order phase transitions emerging at large μ_B and sufficiently small T must end in a second-order phase transition point at a specific T^E and μ_B^E, the QCD critical point. This means, that for $\mu_B < \mu_B^E$ there is no true order parameter which prevents the analytic connectivity of hadronic and QGP phases as the two different phases are not distinguishable by an exact symmetry. Note that such a feature is common to liquids, including water.

At a second-order phase transition point, an order parameter becomes non-analytic which is related to the divergence of the correlation length. The correlation length of fluctuations is of the order of the characteristic microscopic length scale, $\Lambda_{\rm QCD}^{-1}$. At CP, fluctuations in thermodynamic quantities should be sizeably increased and, furthermore, the system becomes scale invariant. Thermodynamic quantities are, then, described by critical exponents whose numerical values can be evaluated from renormalization group methods. Critical exponents are unique for a certain universality class where universality classes assemble different physical systems with the same global symmetries and the same pattern of breaking and restoring these symmetries. QCD, for instance, belongs to the universality class of the 3-dimensional Ising model [14, 43, 218] as far as static critical phenomena are concerned which is the same as for ferromagnetic systems [187]. This was verified in first-principle lattice QCD calculations of the critical exponent for the volume dependence of the Binder cumulant of the chiral condensate [124, 223]. For a classification in dynamic universality classes cf. [224] and for a discussion of dynamical critical properties of QCD cf. [225, 226].

If in nature zero *up* and *down* quark masses would be realized, the QCD phase diagram would look somewhat different [14, 43]. At small baryon density the transition would be of second-order turning into a line of first-order transitions for larger n_B at a tricritical point belonging to the universality class of the Heisenberg $\mathcal{O}(4)$ model in 3 dimensions [208]. The location of the TCP in the T - μ_B thermodynamic parameter space depends on the *strange* quark mass m_s.

For nonzero m_u and m_d, however, the second-order phase transitions turn into crossover type of transformations ending in a CP whose location decisively depends on the explicit quark mass values [124, 227], most notably on m_s. Thus, depending on the value of $m_u = m_d$, a whole line of critical points exists in the T - μ_B thermodynamic parameter space which eventually approaches the TCP for $m_u = m_d \to 0$. As the location of the TCP, however, is strongly affected by m_s, different m_s also influence the location of the critical point for given $m_u = m_d$.

In lattice QCD calculations the QCD CP was found to be located at $T^E = 162$ MeV and $\mu_B^E = 360$ MeV [182] for approximately physical quark masses (cf. chapter 5). Earlier calculations with three times larger light quark masses reported $T^E = 160$ MeV and a larger $\mu_B^E = 725$ MeV [228]. Note that the results in [182] miss a proper continuum limit extrapolation, whereas in [228] both, thermodynamic and continuum limit extrapolations, are missing. Various other numerical calculations [143, 229] as well as model predictions differ in the exact location of the QCD critical point. (For an overview cf. [14] and references therein.)

The location of CP can be determined by the method of Lee-Yang zeros [230–232], making use of the connection between thermodynamic singularities in the

complex thermodynamic parameter space and zeros of the partition function Z. For a system of finite volume, the number of zeros is finite, though, linearly increasing with V. Varying T and μ_B and increasing V, eventually zeros approach the real axis, indicating the presence of a phase transition. In the thermodynamic limit, $V \to \infty$, the conglomeration of zeros develops into a cut in the complex plane, which eventually touches (crosses) the real axis, indicating a second- (first-) order phase transition.

For finite isovector chemical potential, μ_I, i. e. for different *up* and *down* quark flavour chemical potentials, the pseudo-critical line can split into two resulting in two different critical points [233–235]. This result, though, depends on the strength of the flavour mixing [236].

A.3   Access to the QCD equation of state

The equation of state of QCD matter can be obtained from systematic approaches to QCD such as lattice QCD calculations, perturbative QCD or chiral perturbation theory.

In lattice QCD calculations, a discretized version of the full QCD partition function Z in Eq. (A.6) is evaluated by Monte-Carlo sampling methods [8]. Note that the lattice realization of Z is not unique and depends on the employed regularization of the QCD action. Although this technique can be applied in the non-perturbative regime, in principle, standard Monte-Carlo sampling is not possible for computing time-dependent quantities, such as reaction rates, or for thermodynamics at finite chemical potential. The latter problem, known as the sign problem which is caused by the non-positive definite fermion determinant at finite μ, could be circumwent by various approaches, recently. Either from the overlap improving multi-parameter reweighting technique [237], a multi-parameter reweighting with Taylor expansion [164] or the method of imaginary chemical potential [122, 123, 126, 238], the QCD EoS is known in some region of T and small μ. (For an overview, cf. [163, 239].) Furthermore, lattice QCD calculations are limited when considering quantities which are sensitive to small quark masses, like the chiral condensate. In fact, decreasing the quark mass parameters dramatically increases the computational effort. Apart from that, as QCD thermodynamics is studied at finite extensions in space and time, profound thermodynamic and continuum limit extrapolations have to be performed [138, 240]. A detailed discussion of this problem is relegated to Appendix C.

Perturbative QCD is applicable for small couplings α_s, i. e. for large temperatures and/or large chemical potentials, where non-perturbative aspects of QCD, such as confinement, become negligible. However, perturbative expansions are hampered by infrared divergencies in the magnetic sector of QCD which lead to a breakdown of the loop expansion [241, 242]. In the case of the pressure p, this happens at order $\mathcal{O}(g^6)$. The maximum exactly attainable order $\mathcal{O}(g^6 \ln 1/g)$ was computed for p in [243, 244] and for the quark number susceptibility in [245] for some T and μ and zero quark masses. For arbitrary T and μ, the perturbative expansion of p is known up to $\mathcal{O}(g^4)$, for finite quark masses only up to $\mathcal{O}(g^2)$. In contrast, in the large N_f limit, it is known to arbitrary orders [246–249].

Furthermore, the perturbative expansion exhibits only a slow convergence, besides the fact, that g is not really small up to $\mathcal{O}(100\,T_c)$. Thus, and also because naive loop expansions are not equivalent to expansions in α_s, resummation techniques become necessary which reorganize the perturbative expansion and improve convergence properties. Among these methods, screened perturbation theory [250–252], hard thermal loop perturbation theory [253–257] and ϕ-derivable approximation schemes [107–110, 116] have to be mentioned. (For an overview, cf. [13, 111, 258] and references therein.) In these resummations, higher-order contributions are already involved in lower orders of the expansion. Note, however, that in none of these approaches the magnetic sector is properly included. Success in describing lattice QCD results of thermodynamic quantities with resummation techniques was achieved for temperatures $T > 2\,T_c$ [109].

In contrast, chiral perturbation theory is applicable at low T and low μ, where no resonance contributions start to affect the physics. An introductory overview can be found in [259].

In the regions of the QCD phase diagram, where the above mentioned systematic approaches do not work, phenomenological models are used to extract the properties of strongly interacting matter. The advantage of models is that their region of applicability overlaps with the realms where first-principle approaches are valid. This, by comparison, gives restrictions in the model parameters, such that information gained by systematic approaches can be extrapolated into regions where the latter cannot be applied. Here, hadron resonance gas model [132, 133], Nambu–Jona-Lasinio models or quark-meson models and Polyakov loop extensions thereof [152, 260, 261], quasiparticle models [77, 78, 80, 84–87, 262] and models including quark bound states [263] have to be mentioned. Quasiparticle models can be used above but also slightly below T_c by making phenomenologically a large number of degrees of freedom very massive and, thus, thermodynamically inactive, such that a few massive excitations suffice to reproduce lattice QCD thermodynamics. This picture is not too distinct from regrouping several resonances in the HRG into a few representative effective excitations. For a more extreme point of view on quark-hadron duality, cf. [134].

Nonetheless, for the ultimate description of the very nature of the quark-gluon plasma one has to know correlations and spectral functions, propagators and related dispersion relations. Such information is still fairly scarce, but starts accumulating, in particular in first-principle lattice QCD calculations [264–266].

Recently, another approach for considering QCD has become very popular making use of the correspondence between strongly coupled gauge field theories and weakly coupled gravity theories [267–269]. In the so called AdS/CFT duality formalism, however, no exact dual to QCD has been found, yet.

Appendix B   Flow Equations

In this Appendix, the flow equations for a system with one independent chemical potential (Appendix B.1), with imaginary chemical potential (Appendix B.2) and with two independent chemical potentials (Appendix B.3) are summarized. In addition, in Appendix B.3 limitations of the approach presented in section 2.4 are discussed. One possibility of circumventing these limitations by employing an alternative ansatz for the quasiparticle dispersion relations is outlined in Appendix B.4.

B.1   One independent chemical potential

Here, the flow equation for the plasma considered in section 2.1 with two light degenerate quarks and one heavier quark ($N_f = 2 + 1$) with only one independent quark chemical potential $\mu_u = \mu_d = \mu_q = \mu$ and $\mu_s = 0$ is explicitly noted. In this case, $n_s = 0$ and $n_u = n_d$ with $n_q = n_u + n_d$, since the mass symmetric case $m_u = m_d \equiv m_q$ is examined which results in $\omega_u = \omega_d \equiv \omega_q(k, M_q(T, \mu))$ because $M_u^2 = M_d^2 \equiv M_q^2$. Furthermore, one defines $d_q = 2N_c N_q$, where $N_q = N_f$ denotes the number of degenerate (light) quark flavours. In this way, systems involving two or four degenerate quark flavours without an additional heavier quark flavour are included in the following expressions by setting $d_s = 0$, $N_f = N_q$ and N_q to the appropriate value.

The derivatives of $M_i^2(T, \mu)$ entering Eqs. (2.9) and (2.10) in section 2.1 using the expressions in Eqs. (2.14)-(2.17) with replaced g^2 by $G^2(T, \mu)$ read for $l = u, d, s$

$$
\left. \frac{\partial M_l^2(T, \mu)}{\partial T} \right|_\mu = 2\xi_l m_l + 2\xi_l M_{+,l}(T, \mu)
$$

$$
+ \frac{m_l}{6M_{+,l}(T, \mu)} \left(2TG^2(T, \mu) + \left[T^2 + \frac{\mu_l^2}{\pi^2} \right] \left. \frac{\partial G^2(T, \mu)}{\partial T} \right|_\mu \right)
$$

$$
+ \frac{1}{3} \left(2TG^2(T, \mu) + \left[T^2 + \frac{\mu_l^2}{\pi^2} \right] \left. \frac{\partial G^2(T, \mu)}{\partial T} \right|_\mu \right), \qquad \text{(B.1)}
$$

$$
\left. \frac{\partial M_g^2(T, \mu)}{\partial T} \right|_\mu = \frac{1}{6}[6 + N_f]TG^2(T, \mu)
$$

$$
+ \frac{1}{12} \left([6 + N_f]T^2 + 3N_f \frac{\mu^2}{\pi^2} \right) \left. \frac{\partial G^2(T, \mu)}{\partial T} \right|_\mu, \qquad \text{(B.2)}
$$

$$
\left. \frac{\partial M_l^2(T, \mu)}{\partial \mu} \right|_T = \frac{m_l}{6M_{+,l}(T, \mu)} \left(2\frac{\mu_l}{\pi^2}G^2(T, \mu) + \left[T^2 + \frac{\mu_l^2}{\pi^2} \right] \left. \frac{\partial G^2(T, \mu)}{\partial \mu} \right|_T \right)
$$

$$
+ \frac{1}{3} \left(2\frac{\mu_l}{\pi^2}G^2(T, \mu) + \left[T^2 + \frac{\mu_l^2}{\pi^2} \right] \left. \frac{\partial G^2(T, \mu)}{\partial \mu} \right|_T \right), \qquad \text{(B.3)}
$$

$$\left.\frac{\partial M_g^2(T,\mu)}{\partial \mu}\right|_T = \frac{1}{2}N_f\frac{\mu}{\pi^2}G^2(T,\mu)$$

$$+\frac{1}{12}\left([6+N_f]T^2+3N_f\frac{\mu^2}{\pi^2}\right)\left.\frac{\partial G^2(T,\mu)}{\partial \mu}\right|_T. \qquad (B.4)$$

These expressions include the possibility of considering temperature dependent bare quark masses $m_l(T)=\xi_l T$ as employed in some lattice QCD calculations. (In the mass symmetric case of two degenerate light quarks $\xi_u=\xi_d=\xi_q$.) If, in contrast, constant bare quark masses are considered, the corresponding expressions given in Eqs. (B.1)-(B.4) change with $\xi_l=0$ while in the chiral limit, $\xi_l=0$ and $m_l=0$ must be set. These conventions apply for the entire Appendix B.

For completeness, higher-order derivatives of $M_q^2(T,\mu)$ with respect to the chemical potentials (μ_q,μ_I) or (μ_u,μ_d) as needed in section 3.2 for higher-order coefficients are summarized reading

$$\left.\frac{\partial^2 M_q^2}{\partial \mu_q^2}\right|_{\mu_q=\mu_I=0} = \frac{m_q}{\tilde{M}_{+,q}}\left(\frac{1}{3\pi^2}G^2(T)+\frac{1}{6}T^2\left.\frac{\partial^2 G^2}{\partial \mu_q^2}\right|_{\mu_q=\mu_I=0}\right)$$

$$+\frac{2}{3\pi^2}G^2(T)+\frac{1}{3}T^2\left.\frac{\partial^2 G^2}{\partial \mu_q^2}\right|_{\mu_q=\mu_I=0}, \qquad (B.5)$$

where the second derivative of G^2 with respect to μ_q is given in Eq. (2.72),

$$\left.\frac{\partial^2 M_q^2}{\partial \mu_u^2}\right|_{\mu_u=\mu_d=0} = \frac{m_q}{\tilde{M}_{+,q}}\left(\frac{1}{3\pi^2}G^2(T)+\frac{1}{6}T^2\left.\frac{\partial^2 G^2}{\partial \mu_u^2}\right|_{\mu_u=\mu_d=0}\right)$$

$$+\frac{2}{3\pi^2}G^2(T)+\frac{1}{3}T^2\left.\frac{\partial^2 G^2}{\partial \mu_u^2}\right|_{\mu_u=\mu_d=0}, \qquad (B.6)$$

where the second derivative of G^2 with respect to μ_u is given in Eq. (2.73) and

$$\left.\frac{\partial^4 M_q^2}{\partial \mu_q^4}\right|_{\mu_q=\mu_I=0} = \frac{m_q}{\tilde{M}_{+,q}}\left(\frac{2}{\pi^2}\left.\frac{\partial^2 G^2}{\partial \mu_q^2}\right|_{\mu_q=\mu_I=0}+\frac{1}{6}T^2\left.\frac{\partial^4 G^2}{\partial \mu_q^4}\right|_{\mu_q=\mu_I=0}\right)$$

$$+\frac{4}{\pi^2}\left.\frac{\partial^2 G^2}{\partial \mu_q^2}\right|_{\mu_q=\mu_I=0}+\frac{1}{3}T^2\left.\frac{\partial^4 G^2}{\partial \mu_q^4}\right|_{\mu_q=\mu_I=0}$$

$$-\frac{3}{2}\frac{m_q}{\tilde{M}_{+,q}^3}\left(\frac{1}{3\pi^2}G^2(T)+\frac{1}{6}T^2\left.\frac{\partial^2 G^2}{\partial \mu_q^2}\right|_{\mu_q=\mu_I=0}\right)^2, \quad (B.7)$$

with

$$\tilde{M}_{+,q}=M_{+,q}(T,\mu_q=0,\mu_I=0)=\sqrt{\frac{1}{6}T^2G^2(T)} \qquad (B.8)$$

and the fourth derivative of G^2 with respect to μ_q is schematically summarized in [90].

Now, the flow equation is specified. Starting from Maxwell's relation in Eq. (2.18), the explicit T and μ derivatives of s and n_q vanish whereas the remaining contributions stem from derivatives with respect to $M_i^2(T,\mu)$. Using the expressions found in Eqs. (B.1)-(B.4), one can arrange the occuring terms to account

for different derivatives of the effective coupling. In this way, a partial differential equation for $G^2(T, \mu)$ is found viz

$$a_T(T, \mu, G^2)\frac{\partial G^2}{\partial T} + a_\mu(T, \mu, G^2)\frac{\partial G^2}{\partial \mu} = b(T, \mu, G^2)\,, \qquad (\text{B.9})$$

which is of first-order and linear in the derivatives but non-linear in the effective coupling itself. The coefficients of this flow equation read

$$a_T = -\left[T^2 + \frac{\mu^2}{\pi^2}\right]\left(m_q\sqrt{\frac{1}{6\left[T^2 + \frac{\mu^2}{\pi^2}\right]G^2(T, \mu)}} + \frac{1}{3}\right)\mathcal{J}_q\,, \qquad (\text{B.10})$$

$$\begin{aligned} a_\mu = {}& \left[T^2 + \frac{\mu^2}{\pi^2}\right]\left(m_q\sqrt{\frac{1}{6\left[T^2 + \frac{\mu^2}{\pi^2}\right]G^2(T, \mu)}} + \frac{1}{3}\right)\mathcal{I}_q \\ & + \frac{1}{12}\left([6 + N_f]T^2 + 3N_f\frac{\mu^2}{\pi^2}\right)\mathcal{I}_g \\ & + \left(m_s\sqrt{\frac{T^2}{6G^2(T, \mu)}} + \frac{1}{3}T^2\right)\mathcal{I}_s\,, \qquad (\text{B.11}) \end{aligned}$$

$$\begin{aligned} b = {}& \left(2\xi_q\sqrt{\frac{1}{6}\left[T^2 + \frac{\mu^2}{\pi^2}\right]G^2(T, \mu)}\right. \\ & + 2TG^2(T, \mu)m_q\sqrt{\frac{1}{6\left[T^2 + \frac{\mu^2}{\pi^2}\right]G^2(T, \mu)}} \\ & \left. + 2\xi_q m_q + \frac{2}{3}TG^2(T, \mu)\right)\mathcal{J}_q \\ & - \frac{N_f}{2}\frac{\mu}{\pi^2}G^2(T, \mu)\mathcal{I}_g \\ & - \left(m_q\sqrt{\frac{1}{6\left[T^2 + \frac{\mu^2}{\pi^2}\right]G^2(T, \mu)}} + \frac{1}{3}\right)2\frac{\mu}{\pi^2}G^2(T, \mu)\mathcal{I}_q\,. \qquad (\text{B.12}) \end{aligned}$$

The appearing integrals are given by

$$\mathcal{I}_g = \frac{d_g}{\pi^2}\int_0^\infty\frac{dk\,k^2}{T\omega_g\left[e^{\omega_g/T} - 1\right]}\left(1 - \frac{L_g}{\omega_g}\left\{\frac{1}{\omega_g} + \frac{e^{\omega_g/T}}{T\left[e^{\omega_g/T} - 1\right]}\right\}\right)\,, \quad (\text{B.13})$$

$$\mathcal{I}_s = \frac{d_s}{\pi^2}\int_0^\infty\frac{dk\,k^2}{T\omega_s\left[e^{\omega_s/T} + 1\right]}\left(1 - \frac{L_s}{\omega_s}\left\{\frac{1}{\omega_s} + \frac{e^{\omega_s/T}}{T\left[e^{\omega_s/T} + 1\right]}\right\}\right)\,, \quad (\text{B.14})$$

$$
\mathcal{I}_q = \frac{d_q}{2\pi^2} \int\limits_0^\infty dk \Bigg(\frac{k^2}{T\omega_q \left[e^{\{\omega_q-\mu\}/T} + 1 \right]} \Bigg\{ 1 - \frac{L_q}{\omega_q} \Bigg(\frac{1}{\omega_q}
$$

$$
+ \frac{e^{\{\omega_q-\mu\}/T}}{T\left[e^{\{\omega_q-\mu\}/T} + 1 \right]} \Bigg) + \frac{\mu}{2T} \frac{e^{\{\omega_q-\mu\}/T}}{\left[e^{\{\omega_q-\mu\}/T} + 1 \right]} \Bigg\}
$$

$$
+ \frac{k^2}{T\omega_q \left[e^{\{\omega_q+\mu\}/T} + 1 \right]} \Bigg\{ 1 - \frac{L_q}{\omega_q} \Bigg(\frac{1}{\omega_q}
$$

$$
+ \frac{e^{\{\omega_q+\mu\}/T}}{T\left[e^{\{\omega_q+\mu\}/T} + 1 \right]} \Bigg) - \frac{\mu}{2T} \frac{e^{\{\omega_q+\mu\}/T}}{\left[e^{\{\omega_q+\mu\}/T} + 1 \right]} \Bigg\} \Bigg) , \tag{B.15}
$$

$$
\mathcal{J}_q = \frac{d_q}{2\pi^2} \int\limits_0^\infty dk \frac{k^2}{2T\omega_q} \left(\frac{e^{\{\omega_q+\mu\}/T}}{\left[e^{\{\omega_q+\mu\}/T} + 1 \right]^2} - \frac{e^{\{\omega_q-\mu\}/T}}{\left[e^{\{\omega_q-\mu\}/T} + 1 \right]^2} \right) , \tag{B.16}
$$

where $L_i = \frac{2}{3}k^2 + \frac{1}{2}M_i^2$.

By introducing a curve parameter x, the flow equation in Eq. (B.9) can be solved, because the effective coupling becomes a function of x through $G^2(x) = G^2(T(x), \mu(x))$. Thus, for the total derivative of G^2 with respect to x one obtains

$$
\frac{dG^2(x)}{dx} = \frac{\partial G^2}{\partial T} \frac{dT}{dx} + \frac{\partial G^2}{\partial \mu} \frac{d\mu}{dx} . \tag{B.17}
$$

Comparing this result with Eq. (B.9), the quasilinear partial differential equation can be reduced to a system of three linear coupled ordinary differential equations, which can easily be numerically integrated

$$
\frac{dT}{dx} = -a_T , \tag{B.18}
$$

$$
\frac{d\mu}{dx} = -a_\mu , \tag{B.19}
$$

$$
\frac{dG^2}{dx} = -b . \tag{B.20}
$$

The coefficients in Eqs. (B.10)-(B.12) obey the following properties: $a_T(T, \mu \to 0) = 0$, $a_\mu(T \to 0, \mu) = 0$ and $b(T, \mu \to 0) = 0$ while $a_\mu(T, \mu \to 0) \neq 0$. This means that the characteristic curves representing solutions to Eqs. (B.18)-(B.20) end perpendicularly into temperature and chemical potential axes.

B.2   Imaginary chemical potential

In a similar way, by imposing Maxwell's relation on the pressure but now for imaginary chemical potential as defined in Eqs. (2.45)-(2.47), the flow equation for imaginary chemical potential reads

$$
a_T(T, i\mu_i, G^2) \frac{\partial G^2}{\partial T} + a_{\mu_i}(T, i\mu_i, G^2) \frac{\partial G^2}{\partial \mu_i} = b(T, i\mu_i, G^2) , \tag{B.21}
$$

which is solved for $G^2(T, i\mu_i)$ by the method of characteristics described in Appendix B.1. The coefficients a_T, a_{μ_i} and b depending on T, μ_i and $G^2(T, i\mu_i)$ read

for the system with $N_f = 4$ degenerate quark flavours considered in section 2.3

$$
\begin{aligned}
b \;=\; & \left(2\xi_q \sqrt{\frac{1}{6}\left[T^2 - \frac{\mu_i^2}{\pi^2}\right] G^2(T, i\mu_i)} \right. \\
& + 2T G^2(T, i\mu_i) m_q \sqrt{\frac{1}{6\left[T^2 - \frac{\mu_i^2}{\pi^2}\right] G^2(T, i\mu_i)}} \\
& \left. + 2\xi_q m_q + \frac{2}{3} T G^2(T, i\mu_i) \right) \mathcal{I}_1 \\
& - \frac{N_f}{2}\frac{\mu_i}{\pi^2} G^2(T, i\mu_i) \mathcal{I}_2 \\
& - \left(m_q \sqrt{\frac{1}{6\left[T^2 - \frac{\mu_i^2}{\pi^2}\right] G^2(T, i\mu_i)}} + \frac{1}{3} \right) 2\frac{\mu_i}{\pi^2} G^2(T, i\mu_i) \mathcal{I}_3 \,, \quad \text{(B.22)}
\end{aligned}
$$

$$
a_T \;=\; -\left[T^2 - \frac{\mu_i^2}{\pi^2}\right] \left(\frac{1}{3} + m_q \sqrt{\frac{1}{6\left[T^2 - \frac{\mu_i^2}{\pi^2}\right] G^2(T, i\mu_i)}} \right) \mathcal{I}_1 \,, \qquad \text{(B.23)}
$$

$$
\begin{aligned}
a_{\mu_i} \;=\; & -\frac{1}{12}\left([6 + N_f] T^2 - 3N_f \frac{\mu_i^2}{\pi^2} \right) \mathcal{I}_2 \\
& - \left[T^2 - \frac{\mu_i^2}{\pi^2}\right] \left(\frac{1}{3} + m_q \sqrt{\frac{1}{6\left[T^2 - \frac{\mu_i^2}{\pi^2}\right] G^2(T, i\mu_i)}} \right) \mathcal{I}_3 \,. \qquad \text{(B.24)}
\end{aligned}
$$

As in Appendix B.1, possible temperature dependent bare quark masses are included. Comparing Eqs. (B.22)-(B.24) with Eqs. (B.10)-(B.12), changes in signs in front of explicitly chemical potential dependent terms become obvious, signalling the influence of imaginary chemical potential on the flow equation. The entering integral expressions are explicitly given by

$$
\mathcal{I}_1 \;=\; \frac{d_q}{2\pi^2 T} \int_0^\infty dk \frac{k^2}{\omega_q} \frac{\left(e^{\omega_q/T}\sin(\mu_i/T) - e^{3\omega_q/T}\sin(\mu_i/T)\right)}{\left[e^{2\omega_q/T} + 2e^{\omega_q/T}\cos(\mu_i/T) + 1\right]^2} \,, \qquad \text{(B.25)}
$$

$$
\mathcal{I}_2 \;=\; \frac{d_g}{\pi^2 T} \int_0^\infty dk \frac{k^2}{\omega_g} \frac{1}{\left[e^{\omega_g/T} - 1\right]} \left(1 - \frac{L_g}{\omega_g^2}\left\{ 1 + \frac{\omega_g}{T}\frac{e^{\omega_g/T}}{\left[e^{\omega_g/T} - 1\right]} \right\} \right) \,, \qquad \text{(B.26)}
$$

$$
\begin{aligned}
\mathcal{I}_3 \;=\; & \frac{d_q}{2\pi^2 T} \int_0^\infty dk \frac{k^2}{\omega_q} \left(\frac{\left(2e^{\omega_q/T}\cos(\mu_i/T) + 2\right)}{\left[e^{2\omega_q/T} + 2e^{\omega_q/T}\cos(\mu_i/T) + 1\right]} \left\{ 1 - \frac{L_q}{\omega_q^2} \right\} \right. \\
& - \frac{L_q}{\omega_q T} \frac{\left(2e^{3\omega_q/T}\cos(\mu_i/T) + 4e^{2\omega_q/T} + 2e^{\omega_q/T}\cos(\mu_i/T)\right)}{\left[e^{2\omega_q/T} + 2e^{\omega_q/T}\cos(\mu_i/T) + 1\right]^2} \\
& \left. + \frac{\mu_i}{T} \frac{\left(e^{\omega_q/T}\sin(\mu_i/T) - e^{3\omega_q/T}\sin(\mu_i/T)\right)}{\left[e^{2\omega_q/T} + 2e^{\omega_q/T}\cos(\mu_i/T) + 1\right]^2} \right) \,. \\
& \hspace{10cm} \text{(B.27)}
\end{aligned}
$$

B.3 Two independent chemical potentials

The coefficients entering Eqs. (2.65)-(2.67) considering a system with $N_f = 2$ degenerate quark flavours as in section 2.4 read

$$A_1 = \mathcal{I}_3 \frac{1}{12} \left([6 + N_f]T^2 + \frac{6}{\pi^2} \left[\mu_q^2 + \mu_I^2 \right] \right)$$

$$+ \mathcal{I}_4 \left(T^2 + \frac{1}{\pi^2} [\mu_q + \mu_I]^2 \right) \left(\frac{1}{3} + \frac{1}{6} \frac{m_u}{M_{+,u}} \right)$$

$$+ \mathcal{I}_5 \left(T^2 + \frac{1}{\pi^2} [\mu_q - \mu_I]^2 \right) \left(\frac{1}{3} + \frac{1}{6} \frac{m_d}{M_{+,d}} \right) , \qquad \text{(B.28)}$$

$$B_1 = -\mathcal{I}_1 \left(T^2 + \frac{1}{\pi^2} [\mu_q + \mu_I]^2 \right) \left(\frac{1}{3} + \frac{1}{6} \frac{m_u}{M_{+,u}} \right)$$

$$+ \mathcal{I}_2 \left(T^2 + \frac{1}{\pi^2} [\mu_q - \mu_I]^2 \right) \left(\frac{1}{3} + \frac{1}{6} \frac{m_d}{M_{+,d}} \right) , \qquad \text{(B.29)}$$

$$C_1 = -\mathcal{I}_3 \frac{\mu_I}{\pi^2} G^2 - \mathcal{I}_4 \frac{1}{3\pi^2} [\mu_q + \mu_I] G^2 \left(2 + \frac{m_u}{M_{+,u}} \right)$$

$$+ \mathcal{I}_5 \frac{1}{3\pi^2} [\mu_q - \mu_I] G^2 \left(2 + \frac{m_d}{M_{+,d}} \right)$$

$$+ \mathcal{I}_1 \left(2\xi_u m_u + 2\xi_u M_{+,u} + \frac{1}{3} \frac{m_u}{M_{+,u}} TG^2 + \frac{2}{3} TG^2 \right)$$

$$- \mathcal{I}_2 \left(2\xi_d m_d + 2\xi_d M_{+,d} + \frac{1}{3} \frac{m_d}{M_{+,d}} TG^2 + \frac{2}{3} TG^2 \right) , \qquad \text{(B.30)}$$

$$A_2 = \mathcal{I}_3 \frac{1}{12} \left([6 + N_f]T^2 + \frac{6}{\pi^2} \left[\mu_q^2 + \mu_I^2 \right] \right)$$

$$+ \mathcal{I}_4 \left(T^2 + \frac{1}{\pi^2} [\mu_q + \mu_I]^2 \right) \left(\frac{1}{3} + \frac{1}{6} \frac{m_u}{M_{+,u}} \right)$$

$$+ \mathcal{I}_5 \left(T^2 + \frac{1}{\pi^2} [\mu_q - \mu_I]^2 \right) \left(\frac{1}{3} + \frac{1}{6} \frac{m_d}{M_{+,d}} \right) , \qquad \text{(B.31)}$$

$$B_2 = -\mathcal{I}_1 \left(T^2 + \frac{1}{\pi^2} [\mu_q + \mu_I]^2 \right) \left(\frac{1}{3} + \frac{1}{6} \frac{m_u}{M_{+,u}} \right)$$

$$- \mathcal{I}_2 \left(T^2 + \frac{1}{\pi^2} [\mu_q - \mu_I]^2 \right) \left(\frac{1}{3} + \frac{1}{6} \frac{m_d}{M_{+,d}} \right) , \qquad \text{(B.32)}$$

$$C_2 = -\mathcal{I}_3 \frac{\mu_q}{\pi^2} G^2 - \mathcal{I}_4 \frac{1}{3\pi^2} [\mu_q + \mu_I] G^2 \left(2 + \frac{m_u}{M_{+,u}} \right)$$

$$- \mathcal{I}_5 \frac{1}{3\pi^2} [\mu_q - \mu_I] G^2 \left(2 + \frac{m_d}{M_{+,d}} \right)$$

$$+ \mathcal{I}_1 \left(2\xi_u m_u + 2\xi_u M_{+,u} + \frac{1}{3} \frac{m_u}{M_{+,u}} TG^2 + \frac{2}{3} TG^2 \right)$$

$$+ \mathcal{I}_2 \left(2\xi_d m_d + 2\xi_d M_{+,d} + \frac{1}{3} \frac{m_d}{M_{+,d}} TG^2 + \frac{2}{3} TG^2 \right) , \qquad \text{(B.33)}$$

$$A_3 = \mathcal{I}_1 \left(T^2 + \frac{1}{\pi^2} [\mu_q + \mu_I]^2 \right) \left(\frac{1}{3} + \frac{1}{6} \frac{m_u}{M_{+,u}} \right) , \qquad \text{(B.34)}$$

$$B_3 = \mathcal{I}_2 \left(T^2 + \frac{1}{\pi^2} [\mu_q - \mu_I]^2 \right) \left(\frac{1}{3} + \frac{1}{6} \frac{m_d}{M_{+,d}} \right) , \qquad \text{(B.35)}$$

where

$$M_{+,u} = \sqrt{\frac{1}{6}\left(T^2 + \frac{[\mu_q + \mu_I]^2}{\pi^2}\right)G^2(T,\mu_q,\mu_I)}, \tag{B.36}$$

$$M_{+,d} = \sqrt{\frac{1}{6}\left(T^2 + \frac{[\mu_q - \mu_I]^2}{\pi^2}\right)G^2(T,\mu_q,\mu_I)}, \tag{B.37}$$

and the phase-space integrals $\mathcal{I}_k$ are given by

$$\mathcal{I}_1 = \frac{d_u}{2\pi^2}\int_0^\infty dk \frac{k^2}{2\omega_u T}\left(\frac{e^{\{\omega_u+\mu_q+\mu_I\}/T}}{[e^{\{\omega_u+\mu_q+\mu_I\}/T}+1]^2}\right.$$
$$\left.-\frac{e^{\{\omega_u-\mu_q-\mu_I\}/T}}{[e^{\{\omega_u-\mu_q-\mu_I\}/T}+1]^2}\right), \tag{B.38}$$

$$\mathcal{I}_2 = \frac{d_d}{2\pi^2}\int_0^\infty dk \frac{k^2}{2\omega_d T}\left(\frac{e^{\{\omega_d+\mu_q-\mu_I\}/T}}{[e^{\{\omega_d+\mu_q-\mu_I\}/T}+1]^2}\right.$$
$$\left.-\frac{e^{\{\omega_d-\mu_q+\mu_I\}/T}}{[e^{\{\omega_d-\mu_q+\mu_I\}/T}+1]^2}\right), \tag{B.39}$$

$$\mathcal{I}_3 = -\frac{d_g}{\pi^2}\int_0^\infty dk \frac{k^2}{2T^2}\frac{e^{\omega_g/T}}{[e^{\omega_g/T}-1]^2}, \tag{B.40}$$

$$\mathcal{I}_4 = -\frac{d_u}{2\pi^2}\int_0^\infty dk \frac{k^2}{2\omega_u T^2}\left(\frac{\{\omega_u+\mu_q+\mu_I\}e^{\{\omega_u+\mu_q+\mu_I\}/T}}{[e^{\{\omega_u+\mu_q+\mu_I\}/T}+1]^2}\right.$$
$$\left.+[\mu_{q,I}\to-\mu_{q,I}]\right), \tag{B.41}$$

$$\mathcal{I}_5 = -\frac{d_d}{2\pi^2}\int_0^\infty dk \frac{k^2}{2\omega_d T^2}\left(\frac{\{\omega_d+\mu_q-\mu_I\}e^{\{\omega_d+\mu_q-\mu_I\}/T}}{[e^{\{\omega_d+\mu_q-\mu_I\}/T}+1]^2}\right.$$
$$\left.+[\mu_{q,I}\to-\mu_{q,I}]\right). \tag{B.42}$$

Again, the terms involving explicitly ξ_u and ξ_d comply with the lattice calculation set-up of temperature dependent bare quark masses $m_i = \xi_i T$ with constant ξ_i. In the case of constant quark mass parameters, $\xi_u = \xi_d = 0$ must be set in the above expressions while in the chiral limit, in addition, $m_u = m_d = 0$ have to be considered.

The coefficients in Eqs. (2.68) and (2.69) read

$$\mathcal{A}_1 = \mathcal{A}_2 = \frac{1}{12}\mathcal{I}_3\left([6+N_f]T^2 + \frac{3}{\pi^2}\left[\mu_u^2 + \mu_d^2\right]\right)$$
$$+\mathcal{I}_4\left(T^2 + \frac{\mu_u^2}{\pi^2}\right)\left(\frac{1}{3} + \frac{1}{6}\frac{m_u}{M_{+,u}}\right)$$
$$+\mathcal{I}_5\left(T^2 + \frac{\mu_d^2}{\pi^2}\right)\left(\frac{1}{3} + \frac{1}{6}\frac{m_d}{M_{+,d}}\right), \tag{B.43}$$

$$\mathcal{B}_1 = \mathcal{B}_2 = -\mathcal{I}_1\left(T^2 + \frac{\mu_u^2}{\pi^2}\right)\left(\frac{1}{3} + \frac{1}{6}\frac{m_u}{M_{+,u}}\right) \tag{B.44}$$

and

$$\mathcal{C}_1 = \mathcal{I}_1\left(2\xi_u m_u + 2\xi_u M_{+,u} + \frac{1}{3}\frac{m_u}{M_{+,u}}TG^2 + \frac{2}{3}TG^2\right)$$

$$-\mathcal{I}_3\frac{\mu_u}{2\pi^2}G^2 - \mathcal{I}_4\left(\frac{2}{3}\frac{\mu_u}{\pi^2}G^2 + \frac{1}{3}\frac{m_u}{M_{+,u}}\frac{\mu_u}{\pi^2}G^2\right), \tag{B.45}$$

$$\mathcal{C}_2 = \left(\frac{\frac{1}{3} + \frac{1}{6}\frac{m_u}{M_{+,u}}}{\frac{1}{3} + \frac{1}{6}\frac{m_d}{M_{+,d}}}\right)\left(\mathcal{I}_1\left\{2\xi_d m_d + 2\xi_d M_{+,d} + \frac{1}{3}\frac{m_d}{M_{+,d}}TG^2 + \frac{2}{3}TG^2\right\}\right.$$

$$-\mathcal{I}_3\frac{\mu_d}{2\pi^2}G^2\frac{\mathcal{I}_1}{\mathcal{I}_2}$$

$$\left.-\mathcal{I}_5\left\{\frac{2}{3}\frac{\mu_d}{\pi^2}G^2 + \frac{1}{3}\frac{m_d}{M_{+,d}}\frac{\mu_d}{\pi^2}G^2\right\}\frac{\mathcal{I}_1}{\mathcal{I}_2}\right)\left(\frac{T^2 + \mu_u^2/\pi^2}{T^2 + \mu_d^2/\pi^2}\right), \tag{B.46}$$

where μ_q and μ_I in the phase-space integrals $\mathcal{I}_k$ defined above have to be substituted by $\mu_u = \mu_q + \mu_I$ and $\mu_d = \mu_q - \mu_I$. The coefficients in Eqs. (2.72) and (2.73) read

$$\mathcal{N} = T^2\left(\mathcal{I}_3\frac{[6 + N_f]}{12} + \mathcal{I}_4\left\{\frac{1}{3} + \frac{1}{6}\frac{m_u}{M_{+,u}}\right\} + \mathcal{I}_5\left\{\frac{1}{3} + \frac{1}{6}\frac{m_d}{M_{+,d}}\right\}\right), \tag{B.47}$$

$$\mathcal{N}_1 = \frac{d_u}{2\pi^2}\int_0^\infty dk\frac{k^2}{T^2\omega_u}\left(\frac{e^{\omega_u/T}}{(e^{\omega_u/T} + 1)^2} - 2\frac{e^{2\omega_u/T}}{(e^{\omega_u/T} + 1)^3}\right), \tag{B.48}$$

$$\mathcal{N}_2 = \frac{d_d}{2\pi^2}\int_0^\infty dk\frac{k^2}{T^2\omega_d}\left(\frac{e^{\omega_d/T}}{(e^{\omega_d/T} + 1)^2} - 2\frac{e^{2\omega_d/T}}{(e^{\omega_d/T} + 1)^3}\right), \tag{B.49}$$

where $\mathcal{I}_{3,4,5}$, $M_{+,u}$ and $M_{+,d}$ as well as $\omega_{u,d}$ have to be taken at $\mu_q = \mu_I = 0$ or, equivalently, at $\mu_u = \mu_d = 0$.

From Eqs. (B.43)-(B.46) one first notes that $\mathcal{C}_{1,2} \to 0$, $\mathcal{B}_{1,2} \to 0$ whereas $\mathcal{A}_{1,2}$ remain nonzero in the limit $\mu_u = \mu_d = 0$ resulting in $\left.\frac{\partial G^2}{\partial\mu_u}\right|_{\mu_u=\mu_d=0} = 0$ from either Eq. (2.68) or Eq. (2.69) and consequently $\left.\frac{\partial G^2}{\partial\mu_d}\right|_{\mu_u=\mu_d=0} = 0$. In the region of small chemical potentials, $\mu_{u,d} \ll \pi T$, discussed in section 2.4, one finds $M_{+,u} = M_{+,d}$ and in the mass symmetric case, $m_u = m_d$, consequently $\omega_u = \omega_d$. Thus, from Eqs. (B.45) and (B.46) the equality $\mathcal{C}_1 = \mathcal{C}_2$ follows when

$$\mu_u = \mu_d\frac{\mathcal{I}_1}{\mathcal{I}_2}, \tag{B.50}$$

$$\mu_u = \mu_d\frac{\mathcal{I}_5}{\mathcal{I}_4}\frac{\mathcal{I}_1}{\mathcal{I}_2}. \tag{B.51}$$

For small μ_u and μ_d, the phase-space integrals $\mathcal{I}_k$ can be formulated in terms of Taylor series expansions in the quark chemical potentials, where $\mathcal{I}_{1,2}$ turn out to

be odd functions in $\mu_{u,d}$ while $\mathcal{I}_{4,5}$ are even functions in $\mu_{u,d}$ reading

$$
\begin{aligned}
\mathcal{I}_1 \;=\; & \frac{d_u}{2\pi^2} \int_0^\infty dk \frac{k^2}{2\omega_u T} \frac{1}{[e^{\omega_u/T}+1]^2} \left(2\frac{\mu_u}{T} e^{\omega_u/T} \right. \\
& \left. -4\frac{\mu_u}{T} \frac{e^{2\omega_u/T}}{[e^{\omega_u/T}+1]} + \mathcal{O}\left(\frac{\mu_u^3}{T^3}\right) \right), \quad (B.52)
\end{aligned}
$$

$$
\begin{aligned}
\mathcal{I}_2 \;=\; & \frac{d_d}{2\pi^2} \int_0^\infty dk \frac{k^2}{2\omega_d T} \frac{1}{[e^{\omega_d/T}+1]^2} \left(2\frac{\mu_d}{T} e^{\omega_d/T} \right. \\
& \left. -4\frac{\mu_d}{T} \frac{e^{2\omega_d/T}}{[e^{\omega_d/T}+1]} + \mathcal{O}\left(\frac{\mu_d^3}{T^3}\right) \right) \quad (B.53)
\end{aligned}
$$

and

$$
\mathcal{I}_4 \;=\; -\frac{d_u}{2\pi^2} \int_0^\infty dk \frac{k^2}{2\omega_u T} \frac{1}{[e^{\omega_u/T}+1]^2} \left(2\frac{\omega_u}{T} e^{\omega_u/T} + \mathcal{O}\left(\frac{\mu_u^2}{T^2}\right) \right), \quad (B.54)
$$

$$
\mathcal{I}_5 \;=\; -\frac{d_d}{2\pi^2} \int_0^\infty dk \frac{k^2}{2\omega_d T} \frac{1}{[e^{\omega_d/T}+1]^2} \left(2\frac{\omega_d}{T} e^{\omega_d/T} + \mathcal{O}\left(\frac{\mu_d^2}{T^2}\right) \right). \quad (B.55)
$$

Thus, for small μ_u and μ_d one finds $\mu_u \mathcal{I}_2 = \mu_d \mathcal{I}_1$ and $\mathcal{I}_4 = \mathcal{I}_5$. As a result, Eqs. (2.68) and (2.69) can be solved consistently for G^2 and its first derivative with respect to $\mu_{u,d}$ for small μ_u and μ_d.

Second-order susceptibility coefficients depend on G^2 evaluated at $\mu_{u,d} = 0$, while fourth-order coefficients depend on G^2 and $\frac{\partial^2 G^2}{\partial \mu_{u,d}^2}$ at $\mu_{u,d} = 0$. In principle, higher order derivatives of the effective coupling with respect to the chemical potentials, as necessary for higher order susceptibility coefficients, are obtained by mathematical manipulations of the generalized system of flow equations. For instance, the derivative $\frac{\partial^2 G^2}{\partial \mu_u^2}$ following from Eq. (2.68) reads

$$
\frac{\partial^2 G^2}{\partial \mu_u^2} = \frac{1}{\mathcal{A}_1} \frac{\partial \mathcal{C}_1}{\partial \mu_u} - \frac{\mathcal{C}_1}{\mathcal{A}_1^2} \frac{\partial \mathcal{A}_1}{\partial \mu_u} - \left(\frac{1}{\mathcal{A}_1} \frac{\partial \mathcal{B}_1}{\partial \mu_u} - \frac{\mathcal{B}_1}{\mathcal{A}_1^2} \frac{\partial \mathcal{A}_1}{\partial \mu_u} \right) \frac{\partial G^2}{\partial T} - \frac{\mathcal{B}_1}{\mathcal{A}_1} \frac{\partial^2 G^2}{\partial \mu_u \partial T}, \quad (B.56)
$$

while when considering Eq. (2.69), $\mathcal{C}_1$ in Eq. (B.56) has to be replaced by $\mathcal{C}_2$. In general, an n-th order derivative of G^2 with respect to the chemical potentials incorporates derivatives up to and including the $(n-1)$-st order derivative of $\mathcal{C}_1$ or $\mathcal{C}_2$. Since

$$
\begin{aligned}
\frac{\partial \mathcal{C}_1}{\partial \mu_u}\bigg|_{\mu_u=\mu_d=0} \;=\; & \frac{\partial \mathcal{C}_2}{\partial \mu_u}\bigg|_{\mu_u=\mu_d=0} \\
\;=\; & \left(\frac{2}{3} \frac{\partial \mathcal{I}_1}{\partial \mu_u} T G^2 - \frac{1}{2\pi^2} \mathcal{I}_3 G^2 - \frac{2}{3\pi^2} \mathcal{I}_4 G^2 \right)\bigg|_{\mu_u=\mu_d=0}, \quad (B.57)
\end{aligned}
$$

$\frac{\partial^2 G^2}{\partial \mu_u^2}\big|_{\mu_u=\mu_d=0}$ is uniquely determined from the generalized system of flow equations.

But already fourth-order derivatives of G^2 cannot be obtained reliably as

$$\frac{\partial^3 \mathcal{C}_1}{\partial \mu_u^3}\bigg|_{\mu_u=\mu_d=0} = \left(\frac{\partial^2 G^2}{\partial \mu_u^2} \left\{ 2T \frac{\partial \mathcal{I}_1}{\partial \mu_u} - \frac{3}{2\pi^2} \mathcal{I}_3 - \frac{2}{\pi^2} \mathcal{I}_4 \right\} \right.$$
$$\left. + G^2 \left\{ \frac{2}{3} T \frac{\partial^3 \mathcal{I}_1}{\partial \mu_u^3} - \frac{3}{2\pi^2} \frac{\partial^2 \mathcal{I}_3}{\partial \mu_u^2} - \frac{2}{\pi^2} \frac{\partial^2 \mathcal{I}_4}{\partial \mu_u^2} \right\} \right)\bigg|_{\mu_u=\mu_d=0} \tag{B.58}$$

whereas

$$\frac{\partial^3 \mathcal{C}_2}{\partial \mu_u^3}\bigg|_{\mu_u=\mu_d=0} = \frac{\partial^3 \mathcal{C}_1}{\partial \mu_u^3}\bigg|_{\mu_u=\mu_d=0} + \frac{6}{\pi^2 T^2} \frac{\partial \mathcal{C}_1}{\partial \mu_u}\bigg|_{\mu_u=\mu_d=0}. \tag{B.59}$$

This implies that second- and fourth-order susceptibility coefficients and related quantities are uniquely determined whereas $\frac{\partial^4 G^2}{\partial \mu_u^4}\big|_{\mu_u=\mu_d=0}$ entering sixth- and higher-order susceptibility coefficients cannot.

B.4   Alternative approach

The origin of the limitations pointed out in section 2.4 and in Appendix B.3 is the special ansatz for the effective quasiparticle masses in Eqs. (2.60) and (2.61) which is motivated by the contact to 1-loop expressions for the self-energies [102,103]. The pressure in Eqs. (2.57)-(2.59) as such should, in principle, allow for consistency in all orders of powers of $\mu_{u,d}$. Considering, instead, modified effective quasiparticle masses via $2M_{+,l}^2 = \frac{1}{3} T^2 G^2(T, \mu_u, \mu_d)$ and $m_\infty^2 = \frac{1}{12}[6 + N_f] T^2 G^2(T, \mu_u, \mu_d)$, i. e. discarding the explicit μ^2 terms in the original expressions, an uniquely solvable generalized system of flow equations is obtained. The coefficients in Eqs. (2.68) and (2.69) become

$$\mathcal{A}_1 = \mathcal{A}_2 = \frac{T^2}{3} \left(\frac{[6+N_f]}{4} \mathcal{I}_3 + \mathcal{I}_4 + \mathcal{I}_5 \right), \tag{B.60}$$

$$\mathcal{B}_1 = \mathcal{B}_2 = -\frac{T^2}{3} \mathcal{I}_1, \tag{B.61}$$

$$\mathcal{C}_1 = \mathcal{C}_2 = \frac{2}{3} T G^2 \mathcal{I}_1. \tag{B.62}$$

(These expressions are correct for the chiral limit or for temperature independent bare quark masses. For $m_l = m_l(T)$, the equalities hold in the mass symmetric case $m_u = m_d$.) In this way, G^2 and all its derivatives can trustfully be obtained, implying also a consistent determination of the susceptibility coefficients to arbitrary order, which opens the avenue for future investigations.

With these modified quasiparticle dispersion relations, information obtained by adjusting the QPM parameters to lattice QCD results on the temperature axis is transported to nonzero μ_u and μ_d solely by the implicit dependence $G^2(T, \mu_u, \mu_d)$ and the corresponding generalized system of flow equations. In section 3.2.6, it was shown that this alternative ansatz is equally suitable for a proper description of lattice QCD thermodynamics for imaginary chemical potential. The stationarity property of the thermodynamic potential p causes a robustness against modifications in the employed quasiparticle dispersion relations. Concerning the susceptibility coefficients, results for second-order coefficients found in section 3.2.3 remain unchanged by modifying the dispersion relations when keeping the parametrization
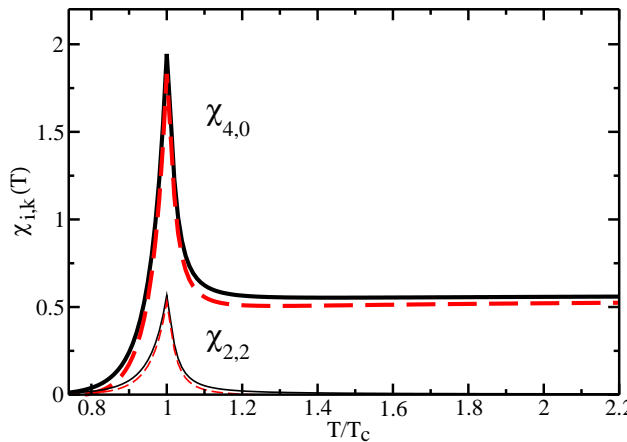
Figure B.1: Comparison of fourth-order susceptibility coefficients $\chi_{4,0}$ (upper curves) and $\chi_{2,2}$ (lower curves) evaluated with the quasiparticle dispersion relations incorporating Eqs. (2.60) and (2.61) (solid curves) and with the modified dispersion relations incorporating only an implicit μ_u and μ_d dependence via G^2 (dashed curves) leaving the parametrization of $G^2(T, \mu_u = 0, \mu_d = 0)$ established in Figure 3.18 unchanged.

of $G^2(T, \mu_u = 0, \mu_d = 0)$ fixed. In contrast, for instance $\left.\frac{\partial^2 G^2}{\partial \mu_u^2}\right|_{\mu_u = \mu_d = 0}$ and thus fourth-order coefficients alter according to Eqs. (B.60)-(B.62). This is illustrated in Figure B.1. Note, however, that the modification of the quasiparticle dispersion relations leaving $G^2(T, \mu_u = 0, \mu_d = 0)$ fixed results in a generic down shift of the original results by less than 9%, i. e. the alternative ansatz, with only an implicit μ_u and μ_d dependence via G^2, provides an equally suitable description of lattice QCD results for the susceptibility coefficients.

Appendix C Extrapolation of Lattice QCD Data to Thermodynamic and Continuum Limits

While the quasiparticle model is formulated for a thermodynamic system infinite in space and time, lattice QCD simulations are performed on a discretized space-time grid with finite extensions in spatial, N_σ, and temporal, N_τ, directions and finite lattice spacing $a \neq 0$. This demands a proper extrapolation of lattice QCD results to thermodynamic ($N_\sigma \to \infty$) and continuum ($N_\tau \to \infty$, $a \to 0$) limits when aiming at a reasonable comparison of simulation results with phenomenological models. As the temperature, though, is defined by $T = 1/(N_\tau a)$, an appropriate continuum extrapolation of lattice QCD results at finite T demands an extrapolation to $N_\tau \to \infty$ at fixed T. Moreover, available lattice QCD data obtained in different simulations deviate, in general, in their numeric set-ups, including lattice sizes, flavour numbers, quark masses, employed actions etc. Thus, in general, different simulations require different extrapolation procedures.

In particular, employing different lattice actions results in different cut-off effects on the data. While for improved actions thermodynamic bulk quantities stay below their corresponding continuum ideal gas limits [131], simulations using standard actions overshoot the latter at larger temperatures exhibiting sizeable cut-off effects [8]. In fact, discretization errors in thermodynamic bulk properties are most significant at high temperatures [270]. For instance, leading-order cut-off effects in the pressure evaluated at finite N_τ are given by [8]

$$\frac{p}{T^4}\Big|_{N_\tau} = \frac{p}{T^4}\Big|_\infty + \frac{c}{N_\tau^2} + \mathcal{O}(N_\tau^{-4}), \tag{C.1}$$

implying temperature dependent cut-off effects. Employing improved actions strongly reduces lattice discretization errors at high temperatures as the influence of the order $\mathcal{O}(N_\tau^{-2})$ correction decreases significantly ($c \to 0$) leaving as dominant contribution $\mathcal{O}(N_\tau^{-4})$ corrections. Thus, simulations with small temporal extension are already close to the continuum limit [270].

Detailed systematic studies of the cut-off dependence of lattice QCD results by considering different N_τ and extrapolating to $N_\tau \to \infty$ exist for pure $SU(3)$ gauge theory using standard actions [138, 271] and improved actions [207, 272, 273]. In these studies, the difference between continuum extrapolated results for the pressure and results obtained at $N_\tau = 8$ is below 3%. Moreover, the cut-off dependence of an ideal gluon gas describes correctly the cut-off dependence of the complex, interacting theory [131]. In this respect, the behaviour observed for the ideal, non-interacting gas can be considered as guidance for analyzing the cut-off dependence

of QCD thermodynamics [131].

Similar studies for systems including light quarks have not been performed, even though discretization errors in pure $SU(3)$ gauge theory and for systems including light quarks seem to be of the same size [131]. This leaves, however, some freedom for the applied continuum extrapolation procedure. In fact, different estimates for a continuum extrapolation are conceivable. One possibility is to multiply available lattice QCD data by a scaling factor given by the ratio of thermodynamic quantities evaluated for $N_\tau \rightarrow \infty$ and for finite N_τ, but, in both cases for the massless, non-interacting gas of quarks and gluons. This procedure explicitly assumes that continuum extrapolations of simulations for QCD and for the Stefan-Boltzmann gas of quarks and gluons are similar [131]. In general, however, such a scaling factor could depend on temperature.

Nonetheless, as discretization errors are of the order $\mathcal{O}(N_\tau^{-n})$, a profound extrapolation of lattice QCD results to the continuum limit must base on a systematic investigation of different N_τ at fixed T and an according extrapolation to $N_\tau \rightarrow \infty$ [8, 138, 270]. In the same way, lattice QCD data have to be extrapolated to the thermodynamic limit by investigating large spatial extensions N_σ.

Bibliography

[1] D. J. Gross and F. Wilczek: Ultraviolet behavior of non-Abelian gauge theories. *Phys. Rev. Lett.* **30**, 1343 (1973).

[2] H. D. Politzer: Reliable perturbative results for strong interactions? *Phys. Rev. Lett.* **30**, 1346 (1973).

[3] N. Cabibbo and G. Parisi: Exponential hadronic spectrum and quark liberation. *Phys. Lett.* **B59**, 67 (1975).

[4] J. C. Collins and M. J. Perry: Superdense matter: Neutrons or asymptotically free quarks? *Phys. Rev. Lett.* **34**, 1353 (1975).

[5] K. Yagi, T. Hatsuda and Y. Miake: Quark-Gluon Plasma: From Big Bang to Little Bang. *Cambridge, UK: Cambridge University Press* (2005).

[6] F. Karsch, E. Laermann and A. Peikert: Quark mass and flavor dependence of the QCD phase transition. *Nucl. Phys.* **B605**, 579 (2001).

[7] Y. Aoki, G. Endrodi, Z. Fodor, S. D. Katz and K. K. Szabo: The order of the quantum chromodynamics transition predicted by the standard model of particle physics. *Nature* **443**, 675 (2006).

[8] F. Karsch: Lattice QCD at high temperature and density. *Lect. Notes Phys.* **583**, 209 (2002).

[9] S. Ejiri, F. Karsch, E. Laermann and C. Schmidt: The isentropic equation of state of 2-flavor QCD. *Phys. Rev.* **D73**, 054506 (2006).

[10] M. Cheng *et al.*: The transition temperature in QCD. *Phys. Rev.* **D74**, 054507 (2006).

[11] B. C. Barrois: Superconducting quark matter. *Nucl. Phys.* **B129**, 390 (1977).

[12] D. Bailin and A. Love: Superfluidity and superconductivity in relativistic fermion systems. *Phys. Rept.* **107**, 325 (1984).

[13] D. H. Rischke: The quark-gluon plasma in equilibrium. *Prog. Part. Nucl. Phys.* **52**, 197 (2004).

[14] M. A. Stephanov: QCD phase diagram: An overview. *Proc. Sci.* **LAT2006**, 024 (2006).

[15] Gesellschaft für Schwerionenforschung, GSI: *http://www.gsi.de* .

[16] B. Kämpfer: Cosmic phase transitions. *Annalen Phys.* **9**, 605 (2000).

[17] A. Friedmann: Über die Krümmung des Raumes. *Z. Phys.* **10**, 377 (1922).

[18] D. Seipt, M. Bluhm, R. Schulze and B. Kämpfer: Strongly interacting matter in the early universe prior to confinement. *Forschungszentrum Dresden-Rossendorf: Annual Report 2007, Structure of Matter - Subatomic Physics,* 7 (2007).

[19] K. Jedamzik: Primordial black hole formation during the QCD epoch. *Phys. Rev.* **D55**, 5871 (1997).

[20] K. N. Abazajian and G. M. Fuller: Bulk QCD thermodynamics and sterile neutrino dark matter. *Phys. Rev.* **D66**, 023526 (2002).

[21] M. Hindmarsh and O. Philipsen: WIMP dark matter and the QCD equation of state. *Phys. Rev.* **D71**, 087302 (2005).

[22] M. Gyulassy and L. McLerran: New forms of QCD matter discovered at RHIC. *Nucl. Phys.* **A750**, 30 (2005).

[23] L. D. Landau and E. M. Lifshitz: Fluid Mechanics, 2nd edn. *Oxford: Pergamon* (1987).

[24] D. T. ter Haar: Collective Papers of L. D. Landau. *New York, USA: Gordon & Breach* p. 569 (1965).

[25] A. Muronga: Dissipative relativistic fluid dynamics for nuclear collisions. *Heavy Ion Phys.* **15**, 337 (2002).

[26] D. Teaney: Effect of shear viscosity on spectra, elliptic flow, and Hanbury Brown-Twiss radii. *Phys. Rev.* **C68**, 034913 (2003).

[27] U. W. Heinz, H. Song and A. K. Chaudhuri: Dissipative hydrodynamics for viscous relativistic fluids. *Phys. Rev.* **C73**, 034904 (2006).

[28] A. K. Chaudhuri: Dissipative hydrodynamics in 2+1 dimension. *Phys. Rev.* **C74**, 044904 (2006).

[29] R. Baier and P. Romatschke: Causal viscous hydrodynamics for central heavy-ion collisions. *Eur. Phys. J.* **C51**, 677 (2007).

[30] P. Romatschke: Causal viscous hydrodynamics for central heavy-ion collisions. II: Meson spectra and HBT radii. *Eur. Phys. J.* **C52**, 203 (2007).

[31] D. Teaney: Simulating RHIC with viscous hydrodynamics. *Nucl. Phys.* **A785**, 44 (2007).

[32] P. Romatschke and U. Romatschke: Viscosity information from relativistic nuclear collisions: How perfect is the fluid observed at RHIC? *Phys. Rev. Lett.* **99**, 172301 (2007).

[33] H. Song and U. W. Heinz: Suppression of elliptic flow in a minimally viscous quark-gluon plasma. *Phys. Lett.* **B658**, 279 (2008).

[34] P. Braun-Munzinger and J. Stachel: The quest for the quark-gluon plasma. *Nature* **448**, 302 (2007).

[35] M. A. Stephanov, K. Rajagopal and E. V. Shuryak: Event-by-event fluctuations in heavy ion collisions and the QCD critical point. *Phys. Rev.* **D60**, 114028 (1999).

[36] S. A. Voloshin, V. Koch and H. G. Ritter: Event-by-event fluctuations in collective quantities. *Phys. Rev.* **C60**, 024901 (1999).

[37] S. Jeon and V. Koch: Fluctuations of particle ratios and the abundance of hadronic resonances. *Phys. Rev. Lett.* **83**, 5435 (1999).

[38] M. Asakawa, U. W. Heinz and B. Müller: Fluctuation probes of quark deconfinement. *Phys. Rev. Lett.* **85**, 2072 (2000).

[39] S. Jeon and V. Koch: Charged particle ratio fluctuation as a signal for QGP. *Phys. Rev. Lett.* **85**, 2076 (2000).

[40] V. Koch, A. Majumder and J. Randrup: Baryon-strangeness correlations: A diagnostic of strongly interacting matter. *Phys. Rev. Lett.* **95**, 182301 (2005).

[41] Y. Hatta and M. A. Stephanov: Proton number fluctuation as a signal of the QCD critical end-point. *Phys. Rev. Lett.* **91**, 102003 (2003).

[42] S. Jeon and V. Koch: Quark Gluon Plasma 3. *Singapore: World Scientific*, 430 (2004).

[43] M. A. Stephanov: QCD phase diagram and the critical point. *Prog. Theor. Phys. Suppl.* **153**, 139 (2004).

[44] T. Hatsuda and T. Kunihiro: Fluctuation effects in hot quark matter: Precursors of chiral transition at finite temperature. *Phys. Rev. Lett.* **55**, 158 (1985).

[45] R. V. Gavai and S. Gupta: Fluctuations, strangeness and quasi-quarks in heavy-ion collisions from lattice QCD. *Phys. Rev.* **D73**, 014004 (2006).

[46] A. Andronic, P. Braun-Munzinger and J. Stachel: Hadron production in central nucleus nucleus collisions at chemical freeze-out. *Nucl. Phys.* **A772**, 167 (2006).

[47] F. Becattini, M. Gazdzicki, A. Keranen, J. Manninen and R. Stock: Study of chemical equilibrium in nucleus nucleus collisions at AGS and SPS energies. *Phys. Rev.* **C69**, 024905 (2004).

[48] P. Braun-Munzinger, K. Redlich and J. Stachel: Quark Gluon Plasma 3. *Singapore: World Scientific*, 491 (2004).

[49] J. Cleymans, B. Kämpfer, M. Kaneta, S. Wheaton and N. Xu: Centrality dependence of thermal parameters deduced from hadron multiplicities in Au + Au collisions at s(NN)**(1/2) = 130-GeV. *Phys. Rev.* **C71**, 054901 (2005).

[50] F. Becattini, J. Manninen and M. Gazdzicki: Energy and system size dependence of chemical freeze-out in relativistic nuclear collisions. *Phys. Rev.* **C73**, 044905 (2006).

[51] J. Cleymans, H. Oeschler, K. Redlich and S. Wheaton: Comparison of chemical freeze-out criteria in heavy-ion collisions. *Phys. Rev.* **C73**, 034905 (2006).

[52] R. Hagedorn: Statistical thermodynamics of strong interactions at high-energies. *Nuovo Cim. Suppl.* **3**, 147 (1965).

[53] M. A. Stephanov, K. Rajagopal and E. V. Shuryak: Signatures of the tricritical point in QCD. *Phys. Rev. Lett.* **81**, 4816 (1998).

[54] D. Teaney, J. Lauret and E. V. Shuryak: Flow at the SPS and RHIC as a quark gluon plasma signature. *Phys. Rev. Lett.* **86**, 4783 (2001).

[55] P. Huovinen: Quark Gluon Plasma 3. *Singapore: World Scientific*, 600 (2004).

[56] P. F. Kolb and U. W. Heinz: Quark Gluon Plasma 3. *Singapore: World Scientific*, 634 (2004).

[57] U. W. Heinz: Hydrodynamics at RHIC: How well does it work, where and how does it break down? *J. Phys.* **G31**, S717 (2005).

[58] P. Huovinen: Anisotropy of flow and the order of phase transition in relativistic heavy ion collisions. *Nucl. Phys.* **A761**, 296 (2005).

[59] U. W. Heinz and P. F. Kolb: Early thermalization at RHIC. *Nucl. Phys.* **A702**, 269 (2002).

[60] U. W. Heinz: The quark-gluon plasma at RHIC. *Nucl. Phys.* **A721**, 30 (2003).

[61] M. Gyulassy: Structure and Dynamics of Elementary Matter, Nato Science Series II, vol. 166. *Dordrecht, Netherlands: Kluwer Academic*, 159 (2004).

[62] E. V. Shuryak: Why does the quark gluon plasma at RHIC behave as a nearly ideal fluid? *Prog. Part. Nucl. Phys.* **53**, 273 (2004).

[63] D. A. Teaney: Viscosity and thermalization. *J. Phys.* **G30**, S1247 (2004).

[64] E. V. Shuryak: What RHIC experiments and theory tell us about properties of quark-gluon plasma? *Nucl. Phys.* **A750**, 64 (2005).

[65] B. A. Gelman, E. V. Shuryak and I. Zahed: Classical strongly coupled QGP I: The model and molecular dynamics simulations. *Phys. Rev.* **C74**, 044908 (2006).

[66] A. Peshier and W. Cassing: The hot non-perturbative gluon plasma is an almost ideal colored liquid. *Phys. Rev. Lett.* **94**, 172301 (2005).

[67] M. Baldo *et al.*: Neutron stars and the transition to color-superconducting quark matter. *Phys. Lett.* **B562**, 153 (2003).

[68] T. Klahn *et al.*: Modern compact star observations and the quark matter equation of state. *Phys. Lett.* **B654**, 170 (2007).

[69] M. Buballa: NJL-model analysis of dense quark matter. *Phys. Rept.* **407**, 205 (2005).

[70] D. Blaschke and H. Grigorian: Unmasking neutron star interiors using cooling simulations. *Prog. Part. Nucl. Phys.* **59**, 139 (2007).

[71] H. Eschrig: The particle world of condensed matter - an introduction to the notion of quasi-particle. *Leipzig: Edition am Gutenbergplatz* (2005).

[72] V. M. Galitzkii and A. B. Migdal: *Sov. Phys. JETP* **7**, 96 (1958).

[73] M. I. Gorenstein and S.-N. Yang: Gluon plasma with a medium dependent dispersion relation. *Phys. Rev.* **D52**, 5206 (1995).

[74] F. G. Gardim and F. M. Steffens: Thermodynamics of quasi-particles. *Nucl. Phys.* **A797**, 50 (2007).

[75] V. M. Bannur: Comments on quasiparticle models of quark-gluon plasma. *Phys. Lett.* **B647**, 271 (2007).

[76] V. M. Bannur: Self-consistent quasiparticle model for quark-gluon plasma. *Phys. Rev.* **C75**, 044905 (2007).

[77] J. Letessier and J. Rafelski: QCD equations of state and the QGP liquid model. *Phys. Rev.* **C67**, 031902 (2003).

[78] R. A. Schneider and W. Weise: On the quasiparticle description of lattice QCD thermodynamics. *Phys. Rev.* **C64**, 055201 (2001).

[79] M. A. Thaler, R. A. Schneider and W. Weise: Quasiparticle description of hot QCD at finite quark chemical potential. *Phys. Rev.* **C69**, 035210 (2004).

[80] A. Rebhan and P. Romatschke: HTL quasiparticle models of deconfined QCD at finite chemical potential. *Phys. Rev.* **D68**, 025022 (2003).

[81] A. Peshier: Hard gluon damping in hot QCD. *Phys. Rev.* **D70**, 034016 (2004).

[82] A. Peshier: Hard parton damping in hot QCD. *J. Phys.* **G31**, S371 (2005).

[83] Yu. B. Ivanov, V. V. Skokov and V. D. Toneev: Equation of state of deconfined matter within dynamical quasiparticle description. *Phys. Rev.* **D71**, 014005 (2005).

[84] A. Peshier, B. Kämpfer, O. P. Pavlenko and G. Soff: An effective model of the quark - gluon plasma with thermal parton masses. *Phys. Lett.* **B337**, 235 (1994).

[85] A. Peshier, B. Kämpfer, O. P. Pavlenko and G. Soff: A massive quasiparticle model of the SU(3) gluon plasma. *Phys. Rev.* **D54**, 2399 (1996).

[86] A. Peshier, B. Kämpfer and G. Soff: The equation of state of deconfined matter at finite chemical potential in a quasiparticle description. *Phys. Rev.* **C61**, 045203 (2000).

[87] A. Peshier, B. Kämpfer and G. Soff: From QCD lattice calculations to the equation of state of quark matter. *Phys. Rev.* **D66**, 094003 (2002).

[88] B. Kämpfer and M. Bluhm: Strangeness and charm in QCD matter. *J. Phys.* **G31**, S1141 (2005).

[89] M. Bluhm, B. Kämpfer and G. Soff: Quasi-particle model of strongly interacting matter. *J. Phys.* **G31**, S1151 (2005).

[90] M. Bluhm, B. Kämpfer and G. Soff: The QCD equation of state near T(0) within a quasi- particle model. *Phys. Lett.* **B620**, 131 (2005).

[91] B. Kämpfer, M. Bluhm, R. Schulze, D. Seipt and U. Heinz: QCD matter within a quasi-particle model and the critical end point. *Nucl. Phys.* **A774**, 757 (2006).

[92] M. Bluhm and B. Kämpfer: Quasi-particle perspective on critical end-point. *Proc. Sci.* **CPOD2006**, 004 (2006).

[93] M. Bluhm, B. Kämpfer, R. Schulze and D. Seipt: Isentropic equation of state of two-flavour QCD in a quasi-particle model. *Acta Phys. Hung.* **A27**, 397 (2006).

[94] M. Bluhm, B. Kämpfer, R. Schulze and D. Seipt: Quasi-particle description of strongly interacting matter: Towards a foundation. *Eur. Phys. J.* **C49**, 205 (2007).

[95] M. Bluhm, B. Kämpfer, R. Schulze, D. Seipt and U. Heinz: A family of equations of state based on lattice QCD: Impact on flow in ultrarelativistic heavy-ion collisions. *Phys. Rev.* **C76**, 034901 (2007).

[96] B. Kämpfer, M. Bluhm, H. Schade, R. Schulze and D. Seipt: Do we know eventually p(e)? *Proc. Sci.* **CPOD2007**, 007 (2007).

[97] (ed.) N. Armesto *et al.*: Heavy ion collisions at the LHC - last call for predictions. *J. Phys.* **G35**, 054001 (2008).

[98] M. Bluhm and B. Kämpfer: Quasiparticle model of quark-gluon plasma at imaginary chemical potential. *Phys. Rev.* **D77**, 034004 (2008).

[99] M. Bluhm and B. Kämpfer: Flavor diagonal and off-diagonal susceptibilities in a quasiparticle model of the quark-gluon plasma. *Phys. Rev.* **D77**, 114016 (2008).

[100] T. S. Biro, P. Levai and B. Müller: Strangeness production with 'massive' gluons. *Phys. Rev.* **D42**, 3078 (1990).

[101] D. H. Rischke, M. I. Gorenstein, A. Schäfer, H. Stöcker and W. Greiner: Nonperturbative effects in the SU(3) gluon plasma. *Phys. Lett.* **B278**, 19 (1992).

[102] J. I. Kapusta and C. Gale: Finite-Temperature Field Theory - Principles and Applications. *Cambridge, UK: Cambridge University Press* (2006).

[103] M. LE BELLAC: Thermal Field Theory. *Cambridge, UK: Cambridge University Press* (1996).

[104] R. D. PISARSKI: Renormalized fermion propagator in hot gauge theories. *Nucl. Phys.* **A498**, 423c (1989).

[105] R. SCHULZE: Quasiparticle description of QCD thermodynamics: Effects of finite widths, Landau damping and collective excitations. *Diploma Thesis at Technische Universität Dresden, Germany* (June 2007).

[106] R. SCHULZE, M. BLUHM and B. KÄMPFER: Plasmons, plasminos and Landau damping in a quasiparticle model of the quark-gluon plasma. *Eur. Phys. J. Spec. Top.* **155**, 177 (2008).

[107] J. P. BLAIZOT, E. IANCU and A. REBHAN: The entropy of the QCD plasma. *Phys. Rev. Lett.* **83**, 2906 (1999).

[108] J. P. BLAIZOT, E. IANCU and A. REBHAN: Self-consistent hard-thermal-loop thermodynamics for the quark-gluon plasma. *Phys. Lett.* **B470**, 181 (1999).

[109] J. P. BLAIZOT, E. IANCU and A. REBHAN: Approximately self-consistent resummations for the thermodynamics of the quark-gluon plasma. I: Entropy and density. *Phys. Rev.* **D63**, 065003 (2001).

[110] J.-P. BLAIZOT and E. IANCU: The quark-gluon plasma: Collective dynamics and hard thermal loops. *Phys. Rept.* **359**, 355 (2002).

[111] J.-P. BLAIZOT, E. IANCU and A. REBHAN: Quark Gluon Plasma 3. *Singapore: World Scientific*, 60 (2004).

[112] J. M. LUTTINGER and J. C. WARD: Ground state energy of a many fermion system. 2. *Phys. Rev.* **118**, 1417 (1960).

[113] G. BAYM: Selfconsistent approximation in many body systems. *Phys. Rev.* **127**, 1391 (1962).

[114] T. D. LEE and C. N. YANG: Many-body problem in quantum statistical mechanics. IV. Formulation in terms of average occupation number in momentum space. *Phys. Rev.* **117**, 22 (1960).

[115] B. A. FREEDMAN and L. D. MCLERRAN: Fermions and gauge vector mesons at finite temperature and density. 1. Formal techniques. *Phys. Rev.* **D16**, 1130 (1977).

[116] A. PESHIER: HTL resummation of the thermodynamic potential. *Phys. Rev.* **D63**, 105004 (2001).

[117] A. PESHIER, B. KÄMPFER, O. P. PAVLENKO and G. SOFF: Thermodynamics of the phi**4 theory in tadpole approximation. *Europhys. Lett.* **43**, 381 (1998).

[118] B. VANDERHEYDEN and G. BAYM: Self-consistent approximations in relativistic plasmas: Quasiparticle analysis of the thermodynamic properties. *J. Stat. Phys.* **93**, 843 (1998).

[119] R. D. PISARSKI: Renormalized gauge propagator in hot gauge theories. *Physica* **A158**, 146 (1989).

[120] D. SEIPT: Quark mass dependence of one-loop self-energies in hot QCD. *Diploma Thesis at Technische Universität Dresden, Germany* (May 2007).

[121] A. ROBERGE and N. WEISS: Gauge theories with imaginary chemical potential and the phases of QCD. *Nucl. Phys.* **B275**, 734 (1986).

[122] P. DE FORCRAND and O. PHILIPSEN: The QCD phase diagram for small densities from imaginary chemical potential. *Nucl. Phys.* **B642**, 290 (2002).

[123] M. D'ELIA and M.-P. LOMBARDO: Finite density QCD via imaginary chemical potential. *Phys. Rev.* **D67**, 014505 (2003).

[124] P. DE FORCRAND and O. PHILIPSEN: The QCD phase diagram for three degenerate flavors and small baryon density. *Nucl. Phys.* **B673**, 170 (2003).

[125] M. D'ELIA and M. P. LOMBARDO: QCD thermodynamics from an imaginary mu(B): Results on the four flavor lattice model. *Phys. Rev.* **D70**, 074509 (2004).

[126] M. P. LOMBARDO: Lattice QCD at finite density: Imaginary chemical potential. *Proc. Sci.* **CPOD2006**, 003 (2006).

[127] Y. SAKAI, K. KASHIWA, H. KOUNO and M. YAHIRO: Polyakov loop extended NJL model with imaginary chemical potential. *Phys. Rev.* **D77**, 051901 (2008).

[128] M. P. LOMBARDO: Lattice QCD at finite density: A primer. *Prog. Theor. Phys. Suppl.* **153**, 26 (2004).

[129] M. D'ELIA, F. DI RENZO and M. P. LOMBARDO: QCD at high temperature: Results from lattice simulations with an imaginary mu. *AIP Conf. Proc.* **806**, 245 (2006).

[130] M. BLUHM: On the equation of state of strongly interacting matter - A quasi-particle description. *Diploma Thesis at Technische Universität Dresden, Germany* (July 2004).

[131] F. KARSCH, E. LAERMANN and A. PEIKERT: The pressure in 2, 2+1 and 3 flavour QCD. *Phys. Lett.* **B478**, 447 (2000).

[132] F. KARSCH, K. REDLICH and A. TAWFIK: Hadron resonance mass spectrum and lattice QCD thermodynamics. *Eur. Phys. J.* **C29**, 549 (2003).

[133] F. KARSCH, K. REDLICH and A. TAWFIK: Thermodynamics at non-zero baryon number density: A comparison of lattice and hadron resonance gas model calculations. *Phys. Lett.* **B571**, 67 (2003).

[134] D. B. BLASCHKE and K. A. BUGAEV: Thermodynamics of resonances with finite width. *Phys. Part. Nucl. Lett.* **2**, 305 (2005).

[135] M. CHENG *et al.*: The QCD equation of state with almost physical quark masses. *Phys. Rev.* **D77**, 014511 (2008).

[136] C. M. HUNG and E. V. SHURYAK: Hydrodynamics near the QCD phase transition: Looking for the longest lived fireball. *Phys. Rev. Lett.* **75**, 4003 (1995).

[137] G. ENDRODI, Z. FODOR, S. D. KATZ and K. K. SZABO: The equation of state at high temperatures from lattice QCD. *Proc. Sci.* **LATTICE2007**, 228 (2006).

[138] G. BOYD *et al.*: Thermodynamics of SU(3) lattice gauge theory. *Nucl. Phys.* **B469**, 419 (1996).

[139] Z. FODOR: QCD thermodynamics. *Proc. Sci.* **LATTICE2007**, 011 (2006).

[140] Y. AOKI, Z. FODOR, S. D. KATZ and K. K. SZABO: The equation of state in lattice QCD: With physical quark masses towards the continuum limit. *J. High Energy Phys.* **1**, 089 (2006).

[141] C. R. ALLTON *et al.*: Thermodynamics of two flavor QCD to sixth order in quark chemical potential. *Phys. Rev.* **D71**, 054508 (2005).

[142] C. R. ALLTON *et al.*: The equation of state for two flavor QCD at non-zero chemical potential. *Phys. Rev.* **D68**, 014507 (2003).

[143] R. V. GAVAI and S. GUPTA: The critical end point of QCD. *Phys. Rev.* **D71**, 114014 (2005).

[144] R. V. GAVAI, S. GUPTA and P. MAJUMDAR: Susceptibilities and screening masses in two flavor QCD. *Phys. Rev.* **D65**, 054506 (2002).

[145] R. V. GAVAI and S. GUPTA: Simple patterns for non-linear susceptibilities near T(c). *Phys. Rev.* **D72**, 054006 (2005).

[146] F. KARSCH, S. EJIRI and K. REDLICH: Hadronic fluctuations in the QGP. *Nucl. Phys.* **A774**, 619 (2006).

[147] S. EJIRI, F. KARSCH and K. REDLICH: Hadronic fluctuations at the QCD phase transition. *Phys. Lett.* **B633**, 275 (2006).

[148] J. LIAO and E. V. SHURYAK: What do lattice baryonic susceptibilities tell us about quarks, diquarks and baryons at T > T(c)? *Phys. Rev.* **D73**, 014509 (2006).

[149] C. SASAKI, B. FRIMAN and K. REDLICH: Quark number fluctuations in a chiral model at finite baryon chemical potential. *Phys. Rev.* **D75**, 054026 (2007).

[150] C. SASAKI, B. FRIMAN and K. REDLICH: Susceptibilities and the phase structure of a chiral model with Polyakov loops. *Phys. Rev.* **D75**, 074013 (2007).

[151] S. K. GHOSH, T. K. MUKHERJEE, M. G. MUSTAFA and R. RAY: Susceptibilities and speed of sound from PNJL model. *Phys. Rev.* **D73**, 114007 (2006).

[152] S. ROESSNER, C. RATTI and W. WEISE: Polyakov loop, diquarks and the two-flavour phase diagram. *Phys. Rev.* **D75**, 034007 (2007).

[153] S. K. GHOSH, T. K. MUKHERJEE, M. G. MUSTAFA and R. RAY: PNJL model with a Van der Monde term. *Phys. Rev.* **D77**, 094024 (2008).

[154] C. RATTI, S. ROESSNER and W. WEISE: Quark number susceptibilities: Lattice QCD versus PNJL model. *Phys. Lett.* **B649**, 57 (2007).

[155] J.-P. BLAIZOT, E. IANCU and A. REBHAN: Quark number susceptibilities from HTL-resummed thermodynamics. *Phys. Lett.* **B523**, 143 (2001).

[156] R. V. GAVAI and S. GUPTA: The continuum limit of quark number susceptibilities. *Phys. Rev.* **D65**, 094515 (2002).

[157] R. V. GAVAI and S. GUPTA: Valence quarks in the QCD plasma: Quark number susceptibilities and screening. *Phys. Rev.* **D67**, 034501 (2003).

[158] R. V. GAVAI and S. GUPTA: Pressure and non-linear susceptibilities in QCD at finite chemical potentials. *Phys. Rev.* **D68**, 034506 (2003).

[159] S. MUKHERJEE, M. G. MUSTAFA and R. RAY: Thermodynamics of the PNJL model with nonzero baryon and isospin chemical potentials. *Phys. Rev.* **D75**, 094015 (2007).

[160] K. RAJAGOPAL and F. WILCZEK: Enforced electrical neutrality of the color-flavor locked phase. *Phys. Rev. Lett.* **86**, 3492 (2001).

[161] M. D'ELIA, F. DI RENZO and M.-P. LOMBARDO: The strongly interacting Quark Gluon Plasma, and the critical behaviour of QCD at imaginary chemical potential. *Phys. Rev.* **D76**, 114509 (2007).

[162] K. K. SZABO and A. I. TOTH: Quasiparticle description of the QCD plasma, comparison with lattice results at finite T and mu. *J. High Energy Phys.* **6**, 008 (2003).

[163] C. SCHMIDT: Lattice QCD at finite density. *Proc. Sci.* **LAT2006**, 021 (2006).

[164] C. R. ALLTON *et al.*: The QCD thermal phase transition in the presence of a small chemical potential. *Phys. Rev.* **D66**, 074507 (2002).

[165] F. KARSCH: Lattice QCD at high temperature and the QGP. *AIP Conf. Proc.* **842**, 20 (2006).

[166] C. BERNARD *et al.*: The equation of state for QCD with 2+1 flavors of quarks. *Proc. Sci.* **LAT2005**, 156 (2006).

[167] P. F. KOLB, J. SOLLFRANK and U. W. HEINZ: Elliptic and hexadecupole flow from AGS to LHC energies. *Phys. Lett.* **B459**, 667 (1999).

[168] P. F. KOLB, J. SOLLFRANK and U. W. HEINZ: Anisotropic transverse flow and the quark-hadron phase transition. *Phys. Rev.* **C62**, 054909 (2000).

[169] T. HIRANO: Is early thermalization achieved only near midrapidity in Au + Au collisions at sNN =130 GeV? *Phys. Rev.* **C65**, 011901 (2002).

[170] T. HIRANO and K. TSUDA: Collective flow and two pion correlations from a relativistic hydrodynamic model with early chemical freeze out. *Phys. Rev.* **C66**, 054905 (2002).

[171] R. RAPP: Hadro-chemistry and evolution of (anti-) baryon densities at RHIC. *Phys. Rev.* **C66**, 017901 (2002).

[172] P. F. KOLB and R. RAPP: Transverse flow and hadro-chemistry in Au + Au collisions at s(NN)**(1/2) = 200-GeV. *Phys. Rev.* **C67**, 044903 (2003).

[173] J. SOLLFRANK *et al.*: Hydrodynamical description of 200-A-GeV/c S + Au collisions: Hadron and electromagnetic spectra. *Phys. Rev.* **C55**, 392 (1997).

[174] P. BRAUN-MUNZINGER, D. MAGESTRO, K. REDLICH and J. STACHEL: Hadron production in Au Au collisions at RHIC. *Phys. Lett.* **B518**, 41 (2001).

[175] T. HIRANO, U. W. HEINZ, D. KHARZEEV, R. LACEY and Y. NARA: Hadronic dissipative effects on elliptic flow in ultrarelativistic heavy-ion collisions. *Phys. Lett.* **B636**, 299 (2006).

[176] K. J. ESKOLA, H. NIEMI and P. V. RUUSKANEN: Dynamical freeze-out condition in ultrarelativistic heavy ion collisions. *Phys. Rev.* **C77**, 044907 (2008).

[177] T. HIRANO, U. W. HEINZ, D. KHARZEEV, R. LACEY and Y. NARA: Elliptic flow from a hybrid CGC, full 3D hydro and hadronic cascade model. *J. Phys.* **G34**, S879 (2007).

[178] J. ADAMS *et al.*: Multi-strange baryon elliptic flow in Au + Au collisions at s(NN)**(1/2) = 200-GeV. *Phys. Rev. Lett.* **95**, 122301 (2005).

[179] A. KRASNITZ and R. VENUGOPALAN: The initial energy density of gluons produced in very high energy nuclear collisions. *Phys. Rev. Lett.* **84**, 4309 (2000).

[180] H. NIEMI, K. J. ESKOLA and P. V. RUUSKANEN: Elliptic flow in nuclear collisions at the Large Hadron Collider. *arXiv:0806.1116* (2008).

[181] R. DASHEN, S.-K. MA and H. J. BERNSTEIN: S Matrix formulation of statistical mechanics. *Phys. Rev.* **187**, 345 (1969).

[182] Z. FODOR and S. D. KATZ: Critical point of QCD at finite T and mu, lattice results for physical quark masses. *J. High Energy Phys.* **4**, 050 (2004).

[183] Y. HATTA and T. IKEDA: Universality, the QCD critical / tricritical point and the quark number susceptibility. *Phys. Rev.* **D67**, 014028 (2003).

[184] B.-J. SCHAEFER and J. WAMBACH: Susceptibilities near the QCD (tri)critical point. *Phys. Rev.* **D75**, 085015 (2007).

[185] R. Guida and J. Zinn-Justin: 3D Ising model: The scaling equation of state. *Nucl. Phys.* **B489**, 626 (1997).

[186] C. Nonaka and M. Asakawa: Hydrodynamical evolution near the QCD critical end point. *Phys. Rev.* **C71**, 044904 (2005).

[187] W. Gebhardt and U. Krey: Phasenübergänge und kritische Phänomene. *Braunschweig/Wiesbaden: Friedr. Vieweg & Sohn* (1980).

[188] L. D. Landau and E. M. Lifshitz: Statistical Physics, 3rd edn. *Oxford, UK: Pergamon* (1980).

[189] K. Paech, H. Stöcker and A. Dumitru: Hydrodynamics near a chiral critical point. *Phys. Rev.* **C68**, 044907 (2003).

[190] K. Paech and A. Dumitru: Density inhomogeneities in heavy ion collisions around the critical point. *Phys. Lett.* **B623**, 200 (2005).

[191] J. Steinheimer *et al.*: (3+1)-dimensional hydrodynamic expansion with a critical point from realistic initial conditions. *Phys. Rev.* **C77**, 034901 (2008).

[192] K. Redlich, B. Friman and C. Sasaki: Charge fluctuations along the QCD phase boundary. *J. Phys.* **G32**, S283 (2006).

[193] M. E. Peskin and D. V. Schroeder: An Introduction to Quantum Field Theory. *Reading, USA: Addison-Wesley* (1995).

[194] C. N. Yang and R. L. Mills: Conservation of isotopic spin and isotopic gauge invariance. *Phys. Rev.* **96**, 191 (1954).

[195] L. D. Faddeev and V. N. Popov: Feynman diagrams for the Yang-Mills field. *Phys. Lett.* **B25**, 29 (1967).

[196] A. M. Polyakov: Thermal properties of gauge fields and quark liberation. *Phys. Lett.* **B72**, 477 (1978).

[197] M. G. Alford, K. Rajagopal and F. Wilczek: QCD at finite baryon density: Nucleon droplets and color superconductivity. *Phys. Lett.* **B422**, 247 (1998).

[198] R. Rapp, T. Schäfer, E. V. Shuryak and M. Velkovsky: Diquark bose condensates in high density matter and instantons. *Phys. Rev. Lett.* **81**, 53 (1998).

[199] R. D. Pisarski and D. H. Rischke: A first order transition to, and then parity violation in, a color superconductor. *Phys. Rev. Lett.* **83**, 37 (1999).

[200] K. Rajagopal and F. Wilczek: At the Frontier of Particle Physics, vol. 3, chpt. 35. *Singapore: World Scientific*, 2061 (2001).

[201] M. G. Alford: Color superconducting quark matter. *Ann. Rev. Nucl. Part. Sci.* **51**, 131 (2001).

[202] S. B. Rüster, I. A. Shovkovy and D. H. Rischke: Phase diagram of dense neutral three-flavor quark matter. *Nucl. Phys.* **A743**, 127 (2004).

[203] M. G. Alford: Color superconductivity in ultra-dense quark matter. *Proc. Sci.* **LAT2006**, 001 (2006).

[204] M. G. Alford, K. Rajagopal and F. Wilczek: Color-flavor locking and chiral symmetry breaking in high density QCD. *Nucl. Phys.* **B537**, 443 (1999).

[205] J. I. Kapusta: Quantum chromodynamics at high temperature. *Nucl. Phys.* **B148**, 461 (1979).

[206] L. G. Yaffe and B. Svetitsky: First order phase transition in the SU(3) gauge theory at finite temperature. *Phys. Rev.* **D26**, 963 (1982).

[207] M. Okamoto *et al.*: Equation of state for pure SU(3) gauge theory with renormalization group improved action. *Phys. Rev.* **D60**, 094510 (1999).

[208] R. D. Pisarski and F. Wilczek: Remarks on the chiral phase transition in chromodynamics. *Phys. Rev.* **D29**, 338 (1984).

[209] K. Rajagopal and F. Wilczek: Static and dynamic critical phenomena at a second order QCD phase transition. *Nucl. Phys.* **B399**, 395 (1993).

[210] S. A. Gottlieb *et al.*: Thermodynamics of lattice QCD with two light quark flavours on a 16**3 x 8 lattice. II. *Phys. Rev.* **D55**, 6852 (1997).

[211] A. Ali Khan *et al.*: Phase structure and critical temperature of two flavor QCD with renormalization group improved gauge action and clover improved Wilson quark action. *Phys. Rev.* **D63**, 034502 (2001).

[212] F. R. Brown *et al.*: On the existence of a phase transition for QCD with three light quarks. *Phys. Rev. Lett.* **65**, 2491 (1990).

[213] S. Aoki *et al.*: Phase structure of lattice QCD at finite temperature for 2+1 flavors of Kogut-Susskind quarks. *Nucl. Phys. Proc. Suppl.* **73**, 459 (1999).

[214] Y. Aoki, Z. Fodor, S. D. Katz and K. K. Szabo: The QCD transition temperature: Results with physical masses in the continuum limit. *Phys. Lett.* **B643**, 46 (2006).

[215] F. Karsch: Recent lattice results on finite temperature and density QCD, part II. *Proc. Sci.* **LATTICE2007**, 015 (2007).

[216] O. Scavenius, A. Mocsy, I. N. Mishustin and D. H. Rischke: Chiral phase transition within effective models with constituent quarks. *Phys. Rev.* **C64**, 045202 (2001).

[217] M. A. Stephanov: Random matrix model of QCD at finite density and the nature of the quenched limit. *Phys. Rev. Lett.* **76**, 4472 (1996).

[218] M. A. Halasz, A. D. Jackson, R. E. Shrock, M. A. Stephanov and J. J. M. Verbaarschot: On the phase diagram of QCD. *Phys. Rev.* **D58**, 096007 (1998).

[219] M. Asakawa and K. Yazaki: Chiral restoration at finite density and temperature. *Nucl. Phys.* **A504**, 668 (1989).

[220] S. P. KLEVANSKY: The Nambu-Jona-Lasinio model of quantum chromodynamics. *Rev. Mod. Phys.* **64**, 649 (1992).

[221] M. D'ELIA, A. DI GIACOMO and C. PICA: Two flavor QCD and confinement. *Phys. Rev.* **D72**, 114510 (2005).

[222] P. DE FORCRAND and O. PHILIPSEN: The chiral critical line of N(f) = 2+1 QCD at zero and non-zero baryon density. *J. High Energy Phys.* **1**, 077 (2007).

[223] F. KARSCH, E. LAERMANN and C. SCHMIDT: The chiral critical point in 3-flavor QCD. *Phys. Lett.* **B520**, 41 (2001).

[224] P. C. HOHENBERG and B. I. HALPERIN: Theory of dynamic critical phenomena. *Rev. Mod. Phys.* **49**, 435 (1977).

[225] H. FUJII and M. OHTANI: Soft modes at the critical end point in the chiral effective models. *Prog. Theor. Phys. Suppl.* **153**, 157 (2004).

[226] D. T. SON and M. A. STEPHANOV: Dynamic universality class of the QCD critical point. *Phys. Rev.* **D70**, 056001 (2004).

[227] C. SCHMIDT *et al.*: The quark mass and mu dependence of the QCD chiral critical point. *Nucl. Phys. Proc. Suppl.* **119**, 517 (2003).

[228] Z. FODOR and S. D. KATZ: Lattice determination of the critical point of QCD at finite T and mu. *J. High Energy Phys.* **3**, 014 (2002).

[229] S. EJIRI *et al.*: Study of QCD thermodynamics at finite density by Taylor expansion. *Prog. Theor. Phys. Suppl.* **153**, 118 (2004).

[230] C.-N. YANG and T. D. LEE: Statistical theory of equations of state and phase transitions. I: Theory of condensation. *Phys. Rev.* **87**, 404 (1952).

[231] T. D. LEE and C.-N. YANG: Statistical theory of equations of state and phase transitions. II: Lattice gas and Ising model. *Phys. Rev.* **87**, 410 (1952).

[232] M. FISCHER: Lectures in Theoretical Physics, vol. 12C. *Boulder, USA: University of Colorado Press* (1965).

[233] B. KLEIN, D. TOUBLAN and J. J. M. VERBAARSCHOT: The QCD phase diagram at nonzero temperature, baryon and isospin chemical potentials in random matrix theory. *Phys. Rev.* **D68**, 014009 (2003).

[234] D. TOUBLAN and J. B. KOGUT: Isospin chemical potential and the QCD phase diagram at nonzero temperature and baryon chemical potential. *Phys. Lett.* **B564**, 212 (2003).

[235] A. BARDUCCI, G. PETTINI, L. RAVAGLI and R. CASALBUONI: Ladder-QCD at finite isospin chemical potential. *Phys. Lett.* **B564**, 217 (2003).

[236] M. FRANK, M. BUBALLA and M. OERTEL: Flavor-mixing effects on the QCD phase diagram at non- vanishing isospin chemical potential: One or two phase transitions? *Phys. Lett.* **B562**, 221 (2003).

[237] Z. FODOR and S. D. KATZ: A new method to study lattice QCD at finite temperature and chemical potential. *Phys. Lett.* **B534**, 87 (2002).

[238] V. AZCOITI, G. DI CARLO, A. GALANTE and V. LALIENA: Finite density QCD: A new approach. *J. High Energy Physics* **12**, 010 (2004).

[239] O. PHILIPSEN: The QCD phase diagram at zero and small baryon density. *Proc. Sci.* **LAT2005**, 016 (2006).

[240] J. ENGELS, J. FINGBERG and M. WEBER: Finite size scaling analysis of SU(2) lattice gauge theory in (3+1)-dimensions. *Nucl. Phys.* **B332**, 737 (1990).

[241] A. D. LINDE: Infrared problem in thermodynamics of the Yang-Mills gas. *Phys. Lett.* **B96**, 289 (1980).

[242] D. J. GROSS, R. D. PISARSKI and L. G. YAFFE: QCD and instantons at finite temperature. *Rev. Mod. Phys.* **53**, 43 (1981).

[243] K. KAJANTIE, M. LAINE, K. RUMMUKAINEN and Y. SCHRÖDER: The pressure of hot QCD up to g**6 ln(1/g). *Phys. Rev.* **D67**, 105008 (2003).

[244] A. VUORINEN: The pressure of QCD at finite temperatures and chemical potentials. *Phys. Rev.* **D68**, 054017 (2003).

[245] A. VUORINEN: Quark number susceptibilities of hot QCD up to g**6 ln(g). *Phys. Rev.* **D67**, 074032 (2003).

[246] G. D. MOORE: Pressure of hot QCD at large N(f). *J. High Energy Physics* **10**, 055 (2002).

[247] A. IPP, G. D. MOORE and A. REBHAN: Comment on 'Pressure of hot QCD at large N(f)' with corrected exact result. *J. High Energy Physics* **1**, 037 (2003).

[248] A. IPP and A. REBHAN: Thermodynamics of large-N(f) QCD at finite chemical potential. *J. High Energy Physics* **6**, 032 (2003).

[249] A. IPP, A. REBHAN and A. VUORINEN: Perturbative QCD at non-zero chemical potential: Comparison with the large-N(f) limit and apparent convergence. *Phys. Rev.* **D69**, 077901 (2004).

[250] F. KARSCH, A. PATKOS and P. PETRECZKY: Screened perturbation theory. *Phys. Lett.* **B401**, 69 (1997).

[251] J. O. ANDERSEN, E. BRAATEN and M. STRICKLAND: Screened perturbation theory to three loops. *Phys. Rev.* **D63**, 105008 (2001).

[252] J. O. ANDERSEN and M. STRICKLAND: Mass expansions of screened perturbation theory. *Phys. Rev.* **D64**, 105012 (2001).

[253] J. O. ANDERSEN, E. BRAATEN and M. STRICKLAND: Hard-thermal-loop resummation of the free energy of a hot gluon plasma. *Phys. Rev. Lett.* **83**, 2139 (1999).

[254] J. O. Andersen, E. Braaten and M. Strickland: Hard-thermal-loop resummation of the thermodynamics of a hot gluon plasma. *Phys. Rev.* **D61**, 014017 (2000).

[255] J. O. Andersen, E. Braaten and M. Strickland: Hard-thermal-loop resummation of the free energy of a hot quark-gluon plasma. *Phys. Rev.* **D61**, 074016 (2000).

[256] J. O. Andersen, E. Braaten, E. Petitgirard and M. Strickland: HTL perturbation theory to two loops. *Phys. Rev.* **D66**, 085016 (2002).

[257] J. O. Andersen, E. Petitgirard and M. Strickland: Two-loop HTL thermodynamics with quarks. *Phys. Rev.* **D70**, 045001 (2004).

[258] J. O. Andersen and M. Strickland: Resummation in hot field theories. *Ann. Phys.* **317**, 281 (2005).

[259] S. Scherer: Introduction to chiral perturbation theory. *Adv. Nucl. Phys.* **27**, 277 (2003).

[260] C. Ratti, M. A. Thaler and W. Weise: Phases of QCD: Lattice thermodynamics and a field theoretical model. *Phys. Rev.* **D73**, 014019 (2006).

[261] B.-J. Schaefer, J. M. Pawlowski and J. Wambach: The phase structure of the Polyakov–quark-meson model. *Phys. Rev.* **D76**, 074023 (2007).

[262] P. Levai and U. W. Heinz: Massive gluons and quarks and the equation of state obtained from SU(3) lattice QCD. *Phys. Rev.* **C57**, 1879 (1998).

[263] E. V. Shuryak and I. Zahed: Towards a theory of binary bound states in the quark gluon plasma. *Phys. Rev.* **D70**, 054507 (2004).

[264] G. Boyd, F. Karsch and S. Gupta: The quark propagator at finite temperature. *Nucl. Phys.* **B385**, 481 (1992).

[265] P. Petreczky, F. Karsch, E. Laermann, S. Stickan and I. Wetzorke: Temporal quark and gluon propagators: Measuring the quasiparticle masses. *Nucl. Phys. Proc. Suppl.* **106**, 513 (2002).

[266] F. Karsch and M. Kitazawa: Spectral properties of quarks above T_c in quenched lattice QCD. *Phys. Lett.* **B658**, 45 (2007).

[267] J. M. Maldacena: The large N limit of superconformal field theories and supergravity. *Adv. Theor. Math. Phys.* **2**, 231 (1998).

[268] S. S. Gubser, I. R. Klebanov and A. M. Polyakov: Gauge theory correlators from non-critical string theory. *Phys. Lett.* **B428**, 105 (1998).

[269] E. Witten: Anti-de Sitter space, thermal phase transition, and confinement in gauge theories. *Adv. Theor. Math. Phys.* **2**, 505 (1998).

[270] F. Karsch: Recent lattice results on finite temperature and density QCD, part I. *Proc. Sci.* **CPOD2007**, 026 (2007).

[271] G. Boyd *et al.*: Equation of state for the SU(3) gauge theory. *Phys. Rev. Lett.* **75**, 4169 (1995).

[272] A. Papa: SU(3) thermodynamics on small lattices. *Nucl. Phys.* **B478**, 335 (1996).

[273] B. Beinlich, F. Karsch, E. Laermann and A. Peikert: String tension and thermodynamics with tree level and tadpole improved actions. *Eur. Phys. J.* **C6**, 133 (1999).

Aknowledgements

Erklärung

Hiermit versichere ich, dass ich die vorliegende Arbeit ohne unzulässige Hilfe Dritter und ohne Benutzung anderer als der angegebenen Hilfsmittel angefertigt habe; die aus fremden Quellen direkt oder indirekt übernommenen Gedanken sind als solche kenntlich gemacht worden. Die Arbeit wurde bisher weder im Inland noch im Ausland in gleicher oder ähnlicher Form einer anderen Prüfungsbehörde vorgelegt.

Die Dissertation wurde am Forschungszentrum Dresden-Rossendorf e. V. unter der wissenschaftlichen Betreuung von Herrn Prof. Dr. Burkhard Kämpfer angefertigt. Ich habe bisher an keiner Institution, weder im Inland noch im Ausland, einen Antrag auf die Eröffnung eines Promotionsverfahrens gestellt. Ich erkläre ferner, dass ich die Promotionsordnung der Fakultät Mathematik und Naturwissenschaften der Technischen Universität Dresden vom 20.03.2000 anerkenne.

Marcus Bluhm